
2 **Consolidation and longevity of the CMS**
3 **Resistive Plate Chamber system in view of the**
4 **High-Luminosity LHC Upgrade**

5



Alexis Fagot

Thesis to obtain the degree of
Doctor of Philosophy in Physics
Academic year 2018-2019

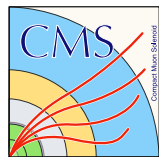


⁷

⁸ Promotors: Dr. Michael Tytgat
Prof. Dr. Dirk Ryckbosch

⁹
¹⁰ Ghent University
¹¹ Faculty of Sciences
¹² Department of Physics and Astronomy
¹³ Proeftuinstraat 86, B-9000 Ghent, Belgium
¹⁴ Tel.: +32 9 264.65.28
¹⁵ Fax.: +32 9 264.66.97

¹⁶



Alexis Fagot

Thesis to obtain the degree of
Doctor of Philosophy in Physics
Academic year 2018-2019



17

Acknowledgements

18

19

XX/XX/2018

Alexis Fagot

Table of Contents

21	Acknowledgements	i
22	Nederlandse samenvatting	vii
23	English summary	ix
24	1 Introduction	1-1
25	2 Investigating the TeV scale	2-1
26	2.1 The Standard Model of Particle Physics	2-1
27	2.1.1 A history of particle physics	2-2
28	2.1.2 Construction and validation of the Standard Model	2-15
29	2.1.3 Investigating the TeV scale	2-16
30	2.2 The Large Hadron Collider & the Compact Muon Solenoid	2-21
31	2.2.1 LHC, the most powerful particle accelerator	2-21
32	2.2.2 Timeline of operation	2-25
33	2.2.3 High Luminosity LHC	2-27
34	2.2.4 CMS, a multipurpose experiment	2-27
35	2.2.4.1 The silicon tracker, core of CMS	2-29
36	2.2.4.2 The calorimeters, measurement of particle's energy	2-30
37	2.2.4.3 The muon system, corner stone of CMS	2-31
38	3 Muon Phase-II Upgrade	3-1
39	3.1 Motivations for HL-LHC and the upgrade of CMS	3-2
40	3.2 Description of the muon system	3-3
41	3.3 Muon system requirements for HL-LHC	3-7
42	3.4 Necessity for improved electronics	3-8
43	3.5 New detectors and increased acceptance	3-10
44	3.5.1 Gas electron multipliers	3-10
45	3.5.2 Improved forward resistive plate chambers	3-14
46	3.5.3 Installation schedule	3-16
47	3.6 Implications of the different upgrades on the Level-1 Trigger. Improvement of physics performance.	3-17
48	3.7 Ecofriendly gas studies	3-21
50	4 Physics of Resistive plate chambers	4-1
51	4.1 Principle	4-1
52	4.2 Rate capability and time resolution of Resistive Plate Chambers	4-3
53	4.2.1 Operation modes	4-3
54	4.2.2 Standard gas mixture for RPCs operated in collider experiments	4-5
55	4.2.3 Detector designs and performance	4-9

56	4.2.3.1	Double gap RPC	4-11
57	4.2.3.2	Multigap RPC (MRPC)	4-13
58	4.2.3.3	Charge distribution and performance limitations	4-16
59	4.3	Signal formation	4-18
60	4.3.1	Energy loss at intermediate energies	4-19
61	4.3.2	Primary ionization	4-23
62	4.3.3	Development and propagation of avalanches	4-27
63	4.3.4	Drift and diffusion of the electron cloud	4-31
64	4.3.5	Space charge effect & streamers	4-33
65	4.4	Effect of atmospherical conditions on the detector's performance	4-37
66	5	Longevity studies and Consolidation of the present CMS RPC subsystem	5-1
67	5.1	Testing detectors under extreme conditions	5-2
68	5.1.1	GIF	5-4
69	5.1.2	GIF++	5-5
70	5.2	Preliminary studies at GIF	5-7
71	5.2.1	RPC test setup	5-7
72	5.2.2	Geometrical acceptance of the setup layout to cosmic muons	5-9
73	5.2.2.1	Description of the simulation layout	5-10
74	5.2.2.2	Simulation procedure	5-11
75	5.2.2.3	Results and limitations	5-12
76	5.2.3	Photon flux at GIF	5-14
77	5.2.4	Results and discussions	5-17
78	5.3	Longevity tests at GIF++	5-20
79	5.3.1	Selection and characterization of CMS RPCs for longevity at GIF++	5-20
80	5.3.2	RPC test setup	5-22
81	5.3.3	GIF++ data flow	5-24
82	5.3.4	Measurements performed during beam periods	5-26
83	5.3.4.1	Efficiency scans	5-26
84	5.3.4.2	Rate scans	5-26
85	5.3.4.3	Offline analysis and Data Quality Monitoring	5-27
86	5.3.5	Measurements performed during irradiation periods	5-28
87	5.3.5.1	Longevity scans	5-29
88	5.3.5.2	Daily rate monitoring scans	5-30
89	5.3.5.3	Weekly noise monitoring scans	5-31
90	5.3.5.4	Weekly source scans	5-31
91	5.3.5.5	Weekly current scans	5-32
92	5.3.5.6	Resistivity measurements	5-32
93	5.3.6	Results and discussions	5-32
94	6	Improved RPC investigation and preliminary electronics studies	6-1
95	6.1	FEE candidate for the production of iRPCs	6-1
96	6.1.1	CMS RPCROC: the RPC upgrade baseline	6-2
97	6.1.2	INFN Front-End Electronics: a robust back-up solution	6-3
98	6.2	Preliminary tests at CERN	6-3
99	7	Conclusions and outlooks	7-1
100	7.1	Conclusions	7-1
101	7.2	Outlooks	7-1

A A data acquisition software for CAEN VME TDCs	A-1
A.1 GIF++ DAQ file tree	A-1
A.2 Usage of the DAQ	A-2
A.3 Description of the readout setup	A-3
A.4 Data read-out	A-3
A.4.1 V1190A TDCs	A-4
A.4.2 DataReader	A-7
A.4.3 Data quality flag	A-10
A.5 Communications	A-12
A.5.1 V1718 USB Bridge	A-13
A.5.2 Configuration file	A-14
A.5.3 WebDCS/DAQ intercommunication	A-17
A.5.4 Example of inter-process communication cycle	A-17
A.6 Software export	A-18
B Details on the offline analysis package	B-1
B.1 GIF++ Offline Analysis file tree	B-1
B.2 Usage of the Offline Analysis	B-2
B.2.1 Output of the offline tool	B-3
B.2.1.1 ROOT file	B-3
B.2.1.2 CSV files	B-5
B.3 Analysis inputs and information handling	B-6
B.3.1 Dimensions file and IniFile parser	B-7
B.3.2 TDC to RPC link file and Mapping	B-8
B.4 Description of GIF++ setup within the Offline Analysis tool	B-9
B.4.1 RPC objects	B-9
B.4.2 Trolley objects	B-10
B.4.3 Infrastructure object	B-10
B.5 Handeling of data	B-12
B.5.1 RPC hits	B-13
B.5.2 Clusters of hits	B-14
B.6 DAQ data Analysis	B-15
B.6.1 Determination of the run type	B-16
B.6.2 Beam time window calculation for efficiency runs	B-17
B.6.3 Data loop and histogram filling	B-18
B.6.4 Results calculation	B-21
B.6.4.1 Rate normalisation	B-21
B.6.4.2 Rate and activity	B-23
B.6.4.3 Correction of muon performance parameters	B-25
B.6.4.4 Strip masking tool	B-27
B.6.4.5 Output CSV files filling	B-29
B.7 Current information extraction	B-31

143

Nederlandse samenvatting –Dutch Summary–

144

English summary

List of Figures

146

- | | | | |
|-----|------|---|------|
| 147 | 2.1 | Solar spectrum with spectral lines as it visually appeared to Fraunhofer. | 2-2 |
| 148 | 2.2 | Through the gold foil experiment, Rutherford could show that most of the mass of atoms was contained in a positively charged nucleus and could then propose a more accurate atomic model than that of Thomson. | 2-3 |
| 150 | | | |
| 151 | 2.3 | Figure 2.3a: The orbits in which the electron may travel according to the Bohr model of the hydrogen atom. An electron jumps between orbits and is accompanied by an emitted or absorbed amount of electromagnetic energy ($h\nu$). The orbits radius increases as n^2 . Figure 2.3b: Elliptical orbits with the same energy and quantized angular momentum $l = 0, 1, \dots, n - 1$ in the case $n = 5$. Figure 2.3c: Illustration of quantum mechanical orbital angular momentum. The cones and plane represent possible orientations of the angular momentum vector for $l = 2$ and $m = -2, -1, 0, 1, 2$ | 2-5 |
| 152 | | | |
| 153 | | | |
| 154 | | | |
| 155 | | | |
| 156 | | | |
| 157 | | | |
| 158 | 2.4 | Figure 2.4a: The spectral lines of mercury vapor lamp anomalous Zeeman effect without magnetic field (A) and with magnetic field (B - transverse Zeeman effect & C - longitudinal Zeeman effect). Figure 2.4b: Stern-Gerlach experiment: Silver atoms traveling through an inhomogeneous magnetic field and being deflected up or down depending on their spin. | 2-6 |
| 159 | | | |
| 160 | | | |
| 161 | | | |
| 162 | | | |
| 163 | 2.5 | Figure 2.5a: decay of a μ -meson in an emulsion. Figure 2.5b: track of a π -meson in an emulsion signed by Lattes, Powell, and Occhialini. | 2-9 |
| 164 | | | |
| 165 | 2.6 | Figure 2.6a: Meson octet. Figure 2.6b: Baryon octet. Figure 2.6c: Baryon decuplet. | 2-10 |
| 166 | | | |
| 167 | 2.7 | Discovery of the J/Ψ by both SPEAR (SLAC [74]) in Figure 2.7a and AGS (BNL [75]) in Figure 2.7b. In Figure 2.7a, the cross section versus energy is showed for (a) multi hadron final states, (b) e^+e^- final states, and (c) $\mu^+\mu^-, \pi^+\pi^-$ and K^+K^- final states. | 2-11 |
| 168 | | | |
| 169 | 2.8 | Figure 2.8a: the color field of QCD only allows for "white" baryons, particles composed of quarks, to exist. Examples are given for mesons, composed of a quark and its anti-quark, and hadrons, composed of three differently colored quarks or anti-quarks. Other exotic baryons have been predicted and observed, such as tetraquarks and pentaquarks. Figure 2.8b: a crossed analysis performed thanks to the data collected by various experiments at different energies have showed that the coupling constant evolves as predicted by the mechanism of asymptotic freedom [87]. | 2-12 |
| 170 | | | |
| 171 | | | |
| 172 | | | |
| 173 | | | |
| 174 | | | |
| 175 | | | |
| 176 | 2.9 | Energy spectrum of beta particles emitted by a source of ^{210}Bi | 2-13 |
| 177 | | | |
| 178 | 2.10 | As explained through Figure 2.10a, the Wu experiment consisted in measuring the preferred direction of emission of beta rays of a Cobalt source placed in a stable magnetic field aligned, in one case, and anti-aligned, in the other case, with the nuclear spin. The result of Figure 2.10b showed a violation of parity. | 2-14 |
| 179 | | | |
| 180 | | | |

181	2.11	The elementary particles of the Standard Model are shown along with their properties. Their interactions with the strong, weak and electromagnetic forces have been made explicit using color squares. In the left column, the scalar Higgs boson is depicted. The center is focused on the matter particles, the fermions, and the right column on the force carriers, the gauge bosons. The role of the Higgs boson in electroweak symmetry breaking is highlighted, and the corresponding way properties of the various particles differ in the (high-energy) symmetric phase (top) and the (low-energy) broken-symmetry phase (bottom) are shown.	2-16
182			
183			
184			
185			
186			
187			
188			
189	2.12	Figure 2.12a: Total proton-proton cross-section as a function of the collisions center-of-mass energy \sqrt{s} [116] with cosmic-ray data from Akeno Observatory and Fly's Eye Collaboration. Figure 2.12b: Total proton-(anti)proton and interaction channel cross-sections in the TeV scale.	2-17
190			
191			
192			
193	2.13	Rotation curve (points) of the galaxy M33 compared with best fitting model (line). The short-dashed line represents the rotation profile that would be expected from the observation of the stellar disc alone [128].	2-18
194			
195			
196	2.14	Cosmic Microwave Background as measured by the space observatory Planck which mean temperature is $T_\gamma = (2.7255 \pm 0.0006)\text{K}$ with anisotropies of the order of a few μK	2-19
197			
198			
199	2.15	CERN accelerator complex.	2-22
200			
201	2.16	Pictures of the different accelerators. From top to bottom: first the LINAC 2 and the Pb source of LINAC 3. Then the Booster and the LEIR. Finally, the PS, the SPS and the LHC.	2-23
202			
203	2.17	Figure 2.17a: schematics of the LHC cryodipoles. 1: Superconducting Coils, 2: Beam pipe, 3: Heat exchanger Pipe, 4: Helium-II Vessel, 5: Superconducting Bus-bar, 6: Iron Yoke, 7: Non-Magnetic Collars, 8: Vacuum Vessel, 9: Radiation Screen, 10: Thermal Shield, 11: Auxiliary Bus-bar Tube, 12: Instrumentation Feed Throughs, 13: Protection Diode, 14: Quadrupole Bus-bars, 15: Spool Piece Bus-bars. Figure 2.17b: magnetic field and resulting motion force applied on the beam particles.	2-24
204			
205			
206			
207			
208			
209			
210	2.18	The LHC quadrupoles (Figure 2.18a) showed together with the magnetic fields and resulting focussing force applied on the beam by two consecutive quadrupoles (Figure 2.18b).	2-24
211			
212			
213	2.19	Distribution of the four-lepton invariant mass for the $ZZ \rightarrow 4l$ analysis as presented by both ATLAS [112] and CMS [113] in 2012.	2-25
214			
215	2.20	Detailed timeline projection of for LHC and HL-LHC operation until 2039 showing the evolution of the instantaneous and integrated luminosity as designed (Figure 2.20a) and in the ultimate case where the instantaneous luminosity is increased to $7.5 \times 10^{34}\text{cm}^{-2}\text{s}^{-1}$ thanks to a new increase of instantaneous luminosity during Run 5 (Figure 2.20b) [175, 176].	2-26
216			
217			
218			
219			
220	2.21	Picture of the CMS barrel. The red outer layer is the muon system hosted into the red iron return yokes. The calorimeters are the blue cylinder inside in magnet solenoid and the tracker is the inner yellow cylinder built around the beam pipe.	2-28
221			
222			
223	2.22	View of the CMS apparatus and of its different components.	2-28
224			
225	2.23	Slice showing CMS sub-detectors and how particles interact with them.	2-29
226			
227	2.24	CMS tracker.	2-30
228	2.25	Figure 2.25a: picture of the ECAL. Figure 2.25b: picture of the lead tungstate crystals composing the ECAL.	2-30
	2.26	CMS hadron calorimeter barrel.	2-31

229	2.27	A quadrant of the muon system, showing DTs (yellow), RPCs (blue), and CSCs (green).	2-32
230			
231	3.1	Slice of the CMS detector showing example of passage of SM particles and R-hadrons. On the one hand, lepton-like HSCPs will appear to behave like slow and heavy muons. On the other hand, R-hadrons are likely to convert into other kind of charged or neutral R-hadrons due to interactions inside the detector volume.	3-3
232			
233	3.2	Figure 3.2a: Barrel wheel with its detector rings and return yokes. Figure 3.2b: CSC endcap disk with the 2 CSC stations. The outer station is made of 10 deg detectors while the inner station is made of 20 deg detectors. Figure 3.2c: RPC endcap disk. The inner station is not equipped and the inner CSC station can be seen.	3-4
234			
235	3.3	Figure 3.3a: Cross section of a DT module showing the two superlayers measuring the ϕ coordinate, perpendicular to the cross section plane, and the superlayer measuring the η coordinate, placed in between the two others with honeycomb and parallel to the cross section plane. The DT detector is sandwiched in between 2 RPCs whose readout strips are perpendicular to the cross section plane, measuring the ϕ coordinate. Figure 3.3b: A DT cell is shown together with its electric field. The path of a muon through a superlayer is shown.	3-4
236			
237	3.4	Figure 3.4a: cathode strips and anode wire layout of a CSC panel. Figure 3.4b avalanche development and charge collection by anode wires and induction on cathode strips inside of a CSC panel.	3-5
238			
239	3.5	Muon track reconstruction through the 6 panels of a CMS CSC using the information of anode wire groups and cathode strip charge distribution combined with comparator bits to decide on which half strip the muon is more likely to have passed.	3-5
240			
241	3.6	Double gap layout of CMS RPCs. Muons passing through the gas volumes will create electron-ions pairs by ionising the gas. this ionisation will immediately translate into a developing avalanche.	3-6
242			
243	3.7	Absorbed dose in the CMS cavern after an integrated luminosity of 3000 fb. Using the interaction point as reference, R is the transverse distance from the beamline and Z is the distance along the beamline.	3-7
244			
245	3.8	A quadrant of the muon system, showing DTs (yellow), RPCs (blue), and CSCs (green). The locations of new forward muon detectors for Phase-II are contained within the dashed box and indicated in red for GEM stations (ME0, GE1/1, and GE2/1) and dark blue for improved RPC (iRPC) stations (RE3/1 and RE4/1).	3-7
246			
247	3.9	Comparison of the simulated time residuals in between reconstructed and true muon times without (blue) and with (red) the upgraded RPC link system.	3-9
248			
249	3.10	RMS of the multiple scattering displacement as a function of muon p_T for the proposed forward muon stations. All of the electromagnetic processes such as bremsstrahlung and magnetic field effect are included in the simulation.	3-10
250			
251	3.11	Schematics of a GEM showing the cathode on top, the GEM foil separating the gas volume into the drift region, in between the cathode and foil, and the induction region, in between the GEM foil and the anode, and the anode on which a 2D readout is installed. A negative voltage is applied on the cathode while the anode is connected to the ground.	3-11
252			
253	3.12	Left: Picture of a CMS GEM foil provided by a scanning electron microscope. Right: Representation of the electric field lines in a GEM hole and of the amplification that electrons and ions undergo in the hole's volume due to the very intense electric field.	3-11
254			

275	3.13 Schematic representation of CMS triple GEMs. The gas volume is divided into 4 areas. The drift area is the region where the primary electrons are created before being amplified a first time while passing through the first GEM foil. Then the process of drift and amplification is repeated twice in following two transfer areas and GEM foils. Finally, the charges have been amplified enough to induce current in the read-out strips while in the last drift area. The dimensions, potentials and electric fields are provided.	3-12
282	3.14 Simulated efficiency and rate of the standalone Level-1 muon trigger using tracks reconstructed in CSCs and all GEM stations compared with Phase-I values in the case where only CSCs are used or CSCs+GE1/1. The zones of inefficiency of the CSC subsystem are compensated by the addition of GEMs during Phase-II and the trigger rates is kept from increasing due to the high luminosity.	3-12
287	3.15 Figure 3.15a: Simulated resolution of the muon direction measurement $\Delta\phi$ with Phase-II conditions. In the second endcap station, the resolution is compared in the case of CSCs (ME2/1) alone and CSCs+GEMs (GE2/1+ME2/1) while a similar resolution measurement is given in the case of the first station (GE1/1+ME1/1). Figure 3.15b: The addition of GEM detectors on stations 1 and 2 (ME0 is considered to contribute to station station 1) as redundant system to CSCs allows to improve the muon momentum improvement through a more accurate measurement of the local bending angles ϕ_1 and ϕ_2	3-13
295	3.16 Simulation of the impact of RPC hit inclusion onto the local trigger primitive efficiency in station 3 (left) and station 4 (right). The contribution of iRPC starts above $ \eta = 1.8$	3-14
298	3.17 Expected hit rate due to neutrons, photons, electrons and positrons at HL-HLC instantaneous luminosity of $5 \times 10^{34} \text{ cm}^{-2}\text{s}^{-1}$ in RE3/1 and RE4/1 chambers. The sensitivities of iRPCs used in the simulation for each particle are reported and differ from one endcap disk to another as the energies of the considered particles varies with the increasing distance from the interaction point.	3-15
303	3.18 Measured average charge per avalanche as a function of the effective electric field for different gas gap thickness in double gap RPCs using HPL electrodes.	3-16
305	3.19 Data flow of the Level-1 Trigger during Phase-II operations.	3-17
306	3.20 Efficiency of the L1 trigger in the endcap region after Phase-II upgrade in the case CSC/GEM/RPC hits are requested in at least 2 stations out of four (3.20a) and in all four stations (3.20b).	3-18
309	3.21 Resolution of the LCT ambiguous events thanks to the combination of CSC and iRPC readout data. Using CSCs only, 2 pairs of hits are possible.	3-19
311	3.22 The angular resolution on reconstructed muon tracks in the GEM overlap region $2.0 < \eta < 2.15$ is compared for Phase-II conditions in the case CSC are alone (Figure 3.22a) and in the case the GEMs' data, including ME0, is combined to which of CSCs (Figure 3.22b).	3-20
315	3.23 Comparison of L1 trigger performances for prompt muons with and without the addition of GEMs in the region $2.1 < \eta < 2.4$ at Phase-II conditions. GEMs would allow a reduction of the trigger accept rate by an order of magnitude (Figure 3.23a) while increasing the trigger efficiency (Figure 3.23b).	3-20

- 366 4.11 Distributions of the induced charge of fast signals on 2 mm (Figure 4.11a) and 8 mm
 367 (Figure 4.11b) RPCs exposed to a radiation rate of 100 Hz/cm². Average induced
 368 charge of fast signals as a function of the high voltage applied on 2 mm and 8 mm
 369 RPCs (Figure 4.11c). In the case of the 2 mm RPC, a saturation of the pre-amplifier
 370 was observed. The average of the distribution is underestimated and the median is
 371 showed together with the average to account for this bias [222]. 4-10
- 372 4.12 Time distributions of the leading, trailing, and average of both leading and trailing
 373 edges for 2 mm (top row) and 8 mm (bottom row) RPCs exposed to a 100 Hz/cm²
 374 radiation rate. The data was collected with RPCs operated at the voltage correspond-
 375 ing to the knee of the efficiency distribution, defined as the point where 95% of the
 376 maximum efficiency is obtained [222]. 4-11
- 377 4.13 Possible double-gap RPC layouts: a) "standard" 1D double-gap RPC, as used in
 378 CMS experiment, where the anodes are facing each other and a 1D read-out plane
 379 is sandwiched in between them, b) double read-out double-gap RPC as used in AT-
 380 LAS experiment, where the cathodes are facing each other and 2 read-out planes are
 381 used on the outer surfaces. This last layout can offer the possibility to use a 2D
 382 reconstruction by using orthogonal read-out planes. 4-12
- 383 4.14 Comparison of performance of CMS double and single gap RPCs using cosmic
 384 muons [218]. Figure 4.14a: Comparison of efficiency sigmoids. Figure 4.14b: Volt-
 385 age distribution at 95% of maximum efficiency. Figure 4.14c: $\Delta_{10\%}^{90\%}$ distribution. . . 4-12
- 386 4.15 Representation of different RPC layouts (wide gap on Figure (a), double gap on
 387 Figure (b) and multigap on Figure (c)), of the corresponding sensitive volume in
 388 gray, and of the associated avalanche size [208]. 4-13
- 389 4.16 Time distributions of the leading, trailing, and average of both leading and trailing
 390 edges for multigap RPCs consisting in two 4 mm (Figure 4.16a) and four 2 mm
 391 (Figure 4.16b) exposed to a 100 Hz/cm² radiation rate. The data was collected with
 392 RPCs operated at the voltage corresponding to the knee of the efficiency distribution,
 393 defined as the point where 95% of the maximum efficiency is obtained [208]. . . . 4-14
- 394 4.17 Presentation of a study of a possible ALICE MRPC cell using 250 μm gas gaps,
 395 620 μm outer glass electrodes, and 550 μm inner floating electrodes (Figure 4.17a),
 396 and of its time resolution performance as a function of the applied high voltage for
 397 different radiation levels referred through different filter settings of the 740 GBq
¹³⁷Cs source the former CERN GIF facility [223]. 4-14
- 398 4.18 Particle identification applied to electrons in the STAR experiment. The identifica-
 399 tion is performed combining ToF and dE/dx measurements [228]. 4-15
- 400 4.19 Comparison of the detector performance of ALICE ToF MRPC [229] at fixed applied
 401 voltage (in blue) and at fixed effective voltage (in red). The effective voltage is kept
 402 fixed by increasing the applied voltage accordingly to the current drawn by the detector. 4-16
- 403 4.20 Ratio between total induced and drifting charge have been simulated for single gap,
 404 double-gap and multigap layouts [230]. The total induced charge for a double-gap
 405 RPC is a factor 2 higher than for a multigap. 4-17
- 406 4.21 Charge spectra have been simulated for single gap, double-gap and multigap lay-
 407 outs [230]. It appears that when single gap shows a decreasing spectrum, double and
 408 multigap layouts exhibit a spectrum whose peak is detached from the origin. The
 409 detachment gets stronger as the number of gaps increases. 4-17
- 410 4.22 The maximal theoretical efficiency is simulated for single gap, double-gap and multi-
 411 gap layouts [230] at a constant gap thickness of 2 mm and using an effective Townsend
 412 coefficient of 9 mm⁻¹. 4-18

414	4.23	Mass stopping power as a function of $\beta\gamma = p/Mc$ for positive muons in copper [115]. The total stopping power is indicated with solid line and local components with dashed lines. the vertical bands are used to indicate boundaries between different approximations used at different energy range.	4-18
415			
416			
417			
418	4.24	Mean mass stopping power for liquid hydrogen, as used in bubble chambers, gaseous helium, carbon, aluminum, iron, tin, and lead without the inclusion of radiative effect at higher $\beta\gamma$ necessary for pions and muons in denser materials [115].	4-20
419			
420			
421	4.25	Mean excitation energies normalized to the atomic number as adopted by the ICRU [115, 234, 235].	4-21
422			
423	4.26	Mean mass stopping power at minimum ionization as a function of the atomic number [115].	4-21
424			
425	4.27	Example of straggling function $f(\Delta)$ of particles passing through 1.2 cm of Argon gas with a $\beta\gamma$ of 3.6 and represented with a solid line. The original Landau distribution is showed with a dashed line [236].	4-22
426			
427			
428	4.28	Evolution of straggling functions $f(\Delta)$ of particles passing through a volume of Argon gas with a $\beta\gamma$ of 3.6 with increasing thickness x [236].	4-22
429			
430	4.29	Photo-absorption cross section as computed by HEED for nobles gases with different electric shell numbers [232].	4-24
431			
432	4.30	Photo-absorption cross section as computed by HEED for typical RPC gas mixtures [232]. The RPC mixture with CO_2 corresponds to the mixture used by CALICE SDHCAL [240] while the other one was foreseen for the experimement ATLAS [241] but has been changed since then.	4-25
433			
434			
435			
436	4.31	Distributions of number of electrons (left) and energy loss (right) for a 5 GeV/c muon passing through 1.2 mm of Helium (Figure 4.31a), Argon (Figure 4.31b) or a typical RPC gas mixture (Figure 4.31c) [232].	4-26
437			
438			
439	4.32	Figure 4.32a: Mean cluster density for muons through different gas volumes [232]. Figure 4.32b: Distribution of the number of electrons per cluster for a 5 GeV/c muon traveling through a mixture of 96.7% $C_2H_2F_4$, 3% i- C_4H_{10} and 0.3% SF_6 [232, 241].	4-27
440			
441			
442			
443	4.33	Townsend and attachment coefficient for a typical 96.7/3/0.3 mixture of $C_2H_2F_4$ /i- C_4H_{10} / SF_6 , at a temperature $T = 296.15$ K and a pressure $P = 1013$ hPa [232, 241].	4-28
444			
445			
446	4.34	Comparison of the distribution law of Furry and the Poisson law for $\bar{n} = 5$ [244].	4-28
447			
448	4.35	Single-electron avalanche size distribution in a proportionnal counter filled with methylal at different E/p values. (a) 70, (b) 76.5, (c) 105, (d) 186.5, (e) 426V/cm torr [245].	4-29
449			
450	4.36	Figure 4.36a: Comparison of avalanche size distributions for different values of Townsend and attachment coefficients. The effective Townsend coefficient is the same for both distributions. Figure 4.36b: Fluctuation in avalanche size for avalanche started by a single electron with $\alpha = 13 \text{ mm}^{-1}$ and $\eta = 3.5 \text{ mm}^{-1}$ [241].	4-31
451			
452			
453	4.37	Figure 4.37a: Electron mean drift velocity v_D in pure $C_2H_2F_4$ and typical RPC gas mixtures. Figure 4.37b: Transverse diffusion coefficient in pure $C_2H_2F_4$ and a typical RPC gas mixture. Figure 4.37c: Longitudinal diffusion coefficient in pure $C_2H_2F_4$ and a typical RPC gas mixture. All results are given with a pressure $P = 760$ Torr and a temperature $T = 296.15$ K [232].	4-32
454			
455			
456			
457			
458	4.38	Comparison of the free charge carriers in the gas after a time $t = 7.90$ ns in the case where no diffusion is taken into account to simulate the avalanche (Figure 4.38a) and in the case where the diffusion is implemented (Figure 4.38b) [232].	4-32
459			
460			
461	4.39	Schematic representation of an avalanche and of the electric field deformation it causes due to the local concentration of charge carriers [214].	4-34
462			

463	4.40 Evolution of the charge induced by an avalanche started by a single electron in a 464 1.2 mm thick RPC with an applied electric field of 54 kV/cm in the case space 465 charge is not taken into account (Figure 4.40a) and in the case it is implemented into 466 the simulation (Figure 4.40b). The total induced charge is correlated to the size of 467 the avalanche [232].	4-35
468	4.41 Distributions of charge carriers within the gas volume of a 1.2 mm thick RPC and 469 the corresponding deformation of the electric field at different time steps with an 470 applied electric field of 55.5 kV/cm [232].	4-36
471	4.42 Representation of the weighting field in the volume of a RPC and the resulting in- 472 duced current in the strip placed at 1 V and its neighbour connected to the ground. 473 The induced current corresponds, as can be understood from Formula 4.22 [214].	4-37
474	4.43 Schematics of CMS RPC FEE logic.	4-38
475	4.44 Equivalence in between the charge of the induced signal in input of the CMS FEE 476 and the signal strength on the output of the pre-amplifier.	4-38
477	4.45 Description of the principle of a CFD. A comparison of threshold triggering (left) 478 and constant fraction triggering (right) is shown in Figure 4.45a. Constant frac- 479 tion triggering is obtained thanks to zero-crossing technique as explained in Fig- 480 ure 4.45b. The signal arriving at the input of the CFD is split into three components. 481 A first one is delayed and connected to the inverting input of a first comparator. A 482 second component is connected to the noninverting input of this first comparator. A 483 third component is connected to the noninverting input of another comparator along 484 with a threshold value connected to the inverting input. Finally, the output of both 485 comparators is fed through an AND gate.	4-39
486	4.46 Typical efficiency sigmoid of a CMS RPC detector. The black dots correspond to the 487 data, the blue line to the sigmoid fit and the opened cross to the knee and working 488 extracted from the fit line.	4-40
489	4.47 Effect of the temperature variation on the rate (Figure 4.47a) and the efficiency (Fig- 490 ure 4.47b) of a RPC [246].	4-41
491	4.48 Effect of the pressure variation on the rate (Figure 4.48a) and the efficiency (Fig- 492 ure 4.48b) of a RPC [247].	4-42
493	 5.1 Mean RPC Barrel (left column) and Endcap (right column) rate (top row) and current 494 (bottom row) as a function of the instantaneous luminosity as measured in 2017 p - p 495 collision data.	5-2
496	5.2 Figure 5.2a: The hit rate per region (Barrel, Endcap) is linearly extrapolated to 497 HL-LHC highest instantaneous luminosity ($5 \times 10^{34} \text{ cm}^{-2} \text{ s}^{-1}$) using the rate as 498 a function of instantaneous luminosity recorded by RPCs in 2017 showing a linear 499 dependence. Figure 5.2b: The integrated charge per region (Barrel, Endcap) is ex- 500 trapolated to HL-LHC integrated luminosity (3000 fb^{-1}) using the data accumulated 501 in 2016 in every HV channels.	5-3
502	5.3 CMS RPC mean integrated charge in the Barrel region (Figure 5.3a) and the Endcap 503 region (Figure 5.3b). The integrated charge per year is shown in blue. The red curve 504 shows the evolution of the accumulated integrated charge through time. The blank 505 period in 2013 and 2014 corresponds to LS1. The total integrated charge for the 506 entire operation period (Oct.2009 - Dec.2017) is estimated to be about 1.66 mC/cm^2 507 in the Barrel and 4.58 mC/cm^2 in the Endcap.	5-3

508	5.4	Layout of the test beam zone called X5c GIF at CERN. Photons from the radioactive source produce a sustained high rate of random hits over the whole area. The zone is surrounded by 8 m high and 80 cm thick concrete walls. Access is possible through three entry points. Two access doors for personnel and one large gate for material. A crane allows installation of heavy equipment in the area.	5-4
509	5.5	^{137}Cs decays by β^- emission to the ground state of ^{137}Ba (BR = 5.64%) and via the 662 keV isomeric level of ^{137}Ba (BR = 94.36%) whose half-life is 2.55min.	5-5
510			
511	5.6	Floor plan of the GIF++ facility. When the facility downstream of the GIF++ takes electron beam, a beam pipe is installed along the beam line (z-axis). The irradiator can be displaced laterally (its center moves from $x = 0.65$ m to 2.15 m), to increase the distance to the beam pipe.	5-6
512			
513	5.7	Simulated unattenuated current of photons in the xz plane (Figure 5.7a) and yz plane (Figure 5.7b) through the source at $x = 0.65$ m and $y = 0$ m [256]. With angular correction filters, the current of 662 keV photons is made uniform in xy planes.	5-6
514			
515	5.8	Description of the RPC setup. Dimensions are given in mm. A tent containing RPCs is placed at 1720 mm from the source container. The source is situated in the center of the container. RE-4-2-BARC-161 chamber is 160 mm inside the tent. This way, the distance between the source and the chambers plan is 2060 mm. Figure 5.8a provides a side view of the setup in the xz plane while Figure 5.8b shows a top view in the yz plane.	5-7
516			
517	5.9	RE-4-2-BARC-161 chamber is inside the tent as described in Figure 5.8. In the top right, the two scintillators used as trigger can be seen. This trigger system has an inclination of 10° relative to horizontal and is placed above half-partition B2 of the RPCs. PMT electronics are shielded thanks to lead blocks placed in order to protect them without stopping photons from going through the scintillators and the chamber.	5-8
518			
519	5.10	Hit distributions over all 3 partitions of RE-4-2-BARC-161 chamber is showed. Top, middle and bottom figures respectively correspond to partitions A, B, and C. The profiles show that some events still occur in other half-partitions than B2, which corresponds to strips 49 to 64, in front of which the trigger is placed, contributing to the inefficiency of detection of cosmic muons. In the case of partitions A and C, the very low amount of data can be interpreted as noise. On the other hand, it is clear that a little portion of muons reach the half-partition B1, corresponding to strips 33 to 48.	5-8
520			
521	5.11	Signals from the RPC strips are shaped by the FEE described on Figure 5.11a. Output LVDS signals are then read-out by a TDC module connected to a computer or converted into NIM and sent to scalers. Figure 5.11b describes how these converted signals are put in coincidence with the trigger.	5-9
522			
523	5.12	Results are derived from data taken on half-partition B2 only. On the 18 th of June 2014, data has been taken on chamber RE-4-2-BARC-161 at CERN building 904 (Prevessin Site) with cosmic muons providing us a reference efficiency plateau of $(97.54 \pm 0.15)\%$ represented by a black curve. A similar measurement has been done at GIF on the 21 st of July with the same chamber giving a plateau of $(78.52 \pm 0.94)\%$ represented by a red curve.	5-10
524			
525	5.13	Representation of the layout used for the simulations of the test setup. The RPC read-out plane is represented as a yellow trapezoid while the two scintillators as blue cuboids looking at the sky. The green plane corresponds to the muon generation plane within the simulation. Figure 5.8a shows a global view of the simulated setup. Figure 5.8b shows a zoomed view that allows to see the 2 scintillators as well as the full RPC plane.	5-11
526			
527			
528			
529			
530			
531			
532			
533			
534			
535			
536			
537			
538			
539			
540			
541			
542			
543			
544			
545			
546			
547			
548			
549			
550			
551			
552			
553			
554			
555			
556			

557	5.14 Geometrical acceptance distribution as provided by the Monte Carlo simulation.	5-12
558	5.15 Correction of the efficiency without source. The efficiency after correction gets	
559	much closer to the Reference measurement performed before the study in GIF by	
560	reaching a plateau of $(93.52 \pm 2.64)\%$	5-13
561	5.16 Hit distributions over read-out partition B of RE-4-2-BARC-161 chamber to-	
562	gether with skew distribution fits corresponding to forward and backward coming	
563	muons.	5-14
564	5.17 Figure 5.17a shows the linear approximation fit performed on data extracted from	
565	table 5.2. Figure 5.17b shows a comparison of Formula 5.5 with the simulated flux	
566	using a and b given in figure 5.17a in formulae 5.3 and the reference value $D_0 =$	
567	50 cm and the associated flux for each absorption factor F_0^{ABS} from table 5.1	5-16
568	5.18 Efficiency (Figure 5.18a) and cluster size (Figure 5.18b) of chamber RE-4-2-BARC-161	
569	measured at GIF with Source OFF (red) and Source ON using different absorber set-	
570	tings: ABS 5 (green), ABS 2 (blue) and ABS 1 (yellow). The results are compared	
571	to the Reference values obtained with cosmics.	5-17
572	5.19 Rates in chamber RE-4-2-BARC-161 measured at GIF with Source OFF (red)	
573	and Source ON using different absorber settings: ABS 5 (green), ABS 2 (blue) and	
574	ABS 1 (yellow). On Figure 5.19b, the rates of Figure 5.19a were normalized to the	
575	measured efficiency and constant fits are performed on Source ON data showing the	
576	gamma rate in the chamber.	5-18
577	5.20 Evolution of the voltages at half maximum and at 95% of the maximum efficiency	
578	(Figure 5.20a), and of the maximum efficiency (Figure 5.20b) as a function of the	
579	rate in chamber RE-4-2-BARC-161. The data is extracted from the fits in Fig-	
580	ures 5.18a and 5.19b.	5-18
581	5.21 Presentation of a double-gap endcap RPC with its 3 RPC gaps. Due to the partitioni-	
582	ng of the read-out strips into 3 rolls, the TOP layer of gap is divided into 2 gaps:	
583	TOP NARROW (TN) and TOP WIDE (TW). The BOTTOM (B) only consists in 1	
584	gap.	5-19
585	5.22 Current density and charge deposition per gamma avalanche, defined as the current	
586	density normalized to the measured rate taken from Figure 5.19a as a function of	
587	the effective high voltage in chamber RE-4-2-BARC-161 measured at GIF with	
588	Source ON using different absorber settings: ABS 5 (green), ABS 2 (blue) and ABS	
589	1 (yellow).	5-20
590	5.23 Characterization of CMS RPC detectors foreseen to be used at GIF++ for longevity	
591	studies of the present system. Using cosmic muons, efficiency (Figure 5.23a) and	
592	cluster size (Figure 5.23b) were measured as well as noise rate (Figure 5.23c) and	
593	current density (Figure 5.23d). For each detector, the working voltage, defined as	
594	in Formula 4.25, was extracted from sigmoid fits performed in Figure 5.23a and the	
595	values of efficiency, cluster size, noise rate and current density at this voltage are	
596	reported using open crosses.	5-21
597	5.24 CMS RPC setup inside of GIF++ bunker during test beam (Figure 5.24a) and ageing	
598	periods (Figure 5.24b). The space in between the RPCs and the source is usually	
599	used by other detectors while the space in between T1 and the upstream wall is	
600	not filled. Due to the presence of the beam pipe, the trolley is moved away from the	
601	beam line during irradiation periods and placed further away from the source for less	
602	intense irradiation. The position of the trolley can vary due to the use of the space	
603	by other setups and is then not exact. In the contrary, the position of the chambers in	
604	the trolley is fixed and given in Figure 5.24c.	5-23

605	5.25	Visualtion of the main data flows in GIF++. The yellow flow lines corresponds to the DIP flow used for source, environmental and gas information. The red flow lines are for the CAEN flow through which the WebDCS communicates the voltages to be applied on the detectors using pressure and temperature informformation and retrieves the monitored voltages and currents. Finally, the blue flow lines corresponds to the DAQ flow through which the RPC data is collected from the TDCs by the computer.	5-24
606	5.26	DIP monitoring history accessed through GIF++ WebDCS interface.	5-25
607	5.27	Example of DQM page available on CMS RPC WebDCS in GIF++. Here is presented the rate measured in one of the tracking chabers, namely GT1_20_20-BKL_JUL16_4. The DQM page allows to click on each histogram to extend its view and to navigate through the histograms thanks to the left and right arrows.	5-27
609	5.28	Example of DQM ROOT Browser page available on CMS RPC WebDCS in GIF++. Here is presented the strip activity profile, defined as the rate profile normalized to the mean rate, in one of the tracking chabers, namely GT1_20_20-BKL_JUL16_4. Available ROOT files and histograms can be browsed thanks to the left panel showing the directory and files structures.	5-28
610	5.29	Longevity statistics of chamber RE2-2-NPD-BARC-9 in GIF++. For each month since July 2017, the integrated charge (in blue) as well as the time efficiency of irradiation (in gray) is reported.	5-28
611	5.30	Example of current monitoring (Figure 5.30a) and of corresponding integrated charge (Figure 5.30b) of chamber RE2-2-NPD-BARC-09. The decrease of current are related to a decrease of the voltage due to the daily rate scan procedure or to periods during which the source was turned OFF.	5-29
612	5.31	Example of rate (Figure 5.31a) and current (Figure 5.31b) monitoring of chamber RE2-2-NPD-BARC-09 with increasing integrated charge. The variations of rate and current are correlated and corresponds to change of source irradiation, gas flow, gas humidity, or environmental conditions.	5-30
613	5.32	Example of strip activity of chamber RE2-2-NPD-BARC-09 monitoring through time. The activity of a strip is defined as the rate of the individual channel normalized to the mean rate measured in the corresponding read-out partition.	5-31
614	5.33	Total integrated charge in the irradiated RPCs, RE2-2-NPD-BARC-9 and RE4-2-CERN-165, before starting August 2018 test beam period. The irradiation of the RE2 chamber started in June 2016 while the RE4 chamber couldn't be irradiated before November 2016.	5-33
615	6.1	PETIROC 2A block diagram.	6-2
616	6.2	The PETIROC time jitter as a function of the input signal amplitude, measured with and without internal clocks.	6-3
617	A.1	(A.1a) View of the front panel of a V1190A TDC module [257]. (A.1b) View of the front panel of a V1718 Bridge module [258]. (A.1c) View of the front panel of a 6U 6021 VME crate [272].	A-3
618	A.2	Module V1190A <i>Trigger Matching Mode</i> timing diagram [257].	A-4
619	A.3	Structure of the ROOT output file generated by the DAQ. The 5 branches (<code>EventNumber</code> , <code>number_of_hits</code> , <code>Quality_flag</code> , <code>TDC_channel</code> and <code>TDC_TimeStamp</code>) are visible on the left panel of the ROOT browser. On the right panel is visible the histogram corresponding to the variable <code>nHits</code> . In this specific example, there were approximately 50k events recorded to measure the gamma irradiation rate on the detectors. Each event is stored as a single entry in the <code>TTree</code>	A-10
620			
621			
622			
623			
624			
625			
626			
627			
628			
629			
630			
631			
632			
633			
634			
635			
636			
637			
638			
639			
640			
641			
642			
643			
644			
645			
646			
647			
648			
649			
650			
651			
652			

653 A.4 The effect of the quality flag is explained by presenting the content of <code>TBranch</code> 654 <code>number_of_hits</code> of a data file without <code>Quality_flag</code> in Figure A.4a and the con- 655 tent of the same <code>TBranch</code> for data corresponding to a <code>Quality_flag</code> where all TDCs 656 were labelled as <code>GOOD</code> in Figure A.4b taken with similar conditions. It can be noted 657 that the number of entries in Figure A.4b is slightly lower than in Figure A.4a due 658 to the excluded events.	A-12
659 A.5 Using the same data as previously showed in Figure A.4, the effect of the quality 660 flag is explained by presenting the reconstructed hit multiplicity of a data file with- 661 out <code>Quality_flag</code> in Figure A.5a and the reconstructed content of the same RPC 662 partition for data corresponding to a <code>Quality_flag</code> where all TDCs were labelled as 663 <code>GOOD</code> in Figure A.5b taken with similar conditions. The artificial high content of bin 664 0 is completely suppressed.	A-12
665 A.6 WebDCS DAQ scan page. On this page, shifters need to choose the type of scan 666 (Rate, Efficiency or Noise Reference scan), the gamma source configuration at the 667 moment of data taking, the beam configuration, and the trigger mode. These in- 668 formation will be stored in the DAQ ROOT output. Are also given the minimal 669 measurement time and waiting time after ramping up of the detectors is over before 670 starting the data acquisition. Then, the list of HV points to scan and the number of 671 triggers for each run of the scan are given in the table underneath.	A-14
672 B.1 Example of expected hit time distributions in the cases of efficiency (Figure B.1a) 673 and noise/gamma rate per unit area (Figure B.1b) measurements as extracted from 674 the raw ROOT files. The unit along the x-axis corresponds to ns. The fact that 675 "the" muon peak is not well defined in Figure B.1a is due to the contribution of all 676 the RPCs being tested at the same time that don't necessarily have the same signal 677 arrival time. Each individual peak can have an offset with the ones of other detectors. 678 The inconsistancy in the first 100 ns of both time distributions is an artefact of the 679 TDCs and are systematically rejected during the analysis.	B-16
680 B.2 The effect of the quality flag is explained by presenting the reconstructed hit multi- 681 plicity of a data file without <code>Quality_flag</code> . The artificial high content of bin 0 is the 682 effect of corrupted data.	B-21
683 B.3 Display of the masking tool page on the webDCS. The window on the left allows the 684 shifter to edit <code>ChannelsMapping.csv</code> . To mask a channel, it only is needed to set the 685 3rd field corresponding to the strip to mask to 0. It is not necessary for older mapping 686 file formats to add a 1 for each strip that is not masked as the code is versatile and 687 the default behaviour is to consider missing mask fields as active strips. The effect 688 of the mask is directly visible for noisy channels as the corresponding bin turns red. 689 The global effect of masking strips will be an update of the rate value showed on the 690 histogram that will take into consideration the rejected channels.	B-28

List of Tables

691

692	3.1	Details of the greenhouse fluorinated gases used in CMS and of their GWP [177]. . .	3-21
693	4.1	Properties of the most used electrode materials for RPCs.	4-3
694	5.1	Total photon flux ($E\gamma \leq 662$ keV) with statistical error predicted considering a 695 ^{137}Cs activity of 740 GBq at different values of the distance D to the source along 696 the x-axis of irradiation field [254].	5-14
697	5.2	Correction factor c is computed thanks to Formula 5.4 taking as reference $D_0 =$ 698 50 cm and the associated flux F_0^{ABS} for each absorption factor available in table 5.1.	5-15
699	5.3	The data at D_0 in 1997 is taken from [254]. Using Formula 5.5, the flux at D , 700 including an error of 1 cm, can be estimated in 1997. Then, taking into account the 701 attenuation of the source activity, the flux at D can be estimated at the time of the 702 tests in GIF in 2014. Assuming a sensitivity of the RPC to $\gamma s = 2 \times 10^{-3}$, an 703 estimation of the hit rate per unit area is obtained.	5-16
704	5.4	Summary of the characterization measurement performed in Ghent on CMS RPC 705 detectors foreseen to be used at GIF++ for longevity studies of the present system. 706 For each detector, the working voltage, defined as in Formula 4.25, was extracted 707 from sigmoid fits performed in Figure 5.23a and the values of efficiency, cluster 708 size, noise rate and current density at this voltage are reported.	5-22
709	A.1	Inter-process communication cycles in between the webDCS and the DAQ through 710 file string signals.	A-18

List of Acronyms

List of Acronyms

713	AFL	Almost Full Level
714	ALCTs	anode local charged track boards
715	BARC	Bhabha Atomic Research Centre
716	BCS	Bardeen–Cooper–Schrieffer
717	BLT	Block Transfer
718	BMTF	Barrel Muon Track Finder
719	BNL	Brookhaven National Laboratory
720	BSM	Physics beyond the Standard Model
721	BR	Branching Ratio
722	CAEN	Costruzioni Apparecchiature Elettroniche Nucleari S.p.A.
723	CERN	European Organization for Nuclear Research
724	CFD	Constant Fraction Discriminator
725	CFEBs	cathode front-end boards
726	CKM	Cabibbo–Kobayashi–Maskawa
727	CMB	Cosmic Microwave Background
728	CMS	Compact Muon Solenoid
729	CSC	Cathode Strip Chamber
730	CuOF	copper-to-optical-fiber translators
731	DAQ	Data Acquisition
732	DCS	Detector Control Software
733	DQM	Data Quality Monitoring
734	DT	Drift Tube
735	EDM	electric dipole moment
736	ECAL	electromagnetic calorimeter
737	EMTF	Endcap Muon Track Finder
738	FCC	Future Circular Collider
739	FEB	Front-End Board
740	FEE	Front-End Electronics
741	FWHM	full-width-at-half-maximum
742	GEANT	GEometry ANd Tracking - a series of software toolkit platforms developed by CERN
743		
744	GEB	GEM Electronics board
745	GEM	Gas Electron Multiplier
746	GIF	Gamma Irradiation Facility
747	GIF++	new Gamma Irradiation Facility
748	GWP	Global Warming Potential
749	HCAL	hadron calorimeter
750	HEP	High-Energy Physics

751	HL-LHC	High Luminosity LHC
752	HPL	High-pressure laminate
753	HSCPs	Heavy Stable Charged Particles
754	HV	High Voltage
755	ICRU	International Commission on Radiation Units & Measurements
756	iRPC	improved RPC
757	IRQ	Interrupt Request
758	ISR	Intersecting Storage Rings
759	LEIR	Low Energy Ion Ring
760	LEP	Large Electron-Positron
761	LHC	Large Hadron Collider
762	LS1	First Long Shutdown
763	LS2	Second Long Shutdown
764	LS3	Third Long Shutdown
765	LSP	lightest supersymmetric particle
766	LV	Low Voltage
767	LVDS	Low-Voltage Differential Signaling
768	MC	Monte Carlo
769	MCNP	Monte Carlo N-Particle
770	Mic1	first version of Minicrate electronics
771	mip's	minimum ionizing particles
772	MRPC	Multigap RPC
773	MSSM	Minimal Supersymmetric Standard Model
774	mSUGRA	minimal SUper GRAvity
775	NIM	Nuclear Instrumentation Module logic signals
776	OH	Optohybrid Board
777	OMTF	Overlap Muon Track Finder
778	PAI	Photo-Absorption Ionisation
779	PAIR	Photo-Absorption Ionisation with Relaxation
780	PMT	PhotoMultiplier Tube
781	PS	Proton Synchrotron
782	PU	pile-up
783	QCD	Quantum Chromodynamics
784	QED	Quantum Electrodynamics
785	RADMON	Radiation Monitoring
786	RMS	Root Mean Square
787	ROOT	a framework for data processing born at CERN
788	RPC	Resistive Plate Chamber
789	SC	Synchrocyclotron
790	SiPM	Silicon Photomultiplier
791	SLAC	Stanford Linear Accelerator Center
792	SM	Standard Model
793	SPS	Super Proton Synchrotron
794	SUSY	supersymmetry
795	TDC	Time-to-Digital Converter
796	TDR	Technical Design Report
797	ToF	Time-of-flight
798	TPG	trigger primitives
799	webDCS	Web Detector Control System

800	WIMPs	Weakly Interacting Massive Particles
801	YETS	Year End Technical Stop



1

802

803

Introduction

804 Grasping an understanding of the world in which they are leaving in has always been part of human
805 life. Beyond the metaphysical questioning of our origins and purpose, curiosity has brought mankind
806 to question its surroundings. Following the philosophy of the ancient Greeks and Indians came
807 the development of the sciences as the systematic experimentation aimed at testing hypothesis and
808 reproducing results obtained by fellow natural philosophers. With the industrial revolution and the
809 organisation of science, it became possible to go always further in the understanding of the universe
810 and of the matter in particular. Investigation on the constituent of matter proved to require more
811 and more powerful machines in order to break apart the bricks of the world into ever smaller pieces,
812 study their behaviour and extract new knowledge to help the development of humanity. So far, the
813 largest and most powerful machine that was built to study the particles composing matter and test
814 the models thought by physicists to explain their behaviour is the Large Hadron Collider (LHC),
815 a circular particle accelerator used to collide protons and heavy ions. After only a few years of
816 investigations conducted thanks to the LHC, several discoveries, predicted by the existing models,
817 have been made. In the future, in order to boost the discovery potential on the LHC and be able to
818 test hypotheses lying beyond the already acknowledged models, the instantaneous luminosity, i.e.
819 the rate of particle interactions, will be slightly increased into a so-called High Luminosity phase to
820 boost its discovery potential.

821 As the Large Hadron Collider will see its instantaneous luminosity be increased, the detectors
822 on the different experimental sites will have to suffer an increased background irradiation due to the
823 byproducts of the interaction of the beams with the infrastructure. This will cause for the detectors
824 a stress which implications need to be understood throughout the High Luminosity LHC (HL-LHC)
825 phase of operations. In the case of the Compact Muon Solenoid (CMS) experiment, it is important
826 to understand if the detectors that will be subjected to the higher levels of radiation will be able to
827 sustain higher detection rates while displaying the same performance they have so far been operated
828 at and if this level of performance of the detectors will stay stable for a period longer than ten years.
829 More specifically, the detectors placed very close to the beam line will be the most subjected to the
830 change of luminosity. In CMS, the endcap detectors will then be particularly affected by the stronger

background radiation. The endcap detectors compose a part of the muon system of CMS and among them, the Resistive Plate Chamber (RPC)s play a key role in providing the experiment a reliable trigger on potentially interesting data.

CMS experiment main focus revolves around testing the Standard Model (SM) of particle physics using a multipurpose detector design to detect the interaction products of the protons and ions colliding along the LHC. Looking at the successive evolution of the theoretical models that gave birth to the SM, the need for very intense particle beams in high energy physics experiment becomes clear in that the higher the center-of-mass energy for each interaction, the greater the probe on very small cross-section processes predicted by the theory, justifying the successive increase in beam energy and intensity at LHC.

The implications for LHC experiments and in particular for the CMS detector explain the need for longevity and rate capability studies conducted on the Resistive Plate Chambers which are an important part of its Muon System as it is needed to certify the quality of operation of the trigger detectors throughout the lifetime of HL-LHC.

RPCs are gaseous detectors which physics principles are non trivial and are still being investigated. Nevertheless, key processes driving the electron multiplication in the gas volume, rate capability and ageing have been successfully identified and will define the parameters that will have to be taken into consideration while producing the detectors extending the pseudo-rapidity coverage of RPCs toward the beam line as well as the ones to be monitored during the on-going longevity and rate capability certification campaign.

On the one hand, the present RPC sub-system consists in two different RPC productions. Indeed, most of the RPC detectors were produced in view of the start of LHC activities in 2010. These detectors were build in between 2007 and 2008 to equip the barrel and the three disks of each endcaps of the CMS apparatus. But during the First Long Shutdown (LS1) of LHC in between end of 2012 and 2015, a fourth disk of endcap was added in order to reinforce the redundancy of the endcap trigger. Hence, new RPC detectors using the same technology were built in between 2012 and 2013. These two sets of detector productions only differ in the properties of the High-pressure laminate (HPL) used for their electrodes that could lead to a different ageing rate. This is why spare detectors of both production periods have been tested over the past years to certify their good operation through HL-LHC.

On the other hand, producing detectors to equip a highly irradiated region such as the extension of CMS RPC endcaps requires to substantially improve the ageing properties of the chosen technology by reducing the charge deposition per ionizing particle. This can be achieved both by modifying the design of the detector volume or by improving the signal to noise ratio of the Front-End Electronics (FEE) used to process the charge collected by the read-out strips making them more sensitive to weaker signals. Two improved RPC (iRPC) designs were selected and tested in order to extend of CMS endcap coverage.

Thanks to the study presented in this document, preliminary conclusions will be brought on the production of iRPCs and on the longevity of the present RPC system, providing with a better understand of the future performance of the RPC sub-system within the CMS experiment.

2

871

872

Investigating the TeV scale

873 Throughout history, physics experiment became more and more powerful in order to investigate finer
874 details of nature to help understanding the building blocks of matter and the fundamental interactions
875 that bind them in the microscopic world. Nowadays, the Standard Model of particle physics is the
876 most accurate theory designed to explain the behaviour of particles and is able to make very precise
877 predictions that are constantly verified. Nevertheless, some hints of new physics are visible as bricks
878 are still missing to obtain a global description of the Universe.

879 To highlight the limits of the SM and test the different alternative theories, evermore powerful
880 machines are needed. It is in this context that the Large Hadron Collider has been thought and built
881 to accelerate and collide particles at energies exceeding anything that had been done before. Higher
882 collision energies and high pile-up imply the use of enormous detectors to measure the properties of
883 the interaction products. The Compact Muon Solenoid is a multipurpose experiment that have been
884 designed to study the proton-proton collisions of the LHC and give answers on various high-energy
885 physics scenarios such as different supersymmetry (SUSY) extensions to the Standard Model or Ex-
886 tra Dimensions models.

887

888 This Chapter will be the occasion to go through the history of the Standard Model of Particle
889 Physics to understand the research conducted today in High-Energy Physics (HEP) facilities. From
890 the discovery of the atom and of its inner structure to the development of the theories governing
891 the fundamental interactions, all the elements leading to the construction SM will be discussed.
892 Furthermore, highlights on the Physics beyond the Standard Model (BSM) will be given to replace
893 the document in the context of today's research. Finally, a full description of the LHC and of the
894 CMS detector will be provided.

895 2.1 The Standard Model of Particle Physics

896 In the early 21st century it is now widely accepted that matter is made of elementary blocks referred
897 to as *elementary particles*. The physics theory that classifies and describes the best the behaviour and

interaction of such elementary particles is the so-called Standard Model. The SM formalizes three of the four fundamental interactions (electromagnetic, weak and strong interactions). Its development happened since the 1960s thanks to a strong collaboration between theoretical and experimental physicists.

2.1.1 A history of particle physics

The idea that nature is composed of elementary bricks, called *atomism*, is not contemporary as it was already discussed by Indian or Greek philosophers during antiquity. In Greece, atomism has been rejected by *Aristotelianism* as the existence of *atoms* would imply the existence of a void that would violate the physical principles of Aristotle philosophy. Aristotelianism has been considered as a reference in the european area until the 15th century. With the *Rinascimento*, antic text and history started to be more deeply studied. The re-discovery of Platon's philosophy allowed opening the door to alternative theories and give a new approach to natural sciences where experimentation would become central. A new era of knowledge was starting. By the beginning of the 17th century, atomism was re-discovered by philosophers. The very first attempt at estimating the number of *particles* in a volume was provided by Magnenus in 1646 by calculating that the number of *particles* in a stick of incense [1]. He found a value of the order of 10^{18} simply by considering the time necessary to smell it everywhere in a large church after the stick was lit on. It is now known that this number only falls short only by 1 order of magnitude.

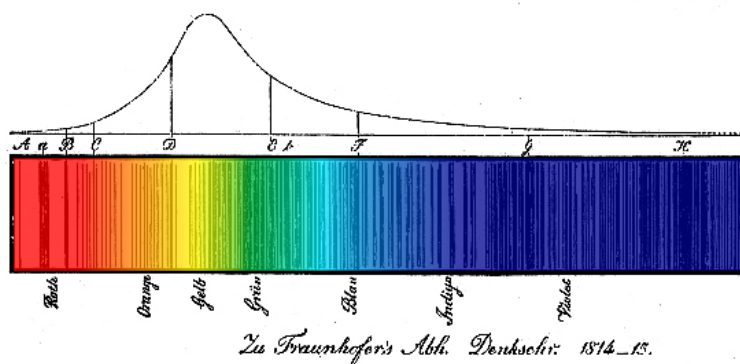


Figure 2.1: Solar spectrum with spectral lines as it visually appeared to Fraunhofer.

An alternative philosophy to atomism popularized by Descartes was *corpuscularianism*. Built on ever divisible corpuscles, contrary to atoms, its principles were mainly used by alchemists like Newton who would later develop a corpuscular theory of light. Boyle combined together ideas of both atomism or corpuscularianism leading to mechanical philosophy. The 18th century has seen the development of engineering providing philosophical thought experiments with repeatable demonstration and a new point of view to explain the composition of matter. Lavoisier greatly contributed to chemistry and atomism by publishing in 1789 a list of 33 chemical elements corresponding to what are now called *atoms* [2]. In the early 19th century Dalton summarized the knowledge on composition of matter [3]. In his atomic model, the atoms are ball-like constituents of the chemical elements. All atoms of a given element are identical, in size, mass, and other properties while the atoms of different elements differ. He also considered that atoms cannot be divided into smaller particles, created nor destroyed and that they combine into chemical compounds. The essence of

928 chemical reaction was then the combination, separation or rearrangement of atoms. Soon after,
 929 Fraunhofer invented the spectrometer and discovered the spectral lines in the sunlight spectrum, as
 930 showed in Figure 2.1 [4]. These were later linked to the absorption by chemical elements present in
 931 the solar atmosphere by Kirchhoff and Bunsen. The rise of atomic physics, chemistry and mathe-
 932 matical formalism unraveled the different atomic elements and ultimately, the 20th century saw the
 933 very first sub-atomic particles.

934 **Discovery of the inner structure of the atom**

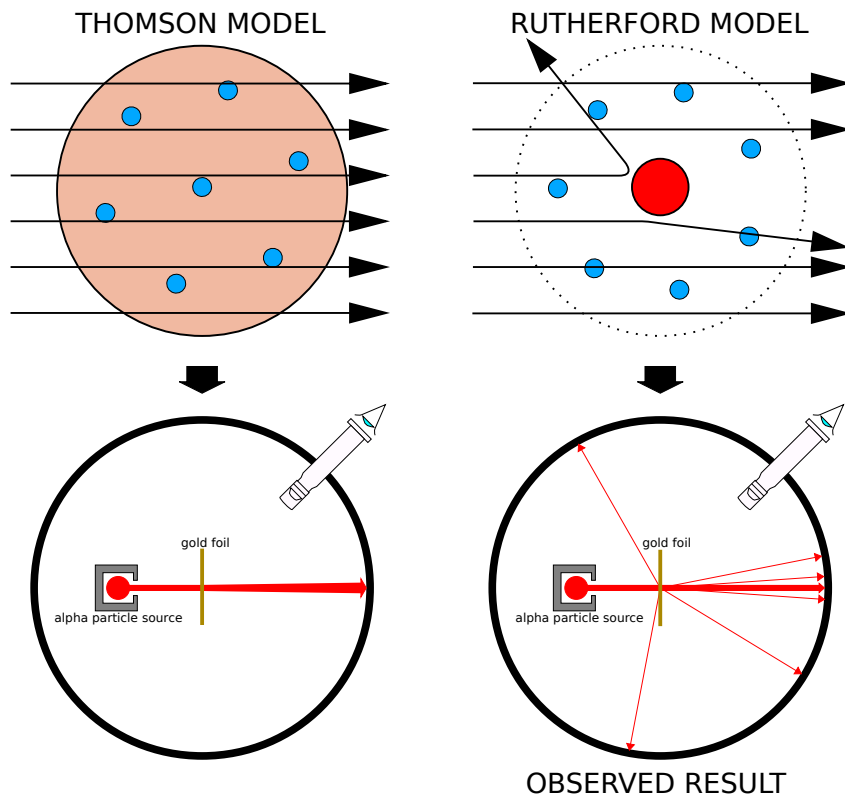


Figure 2.2: Through the gold foil experiment, Rutherford could show that most of the mass of atoms was contained in a positively charged nucleus and could then propose a more accurate atomic model than that of Thomson.

935 The negatively charged *electron* was the first to be discovered in 1897 by Thomson after three
 936 decades of research on cathode rays [5]. He proved that the electrification observed in an elec-
 937 troscope, as reported by Perrin [6], was due to the rays themselves. Hence, they had to be composed
 938 of electrically charged particles. In 1900, Becquerel showed the *beta rays* emitted by radium had the
 939 same charge over mass ratio as was measured by Thomson for cathode rays, pointing to electrons as
 940 a constituent of atoms [7]. This discovery leads to Thomson's plum pudding atomic model in which
 941 electrons are embed into a uniform positively charged atom [8]. In 1907, Rutherford and Royds
 942 showed that *alpha* particles were helium ions [9]. Indeed, once captured in a tube and subjected to
 943 an electric spark causing an electron avalanche, they could combine with two electrons to form a

944 ${}^4\text{He}$.

945 This discovery was directly followed by the constraint of the atom structure in between 1908
 946 and 1913 through the Geiger–Marsden gold foil experiments in which the deflection angle of alpha
 947 particles fired at a very thin gold foil was measured [10–13]. It highlighted that atoms were mainly
 948 empty with nearly all their mass contained into a tiny positively charged *nucleus*. With these two
 949 observations, Rutherford could formulate the Rutherford planetary model of the atom in 1911 [14],
 950 shown together with the Thomson plum pudding model in Figure 2.2. The link between atomic
 951 number and number of positive and negative charges contained into the atoms would fast be under-
 952 stood. Hence, the different kinds of element transmutations appeared to be purely nuclear processes
 953 making clear that the electromagnetic nature of chemical transformations could not possibly change
 954 nuclei. A new branch in physics appeared to exclusively study nuclei: *nuclear physics*. By studying
 955 alpha emission and the product of their interaction with nitrogen gas, Rutherford reported in 1919
 956 the very first nuclear reaction [15]. It leads to the discovery that the hydrogen nucleus was composed
 957 of a single positively charged particle that was later baptised *proton* [16]. This idea came from 1815
 958 Prout’s hypothesis proposing that all atoms are composed of “*protyles*” (i.e. hydrogen atoms) [17,
 959 18]. By using scintillation detectors, Rutherford could highlight typical hydrogen nuclei signature
 960 and understand that the impact of alpha particles with nitrogen would knock out a hydrogen nucleus
 961 and produce an oxygen 17, as showed in Formula 2.1 and would then postulate that protons are
 962 building bricks of all elements.



963 With this assumption and the discovery of *isotopes* together with Aston, elements with identical
 964 atomic number but different masses, Rutherford proposed that all elements’ nuclei but hydrogen
 965 are composed of both charged particles, protons, and of chargeless particles, which he called *neu-*
 966 *trons* [16, 19]. These neutral particles helped maintaining nuclei as one, as charged protons were
 967 likely to electrostatically repulse each other. He then introduced the idea of a new force, a *nuclear*
 968 force. The first idea concerning neutrons was a bond state of protons and electrons as it was known
 969 that the beta decay, emitting electrons, was taking place in the nucleus. However, it was then shown
 970 that electrons being confined into the nucleus would hardly be possible due to Heisenberg’s uncer-
 971 tainty principle. Finally, in 1932, following the discovery of a new neutral radiation, Chadwick could
 972 discover the neutron as an uncharged particle with a mass similar to that of the proton which would
 973 solve the nucleus puzzle [20–24].

974 Development of the Quantum Electrodynamics

975 Historically, the development of the quantum theory revolved around the question of emission and
 976 absorption of discrete amount of energy through light. Einstein used the initial intuition of Planck
 977 about the black-body radiation to develop in 1905 a model to explain the photoelectric effect in
 978 which light was described by discrete *quanta* now called *photons* [25, 26]. For this model, Ein-
 979 stein introduced the concept of wave-particle duality as classical theory was not able to describe
 980 the phenomenon. With the new understanding of atoms and of their structure, classical theories
 981 also proved unable to explain atoms’ stability. Indeed, using classical mechanics, electrons orbiting
 982 around a nucleus should radiate an energy proportional to their angular momentum and hence, loose
 983 energy through time and the spectrum of energy emission should then be continuous. However, it

984 was known since the 19th century and the discovery of spectral lines that the emission spectrum of
 985 material was discrete [4].

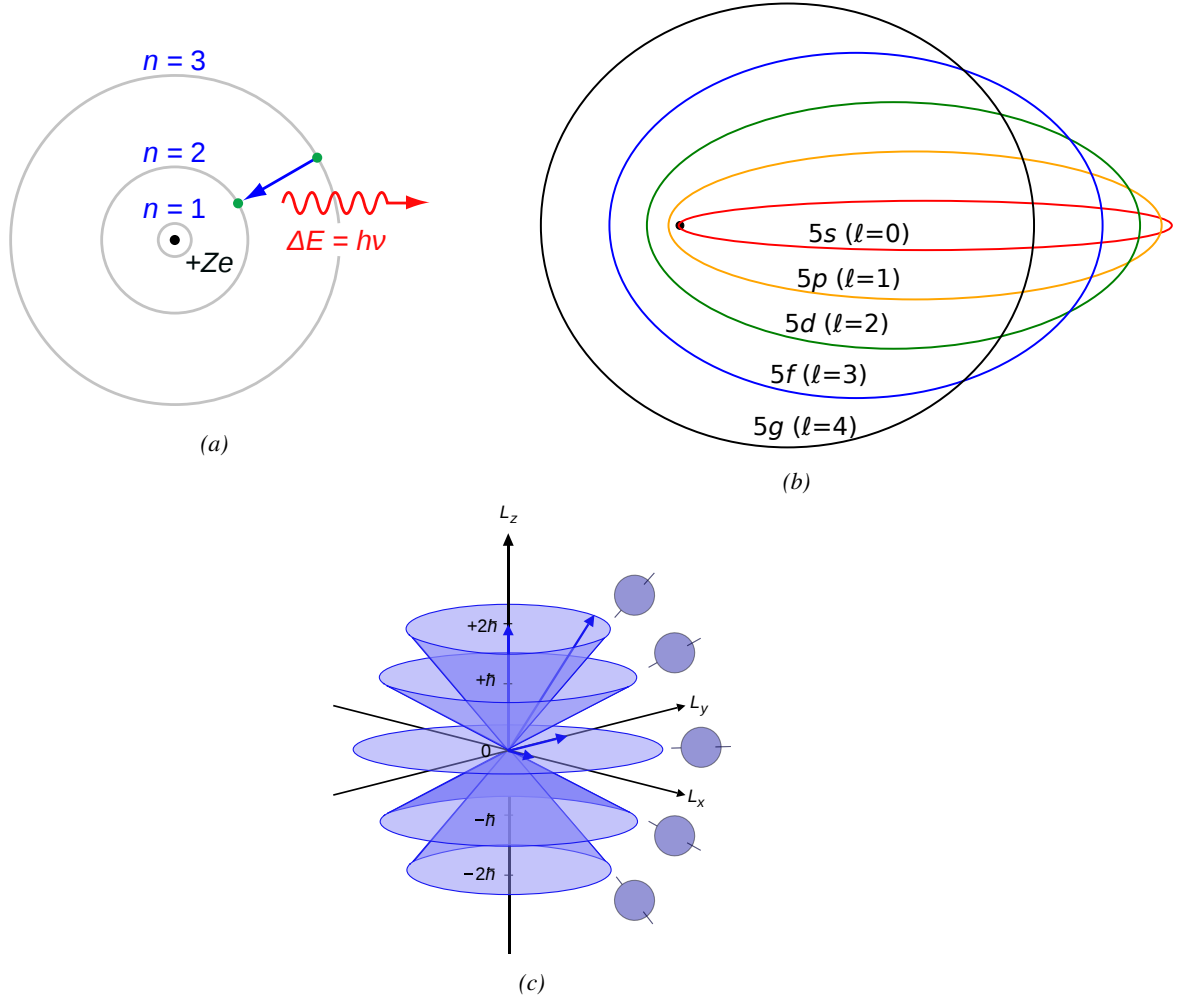


Figure 2.3: Figure 2.3a: The orbits in which the electron may travel according to the Bohr model of the hydrogen atom. An electron jumps between orbits and is accompanied by an emitted or absorbed amount of electromagnetic energy ($h\nu$). The orbits radius increases as n^2 . Figure 2.3b: Elliptical orbits with the same energy and quantized angular momentum $l = 0, 1, \dots, n - 1$ in the case $n = 5$. Figure 2.3c: Illustration of quantum mechanical orbital angular momentum. The cones and plane represent possible orientations of the angular momentum vector for $l = 2$ and $m = -2, -1, 0, 1, 2$.

986 In 1913, quantum physics was introduced into the atomic model by Bohr to overcome the elec-
 987 tron's energy loss due to orbiting radiation emission [27]. Using the correspondence principle stating
 988 that for large enough numbers the quantum calculations should give the same results than the clas-
 989 sical theory, he proposed the very first quantum model of the hydrogen atom explaining the line
 990 spectrum by introducing the *principal quantum number* n describing the electron *shell*. The same
 991 year, Moseley confirmed Bohr's model through the Moseley's law [28]. Debye and then Sommer-
 992 feld extended it by introducing the quantization of the angular momentum [29]. The quantization the

993 z-component of the angular momentum led to the *second* and *third quantum numbers*, or *azimuthal*
 994 and *magnetic quantum number*, l and m . The second defines the orbital angular momentum of the
 995 electrons on their shells and hence, the shape of the orbital, while the third the available orbital on
 996 the subshell for each electron as shown in Figure 2.3.

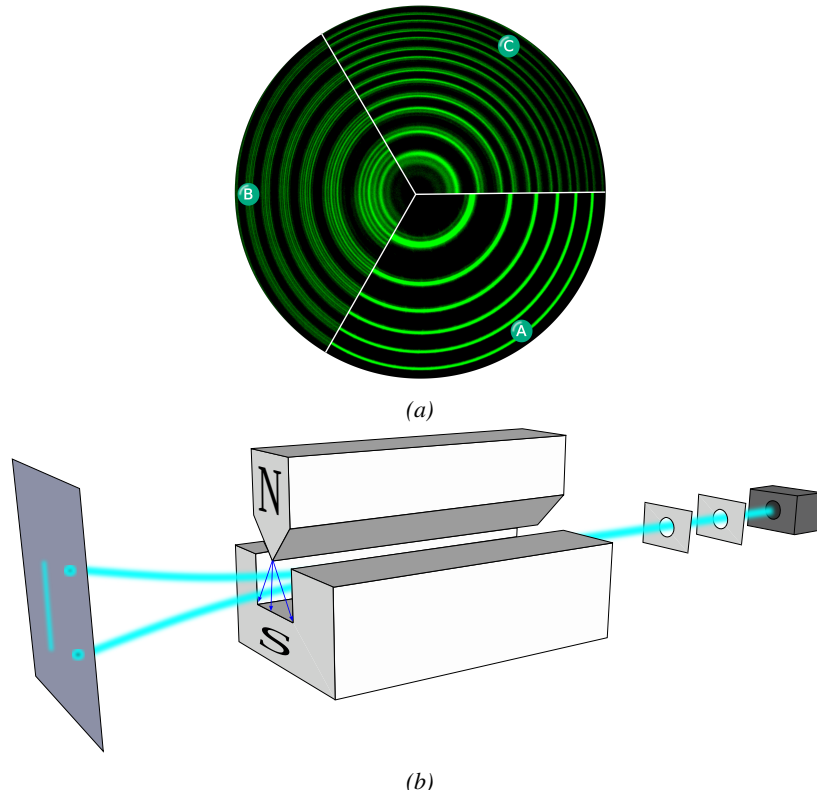


Figure 2.4: Figure 2.4a: The spectral lines of mercury vapor lamp anomalous Zeeman effect without magnetic field (A) and with magnetic field (B - transverse Zeeman effect & C - longitudinal Zeeman effect). Figure 2.4b: Stern-Gerlach experiment: Silver atoms traveling through an inhomogeneous magnetic field and being deflected up or down depending on their spin.

997 Nevertheless, although the model was not only limited to spherical orbitals anymore, making
 998 the atom more realistic, the Zeeman effect couldn't be completely explained by just using n , l and
 999 m [30–33] nor could the result of the Stern-Gerlach experiment [34]. Both experiments are shown in
 1000 Figure 2.4. A solution was brought after Pauli in 1925 proposed together with his exclusion principle
 1001 the idea of a new quantum degree of freedom in order to resolve the apparent problem [35, 36]. This
 1002 degree of freedom was interpreted as an intrinsic angular momentum vector associated to the particle
 1003 itself, not to the orbital [37], and associated to a new quantum number s , the *spin* projection quantum
 1004 number explaining the lift of degeneracy to an even number of energy levels [38]. The new quantum
 1005 number helped in theorizing the neutron as a neutral particle rather than a bond state of a proton and
 1006 an electron confined in the nucleus itself.

1007 The introduction of the *spin* happened one year after another attempt of improvement of the
 1008 theory was made by De Broglie in his Ph.D. thesis [39]. The original formulation of the quantum
 1009 theory only considered photons as energy quanta behaving as both *waves* and *particles*. De Broglie

1010 proposed that *all* matter are described by waves and that their momentum is proportional to the
 1011 oscillation of quantized electromagnetic field oscillators. This interpretation was able to reproduce
 1012 the previous version of the quantum energy levels by showing that the quantum condition involves
 1013 an integer multiple of 2π , as shown by Formula 2.2.

$$(2.2) \quad p = \hbar k \Leftrightarrow \int pdx = \hbar \int kdx = 2\pi\hbar n$$

1014 Although the intuition of De Broglie about the wave-particle duality of all matter was a step in the
 1015 right direction, his interpretation was semiclassical and it is in 1926 that the first full quantum wave
 1016 equation would be introduced by Schrödinger to describe electron-like particles, reproducing the
 1017 previous semiclassical formulation without inconsistencies [40]. This complex equation describes
 1018 the evolution of the wave function Ψ of the quantum system, defined by its position vector \mathbf{r} and time
 1019 t as an energy conservation law, in which the hamiltonian of the system \hat{H} is explicit, by solving the
 1020 Equation 2.3.

$$(2.3) \quad i\hbar \frac{\partial}{\partial t} |\Psi(\mathbf{r}, t)\rangle = \hat{H} |\Psi(\mathbf{r}, t)\rangle$$

1021 The spin was then included into Schrödinger equation by Pauli to take into account the interaction
 1022 with an external magnetic field, as shown in Equation 2.4 in which the Hamiltonian operator is a 2×2
 1023 matrix operator due to the Pauli matrices [38]. \mathbf{A} is the vector potential and ϕ is the scalar electric
 1024 potential.

$$(2.4) \quad i\hbar \frac{\partial}{\partial t} |\Psi\rangle = \left[\frac{1}{2m} (\sigma \cdot (\mathbf{p} - q\mathbf{A})^2 + q\phi) \right] |\Psi\rangle$$

1025 Later in 1927, Dirac went further in his paper about emission and absorption of radiation by
 1026 proposing a second quantization not only of the physical process at play but also of the electromagnetic
 1027 field [41]. His equation provided the ingredients to the first formulation of *Quantum Electrodynamics (QED)*
 1028 and the description of photon emission by electrons dropping into a lower energy state
 1029 in which the final number of particles is different than the initial one. Nevertheless, in order to properly
 1030 treat electromagnetism, the incorporation of the special relativity developed by Einstein was
 1031 necessary. Derived in 1928, the Dirac equation, shown as Equation 2.5, similarly to Schrödinger
 1032 equation, is a single-particle equation but it incorporates special relativity in addition to quantum
 1033 mechanics rules [42].

$$(2.5) \quad i\hbar\gamma^\mu \partial_\mu \psi - mc\psi = 0$$

1034 It features the 4×4 gamma matrices γ^μ built using 2×2 Pauli matrices and the unitary matrix,
 1035 the 4-gradient ∂_μ , the rest mass m of any half integer spin massive particle described by the wave
 1036 function $\psi(x, t)$, also called a Dirac spinor and the speed of light c . In addition to perfectly reproduce
 1037 the results obtained with quantum mechanics so far, it also provided *negative-energy solutions* that
 1038 would later be interpreted as a new form of matter, *antimatter* [43, 44]. In the non-relativistic limit,
 1039 the Dirac equation gives a theoretical justification to the Pauli equation that was phenomenologically
 1040 constructed to account for the spin.

1041 The successes of the QED were soon followed with theoretical problems as computations of any
1042 physical process involving photons and charged particles were shown to be only reliable at the first
1043 order of the *perturbation theory* [45]. At higher order of the theory, divergent contributions were
1044 appearing giving nonsensical results. Only two effects were contributing to these infinities.

- 1045 • The self-energy of the electron (or positron), the energy that the particle has due to its own
1046 interaction with its environment.
- 1047 • The vacuum polarization, virtual electron–positron pairs produced by a background electro-
1048 magnetic field in the vacuum which is not an "empty" space. These virtual pairs affect the
1049 charge and current distributions generated by the original electromagnetic field.

1050 Solving this apparent problem was done by carefully defining the concepts of each observable,
1051 for example mass or charge, as these quantities are understood within the context of a non-interacting
1052 field equation. From the experimental point of view, they are abstractions as what is measured is
1053 "renormalized observables" shifted from their "bare" value by the interaction taking place in the
1054 measuring process. The infinities needed to be connected to corrections of mass and charge as those
1055 are fixed to finite values by experiment. This was the intuition of Bethe in 1947 who successfully
1056 computed the effect of such *renormalization* in the non-relativistic case [46]. Full covariant formula-
1057 tions of QED including renormalization were achieved by 1949 by Tomonaga, Schwinger, Feynman,
1058 and Dyson [47]. With the resolution of infinities, QED had mostly reached its final form, being still
1059 today the most accurate physical theory, and would serve as a model to build all other quantum field
1060 theories.

1061 **Development of the quark model and Quantum Chromodynamics**

1062 To explain the nuclear force that holds *nucleons* (protons and neutrons) together, Yukawa proposed
1063 in 1934 the existence of a force carrier called *meson* due to its predicted mass in the range in between
1064 the electron and nucleon masses [48]. Discovered in 1936 by Anderson and Neddermeyer [49, 50],
1065 and confirmed using bubble chambers in 1937 by Street and Stevenson [51], a first meson candidate
1066 was observed in the decay products of cosmic rays. Assuming it had the same electric charge as
1067 electrons and protons, this particle was observed to have a curvature due to magnetic field that was
1068 sharper than protons but smoother than electrons resulting in a mass in between the two. But its
1069 properties were not compatible with Yukawa's theory, which was emphasized by the discovery of a
1070 new candidate in 1947, again in cosmic ray products using photographic emulsions [52–54]. The
1071 detections of the mu-meson and of the pi-meson in emulsions are showed in Figure 2.5.

1072 This new candidate, although it had a similar mass than the already believed *meson*, would rather
1073 decay into it. For distinction, the first candidate would then be renamed "*mu meson*" when the second
1074 would be the "*pi meson*". The *mu meson* was behaving like a heavy electron and didn't participate
1075 in the strong interaction whereas the pion was believed to be the carrier of the nuclear interaction.
1076 This led to classify the *mu* in a new category of particles that shared similar properties called *leptons*
1077 under the name of *muon* together with the electron. The *pi meson* was finally found to be a triplet of
1078 particles: a positively charged, a negatively charged, and a neutral particle. The neutral *pi meson* has
1079 been more difficult to identify as it wouldn't leave tracks on emulsions nor on bubble chambers and
1080 needed to be studied via its decay products. It was ultimately identified in University of California's
1081 cyclotron in 1950 through the observation of its decay into 2 photons [55].

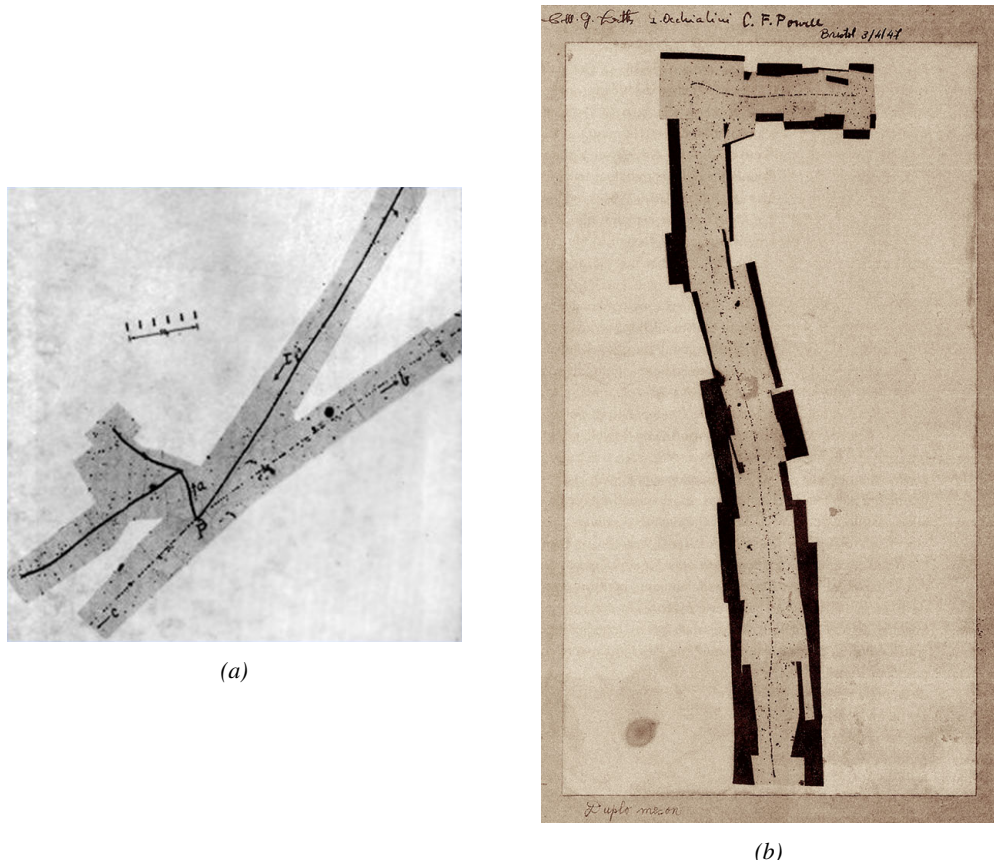


Figure 2.5: Figure 2.5a: decay of a μ -meson in an emulsion. Figure 2.5b: track of a π -meson in an emulsion signed by Lattes, Powell, and Occhialini.

Also discovered in 1947 but in cloud chamber photographs, the *K meson* has also been an important step towards the establishment of the Standard Model [56]. A triplet of particles, two charged and a neutral, with a mass roughly half that of a proton, were reported. These particles were baptised *K meson* in contrast to the "light" *pi* and *mu* "L-mesons". The particularity of the *K* is their very slow decays with a typical lifetime of the order of 10^{-10} s much longer than the 10^{-23} s of *pi*-proton reactions. The concept of *strangeness*, a new quantum number was then introduced thanks to an idea of Pais as an attempt to explain this phenomenon as *strange* particles appeared as the pair production of a strange and anti-strange particle [57].

With the development of synchrotrons, the particle *zoo* grew to several dozens during the 1950s as higher energies were reachable through acceleration. In 1961, a first classification system, called *Eightfold Way*, was proposed by Gell-Mann [58]. It found its roots in the Gell-Mann–Nishijima formula, which relates the electric charge Q , the third component of the isospin I_3 , the *baryon* number B and the strangeness S , as showed in Formula 2.6 [59–61].

$$(2.6) \quad Q = I_3 + \frac{1}{2}(B + S)$$

The isospin is a quantum number introduced in 1932 to explain symmetries of the newly dis-

1096 covered neutron using representation theory of $SU(2)$ [62]. The baryon number, was introduced
 1097 by Nishijima as a quantum number for baryons, i.e. particles of the same family as nucleons [59].
 1098 The mesons were classified in an octet and baryons of spin $\pm \frac{1}{2}$ and $\pm \frac{3}{2}$ were respectively classified
 1099 into an octet and a decuplet, as shown in Figure 2.6. To complete the baryon decuplet, Gell-Mann
 1100 predicted the existence of baryon Ω^- which would later be discovered in 1964 [63].

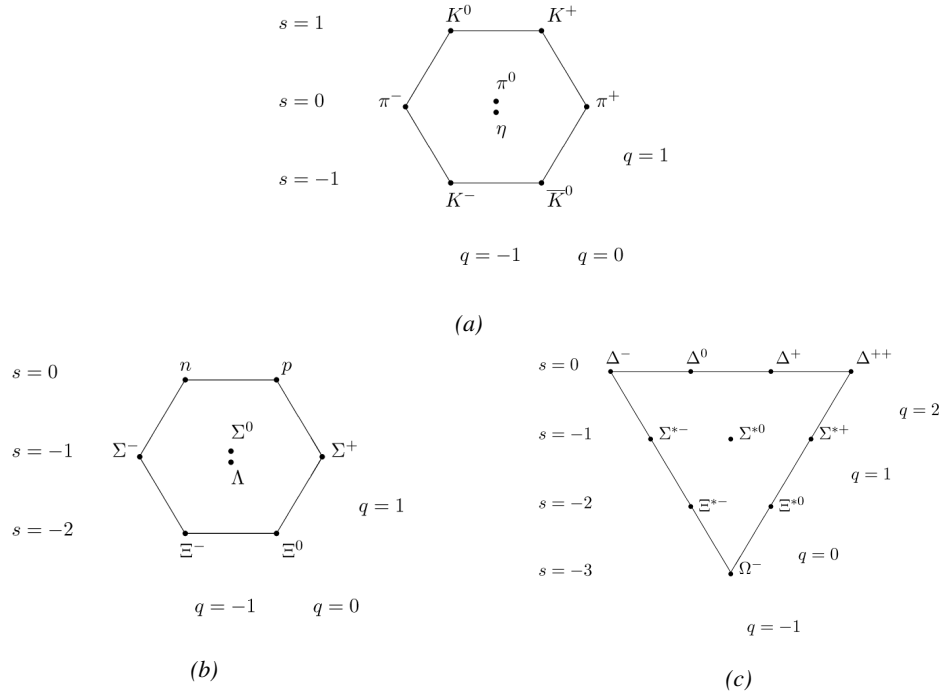


Figure 2.6: Figure 2.6a: Meson octet. Figure 2.6b: Baryon octet. Figure 2.6c: Baryon decuplet.

1101 Gell-Mann, and independently Zweig, then proposed a full theoretical model in which *hadrons*
 1102 (strongly interacting particles, i.e. mesons and baryons) were not elementary particles anymore [64–
 1103 66]. They were rather composed of three flavors of particles called *quarks* and their anti-particles.
 1104 The three flavors were called *up*, *down* and *strange*. *Up* and *down* were used to explain the nucleons
 1105 and non-strange mesons, while *strange* came into the composition of hadrons showing strangeness.
 1106 *Up* and *down* flavors were discovered in 1968 thanks to the deep inelastic scattering experiments
 1107 conducted at the Stanford Linear Accelerator Center (SLAC) [67, 68], and *strange* could only be
 1108 indirectly validated even though it provided a robust explanation to *kaon* (K) and *pion* (π).

1109 However, in the decade following the Gell-Mann-Zweig quark model proposition, several im-
 1110 provement to the model were brought. First by Glashow and Bjorken the same year that predicted
 1111 the existence of a fourth quark flavor, the *charm*, that would equalize the then known number of
 1112 quarks and leptons [69, 70]. Finally in 1973 by Kobayashi and Maskawa that increased the number
 1113 of quarks to six to explain the experimental observation of CP violation [71, 72]. These two quarks
 1114 were referred to as *top* and *bottom* for the first time in 1975 [73]. It's only after these additions to the
 1115 quark model that finally the *charm* was discovered in 1974 at both SLAC and Brookhaven National
 1116 Laboratory (BNL) [74, 75]. A meson in which the *charm* is bonded with an *anti-charm*, called J/ψ
 1117 and presented in Figure 2.7, helped convince the physics community of the validity of the model.

1118 The *bottom* was discovered soon after in 1977 in Fermilab [76] and indicated the existence of the
 1119 *top* that resisted to discovery until Fermilab's experiments CDF and D \emptyset in 1995 due its very large
 1120 mass and the energy needed to produce it [77, 78].

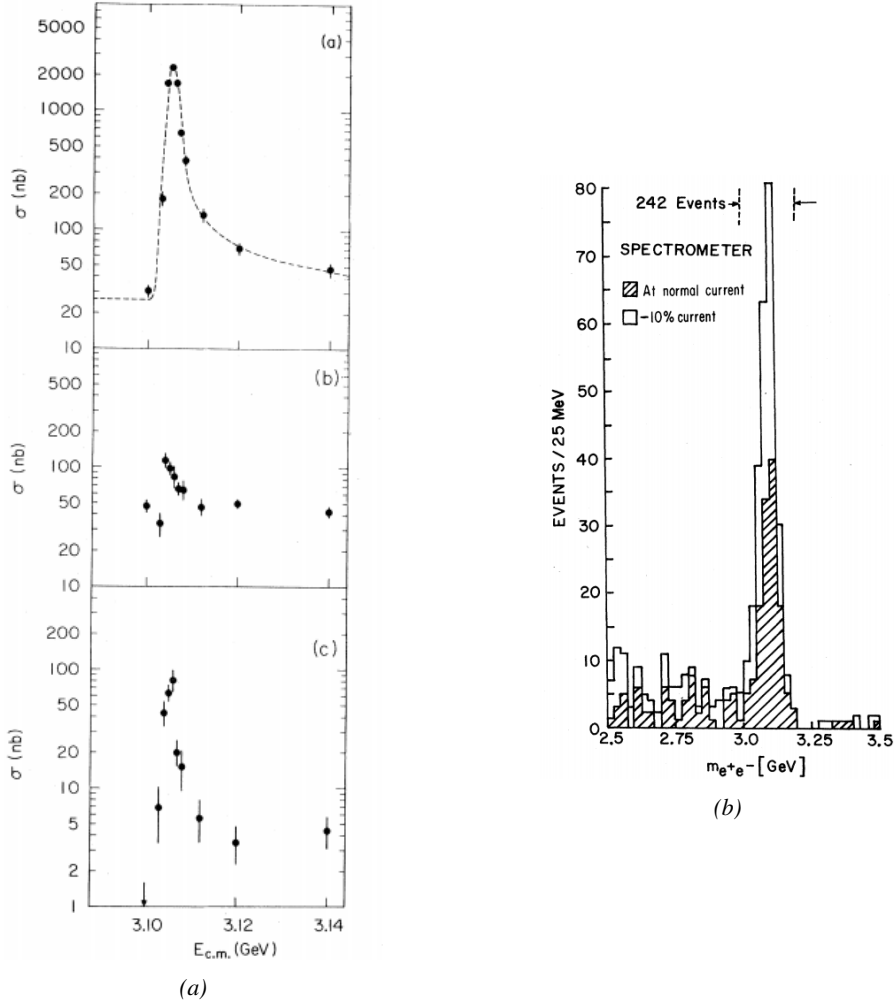


Figure 2.7: Discovery of the J/Ψ by both SPEAR (SLAC [74]) in Figure 2.7a and AGS (BNL [75]) in Figure 2.7b. In Figure 2.7a, the cross section versus energy is showed for (a) multi hadron final states, (b) e^+e^- final states, and (c) $\mu^+\mu^-$, $\pi^+\pi^-$ and K^+K^- final states.

1121 As remarked by Struminsky, due to mesons such as Ω^- or Δ^{++} , the first SU(3) model already
 1122 should have possessed an additional quantum number [79]. Indeed, these mesons are composed of
 1123 three identical quarks, respectively three *strange* and *up* quarks, with parallel spins, which should be
 1124 forbidden by the exclusion principle. Independently, Greenberg, and Han and Nambu proposed an
 1125 additional SU(3) degree of freedom for the quarks [80, 81]. It was later referred to as *color charge*
 1126 *gauge*, that could interact through *gluons*, the gauge boson octet corresponding to this degree of
 1127 freedom. The color field is presented in Figure 2.8a. Nevertheless, as observing free quarks to prove
 1128 their existence proved to be impossible, two visions of the quarks were argued. On one side, Gell-

Mann proposed to see quarks as mathematical construct instead of real particles, as they are always confined, implying that quantum field theory would not describe entirely the strong interaction. He promoted the S-matrix approach to treat the strong interaction. Opposed to this vision, Feynman on the contrary argued that quarks are real particles, that he would call *partons*, that should be described as all other particles by a distribution of position and momentum [82]. The implications of quarks as point-like particles were verified at SLAC and helped abandon the S-matrix to the benefit of QFT [83]. The concept of *color* was then added to the quark model in 1973 by Fritzsch and Leutwyler together with Gell-Mann to propose a description of the strong interaction through the theory of Quantum Chromodynamics (QCD) [84]. The discovery the same year of asymptotic freedom within the QCD by Gross, Politzer, and Wilczek, allowed for very precise predictions thanks to perturbation theory [85, 86]. The evolution of the gauge constant of QCD with respect to the energy as described by asymptotic freedom is showed in Figure 2.8b.

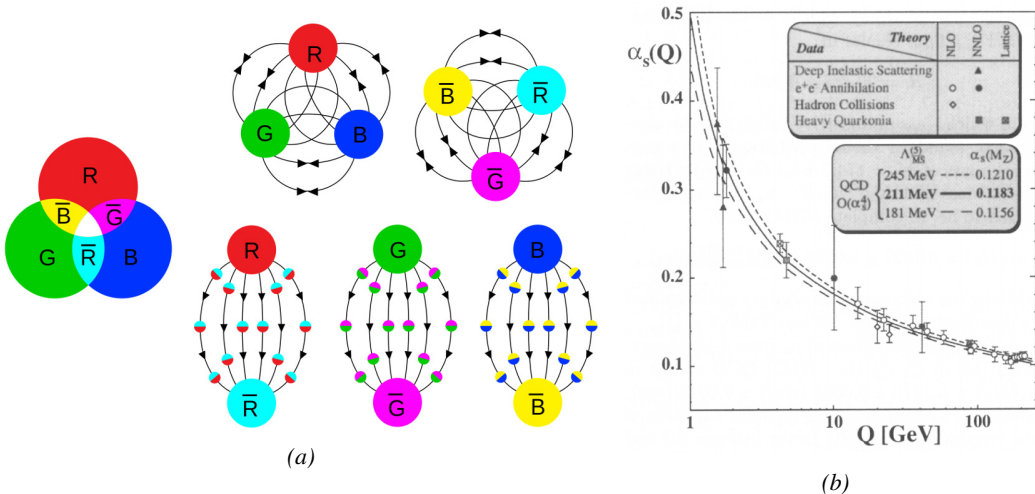


Figure 2.8: Figure 2.8a: the color field of QCD only allows for "white" baryons, particles composed of quarks, to exist. Examples are given for mesons, composed of a quark and its anti-quark, and hadrons, composed of three differently colored quarks or anti-quarks. Other exotic baryons have been predicted and observed, such as tetraquarks and pentaquarks. Figure 2.8b: a crossed analysis performed thanks to the data collected by various experiments at different energies have showed that the coupling constant evolves as predicted by the mechanism of asymptotic freedom [87].

The Weak interaction, spontaneous symmetry breaking, the Higgs mechanism and the Electroweak unification

The weak interaction is the process that causes radioactive decays. Thanks to the neutron discovery [23], Fermi could explain in 1934 beta radiations through the beta decay process in which the neutron decays into a proton by emitting an electron [88]. Though the missing energy observed during this process triggered a huge debate about the apparent non-conservation of energy, momentum and spin of the process, Fermi, as Pauli before him [89], proposed that the missing energy was due to a neutral not yet discovered particle that was then baptised *neutrino*. The impossibility to detect such a particle left some members of the scientific community sceptical, but hints of energy conservation and of the existence of the neutrino were provided by measuring the energy spectrum of electrons emitted through beta decay, as there was a strict limit on their energy, as showed in Figure 2.9.

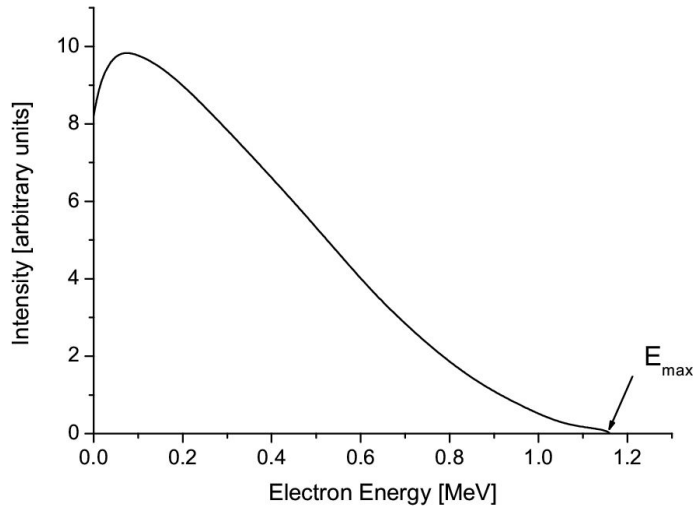


Figure 2.9: Energy spectrum of beta particles emitted by a source of ^{210}Bi .

It's only 30 years later in 1953 that it was discovered by the team of Cowan and Reines using the principle of inverse beta decay described through Formula 2.7 [90].



The experiment consisted in placing water tanks sandwiched in between liquid scintillators near a nuclear reactor with an estimated neutrino flux of $5 \times 10^{13} \text{ cm}^{-2} \text{ s}^{-1}$. However, in order to explain the absence of some reactions in the experiment of Cowan and Reines and constraint the beta decay theory of Fermi and extend it to the case of the muon, Konopinski and Mahmoud proposed in 1953 that the muon decay would eject a particle similar to the neutrino [91]. They predicted the existence of a muon neutrino that would be different to the one involved in the beta decay, related to the electron. With this, the idea of *lepton number* arised. The *muon neutrino* was successfully detected in 1962 by Lederman, Schwartz, and Steinberger [92].

The theory could not be valid though as the probability of interaction, called *cross-section*, would have been increasing without limitation with the square of the energy. Fermi had proposed a two vector current coupling but Lee and Yang noted that an axial current could appear and would violate parity [93]. Gamov and Teller had already tried to account for such parity violation by describing Fermi's interaction through allowed (parity-violating) and superallowed (parity-conserving) decays [94]. The Wu experiment in 1956 confirmed the parity violation [95], as showed by Figure 2.10. But the success of QED as a quantum field theory sparked the development of similar theory to describe the weak interaction.

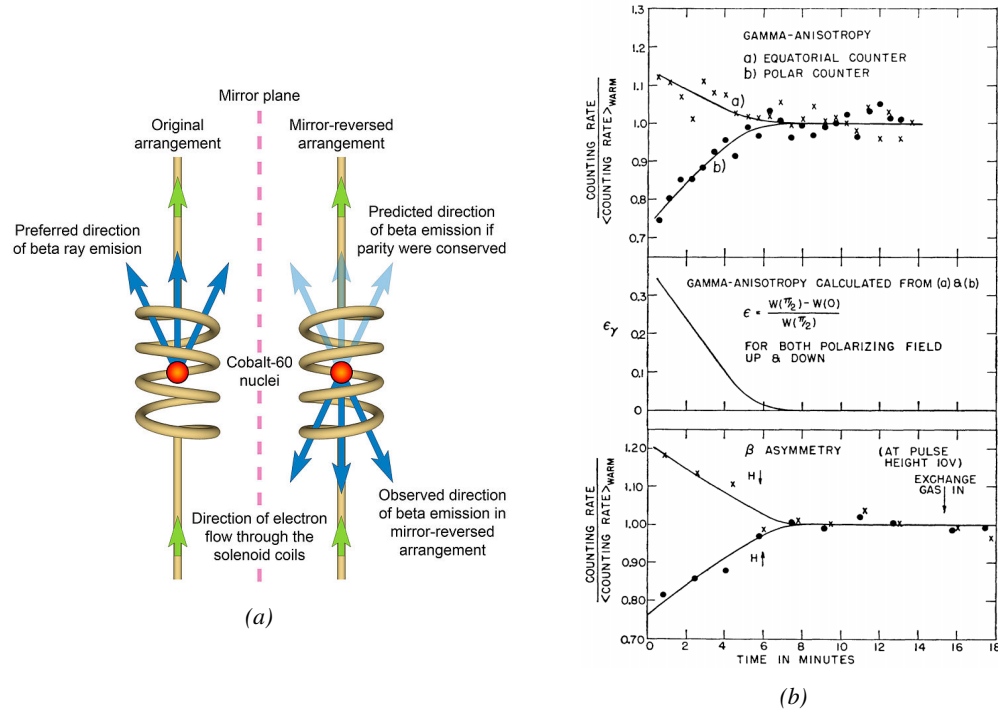


Figure 2.10: As explained through Figure 2.10a, the Wu experiment consisted in measuring the preferred direction of emission of beta rays of a Cobalt source placed in a stable magnetic field aligned, in one case, and anti-aligned, in the other case, with the nuclear spin. The result of Figure 2.10b showed a violation of parity.

As previously discussed, the great success of QED was built on an underlying symmetry, interpreted as a gauge invariance so that the effect of the force is the same in all space-time coordinates, and of the possibility to renormalize it in order to resolve infinities. In 1967, Weinberg found a way to unite both the electromagnetic and weak interaction into a gauge theory involving four gauge bosons, three of which are massive and carry out the weak interaction and the last is a massless boson carrying the electromagnetic interaction [96]. Among the three massive bosons, two are charged and one is neutral, similarly to the previously theorized *pi meson* vector of the Yukawa model [48] and all have a mass much greater than nucleons and thus a very short life time implying a finite very short range, contrary to the contact interaction originally proposed by Fermi.

Breakthroughs in other fields of physics contributed in giving theoretical support and interpretation to the unified electroweak theory. The stepping stone was the use of spontaneous symmetry breaking that was inspired to Nambu at the beginning of the 1960s [97, 98] following the development of the Bardeen–Cooper–Schrieffer (BCS) superconductivity mechanism in 1957 [99]. Cooper had shown that BCS pairs, pairs of electrons bound together at low temperature, can have lower energy than the Fermi Energy and are responsible for superconductivity. This led to the discovery of Goldstone-Nambu bosons [100, 101] as a result of the spontaneous breaking of the chiral symmetry in a theory describing nucleons and mesons developed by Nambu and Jona-Lasinio in 1961, and now understood as a low-energy approximation of QCD. Similarly to the mechanism of energy gap appearance in superconductivity, the nucleon mass is suggested to be the result of a self-energy of a fermion field and is studied through a four-fermion interaction in which, as a consequence of the symmetry, bound states of nucleon-antinucleon pairs appear and can be regarded as virtual pions.

1192 Though the symmetry is maintained in the equations, the ground state is not preserved. Goldstone
 1193 showed that the bound states correspond to spinless bosons with zero mass [101].

1194 Although the model in itself didn't revolutionize particle physics, spontaneous symmetry breaking
 1195 was generalized to quantum field theories. As all fundamental interactions are described using
 1196 gauge theories based on underlying symmetries, processes such as the chiral symmetry breaking
 1197 were introduced soon after the publication of Nambu and Jona-Lasinio. In 1962, Anderson,
 1198 discussed the implications of spontaneous symmetry breaking in particles physics [102]. He did so by
 1199 following the idea of Schwinger who suggested that zero-mass vector bosons were not necessarily
 1200 required to describe the conservation of baryons, contrary to the bosons emerging from chiral sym-
 1201metry breaking [103]. A model was finally independently built in 1964 by Brout and Englert [104],
 1202 Higgs [105], and Guralnik, Hagen, and Kibble [106], who discovered that combining an additional
 1203 field into a gauge theory in order to break the symmetry, the resulting gauge bosons acquire a nonzero
 1204 mass. Moreover, Higgs stated that this implied the existence of at least one new massive, i.e. self-
 1205 interacting, scalar boson corresponding to this additional field, that is now known as *Higgs boson*.
 1206 The Higgs mechanism today specifically refers to the process through which the gauge bosons of
 1207 the weak interaction acquire mass. In 1967, Weinberg could point to the Higgs mechanism to inte-
 1208 grate a Higgs field into a new version of the electroweak theory in which the spontaneous symmetry
 1209 breaking mechanism of the Higgs field would explicitly explain the masses of the weak interaction
 1210 gauge bosons and the zero-mass of photons [96].

1211 2.1.2 Construction and validation of the Standard Model

1212 The Standard Model of particle physics was built in the middle of the 1970s after the experimental
 1213 confirmation of the existence of quarks [107]. It is based on the assembly of the models previously
 1214 introduced and describing the fundamental interactions and their gauge bosons, except for gravita-
 1215 tion, as well as the way elementary "matter" particles interact with the fields associated with these
 1216 force carriers. In this sense, the development of QED and the unification of the electroweak interac-
 1217 tion, of the Yukawa interaction and of QCD, and of the Higg mechanism made it possible to explain
 1218 most of the contemporary physics.

1219 In the SM, "matter" particles, are described by twelve fermion fields of spin $\frac{1}{2}$ obeying the
 1220 Fermi-Dirac statistics, i.e. subjected to the Pauli exclusion principle. To each fermion is associated
 1221 its corresponding anti-particle. The fermions are classified according to the way they interact and
 1222 thus according to the charges they carry. Six of them are classified as quarks (u , d , c , s , t , and b) and
 1223 are subjected to all interactions and the six others as leptons (e^- , μ^- , τ^- , ν_e , ν_μ , and ν_τ). Leptons
 1224 are not subjected to the strong interaction and among them, the three neutrinos only interact weakly
 1225 as they are neutral particles, which explains why they are so difficult to detect. The gauge boson
 1226 fields are the gluons g for the strong interaction, the photon γ for the electromagnetic interaction
 1227 and the weak bosons W^+ , W^- , and Z^0 for the weak interaction. Finally, the Higgs field H^0 is
 1228 responsible, through the spontaneous symmetry breaking, of the mixing of the massless electroweak
 1229 boson fields W_1 , W_2 , W_3 , and B leading to the observable states γ , W^+ , W^- , and Z^0 that can
 1230 gain mass while interacting with the Higgs field. This picture of the SM is summarized through
 1231 Figure 2.11 where the antifermions are not shown.

1232 When the model was first finalized, the existence of the weak gauge bosons, of the charm, of the
 1233 third quark generation composed of top and bottom quarks to explain the observed CP violation was
 1234 not proven but the predictions were measured with good precision in the years following [74–78].
 1235 The weak bosons W and Z were discovered during the next decade in 1983 [108–111]. The very

1236 last predicted elementary particle of the model that was not observed yet proved to be very difficult
 1237 to observe. The Higgs boson needed the start of the LHC to finally be observed in 2012 [112, 113].
 1238 A few years more of tests were necessary to measure its properties to confirm the observation of a
 1239 scalar boson compatible with the predicted Higgs boson H^0 [114].

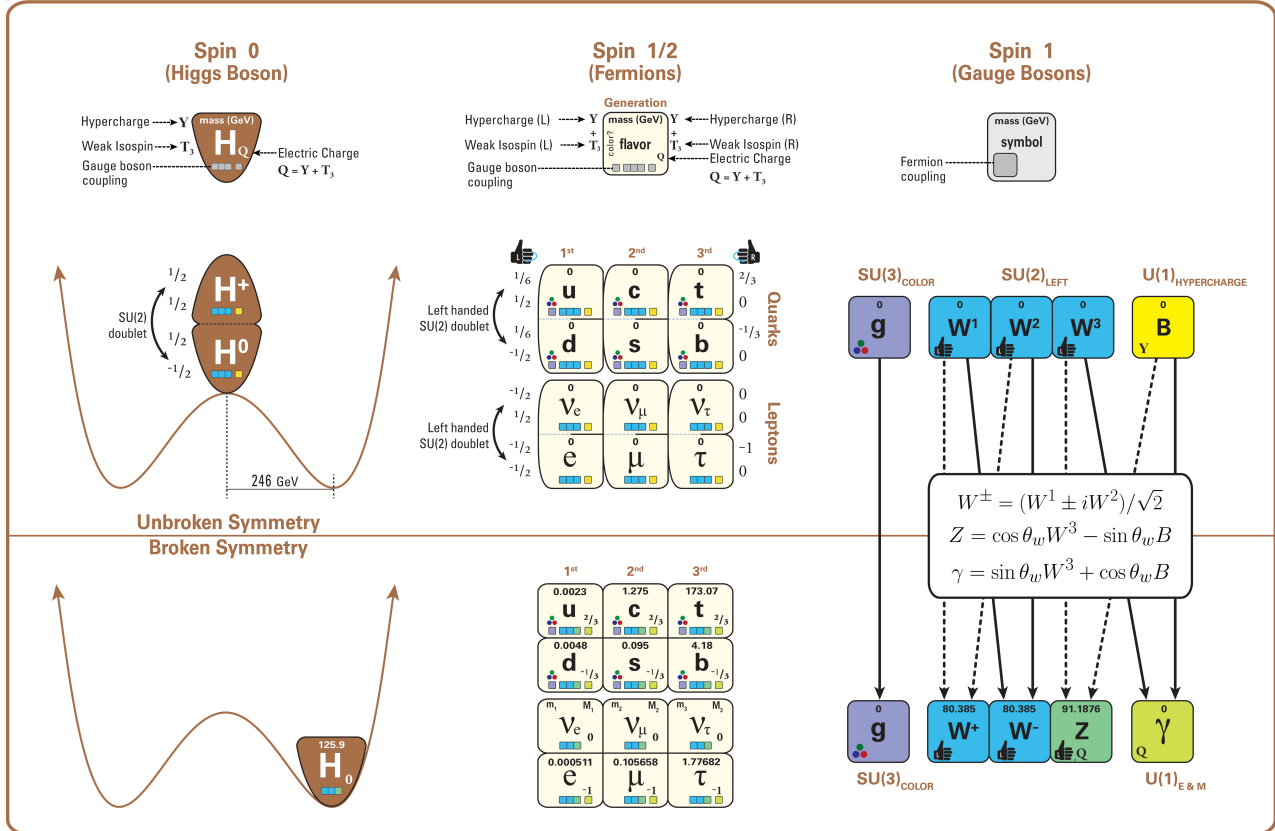


Figure 2.11: The elementary particles of the Standard Model are shown along with their properties. Their interactions with the strong, weak and electromagnetic forces have been made explicit using color squares. In the left column, the scalar Higgs boson is depicted. The center is focused on the matter particles, the fermions, and the right column on the force carriers, the gauge bosons. The role of the Higgs boson in electroweak symmetry breaking is highlighted, and the corresponding way properties of the various particles differ in the (high-energy) symmetric phase (top) and the (low-energy) broken-symmetry phase (bottom) are shown.

1240 2.1.3 Investigating the TeV scale

1241 In High-Energy Physics, the number of experimental events depends on the total interaction cross-
 1242 section of the colliding particles and of the *instantaneous luminosity* [115]. The luminosity is a
 1243 quantity providing an information on the interaction rate normalised to the interaction cross-section.
 1244 The relationship between number of events N , cross-section and instantaneous luminosity \mathcal{L} is given
 1245 in Formula 2.8.

$$(2.8) \quad \mathcal{L} = \frac{1}{\sigma} \frac{dN}{dt} \Leftrightarrow N = \sigma \int \mathcal{L} dt = \sigma \mathcal{L}_{int}$$

The integral of the luminosity over time is referred to as the *integrated luminosity* \mathcal{L}_{int} . In fact, the instantaneous luminosity can be deduced from the beam parameters. New colliders now use bunched beams. The instantaneous luminosity then depends on the bunch crossing frequency f_{BX} , on the number of particles contained in each bunch n , and on the RMS transverse beam sizes in the horizontal, σ_x^* , and vertical directions, σ_y^* , at the level of the interaction point. The beam sizes can be assumed to be identical, leading to the relation of Formula 2.9.

$$(2.9) \quad \mathcal{L} = f_{BX} \frac{n^2}{\sigma^*}$$

This expression doesn't depend on time anymore and leads to a simple estimation of the integrated luminosity and hence, knowing the cross-section of each available physics channel, to the expected number of events in each channel. The total interaction cross section is the sum of all the different output channels allowed by the interaction process. In the case of highly relativistic protons, the proton-proton (pp) total cross-section increases with the center-of-mass energy of interactions, as can be seen from Figure 2.12.

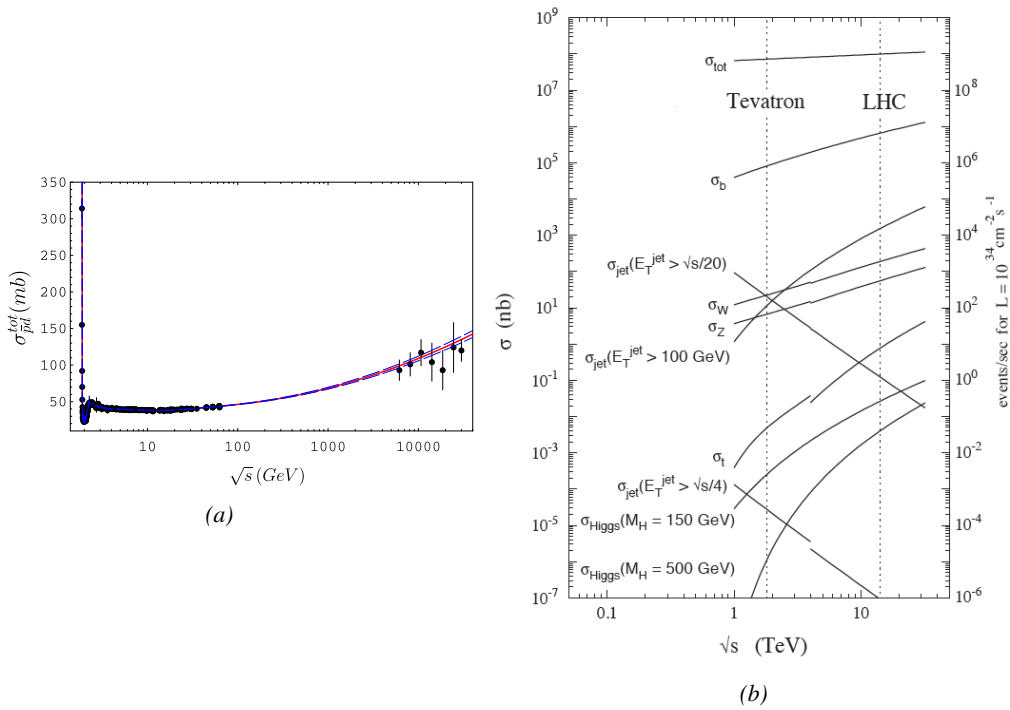


Figure 2.12: Figure 2.12a: Total proton-proton cross-section as a function of the collisions center-of-mass energy \sqrt{s} [116] with cosmic-ray data from Akeno Observatory and Fly's Eye Collaboration. Figure 2.12b: Total proton-(anti)proton and interaction channel cross-sections in the TeV scale.

Enhancing rare processes that allow to finely test the Standard Model is then achieved through an increase in both energy and luminosity. At the energy range that were scanned thanks to high-energy colliders, the SM has so far been a well tested theory. Nevertheless, several hints of physics going beyond its scope have been observed.

Dark matter and gravity: The discrepancy of velocity dispersion of stars in galaxies with respect to the visible mass they contain is known since the end of the 19th century where Kelvin proposed that this problem could be solved if a great majority of the stars would be dark bodies, idea strongly criticized by Poincaré [117]. Throughout the 20th century, physicists like Kapteyn [118] or Zwicky [119, 120], showed the first hints of a *dark matter* by studying star velocities and galactic clusters, followed by robust measurements of galaxy rotation curves by Babcock which suggested that the mass-to-luminosity ratio was different from what would be expected from watching the visible light [121]. Later in the 1970s, Rubin and Ford from direct light observations [122] and Rogstad and Shostak from radio measurements [123] showed that the radial velocity of visible objects in galaxies was increasing with increasing distance to the center of the galaxy. An example of galaxy rotation curve is provided in Figure 2.13. Finally observation of lensing effect by galaxy clusters, temperature distribution of hot gas in galaxies and clusters, and the anisotropies in the Cosmic Microwave Background (CMB), showed in Figure 2.14, kept on pointing to a *dark matter* [124]. From all the data accumulated, the visible matter would only account to no more than 5% of the total content on the visible universe [125]. Alternative theories have tried to investigate modified versions of the General Relativity as this theory is only well tested at the scale of the solar system but is not sufficiently tested on wider ranges or even theories in which gravitation is not a fundamental force but rather an emergent one [126, 127]. But so far, such theories have difficulties to reproduce all the experimental observations as easily as through dark matter.

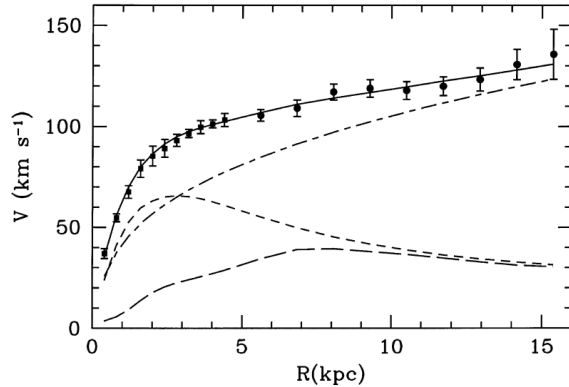


Figure 2.13: Rotation curve (points) of the galaxy M33 compared with best fitting model (line). The short-dashed line represents the rotation profile that would be expected from the observation of the stellar disc alone [128].

A possible theory to offer dark matter candidates would be *supersymmetry* (SUSY) which proposes a relationship in between bosons and fermions in the frame of the Minimal Supersymmetric Standard Model (MSSM). In this model, each elementary particle, through a spontaneous space-time symmetry breaking mechanism would have a *super partner* from the other family of particles, pairing bosons and fermions together. The model was first introduced as a way to solve the *Hierarchy Problem* [129]. The discrepancy between the strength of the weak force and gravity translates into a light Higgs boson compared to the *Planck Mass*. In the SM, the Higgs mass is left to be a measured parameter rather than a calculated one even though the model requires a mass in between 100 and 1000 GeV/c² to stay unitary. Nevertheless, quantum corrections to the Higgs mass coming from its interactions with virtual particles should make the scalar boson much heavier than what

1291 measured [130]. Through the MSSM, the stability of fermion masses would provide stability to the
1292 Higgs boson mass via the introduction of a fermionic super partner.

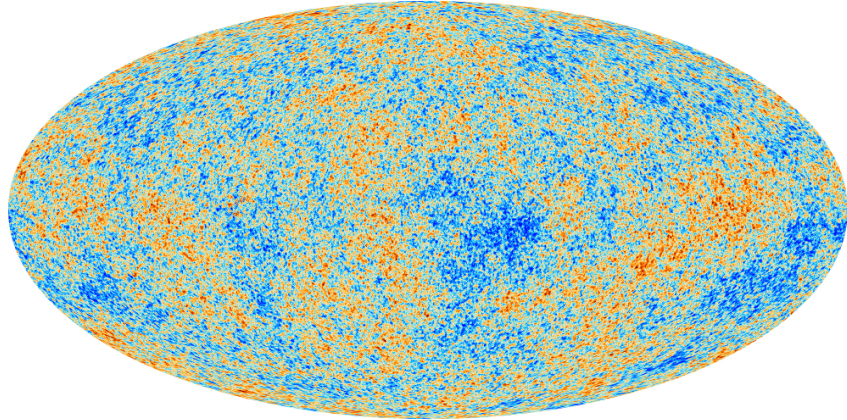


Figure 2.14: Cosmic Microwave Background as measured by the space observatory Planck which mean temperature is $T_\gamma = (2.7255 \pm 0.0006)\text{K}$ with anisotropies of the order of a few μK .

1293 On top of providing a solution to the Hierarchy Problem, the model comes with heavy dark
1294 matter candidates in the TeV scale [131]. Indeed, in the case *R-parity* is not violated, the lightest
1295 supersymmetric particle (LSP) cannot decay and could then explain the dark matter. The LSP in
1296 the model is neutral and can only interact through the weak and gravitational interactions. Typical
1297 candidates are the *neutralino*, the *sneutrino* or the *gravitino*.

1298 Finally, gravity is not explained through the SM, and huge difficulties are encountered when
1299 trying to include it. The strength of gravitational interaction is expected to be negligible at the scale
1300 of elementary particles, nevertheless, adding gravitation in the perspective of developing a "*theory of
1301 everything*" leads to divergent integrals that could not be fixed through renormalization. Extensions
1302 to the MSSM, and in particular minimal SUper GRAvity (mSUGRA), include general relativity as
1303 mediator of the symmetry breaking. mSUGRA gives access to the hidden sector in which the MSSM
1304 only interacts gravitationally and suppresses the infinities arising from attempts to include gravity
1305 into the SM thanks to possible renormalization [132].

1306 Signatures for the MSSM would come from the super partners of quarks and gluons that can
1307 decay into an LSP that could then be identified as missing energy as it escapes the detectors unde-
1308 tected. But even in the case MSSM predictions are not to be seen, the other models treating dark
1309 matter also propose Weakly Interacting Massive Particles (WIMPs) that could be observed in simi-
1310 lar ways than LSPs [133]. Moreover alternative models exist to provide solutions to the Hierarchy
1311 Problem. The most investigated models are extra dimensions such as Arkani-Hamed Dimopoulos
1312 Dvali [134, 135], Kaluza–Klein [136, 137] or Randall-Sundrum models [138, 139] that usually also
1313 include gravitation. Finally, alternative models also exist for the production of dark matter candi-
1314 dates. Models with a hidden valley that would unravel the existence of a new group of light particles
1315 through the extension of the SM with a new confining gauge group [140].

1316

1317 **Baryon asymmetry:** Another intriguing fact is that the universe is dominated by matter. However,
1318 the SM predicted that matter and antimatter should have been created in equal amounts. For an inter-

action to produce matter and antimatter at different rates within the SM, three necessary conditions were highlighted by Sakharov[141]. First of all, there must be a violation of the baryon number B . Then, there must be a C-symmetry and CP-symmetry violation. The C-symmetry violation must happen to make sure that the processes creating more baryons than antibaryons are not compensated by processes creating more anti-baryons and similarly, the CP-symmetry violation makes sure that there are not equal numbers of left-handed baryons and right-handed anti-baryons produced. Finally, the interactions must happen out of thermal equilibrium to make sure that CPT-symmetry does not balance the processes increasing the baryon number with processes doing otherwise [142]. An out-of-equilibrium interaction implies a new instable heavy particle.

The favoured model to explain this imbalance is the *baryogenesis* that requires electroweak symmetry breaking to be first order phase transition to fall within the scope of SM [143, 144]. This means that the symmetry breaking process must involve the absorption or release of a fixed latent heat. Through the baryogenesis, the phase transition breaks P-symmetry spontaneously and allows for CP-symmetry violation. In turn, the CP violation makes the amplitude of interactions involving quarks different than the ones involving anti-quarks leading to the greater creation rate of baryons with respect to anti-baryons. The key to this baryon net creation would be found into the *sphaleron*. A sphaleron is a particle-like saddle point of the energy functional that appears at the top of the transition barrier and that could be created if a sufficiently large amount of energy is brought as the tunneling effect through the barrier is largely suppressed for electroweak interactions. The existence of the sphaleron would allow violation of the conservation of B but also of the leptonic number L while conserving $B - L$. The detection at $p - p$ -colliders of such a transition is foreseen to be made through processes with high-multiplicity final states such as $u + u \rightarrow e^+ \mu^+ \tau^+ t\bar{t} b\bar{c} c\bar{s} d\bar{d} + X$ [145]. To be probed, the sphaleron transition requires an energy $E_{sph} \approx 9$ TeV. Nevertheless, if such transition cannot be observed, other BSM models such as the WIMP baryogenesis could be then observed thanks to the detection of displaced vertices, featuring the decay of a WIMP leading to violation of B [146].

Another possibility to explain the apparent asymmetry would be the existence of an electric dipole moment (EDM) in any fundamental particle that would permit matter and antimatter particles to decay at different rates [147]. Indeed, the presence of an EDM violates in itself both P and T symmetries. Experiments are able to probe for the EDM of various fundamental particles such as the electron [147], the charm and strange quarks [148] or even a heavy neutrino EDM [149].

Neutrino mass and sterile neutrino scenario: The SM considers neutrinos to be massless. But it was showed in the late 1960s by the Homestake experiment that the flux of solar neutrinos (i.e. ν_e) measured didn't match the predicted values [150]. The mechanism of neutrino oscillations as a solution to the discrepancy was proposed by Pontecorvo [151] and confirmed in the early 2000s by the Sudbury Neutrino Observatory [152]. This oscillation implies that neutrinos that can be observed are a superposition of massive neutrino states. The research on neutrino oscillation is already quite advanced with experiments looking at atmospheric, reactor or beam neutrinos in order to determine the elements of the mixing matrix (Pontecorvo–Maki–Nakagawa–Sakata matrix [153]) similar to the Cabibbo–Kobayashi–Maskawa (CKM) matrix describing the mixing of quarks [72]. Nevertheless, no answer to the origin of neutrino mass is yet provided.

Explaining the light non-zero mass of the neutrinos ν_l ($l = e, \mu, \tau$) of the order of the eV can be done through the Seesaw mechanism [154, 155]. This model features heavy Majorana counterparts N_l ($l = e, \mu, \tau$) to the ν_l . The masses of the light and heavy neutrinos are linked through a 2×2

¹³⁶⁴ mass matrix A with eigenvalues λ_{\pm} expressed as in Equation 2.10.

$$(2.10) \quad \begin{aligned} A &= \begin{pmatrix} 0 & M \\ M & B \end{pmatrix} \\ \lambda_{\pm} &= \frac{B \pm \sqrt{B^2 + 4M^2}}{2} \end{aligned}$$

¹³⁶⁵ The Majorana mass term B is assumed to be comparable to the Grand Unified Theory scale
¹³⁶⁶ (10^{16} GeV) while the Dirac mass term M is of the order of electroweak scale (246 GeV). In these
¹³⁶⁷ conditions, the eigenvalue λ_+ is almost B while λ_- is close to the ratio $-M^2/B$ compatible with
¹³⁶⁸ very light neutrinos with masses of the order of 1 eV. Studying the left-right symmetric model
¹³⁶⁹ seeking for the parity violation in weak interactions leads to the incorporation of three additional
¹³⁷⁰ gauge bosons W_R and Z' as a result of the spontaneous symmetry breaking. The processes that are
¹³⁷¹ predicted by the model and can be probed at colliders are processes such as $pp \rightarrow W_R \rightarrow l + N_l + X$
¹³⁷² and $pp \rightarrow Z' \rightarrow N_l + N_l + X$ where the heavy neutrinos decay as $N_l \rightarrow l + j_1 + j_2$, j_i being
¹³⁷³ jets [156]. Other version of seesaw mechanisms exist to account for the neutrino mass that can also
¹³⁷⁴ be explained thanks to supersymmetric models [157].

¹³⁷⁵ 2.2 The Large Hadron Collider & the Compact Muon Solenoid

¹³⁷⁶ Throughout its history, CERN has played a leading role in high-energy physics. Large regional facilities
¹³⁷⁷ such as CERN were planned after the second world war in an attempt to increase international
¹³⁷⁸ scientific collaboration and to allow scientists to share the forever increasing costs of experimental
¹³⁷⁹ facilities. Indeed, it is necessary to use always more powerful tools to improve the fine understanding
¹³⁸⁰ of our Universe. The construction of the first CERN accelerators at the end of the 50s, the Synchro-
¹³⁸¹ cyclotron (SC) and the Proton Synchrotron (PS), was directly followed by the first observation of
¹³⁸² antinuclei in 1965 [158]. The very first proton-proton collider showing hints of protons not being
¹³⁸³ elementary particles was the Intersecting Storage Rings (ISR). From this experience, the Super Pro-
¹³⁸⁴ ton Synchrotron (SPS) was built in the 70s to investigate the structure of protons, the preference
¹³⁸⁵ for matter over antimatter, the state of matter in the early universe or exotic particles, and led to
¹³⁸⁶ the discovery in 1983 of the W and Z bosons [108–111]. These newly discovered particles and the
¹³⁸⁷ electroweak interaction were then studied in detail by the Large Electron-Positron (LEP) collider
¹³⁸⁸ that proved that there only are three generations of elementary particles in 1989 [159]. The LEP was
¹³⁸⁹ then dismantled in 2000 to allow for the LHC to be constructed in the existing tunnel.

¹³⁹⁰ 2.2.1 LHC, the most powerful particle accelerator

¹³⁹¹ The different aspects of physics beyond the Standard Model of particle physics and the Standard
¹³⁹² Model itself can be tested through the use of very energetic and intense hadron and ion colliders.
¹³⁹³ Powerful hadron colliders are suited for searching for strongly interacting particles. The LHC at
¹³⁹⁴ CERN is a perfect tool to seek answers to these open questions and the experiments build along its
¹³⁹⁵ beam lines already started investigating further into the SM and BSM physics. The LHC has always
¹³⁹⁶ been considered as an option for the future of CERN. At the moment of the construction of the LEP
¹³⁹⁷ beneath the border between France and Switzerland, the tunnel was built in order to accommodate
¹³⁹⁸ what would be a Large Hadron Collider with a dipole field of 10 T and a beam energy in between
¹³⁹⁹ 8 and 9 TeV [160]. In 1985, the creation of a 'Working Group on the Scientific and Technological
¹⁴⁰⁰ Future of CERN' took place to investigate such a collider [161]. The decision was finally taken

almost ten years later, in 1994, to construct the LHC in the LEP tunnel [162] and the approval of the 4 main experiments that would take place at the four interaction points came in 1997 [163] and 1998 [164]:

- ALICE [165] has been designed for the purpose of studying the confinement of quarks through exploration of the quark-gluon plasma that is believed to have been a state of matter that existed in the very first moment of the universe.
 - ATLAS [166] and CMS [167] are general purpose experiments that have been designed with the goal of continuing the exploration of the Standard Model and the investigation of new physics.
 - LHCb [168] has been designed to investigate the preference of matter over antimatter in the universe through CP violation.

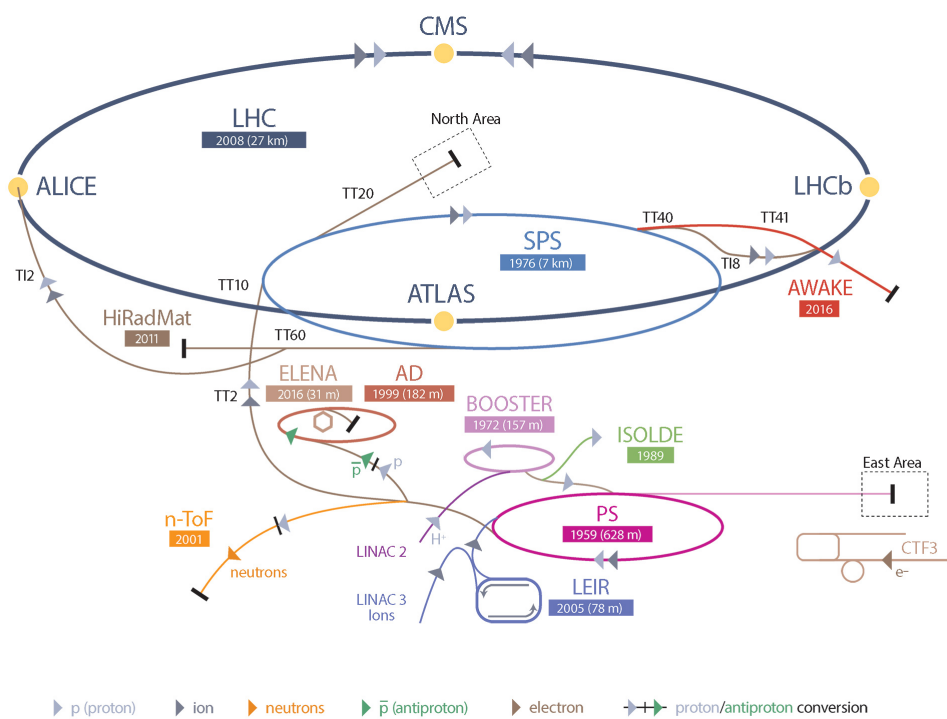


Figure 2.15: CERN accelerator complex.

These large-scale experiments, as well as the full CERN accelerator complex, are displayed in Figure 2.15. The LHC is a 27 km long hadron collider and the most powerful accelerator used for particle physics since 2008 [169]. The LHC is designed to collide protons at a center-of-mass energy of 14 TeV and luminosity of $10^{34} \text{ cm}^{-2}\text{s}^{-1}$, as well as Pb ions at a center-of-mass energy of 2.8 TeV/A with a peak luminosity of $10^{27} \text{ cm}^{-2}\text{s}^{-1}$. The collider is the last of a long series of accelerating devices. Indeed, before being accelerated by the LHC, the particles need to pass through different acceleration stages. All these acceleration stages are visible on Figure 2.15 and pictures of the accelerators are shown in Figure 2.16.

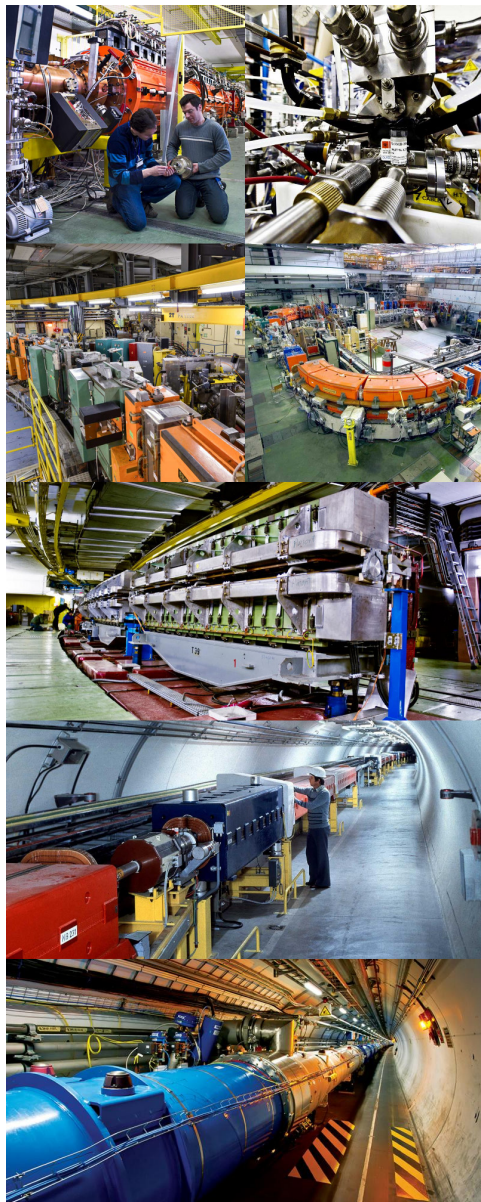


Figure 2.16: Pictures of the different accelerators. From top to bottom: first the LINAC 2 and the Pb source of LINAC 3. Then the Booster and the LEIR. Finally, the PS, the SPS and the LHC.

The story of accelerated protons at CERN starts with a bottle of hydrogen gas injected into the source chamber of the linear particle accelerator *LINAC 2* in which a strong electric field strips the electron off the hydrogen molecules only to keep their nuclei, the protons. The cylindrical conductors then accelerate the protons to an energy of 50 MeV. When exiting the LINAC 2, the protons are divided into four bunches and injected into the four superimposed synchrotron rings of the *Booster* where they are then accelerated to reach an energy of 1.4 GeV before being injected into the *PS*. The four proton bunches are hence sent as one to the *PS* where their energy eventually reaches 26 GeV. The *PS* not only accelerates protons. It also accelerates heavy ions from the *Low Energy Ion Ring* (*LEIR*) to an energy of 150 GeV before they are injected into the *Super Proton Synchrotron* (*SPS*). The *SPS* accelerates the particles to an energy of 450 GeV before they are injected into the *Large Hadron Collider* (*LHC*).

1428 *Ion Ring (LEIR)*. Lead is first injected into the dedicated linear collider *LINAC 3*, that accelerates
1429 the ions. Electrons are striped off the lead ions all along the acceleration process and eventually,
1430 only bare nuclei are injected in the LEIR whose goal is to transform the long ion pulses received
1431 into short dense bunches for LHC. Ions injected and stored in the PS were accelerated by the LEIR
1432 from 4.2 MeV to 72 MeV. Directly following the PS, is finally the last acceleration stage before the
1433 LHC, the 7 km long *SPS*. The SPS accelerates the protons to 450 GeV and inject them in both LHC
1434 accelerator rings that will increase their energy up to 7 TeV. When the LHC runs with heavy lead
1435 ions for ALICE and LHCb, ions are injected and accelerated to reach the energy of 2.8 TeV/A.

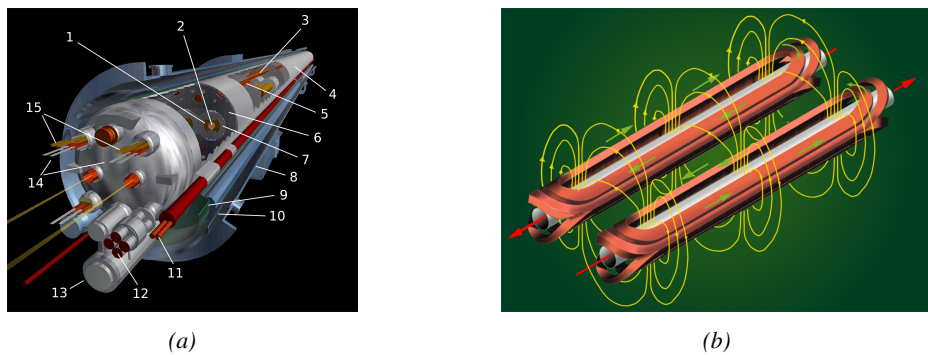


Figure 2.17: Figure 2.17a: schematics of the LHC cryodipoles. 1: Superconducting Coils, 2: Beam pipe, 3: Heat exchanger Pipe, 4: Helium-II Vessel, 5: Superconducting Bus-bar, 6: Iron Yoke, 7: Non-Magnetic Collars, 8: Vacuum Vessel, 9: Radiation Screen, 10: Thermal Shield, 11: Auxiliary Bus-bar Tube, 12: Instrumentation Feed Throughs, 13: Protection Diode, 14: Quadrupole Bus-bars, 15: Spool Piece Bus-bars. Figure 2.17b: magnetic field and resulting motion force applied on the beam particles.

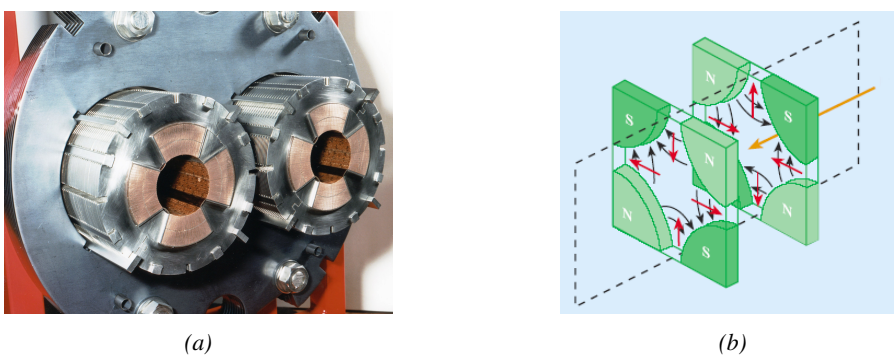


Figure 2.18: The LHC quadrupoles (Figure 2.18a) showed together with the magnetic fields and resulting focussing force applied on the beam by two consecutive quadrupoles (Figure 2.18b).

1436 The LHC beams are not continuous but are rather organised in bunches of particles. When in
1437 *pp*-collision mode, the beams are composed of 2808 bunches of 1.15×10^{11} protons separated by
1438 25 ns. When in *Pb*-collision mode, the 592 *Pb* bunches are on the contrary composed of 2.2×10^8
1439 ions separated by 100 ns. The two parallel proton beams of the LHC are contained in a single twin-
1440 bore magnet due to the space restriction in the LEP tunnel. Indeed, building two completely separate
1441 accelerator rings next to each other was impossible. The dipoles of the 1232 twin-bore magnets are
1442 shown in Figure 2.17 alongside the magnetic field generated along the dipole section to accelerate the

1443 particles. The dipoles generate a nominal field of 8.33 T, needed to give protons and lead nucleons
 1444 their nominal energy. Some 392 quadrupoles, presented in Figure 2.18, are also used to focus to the
 1445 beams, as well as other multipoles to correct smaller imperfections.

1446 2.2.2 Timeline of operation

1447 LHC accelerated its first proton in September 2008 but the first collisions only started one year later
 1448 in November 2009. At this moment the LHC machine officially became the world's most powerful
 1449 particle accelerator and entered its Physics Run 1 that lasted until February 2013. During Run 1
 1450 of the LHC program, the center-of-mass energy was only half of the nominal LHC energy. Never-
 1451 theless, the energy and luminosity displayed during Run 1 were enough for both CMS and ATLAS
 1452 to discover the Higgs boson [112, 113] as showed in Figure 2.19 and for LHCb to discover pen-
 1453 taquarks [170] and confirm the existence of tetraquarks [171]. During this period, ALICE also re-
 1454 ported a successful observation of the quark-gluon plasma aimed at studying the early universe [172],
 1455 ATLAS reported the observation of a new particle before the discovery of the Higgs [173] and a first
 1456 test of super-symmetric models was performed [174].

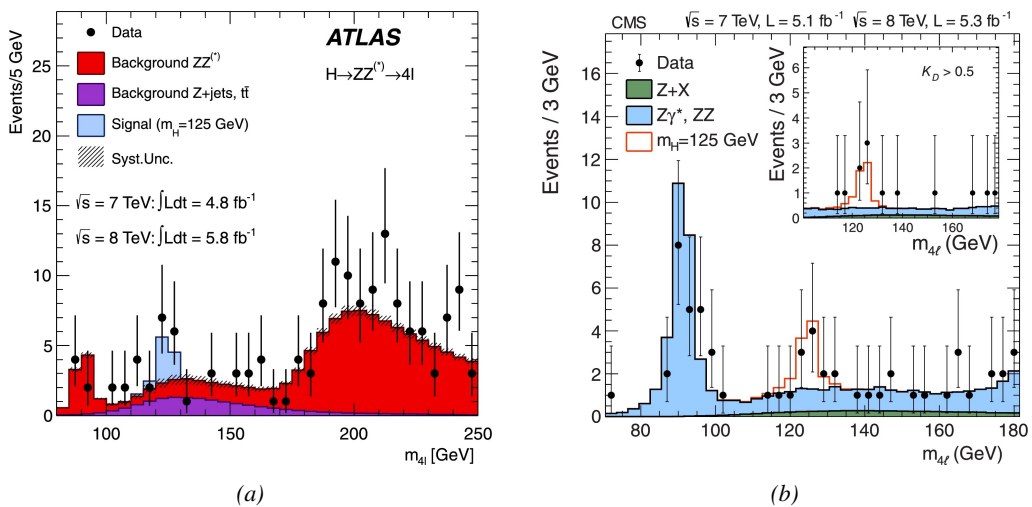


Figure 2.19: Distribution of the four-lepton invariant mass for the $ZZ \rightarrow 4l$ analysis as presented by both ATLAS [112] and CMS [113] in 2012.

1457 Run 1 was brought to an end with the start of the First Long Shutdown, an almost two years
 1458 technical stop aimed at increasing the energy of the center-of-mass collisions to $\sqrt{s} = 13$ TeV
 1459 as well as the instantaneous luminosity. This maintenance stop was also effectively used by the
 1460 experiments which upgraded part of their detection systems. Run 2 then started in 2015 and lasted
 1461 until end of 2018 where the activities ended with a last heavy ion run. During the operation, the
 1462 instantaneous was successfully brought to a value of $1.7 \times 10^{34} \text{ cm}^{-2} \text{ s}^{-1}$ exceeding the design value
 1463 almost by a factor 2. Run 2 has been the occasion to acquire more data to study the properties of
 1464 the Higgs boson with more precision. The boson discovered in the first physics run seems to be
 1465 consistent with the SM Higgs boson [114].

1466 From the end of 2018 to early 2021 the Second Long Shutdown will take place. This second
 1467 maintenance stop will be the occasion to boost once again the beam energy to finally reach the de-

sign energy of LHC, 14 TeV. On the side of the maintenance work, preliminary work for the High Luminosity LHC will be performed. The preparations will consist of detector, on the side of the experiments, and beam machine upgrades, on the side of LHC. In 2021, the physics program will be resumed with an instantaneous luminosity fixed at $2 \times 10^{34} \text{ cm}^{-2} \text{ s}^{-1}$. The timeline so far described is summarized through the evolution of the instantaneous luminosity and of the corresponding integrated luminosity provided in Figure 2.20.

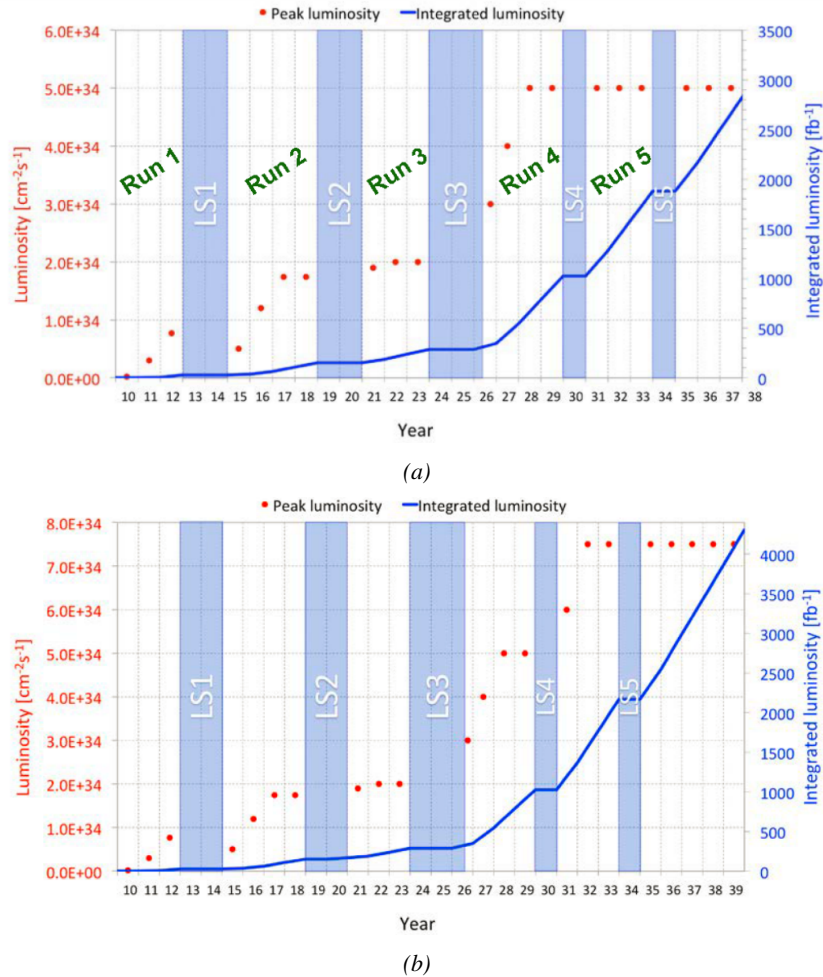


Figure 2.20: Detailed timeline projection of for LHC and HL-LHC operation until 2039 showing the evolution of the instantaneous and integrated luminosity as designed (Figure 2.20a) and in the ultimate case where the instantaneous luminosity is increased to $7.5 \times 10^{34} \text{ cm}^{-2} \text{ s}^{-1}$ thanks to a new increase of instantaneous luminosity during Run 5 (Figure 2.20b) [175, 176].

After the Third Long Shutdown (2024-2026) that will close the activities of Run 3, the accelerator will enter the HL-LHC configuration [175], increasing the instantaneous luminosity to an unprecedented level of $5 \times 10^{34} \text{ cm}^{-2} \text{ s}^{-1}$ for pp -collisions ($4.5 \times 10^{27} \text{ cm}^{-2} \text{ s}^{-1}$ for Pb -collisions), boosting the discovery potential of the LHC. The HL-LHC phase should last at least another 10 years depending on the breakthrough this machine would lead to. Already a new accelerating device, the

1479 FCC, as been proposed and is being investigated to prepare the future of high-energy physics after
1480 the LHC.

1481 **2.2.3 High Luminosity LHC**

1482 After approximately fifteen years of operation, the LHC will undergo a new series of upgrades during
1483 the LS3 in order to boost its discovery potential as previously discussed. This moment onward is
1484 what is referred to HL-LHC or Phase-II. The goal is to aim for a luminosity 5 to 7 times stronger
1485 than the nominal one trying to reach even 10 times this value if possible [175, 176]. Increasing
1486 the luminosity means that the beam size at the collision points needs to be reduced to boost the
1487 number of collisions per bunch crossing. For this purpose, new focusing and bending magnets and
1488 collimators will be installed at the collision points as well as newly developed "*crab cavities*" that
1489 will tilt the particle bunches just prior to the collisions by giving them transverse momentum and
1490 thus increasing their meeting area. In addition, the full proton injection line will be upgraded.

1491 On the experiments side, the pile-up (PU) will be increased up to 150 to 200 interactions per
1492 bunch crossing in ATLAS and CMS, making necessary a strong upgrade of the trigger system and
1493 of the inner trackers and of the calorimeters. Both ATLAS and CMS will also need to upgrade the
1494 muon trigger at the level of their endcaps mainly focusing on the coverage near the beam line in
1495 order to increase the detection acceptance and event selection. Moreover, the increased luminosity
1496 will also lead to an increased background rate and a faster ageing of the detectors. This PhD work
1497 takes place into this very specific context of muon detector consolidation and certification for the
1498 HL-LHC period in order to provide the CMS experiment with robust new detectors and confirm that
1499 the present system will survive through the next 20 years of HL-LHC.

1500 The end of 2018 marked the beginning of LS2 and the start of Phase-II upgrade activities. From
1501 the HL-LHC period onwards, i.e. past LS3, the performance degradation due to integrated radiation
1502 as well as the average number of inelastic collisions per bunch crossing, seen as pile-up into the
1503 detectors' readout that far exceeds this of the original LHC plans, will rise substantially and become
1504 a major challenge for all of the LHC experiments, like CMS, that were forced to address an upgrade
1505 program for Phase-II [177]. Dealing with the data from the muon detectors will force to upgrade
1506 the detectors and electronics towards the most recent technologies. Simultaneously, this will push
1507 new latency requirements onto the Level-1 trigger and the Data Acquisition (DAQ) that will only
1508 be fulfilled by upgrading the system with electronics having deeper buffering and faster processing.
1509 Simulations of the expected distribution of absorbed dose in the CMS detector under HL-LHC
1510 conditions show, in Figure 3.7, that detectors placed close to the beam line will have to withstand high
1511 irradiation, the radiation dose being of the order of a few tens of Gy.

1512 **2.2.4 CMS, a multipurpose experiment**

1513 Among the four main LHC experiments is the Compact Muon Solenoid used as a multipurpose
1514 tool to investigate the SM and the physics beyond its scope. Proposed through a letter of intention
1515 in 1992 [167], and as its name suggests, this very compact detector's uses the muons as a clear
1516 tag of most of SM and new physics interesting channels. In the original 1997 Technical Design
1517 Report (TDR) [178], the very first sentences were stating that "*Muons are an unmistakable signature*
1518 *of most of the physics LHC is designed to explore. The ability to trigger on and reconstruct muons*
1519 *at the highest luminosities is central to the concept of CMS, the Compact Muon Solenoid.*" CMS
1520 participated in the discovery of the Higgs boson and the measurement of its properties and couplings

¹⁵²¹ together with ATLAS and is also actively involved in the search for SUSY and heavy ion collisions.
¹⁵²² Other exotic physics are also being investigated using the data collected by CMS.

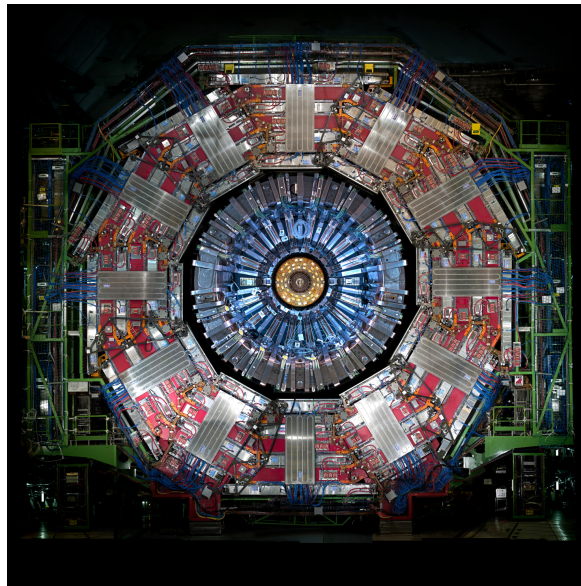


Figure 2.21: Picture of the CMS barrel. The red outer layer is the muon system hosted into the red iron return yokes. The calorimeters are the blue cylinder inside in magnet solenoid and the tracker is the inner yellow cylinder built around the beam pipe.

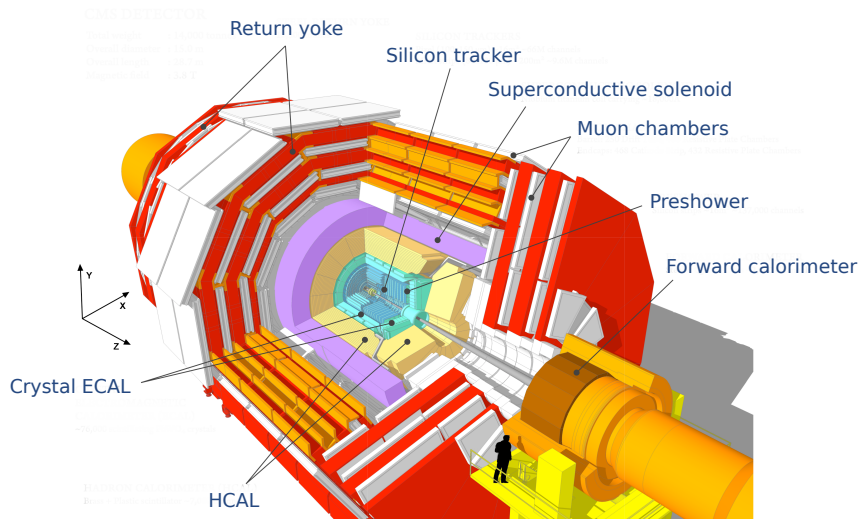


Figure 2.22: View of the CMS apparatus and of its different components.

¹⁵²³ The CMS apparatus in itself is the heaviest detector ever built starring a SI15m diameter and a
¹⁵²⁴ 29 m length for a total weight of 14 kT. A thick 4 T solenoid magnet located at the beam interaction
¹⁵²⁵ point hosts trackers and calorimeters. Extending in all directions around the magnet, heavy iron

1526 return yokes are installed to extend the magnetic field and support a muon system. The apparatus
 1527 consists of a barrel, referring to the magnet and the detectors contained in it and the part of the
 1528 muon system built directly in the cylinder around the magnet, and of two endcaps in the forward and
 1529 backward region of the detector that closes the apparatus and complete the detection coverage along
 1530 the beam line. A front view on the barrel is provided in Figure 2.21 while a detailed view of the
 1531 apparatus is given in Figure 2.22.

1532 In order to efficiently detect all long leaving particles and measure their properties with good
 1533 precision, the CMS detector uses an onion like layout around of the interaction point in order to
 1534 maximize the covered solid angle. As detailed in Figure 2.23, in the innermost region of the detector,
 1535 closest to the interaction point, the silicon tracker records the trajectory of charged particles. Around
 1536 it, the electromagnetic calorimeter (ECAL) stops and measure the energy deposition of electrons
 1537 and photons. In the next layer, the hadron calorimeter (HCAL), hadrons are stopped and their energy
 1538 measured. These layers are contained inside of the magnet of CMS, the superconducting solenoid.
 1539 Outside of the magnet are the muon chambers embedded into iron return yokes used to control the
 1540 magnetic field and gives muons, the only particles traveling completely through the whole detector, a
 1541 double bending helping in reconstructing their energy and trajectory. Note that photons and neutral
 1542 hadrons are differentiated from electrons and charged hadrons in the calorimeters by the fact that
 1543 don't interact with the silicon tracker and that they are not influenced by the magnetic field.

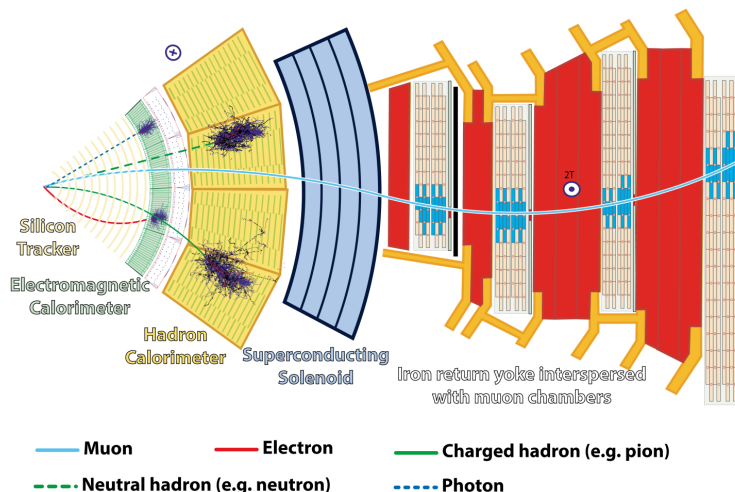


Figure 2.23: Slice showing CMS sub-detectors and how particles interact with them.

1544 2.2.4.1 The silicon tracker, core of CMS

1545 The silicon tracker visible on Figure 2.24 is divided into two different sub-systems: the *pixel detector*
 1546 at the very core and the *microstrip detector* around it. This system is composed of 75 million
 1547 individual readout channels with up to 6000 channels per squared centimeter for the pixels making
 1548 it the world's biggest silicon detector. This density allows for measurements of the particle tracks
 1549 with a precision of the order of $10 \mu\text{m}$. This is necessary to reconstruct all the different interaction
 1550 vertices with precision and have a precise measure of the curvature of the charged particles traveling
 1551 through the magnetic field to estimate their charge and momentum.

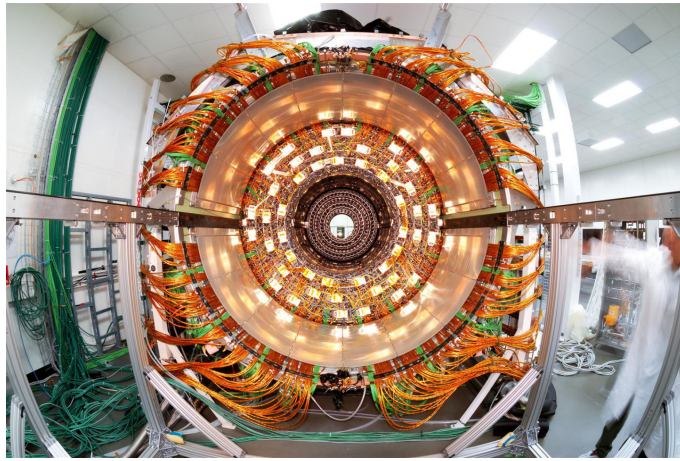


Figure 2.24: CMS tracker.

1552 2.2.4.2 The calorimeters, measurement of particle's energy

1553 The ECAL directly surrounding the tracker is composed of crystals of lead tungstate, $PbWO_4$, a
 1554 very dense but optically transparent material used to stop high-energy electrons and photons. These
 1555 crystal blocks basically are extremely dense scintillators which scintillate in fast, short light bursts
 1556 proportionally to the energy deposition. The light is yielded rapidly and contained at 80% in the
 1557 corresponding 25 ns lasting bunch crossing. Each crystal is isolated from the other by the carbon
 1558 fiber matrix they are embedded in. It is composed of a barrel containing more than 60,000 crystals
 1559 and of closing endcaps containing another 15,000 crystals. In front of the ECAL endcap is installed
 1560 a preshower detector made out of two layers of lead and silicon strip detectors to increase the spatial
 1561 resolution close to the beam line for pion-photon and single-double photon discrimination purposes.
 1562 Figure 2.25 shows the calorimeter inside of the magnet and the crystals.

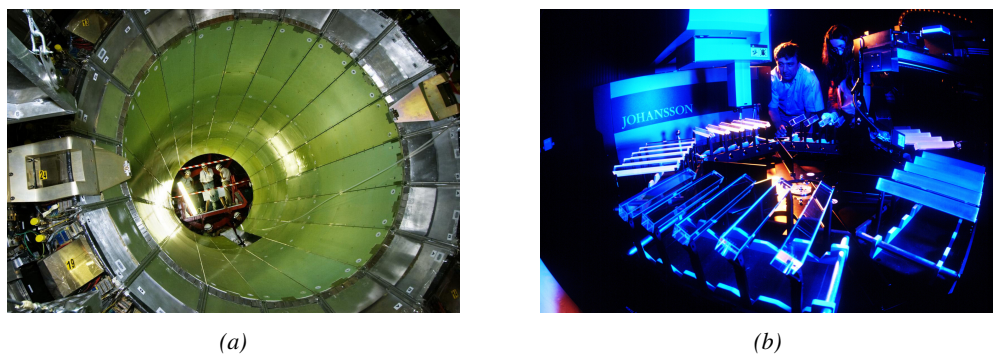


Figure 2.25: Figure 2.25a: picture of the ECAL. Figure 2.25b: picture of the lead tungstate crystals composing the ECAL.

1563 The next layer is the HCAL measuring the hadrons momentum and providing indirect hints of
 1564 non-interacting neutral particles, such as neutrinos, as missing transverse momentum. Several layers
 1565 of brass or steel are interleaved with plastic scintillators readout by photodiodes using wavelength-
 1566 shifting fibers. The HCAL is also composed of a barrel, shown in Figure 2.26 and of endcaps. It

1567 also features forward calorimeters on both sides of CMS in the region very close to the beam line at
 1568 high pseudorapidity ($3.0 < |\eta| < 5.0$). The role of these forward calorimeters, made using steel and
 1569 quartz fibers, is to measure very energetic hadrons.

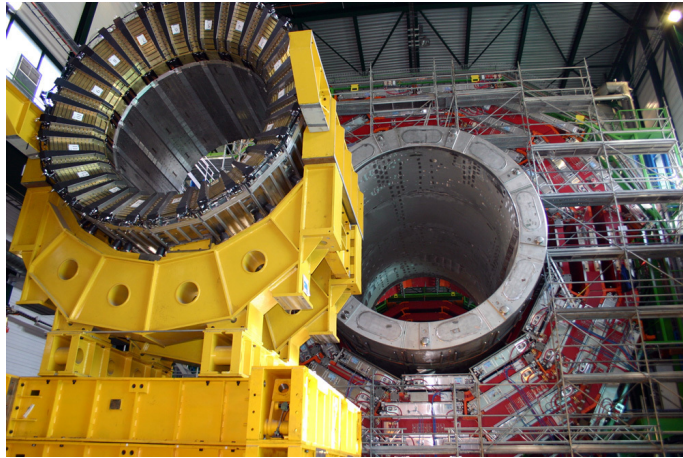


Figure 2.26: CMS hadron calorimeter barrel.

1570 2.2.4.3 The muon system, corner stone of CMS

1571 Finally, in the outer region of the apparatus, a muon system is used to trigger on potentially interesting
 1572 event by identifying muons. Indeed, the muon system is a very important part of the CMS
 1573 trigger infrastructure. It is designed to efficiently select data from the enormous data flow received
 1574 by the detectors. The LHC delivers collisions at a rate of 40 MHz with a pile-up of 20 to 30 colli-
 1575 sions per bunch crossing during Phase-I. The level of pile-up is foreseen to increase to 200 during
 1576 Phase-II. This represents billions of interactions per second among which a large quantity is low en-
 1577 ergy collisions that are not likely to produce new reactions. Moreover, it is physically impossible for
 1578 nowadays technologies to cope with a so huge data flow. Working at a maximum rate of 100 kHz,
 1579 the trigger system is able to select the 100,000 more interesting events by looking at the energy
 1580 distribution of the interaction products and clear signatures like muons reconstructed by the muon
 1581 system. The vast majority of these events will not finally be stored after physics tests are applied.

1582 The challenge for the muon system is to provide a robust and fast measurement of muons. Three
 1583 different subsystems compose the muon system as shown in Figure 2.27 in which a quadrant of the
 1584 CMS detector focuses on muon system. Drift Tube (DT) are found in the barrel region covering
 1585 the low pseudorapidity region where particles transverse momentum is lower and Cathode Strip
 1586 Chamber (CSC) are found in the endcap region covering higher pseudorapidity region closer to
 1587 beam line where particles have a stronger momentum. The redundancy of the system is insured
 1588 by Resistive Plate Chambers in both the barrel and endcap. Nevertheless, the region closest to the
 1589 beam line ($|\eta| > 1.8$) was not equipped with RPCs. This lack of redundancy in the high pseudo
 1590 rapidity region will be solved during LS2, the following Year End Technical Stop (YETS) in 2021
 1591 and 2022, and LS3 where the necessary services, detectors and Link System, that collects the data
 1592 and synchronizes them, will be installed.

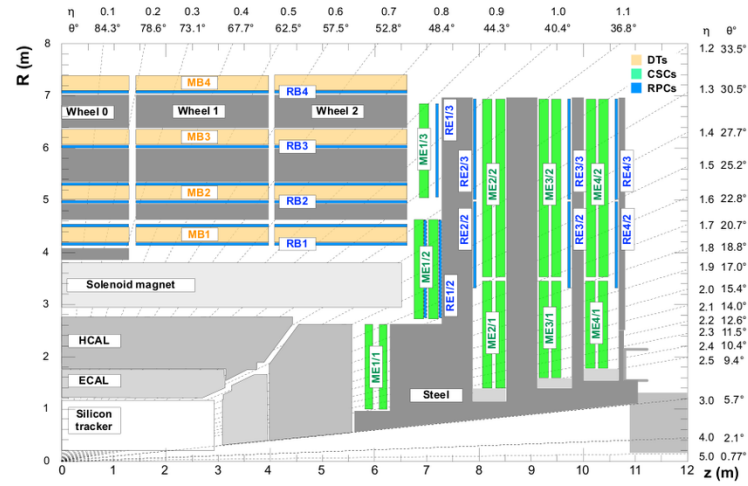


Figure 2.27: A quadrant of the muon system, showing DTs (yellow), RPCs (blue), and CSCs (green).

3

1593

1594

Muon Phase-II Upgrade

1595 The very first proton beam successfully circulated in the LHC in September 2008 directly followed
1596 by an incident leading to mechanical damage that would delay the LHC program for a year until
1597 November 2009, the very first collisions at a center-of-mass energy of 7 TeV taking place in March
1598 2010. The energy of the beam would be increased after a First Long Shutdown (LS1) starting
1599 early 2013 after less than 3 years of data taking. During the 2 years of shutdown, the upgrade of
1600 the accelerator allowed for several maintainances along the beam pipes, repair and consolidation
1601 of magnet connection and high-current splices. But not only the LHC was upgraded. Indeed, the
1602 experiments at the 4 collision points also took the advantage of this time to upgrade their system
1603 in prevision of the next LHC run (Run-II) until 2018 and the Second Long Shutdown (LS2) as
1604 the luminosity and energy of the beam would be continuously increasing. By the end of Run-
1605 II, the luminosity will have reached twice its nominal value when the center-of-mass energy has
1606 already got close to its nominal value by reaching an historical 13 TeV for the first time in 2017.
1607 The luminosity delivered by the collider will in the future be even further increased to improve its
1608 discovery potential giving no choice to experiments such as CMS to upgrade their technologies to
1609 cope with the increased radiation levels and detection rates.

1610 The next long shutdown will occur at the end of this year and will again be the occasion for sim-
1611 ilar maintenance and consolidation in prevision of Run-III and the future upgrade of LS3. Still, the
1612 main occupation of LS2 on LHC side will be the upgrade of LHC injectors. On the experiments side,
1613 LHCb and ALICE will, in a very tight schedule, implement major upgrades while ATLAS and CMS
1614 will wait until LS3 to upgrade their detectors in prevision of high luminosity *LHC-Phase-II*. ALICE
1615 main challenge is an upgrade of their apparatus to cope with the 50 kHz $Pb - Pb$ collisions. Simi-
1616 larly, LHCb will upgrade their frontend readout electronics to cope with the full 40 MHz collisions
1617 delivered by LHC. ATLAS will perform standard maintenance and CMS will focus on the urgent up-
1618 grade of the pixel detector and on the installation of new muon detectors in order to take profit of LS2
1619 time to mitigate the upgrade of detectors foreseen during LS3. Run-III will start in 2021 with the LHC
1620 at its nominal center-of-mass energy and will bring LHC-Phase-I to an end at the end of 2023. By
1621 then the luminosity will only increase to reach 2.5 times the nominal luminosity but during these 3

1622 years of run, the LHC will deliver as much integrated luminosity as what what brought during the al-
1623 most 7 years of both Run-I and II of data taking. Phase-I will end with an overall 300 fb^{-1} delivered.

1624

1625 3.1 Motivations for HL-LHC and the upgrade of CMS

1626 The first data taking period that took place until the start of LS1 and during which the LHC was
1627 only operated at a center-of-mass energy of 7 TeV was sufficient to claim the discovery of a new
1628 $125 \text{ GeV}/c^2$ particle compatible with the Higgs boson by both CMS and ATLAS in July 2012 and
1629 hence achieve a major milestone in the history of science towards the understanding of the funda-
1630 mental nature of the universe. Nevertheless, the LHC machine holds the potential to go further and
1631 help unravel hte remaining misteries the high energy physics community is facing.

1632 Over its full lifetime, the HL-LHC is expected to deliver an outstanding integrated luminosity
1633 of 3000 fb^{-1} leading, in the case of Higgs studies to measuring the couplings of the boson to a
1634 precision of 2 to 5% thanks to the estimated 15 millions of Higgs created every year providing a
1635 more precise measurement of potential deviations from the theoretical predictions and hence test its
1636 properties with respect to the SM Higgs neutral boson. SUSY and heavy gauge boson studies would
1637 also see their mass range limits pushed away by at least 1 TeV and could lead to a new breakthrough.
1638 SUSY is a particularly important topic as it could give an answer to why the Higgs boson can stay so
1639 light while coupled to heavy particles by introducing the contributions of the super partners on top
1640 of providing dark matter candidates. Finally, the increase of luminosity will give the possibility to
1641 investigate "exotic" mode like for example the models introducing extra dimensions to explain the
1642 hierarchy problem.

1643 Many of these Standard Model extensions yield Heavy Stable Charged Particles (HSCPs), heavy
1644 long-lived particles displaying a high momentum but a velocity significantly lower than the speed of
1645 light [179–182] and/or a charge that differs from the elementary charge $\pm e$ [182–186]. Depending
1646 on the model considered, Heavy Stable Charged Particles could be lepton-like heavy particles or on
1647 the contrary R-hadron, particles composed of a supersymmetric particle and at least one quark. Due
1648 to lifetimes of the order of a few ns HSCPs would travel for long enough distances to cross through
1649 entire typical collider detectors while appearing almost stable but because of their slow velocity,
1650 they can be reconstructed in different bunch crossings it reconstructed at all. Indeed, the trigger
1651 algorithms in use at CMS were not designed for such slow particles and assume most particles of
1652 interest will have a velocity close to the speed of light [182, 187]. As HSCPs are long-lived par-
1653 ticles, their identification will be possible thanks to the muon system. The tracks associated to the
1654 HSCPs would then be requested to be reconstructed in both the silicon detectors, for precise dE/dx
1655 measurement, and the muon system detectors. In this case, the muon system will be used to per-
1656 form Time-of-flight (ToF) measurements to discriminate between near spead-of-light particles and
1657 slower ones. The full reconstruction will then look for useful signatures such as the large transverse
1658 momentum of the candidates, their large ionisation energy loss alongside the low velocity accu-
1659 rately measured thanks to the muon system. The main background will consist of wrongly measured
1660 muons which should have a lower transverse momentum, a near to speed-of-light velocity and a low
1661 ionisation energy loss. An example of passage of HSCPs through a slice of the CMS detector is
1662 showed in Figure 3.1.

1663 The ToF measurement to identify beyond the Standard Model particles will mostly rely on the
1664 time information provided by the Drift Tubes, in the barrel region of the detector, and Cathode Strip

1665 Chambers, in the endcaps. From CMS point of view it will then become necessary to increase the
 1666 acceptance and redundancy of the endcaps toward higher pseudo-rapidity. Moreover, the increased
 1667 background will become problematic in many ways and will force for upgrades or many sub-systems
 1668 of CMS.

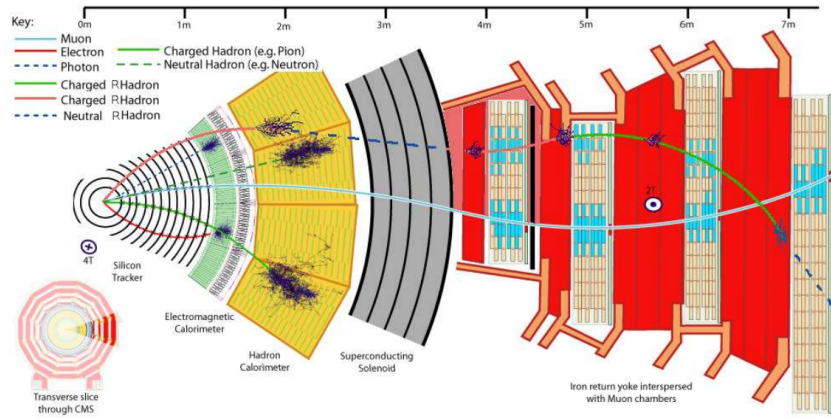


Figure 3.1: Slice of the CMS detector showing example of passage of SM particles and R-hadrons. On the one hand, lepton-like HSCPs will appear to behave like slow and heavy muons. On the other hand, R-hadrons are likely to convert into other kind of charged or neutral R-hadrons due to interactions inside the detector volume.

1669 3.2 Description of the muon system

1670 The barrel region is divided into 5 *wheels* made out of 4 *rings* of detectors with iron return yokes in
 1671 between them whereas the endcaps are made out of 4 disks, each divided into pseudorapidity stations,
 1672 2 for CSCs (except for the first disk where 3 stations are equipped) and 3 for RPCs, although only 2
 1673 RPCs stations are equipped at present. The wheels and disks are shown in Figure 3.2. So far, each
 1674 subsystem was dedicated to a particular task. DTs, in the barrel, and CSCs, in the endcaps, are used
 1675 mainly for their spatial resolution. Indeed, DTs' resolution is of the order of 100 μm along both the
 1676 ($r - \phi$) and ($r - z$) components while the resolution of CSCs is similar but varies in a range from
 1677 50 μm to 140 μm depending on the distance to the beamline. On the other hand, RPCs are used for
 1678 their time resolution as they can deliver an information on the muon tracks within 1.5 ns.

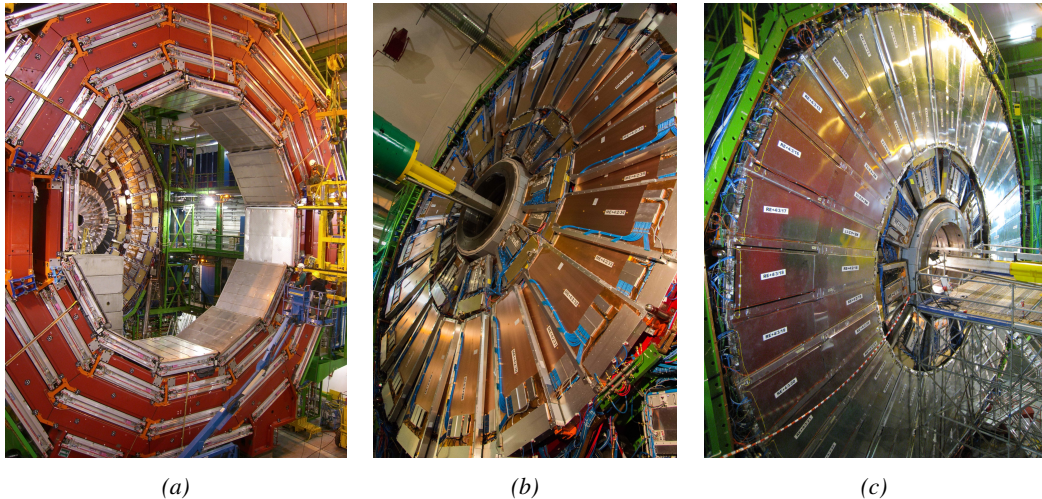


Figure 3.2: Figure 3.2a: Barrel wheel with its detector rings and return yokes. Figure 3.2b: CSC endcap disk with the 2 CSC stations. The outer station is made of 10 deg detectors while the inner station is made of 20 deg detectors. Figure 3.2c: RPC endcap disk. The inner station is not equipped and the inner CSC station can be seen.

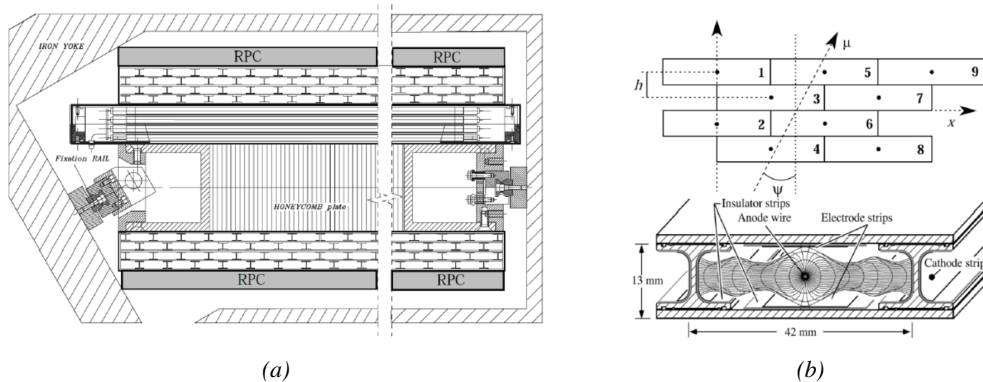


Figure 3.3: Figure 3.3a: Cross section of a DT module showing the two superlayers measuring the ϕ coordinate, perpendicular to the cross section plane, and the superlayer measuring the η coordinate, placed in between the two others with honeycomb and parallel to the cross section plane. The DT detector is sandwiched in between 2 RPCs whose readout strips are perpendicular to the cross section plane, measuring the ϕ coordinate. Figure 3.3b: A DT cell is shown together with its electric field. The path of a muon through a superlayer is shown.

1679 The 250 CMS DTs, found in the barrel covering the pseudorapidity region $0 < |\eta| < 1.2$
 1680 and whose structure is shown in Figure 3.3, are composed of 3 *superlayers* of DT cells. Two of
 1681 these superlayers are dedicated to measuring the ϕ coordinate of the muons and while the last one
 1682 measures the η (or z) coordinate. Each superlayer consists on 4 layers of 60 to 70 DT cells arranged
 1683 in quincunx to allow for a precise reconstruction of the muon path through the DT layers. Each DT
 1684 cell is a rectangular aluminium gas volume with a central anode wire. Cathode strips are placed on
 1685 the narrow surface of the cells and electrode strips are placed on the wide surface to help shaping

1686 the electric field to ensure a consistent drift velocity of electrons in the drift volume. These detectors
 1687 are operated using a 85/15 mixture of Ar and CO_2 .

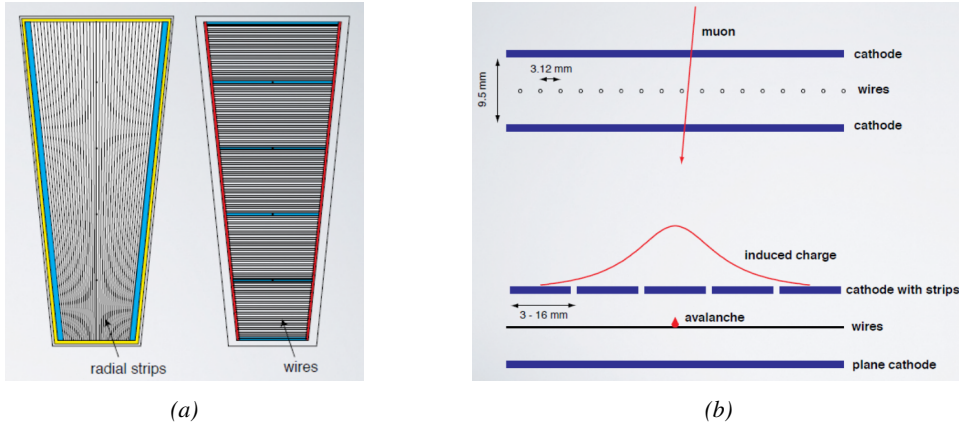


Figure 3.4: Figure 3.4a: cathode strips and anode wire layout of a CSC panel. Figure 3.4b avalanche development and charge collection by anode wires and induction on cathode strips inside of a CSC panel.

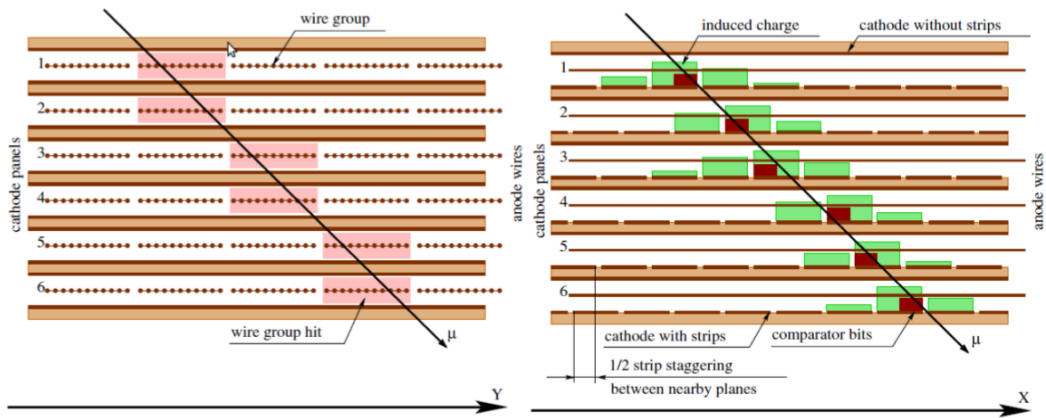


Figure 3.5: Muon track reconstruction through the 6 panels of a CMS CSC using the information of anode wire groups and cathode strip charge distribution combined with comparator bits to decide on which half strip the muon is more likely to have passed.

1688 The 540 CMS CSCs, found in the endcaps covering the pseudorapidity region $0.9 < |\eta| < 2.5$
 1689 and described through Figures 3.4 and 3.5, are composed of 6 panels of CSC, each panel consisting
 1690 in a wide gas volume of 9.5 mm (7 mm in the case of ME1/1 station) containing anode wires and
 1691 whose surfaces are cathodes. The top cathode is a wide copper plane of the size of the gas volume.
 1692 The bottom cathode is divided into thin trapezoidal copper strips radially arranged to measure the
 1693 azimuthal coordinate ϕ with a pitch ranging from 8 to 16 mm. The $0.50 \mu\text{m}$ anode wires are placed
 1694 perpendicularly to the strips to measure radial coordinate r and are grouped by 10 to 15 with a wire
 1695 to wire space of 3.2 mm. In the specific case of ME1/1 placed against the HCAL endcap, the $0.30 \mu\text{m}$
 1696 anode wires have a wire to wire distance of 2.5 mm and are not disposed perpendicularly to the strips
 1697 but slightly tilted by an angle of 29 deg to compensate for the lorentz force due to the very strong

1698 local magnetic field of 4 T. These detectors are operated with a 40/50/10 mixture of Ar, CO₂ and
 1699 CF₄. Combining the information of the multiple CSC panels, the detectors achieve a very precise
 1700 measurement of the muon track.

1701 Despite their excellent spatial resolution, the wire chambers (DTs and CSCs) are limited in terms
 1702 of time resolution by the fact that the charge needs to drift towards the anode wire and be collected
 1703 before having the confirmation that a particle was detected as the drift volume is not used to develop
 1704 avalanches. Indeed, the stronger electric field close to the anode wire triggers the avalanche and the
 1705 gain of the detector. Due to the drift, the time resolution is thus limited at best to approximately 2 to
 1706 3 ns. In addition, even though the intrinsic time resolution of the tracking chambers is rather good
 1707 compared to the 25 ns in between successive collisions, the processing time of the trigger system
 1708 doesn't allow for very fast triggering as it provides a time precision of only 12.5 ns. Thus, detectors
 1709 fully dedicated to timing measurement have been installed as a redundant system. These detectors
 1710 are RPCs, also gaseous detectors but that use current induction instead of charge collection allowing
 1711 for a time resolution of the order of 1.5 ns only. Theoretically, depending on the design used, RPCs
 1712 could reach a time resolution of the order of 10 ps but in the context of LHC where bunch crossing
 1713 happen every 25 ns, a time resolution of 1.5 ns is sufficient to accurately assign the right bunch
 1714 crossing to each detected muon.

1715 The 1056 RPCs equipping the CMS muon system both in the barrel and endcap regions and
 1716 covering the pseudorapidity region $0 < |\eta| < 1.6$ are composed of two layers of RPC *gaps* as
 1717 described in Figure 3.6. Each gap consists in two resistive electrodes made out of 2 mm thick
 1718 Bakelite enclosing a 2 mm thick gas volume containing a 95.2/4.5/0.3 mixture of C₂H₂F₄, i –
 1719 C₄H₁₀ and SF₆. Due to this geometry, the electric field inside of a gap is homogeneous and linear
 1720 at every point in the gas translating into a uniform development of avalanches in the gas volume as
 1721 soon as a passing muon ionises the gas. The two gaps sandwich a readout copper strip plane. A
 1722 negative voltage is applied on the outer electrodes, used as cathodes, and the inner electrodes, the
 1723 anodes, are simply connected to the ground as well as the readout panel that picks up the current
 1724 induced by the accumulated charge of the growing avalanches in one or both of the gas gaps. This
 1725 OR system allows for a lower gain (i.e. a lower electric field) on both gaps to reach the maximal
 1726 efficiency of such a detector.

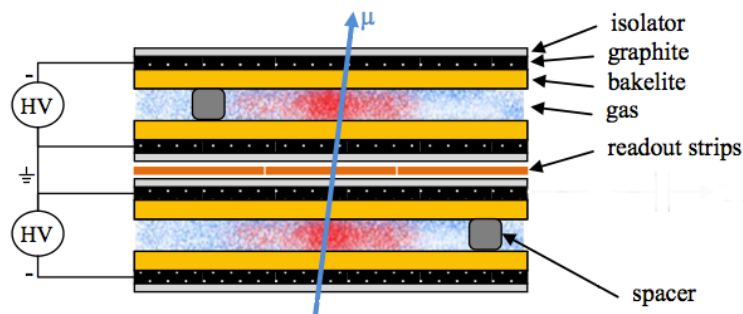


Figure 3.6: Double gap layout of CMS RPCs. Muons passing through the gas volumes will create electron-ions pairs by ionising the gas. this ionisation will immediately translate into a developing avalanche.

1727 3.3 Muon system requirements for HL-LHC

1728 The increase of irradiation close to the beam line will affect the background rate seen by the muon
 1729 detectors in this area and tracking muons will prove to be difficult as this region is not yet equipped
 1730 with all the detectors that were already foreseen for Phase-I. Improving this situation will come with
 1731 the increase of hit numbers recorded along the particle track to reduce the ambiguity on muon versus
 1732 background detection. Moreover, the measurement of small production cross-section and/or decay
 1733 branching ratio processes, such as the Higgs boson coupling to charge leptons, and in particular to
 1734 muons, or the $B_s \rightarrow \mu^+ \mu^-$ decay, is of major interest and specific upgrades in the forward regions
 1735 of the detector will be required to maximize the physics acceptance to the largest possible solid
 1736 angle.

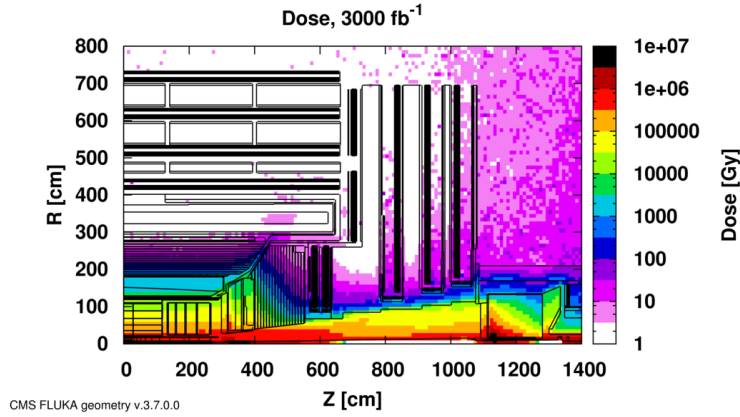


Figure 3.7: Absorbed dose in the CMS cavern after an integrated luminosity of 3000 fb. Using the interaction point as reference, R is the transverse distance from the beamline and Z is the distance along the beamline.

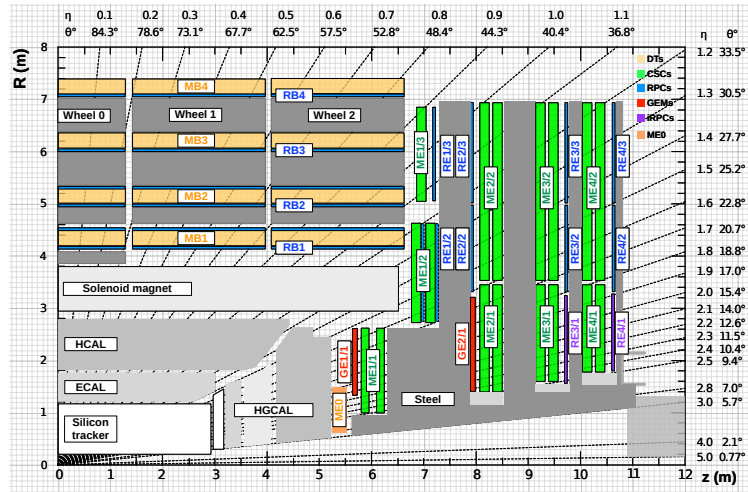


Figure 3.8: A quadrant of the muon system, showing DTs (yellow), RPCs (blue), and CSCs (green). The locations of new forward muon detectors for Phase-II are contained within the dashed box and indicated in red for GEM stations (MEO, GE1/I, and GE2/I) and dark blue for improved RPC (iRPC) stations (RE3/I and RE4/I).

1737 To ensure proper trigger performance within the present coverage, the muon system will be
 1738 completed with new chambers and the electronics of the present system will need to be upgraded to
 1739 ensure an efficient triggering. Figure 3.8 shows the addition of Gas Electron Multiplier (GEM) and
 1740 improved RPC (iRPC) in the pseudo-rapidity region $1.6 < |\eta| < 2.4$ to complete the redundancy of
 1741 the already existing CSCs as originally scheduled in the CMS Technical Proposal [188]. A first step
 1742 into this direction will be taken by installing GEMs on the first endcap disk in position GE1/1 during
 1743 LS2, during which preparations for the future installation of more GEMs and RPCs will take place
 1744 by installing the needed services. During the YETS following LS2, iRPCs will be installed on the
 1745 third and fourth endcap disks in position RE3/1 and RE4/1, and more GEMs will equip the second
 1746 endcap in position GE2/1 and the inner layer, closest to the HCAL endcap called ME0 during LS3,
 1747 finally completing the redundant coverage of the muon system and extending it a little by extending
 1748 the reach to $|\eta| = 2.8$, the redundancy in the region $2.4 < |\eta| < 2.8$ being maintained by the 6
 1749 GEM layers contained in each ME0 detector that provide enough tracking points to efficiently reject
 1750 neutron-induced background.

1751 Nevertheless, the region beyond $|\eta| > 2.8$ and extending to $|\eta| = 5.0$ only is covered by the
 1752 forward HCAL detectors and lack redundant muon detector coverage. Extensions of the tracker in
 1753 the context of HL-LHC will increase its coverage up to $|\eta| = 4.0$ but the identification of muons and
 1754 measurement of their energy with reasonable precision only using the tracker is nearly impossible.
 1755 Thus, this increased tracker coverage range needs to be put in parallel with a matching muon detector
 1756 and will open doors to multi-lepton final states in which leptons are likely to have a low transverse
 1757 momentum and to be found near the beam line.

1758 Finally, as the muon system is composed only of gaseous detectors, strong environmental con-
 1759 cerns have risen over the last years as the European directives will restrict the use of fluorine based
 1760 gas mixtures. Both the CSC and RPC subsystems, using CF_4 , $C_2H_2F_4$, or SF_6 , will need to adapt
 1761 their working gas in order to strongly reduce the greenhouse potential of the mixtures released into
 1762 the atmosphere due to gas leaks.

1763 3.4 Necessity for improved electronics

1764 Drift Tubes and Cathode Strip Chambers are important components used to identify and measure
 1765 muons, especially thanks to their spatial resolution of the order of $100\text{ }\mu\text{m}$. Nevertheless, the lumi-
 1766 nosity and irradiation during HL-LHC will cause serious event loss and ageing on the electronics of
 1767 these subsystems that will comprise the triggering and data transferring needs of CMS. Thus, elec-
 1768 tronics upgrade are foreseen to address these expected problems. While only the RPCs' electronic
 1769 system is able to operate under Phase-II requirements, DTs and CSCs will need to improve their
 1770 trigger accept rate and latency to ensure that Level-1 trigger threshold stays at the same level [189],
 1771 and DAQ data transfer rate, that respectively need to achieve a minimum of 500 kHz , get down to
 1772 $12.5\text{ }\mu\text{s}$ [190], and increase to 1082 Gbit/s DTs and to 1026 Gbit/s for CSCs. As of today, the
 1773 Level-1 trigger accept rate of DTs doesn't reach 300 kHz while this of CSCs is below 250 kHz but
 1774 the foreseen upgrades are expected to increase the rate way beyond the requirement in the of DTs
 1775 and up to 4 MHz for CSCs [177].

1776 The first version of Minicrate electronics (MiC1) used by DTs don't allow for high enough
 1777 trigger rate. In addition to this problem, it was showed that these electronics contain components
 1778 that are not radiation hard enough to sustain HL-LHC conditions and thus, a too large number of
 1779 channels may fail due to radiations. The MiC1 will be replaced on each detector by an improved

version referred to as MiC2 while front-end electronics and high-voltage modules will not need any replacement. On the other hand, CSCs showed that there electronics would be able to live through the 10 years of Phase-II but the limited buffer depth might cause memory overflows and readout inefficiencies with a fraction of event loss ranging from 5 to more than 10% at an instantaneous luminosity similar to which of HL-LHC depending on the expected background. Thus the replacement of CSCs' cathode front-end boards (CFEBs) by digital ones, DCFEBs, with deeper buffer would permit to make event loss negligible and satisfy HL-LHC requirements [177]. All these new DT and CSC electronics will be connected to the trigger electronics via optical links to ensure a faster communication.

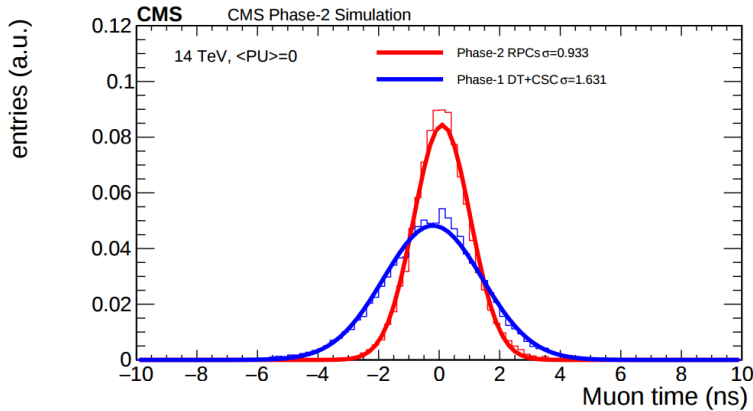


Figure 3.9: Comparison of the simulated time residuals in between reconstructed and true muon times without (blue) and with (red) the upgraded RPC link system.

The upgrade on the side of Resistive Plate Chambers will then not come from their on-board electronics but from the Link System located in the service cavern of CMS and that connects the front-end electronics data of RPCs into CMS trigger processors. The main motivation for such an upgrade is that the electronic board composing the link system are built using obsolete components and weak components that can easily suffer from the electromagnetic noise. These components may be the source of failing channels throughout Phase-II. Moreover, these link boards were originally designed only to match RPC digitized signals with the corresponding bunch crossing. Due to this feature, the time resolution of the full RPC chain is thus limited to 25 ns and does not exploit the full time resolution of the detectors. This would make the synchronization of the RPC system easier and allow to have a finer offline background removal within the 25 ns in between bunch crossings thanks to the order of magnitude gained in terms of time resolution.

Upgrading RPC link system will require the installation of 1376 new link boards and 216 control boards. The new boards will make use of the recent progress made with fast FPGAs and will be a great improvement to the ASICs formerly used as they will be able to process signals from several detectors in parallel. The benefit from using the full RPC time resolution thanks to the upgraded link system can be seen through Figure 3.9 where the resolution of the RPC system itself is better than which of DTs and CSCs that was used until now.

1806 3.5 New detectors and increased acceptance

1807 In the present muon system, the redundancy of was assured by RPCs used for their good timing per-
 1808 formances. The extension of the muon system towards higher pseudo-rapidity in order to complete
 1809 the redundancy in this very region and to contribute to the precision of muon momentum measure-
 1810 ments will require muon chambers with a spatial resolution less or comparable to the contribution
 1811 muon of multiple scattering through the detector volume [178]. Most of the plausible physics is
 1812 covered only considering muons with $p_T < 100$ GeV hence, in order to match CMS requirements,
 1813 a spatial resolution of $\mathcal{O}(\text{few mm})$ will be necessary for the proposed new RPC stations while the
 1814 GEMs will need a resolution better than 1 mm, as showed by the simulation in Figure 3.10.

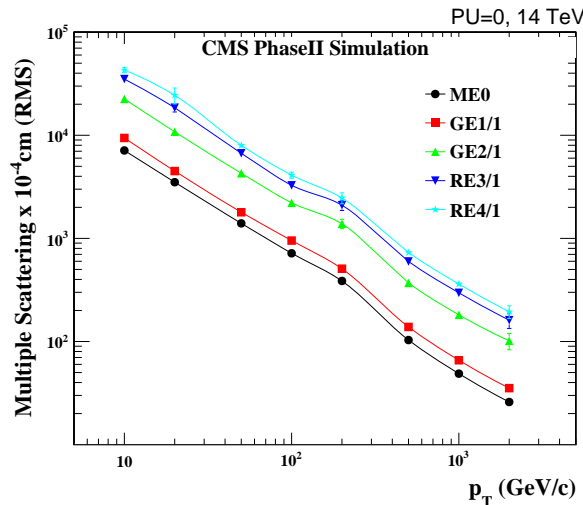


Figure 3.10: RMS of the multiple scattering displacement as a function of muon p_T for the proposed forward muon stations. All of the electromagnetic processes such as bremsstrahlung and magnetic field effect are included in the simulation.

1815 3.5.1 Gas electron multipliers

1816 In the region closer to the interaction point where the spatial resolution is requested to be better
 1817 than 1 mm for the new detectors (at least for GE1/1 and ME0, GE2/1 being in the same order of
 1818 requested spatial resolution than the new iRPCs that will equip the third and fourth endcaps), the
 1819 choice has been made to use triple GEMs, micro pattern gaseous detectors, in the place of RPCs.
 1820 The GE1/1 project had been the first to be approved and demonstrators had been installed in CMS
 1821 already during LS1. The rest of the detectors will be installed during LS2 while the GE2/1 and ME0
 1822 projects are still under development. ME0, GE1/1 and GE2/1 will be installed respectively next to
 1823 the HCAL endcap, on the first and on the second muon endcap disks as can be seen from Figure 3.8.

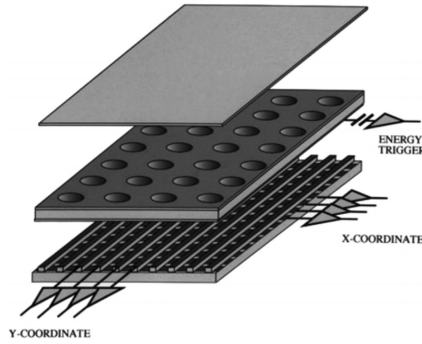


Figure 3.11: Schematics of a GEM showing the cathode on top, the GEM foil separating the gas volume into the drift region, in between the cathode and foil, and the induction region, in between the GEM foil and the anode, and the anode on which a 2D read-out is installed. A negative voltage is applied on the cathode while the anode is connected to the ground.

1824 Gas Electron multipliers are gaseous detectors [191] which gas volume is confined in between
 1825 2 planar electrodes, the anode serving as read-out panel. The gas volume is divided in 2 or more
 1826 regions by a single or multiple *GEM foils* as showed in Figure 3.11. These foils are very thin, of
 1827 the order of a few tens of μm , and are pierced with holes as can be seen in Figure 3.12. Both
 1828 surfaces of the GEM foils are clad with copper in order to apply a strong electric field in between
 1829 each side that will generate very strong potentials in the holes. The gas region contained in between
 1830 the cathode and the GEM foil is called the drift region as the electric field is not strong enough to
 1831 cause avalanches and thus start an amplification. The primary electrons drift toward the foil and are
 1832 accelerated and amplify by the very high potential within the holes, as showed in Figure 3.12. Then
 1833 the electrons reach the second drift region in which they will induce signal on the read-out located
 1834 on the anode. By restraining the amplification process at the level of the holes, the electrons can stay
 1835 in a very confined space and thus induce a very localized current, providing the GEMs with a very
 1836 good spatial resolution.

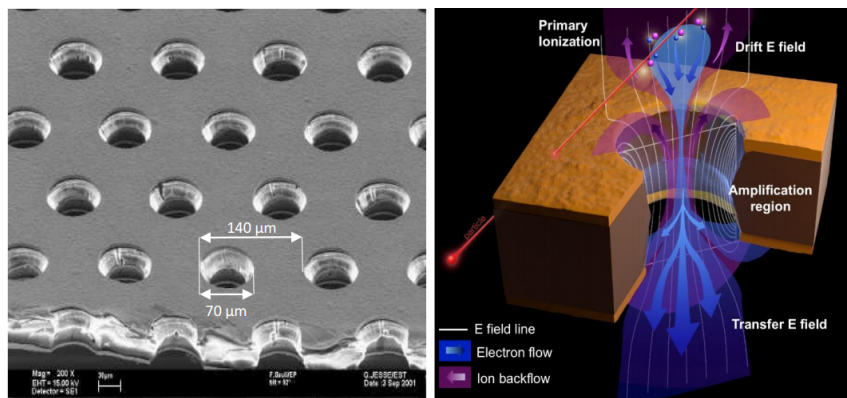


Figure 3.12: Left: Picture of a CMS GEM foil provided by a scanning electron microscope. Right: Representation of the electric field lines in a GEM hole and of the amplification that electrons and ions undergo in the hole's volume due to the very intense electric field.

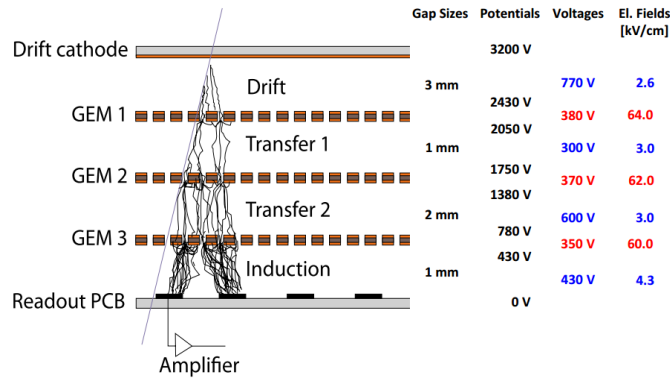


Figure 3.13: Schematic representation of CMS triple GEMs. The gas volume is divided into 4 areas. The drift area is the region where the primary electrons are created before being amplified a first time while passing through the first GEM foil. Then the process of drift and amplification is repeated twice in following two transfer areas and GEM foils. Finally, the charges have been amplified enough to induce current in the read-out strips while in the last drift area. The dimensions, potentials and electric fields are provided.

1837 In order to achieve a stronger amplification, the amplification process can be repeated several
 1838 times in a row. The GEMs that will be used in CMS are triple GEM detectors operated with a 70/30
 1839 gas mixture of Ar/CO_2 . They contain 3 GEM foils and thus 3 electron amplifications, as can be
 1840 seen in Figure 3.13. The GEM foils used in CMS are 50 μm foils clad with 5 μm of copper on
 1841 each side. The foils are pierced with double-canonical holes which inner and outer diameters are
 1842 respectively 50 and 70 μm which are placed 140 μm from each other in an hexagonal pattern, as
 1843 showed in Figure 3.12. These detectors have a time resolution better than 10 ns and reach very good
 1844 spatial resolutions of less than 200 μrad as indeed the position of the hits is not measured along the
 1845 strips but following the azimuthal angle granularity of the radially organized trapezoidal strips.

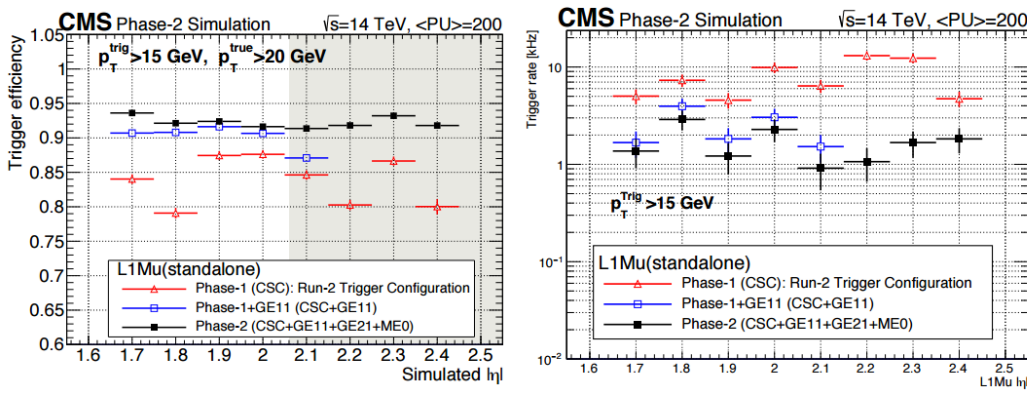


Figure 3.14: Simulated efficiency and rate of the standalone Level-1 muon trigger using tracks reconstructed in CSCs and all GEM stations compared with Phase-I values in the case where only CSCs are used or CSCs+GE1/I. The zones of inefficiency of the CSC subsystem are compensated by the addition of GEMs during Phase-II and the trigger rates is kept from increasing due to the high luminosity.

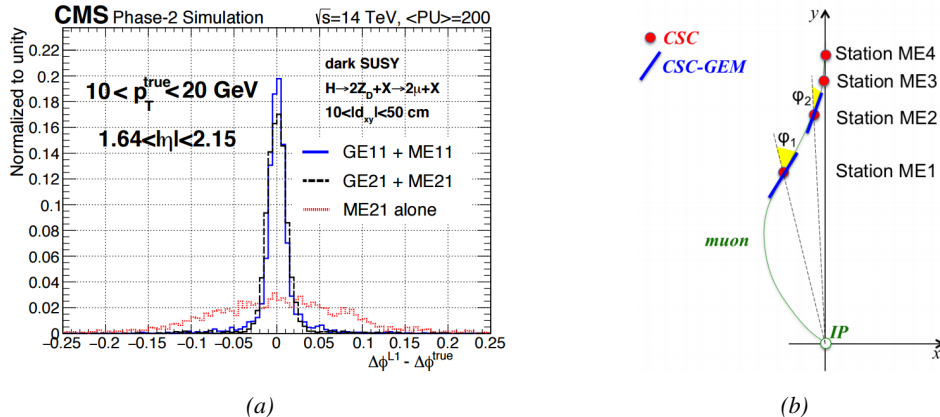


Figure 3.15: Figure 3.15a: Simulated resolution of the muon direction measurement $\Delta\phi$ with Phase-II conditions. In the second endcap station, the resolution is compared in the case of CSCs (ME2/1) alone and CSCs+GEMs (GE2/1+ME2/1) while a similar resolution measurement is given in the case of the first station (GE1/1+ME1/1). Figure 3.15b: The addition of GEM detectors on stations 1 and 2 (ME0 is considered to contribute to station station 1) as redundant system to CSCs allows to improve the muon momentum improvement through a more accurate measurement of the local bending angles ϕ_1 and ϕ_2 .

The GEM Upgrade is divided into 3 subsystems as GE1/1 was the first approved project [192] and that the detectors will already be installed during LS2. GE2/1 and ME0, on the other hand, will profit of the R&D knowledge and skills developed for GE1/1 while the requirements for each subsystem are different as they are not placed at the same distance from the interaction point. In this very forward region, a different position with respect to the center of the detector can change dramatically the conditions in which the detectors will have to be operated. In terms of rate capability, GE2/1, which is the furthest, is required to withstand 2.1 kHz/cm^2 while GE1/1 needs to be better than 10 kHz/cm^2 and ME0, better than 150 kHz/cm^2 . In terms of ageing with respect to charge deposition, ME0 needs to be certified to 840 mC/cm^2 , GE1/1 to 200 mC/cm^2 and GE2/1 only to 9 mC/cm^2 . All 3 detectors need to have a time resolution better than 10 ns and an angular resolution better than $500 \mu\text{rad}$.

On each GE1/1 ring, 36 super chambers, consisting of 2 single GEM layers and spanning 10° , will be installed covering the pseudo-rapidity region $1.6 < |\eta| < 2.2$ together with ME1/1 CSCs and the reach of the muon system will be improved thanks to the GE2/1 that will overlap with the GE1/1 and cover a region from $|\eta| > 1.6$ to $|\eta| < 2.4$ and complete the redundancy of ME2/1. The super chambers, built with 2 triple GEM layers each consisting of 4 single GEM modules due to the rather large surface of the GE2/1 chambers, that will be installed on the first ring of the second endcap will span 20° each, hence, a total of 72 chambers will be assembled to equip the muon system. Finally, the ME0 installed near the HCAL endcap will cover the region $2.0 < |\eta| < 2.8$ and this subsystem will consist in super modules of 6 layers of triple GEM detectors covering an azimuthal angle of 20° leading to the construction of 216 single detectors.

Adding the GEMs into the forward region of the muon system will allow to strongly enhance the Level-1 Trigger performance by reducing the inefficiency regions and the trigger rate as showed in Figure 3.14. Moreover, benefiting from the good spatial and angular resolution of the GEMs, the precision into the muon measurement will also be greatly improved by the addition of GEMs as can be seen from the simulation presented in Figure 3.15.

3.5.2 Improved forward resistive plate chambers

Figure 3.8 shows that the iRPCs that will equip the third and fourth endcap disks in position RE3/1 and RE4/1 will finally be the partners of the CSCs in position ME3/1 and ME4/1 and complete Phase-I plans but bringing the needed upgrades in the scope of Phase-II as the older chambers are not suitable to equip the forward region of CMS due to HL-LHC rates and charge deposition. By completing the redundancy, more track along the muon trajectory will be available and the lever arm will be improved. The benefits from extending the redundancy of the muon system with iRPCs to the forward most region is showed in Figure 3.16 in which the trigger efficiency is showed with and without RPCs in which it is possible to see that the efficiency of CMS trigger with the complete redundancy is improved is above 95% in the region $|\eta| > 1.8$ as the iRPCs help filling the holes in the CSC system.

The detectors that will be installed in the coming years will be similar to the already existing RPC system. 18 of the new chambers, each spanning 20° in φ around the beam axis with 96 radially oriented trapezoidal read-out strips, will cover each muon endcap disk leading to the production of 72 iRPCs. The main difference with the old RPC chambers is that these detectors will not have readout strips segmented in η as by using fast front-end electronics the strips will be read-out on both sides allowing for a radial spatial resolution of the order of 2 cm in order to contribute to the better reconstruction of muon in the forward region where the bending of muons by the magnetic field is low. This is motivated by the fact that, in the case a η segmentation was used, at least 5 pseudorapidity partitions would have been necessary to reach the minimal radial spatial resolution (≈ 20 cm). Having only one strip read-out from both along the chamber reduces by 60% the total number of channels and the necessary cabling and allows for a better spatial resolution. The strip pitch will range from 6.0 mm (5.9 mm) on the high pseudo-rapidity end to 12.3 mm (10.9 mm) on the low one on position RE3/1 (RE4/1). The spatial resolution in the direction perpendicular to the strips should reach approximately 3 mm, better than the minimal needed resolution (Figure 3.10), and the overall time resolution of the new installation will be equally 1.5 ns, as for the present due to the same link system being used.

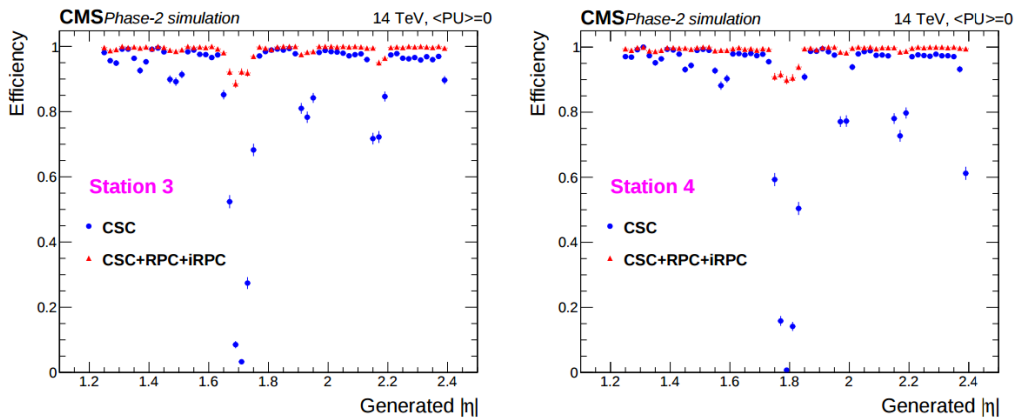


Figure 3.16: Simulation of the impact of RPC hit inclusion onto the local trigger primitive efficiency in station 3 (left) and station 4 (right). The contribution of iRPC starts above $|\eta| = 1.8$.

Nevertheless, having only a single strip instead of pseudo-rapidity segmentation will increase

the probability of double hits in the same channel. This probability was estimated to be low enough as it shouldn't exceed 0.7%. This estimation was made assuming an average hit rate per unit area of 600 Hz/cm^2 in the iRPCs (see Figure 3.17), a cluster size (average number of strips fired per muon) of 2, a strip active area of $158.4 \times 0.87 \text{ cm}^2$ and a safety factor 3 leading to an estimated rate per strip of 380 kHz corresponding to an average time interval of 2600 ns in between 2 consecutive hits. The time for a signal to go through the full strip length is about 10 ns to which can be added 1 ns of dead time and 2 TDC clock cycles of 2.5 ns for a minimal time interval of 16 ns necessary to avoid ambiguities. The probability of having ambiguous double hits in a strip in then the ratio in between this minimal time interval in between 2 consecutive hits and the average time interval estimated from the rate the detectors are subjected to.

The instantaneous luminosity at HL-LHC being very high, the rates at the level of the new chambers needed to be simulated in order to understand the necessary requirements for these detectors. The simulated results for different background components (neutrons, photons, electrons and positrons) are showed in Figure 3.17 assuming known sensitivities to these particles. It is showed that on average over the iRPC areas the rates would be of the order of 600 Hz/cm^2 (600 Hz/cm^2 seen in RE3/1 and 480 Hz/cm^2 in RE4/1) [193]. Thus, taking into account a safety factor of about 3, it was decided that improved RPCs should at least be certified for rates reaching 2 kHz/cm^2 which would be achieved thanks to several improvements on the design and on the electronics. The detectors design will be based on the existing RPC design as they will be double gaps. Similarly to the existing RPC system, the electrode material will be HPL although the thickness of the electrodes and of the gas gap will be reduced to 1.4 mm as a thinner gas gap leads to a decrease of deposited charge per avalanche as showed in Figure 3.18. The smaller the gas gap, the more the detector becomes sensitive to gap non-uniformities across the electrode planes making a gap of 1.4 mm a good compromise in between these two competing factors.

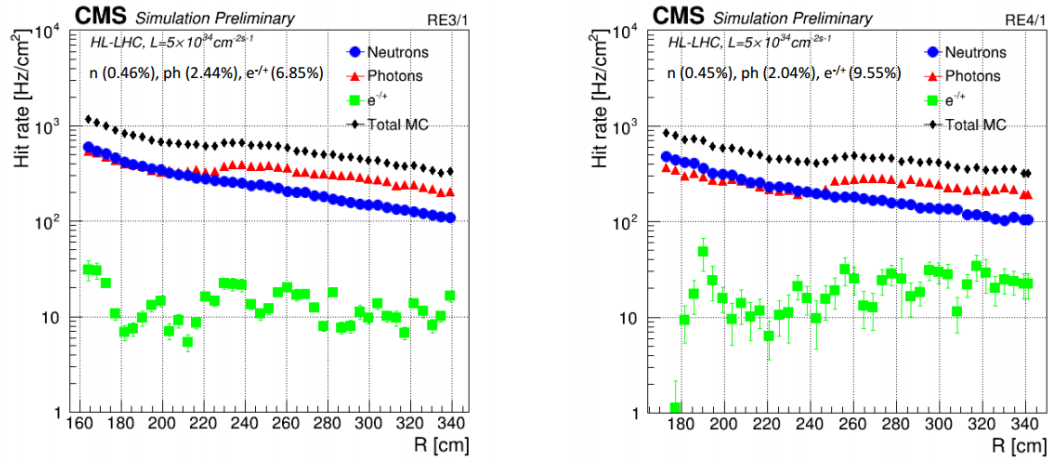


Figure 3.17: Expected hit rate due to neutrons, photons, electrons and positrons at HL-HLC instantaneou...
luminosity of $5 \times 10^{34} \text{ cm}^{-2}\text{s}^{-1}$ in RE3/1 and RE4/1 chambers. The sensitivities of iRPCs used in the simulation for each particle are reported and differ from one endcap disk to another as the energies of the considered particles varies with the increasing distance from the interaction point.

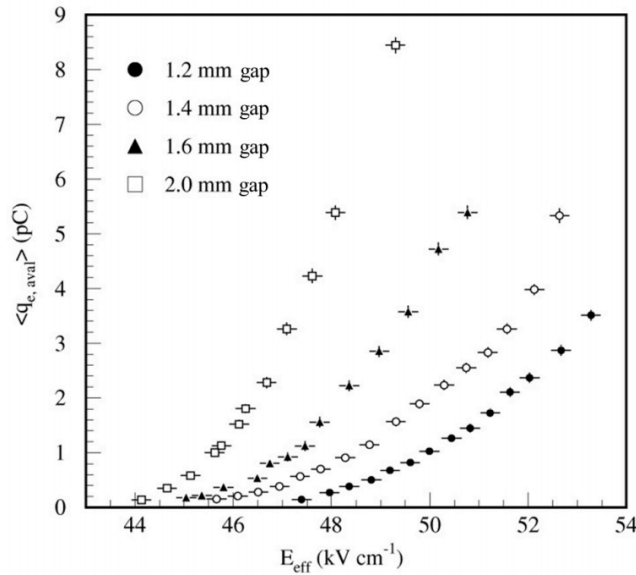


Figure 3.18: Measured average charge per avalanche as a function of the effective electric field for different gas gap thickness in double gap RPCs using HPL electrodes.

1924 A lower charge deposition inside of the detector volume means a slower ageing and a longer
 1925 lifetime for detectors subjected to high irradiation. But, in order to take advantage of the lower
 1926 detector gain, more sensitive electronics are required so that the part of gain that was formerly done
 1927 in the gas volume can be moved to the electronics. Achieving this with the technology developed
 1928 more than 10 years ago for the present system is not possible as the signal over noise ratio of such
 1929 electronics doesn't allow to detect charges as low as 10 fC. Moreover, the new front-end electronics
 1930 will need to be radiation hard to survive to more than 10 years of HL-LHC conditions. The new
 1931 technology that has been chosen is based on the PETIROC ASIC manufactured by OMEGA and is
 1932 a 64-channel ASIC called CMS RPCROC. The properties of these electronics will be discussed in
 1933 Chapter 6.

1934 3.5.3 Installation schedule

1935 The previous discussion on the different upgrade projects makes it clear that a lot of work is scheduled
 1936 for CMS to be ready at the end of LS3 for HL-LHC. Conducting all the upgrades of the muon system
 1937 together with upgrades of the other subsystems like the replacement of the Tracker and of part of the
 1938 ECAL, will prove to be very difficult as the opening of CMS to access the Barrel will be done by
 1939 fully opening the endcaps leaving only the first disk to be accessible. Thus, most subsystems have
 1940 planned early installation over LS2, and the following YETS until LS3 in order to give more space to
 1941 LS3 schedule.

1942 First of all, LS2 will see the installation of GE1/1 detectors, all the on-detector schedule of CSCs
 1943 and the installation of the necessary services for the improved RPCs to be installed later, such as
 1944 the HV and LV power supply lines, the gas and cooling lines or signal cables. CSCs will have a
 1945 huge work to do during LS2 as they will need to extract all of their detectors to refurbish them with
 1946 upgraded DCFEB and ALCT mezzanine boards. The GE1/1 services were installed during LS1

1947 together with a few demonstrator and only the detectors needs to be integrated into the first endcap
 1948 disk. The detectors are presently being built and tested at the different assembly site to prepare for a
 1949 smooth LS2 work.

1950 The work of GEMs will be continued during the following YETS during which is planned the
 1951 installation of the GE2/1 stations to only leave the ME0 to be installed during LS3. The iRPC
 1952 program will follow a similar path as the new detectors will be installed during the YETS preceding
 1953 LS3 in prevision of the fact that the endcap disks will not be accessible during LS3. This way, all the
 1954 subsystems, but DTs, made great effort on planing their installation and integration within CMS only
 1955 to have to deal with off-detector issues during the LS3 period, such as the replacement of ODMBs
 1956 and HV system in the case of CSCs or the upgrade of the RPC Link System. Finally, during LS3
 1957 are schedules the replacement of DT minicrates electronics and the installation and integration of
 1958 ME0 GEMs together with the HGCAL.

1959 3.6 Implications of the different upgrades on the Level-1 Trigger. 1960 Improvement of physics performance.

1961 The upgrades of the different subsystems will have a subsequent impact on the Level-1 Trigger.
 1962 Indeed, although its main scheme will not be affected, the efficiency of the trigger in efficiency
 1963 identifying muons and provide the DAQ with good and fast trigger that can cope with HL-LHC
 1964 instantaneous luminosity is a major improvement. In addition to the upgrade of the muon system in
 1965 terms of trigger accept rate and latency, the Level-1 Trigger will get extra information in including
 1966 the Tracker Trigger into its Muon Track Finder logic and combine the L1 Muon Trigger with Tracker
 1967 and Calorimeter Triggers to generate a Global L1 Trigger with a much better momentum resolution,
 1968 as showed in Figure 3.19.

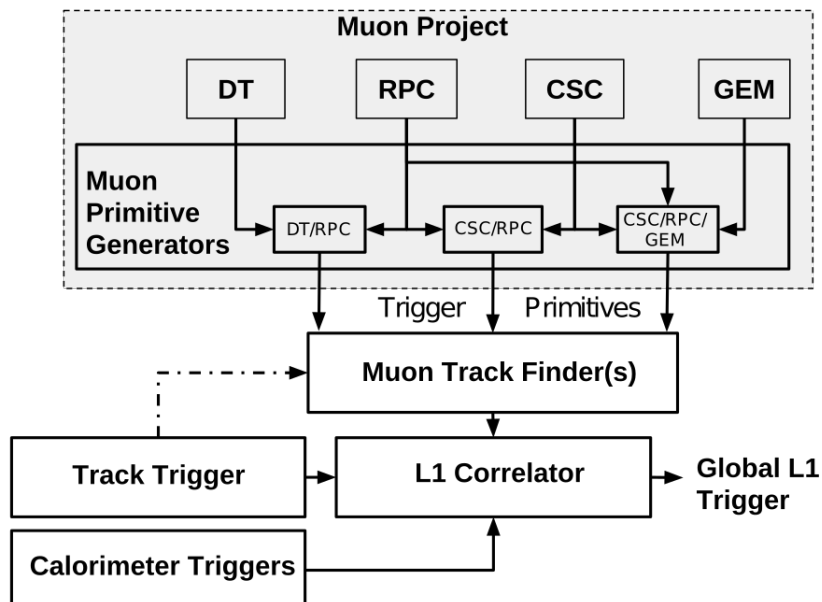


Figure 3.19: Data flow of the Level-1 Trigger during Phase-II operations.

In terms of muon trigger, 3 regions are considered due to their different track finding logic: the Barrel Muon Track Finder (BMTF), the Endcap Muon Track Finder (EMTF) for both the barrel and endcap regions, and finally the Overlap Muon Track Finder (OMTF) which concerns the pseudo-rapidity region in which there is a common coverage by both the barrel and endcap muon systems. This region can be seen in Figure 3.8 for $0.9 < |\eta| < 1.2$ and requires a specific more complex logic to provide with an efficient reconstruction of the muons due to the different orientation of the detectors and of the more complex magnetic field of this region that needs to be taken into account. The benefits of the upgrade for each of these track finders will be coming from different improvements and will be detailed sector by sector.

The main contribution to the improvement of the BMTF is the time resolution improvement of RPC link systems that will allow to take profit of the full 1.5 ns resolution of the detectors. From the perspective of RPCs only, this improvement will help reducing the neutron induced background and slightly improve the bunch crossing assignment. The upgrade of DT electronics is also to take into account as the trigger primitive generator will be renewed through the use of TDCs that will send the digitized signals directly to the back-end electronics instead of having an on-detector trigger logic as it will be the case until the end of Phase-I. The front data of both DTs and RPCs will be sent to the same back-end electronics. These upgrades were detailed in section 3.4 and will lead to a more robust operation of the trigger in the barrel region. Indeed, the combination of RPC hits together with DT primitives will bring improvement in the bunch crossing assignment and improve the efficiency of the trigger in between the wheels were the quality of DT primitives is the poorest. Moreover, having a redundant information is important in the case of failure and loss of efficiency of one of either subsystems.

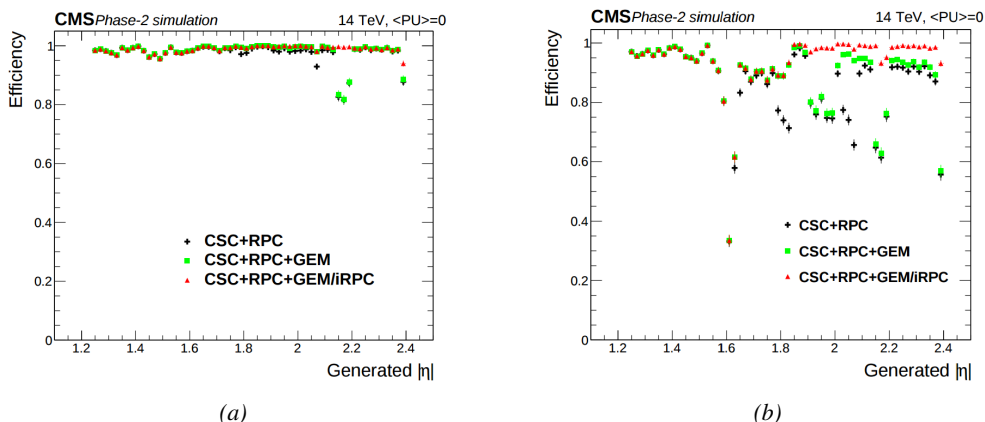


Figure 3.20: Efficiency of the L1 trigger in the endcap region after Phase-II upgrade in the case CSC/GEM/RPC hits are requested in at least 2 stations out of four (3.20a) and in all four stations (3.20b).

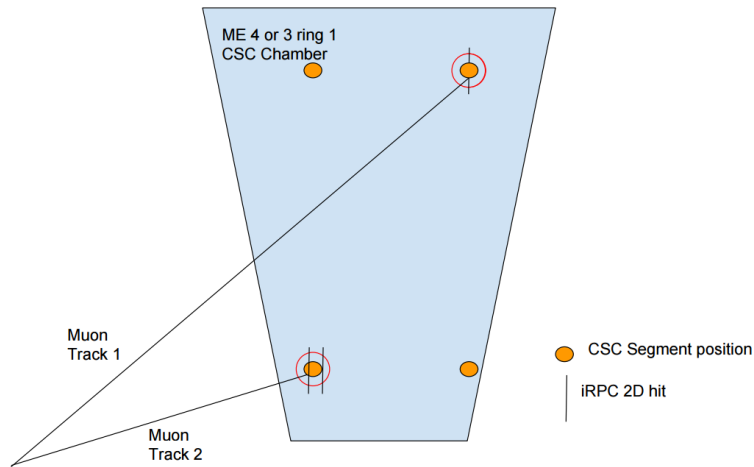


Figure 3.21: Resolution of the LCT ambiguous events thanks to the combination of CSC and iRPC readout data. Using CSCs only, 2 pairs of hits are possible.

With new detectors to cover the very forward region and the upgrade of RPC Link System, the EMTF will be greatly improved. The current EMTF already use more sophisticated algorithms by combining together RPC hits and CSC primitives and will also benefit from the improved time resolution of the RPC system. The GEMs, in stations 1 and 2, and the iRPCs, in stations 3 and 4, will be added into the EMTF algorithm. Both these contributions will help increasing the efficiency of the L1 trigger in the endcap region in one hand, as showed by Figure 3.20, and help lowering the L1 trigger rate in the other hand, especially in the most forward region. The improvement of the efficiency will come both from the better time resolution of RPC link boards and from the addition of more hits along the muon tracks and also a contribution from the GEMs to the lever arm of each track thanks to there high angular resolution.

The rate will be partly reduced in the forward region thanks to the better spatial resolution of iRPCs, with respect to the current RPC system, that will reduce the ambiguity brought by multiple local charged tracks in CSCs, as explained through Figure 3.21. Indeed, as the rates will increase, the probability to record more than a single local charged track will greatly increase. This is due to the fact that the trigger algorithm uses information from 3 consecutive bunch crossings to find muon tracks. It is estimated that with iRPCs operated at 95% efficiency the resolution of ambiguous events would be of the order of 99.7%.

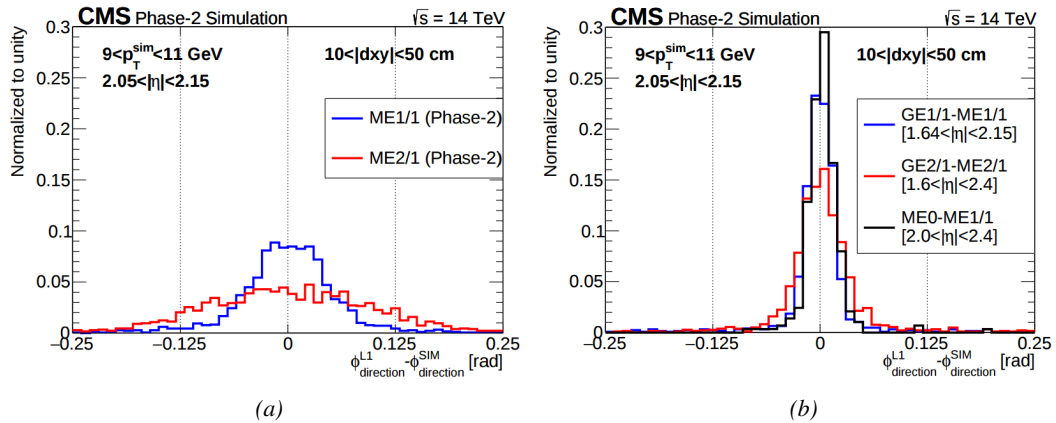


Figure 3.22: The angular resolution on reconstructed muon tracks in the GEM overlap region $2.0 < |\eta| < 2.15$ is compared for Phase-II conditions in the case CSC are alone (Figure 3.22a) and in the case the GEMs' data, including MEO, is combined to which of CSCs (Figure 3.22b).

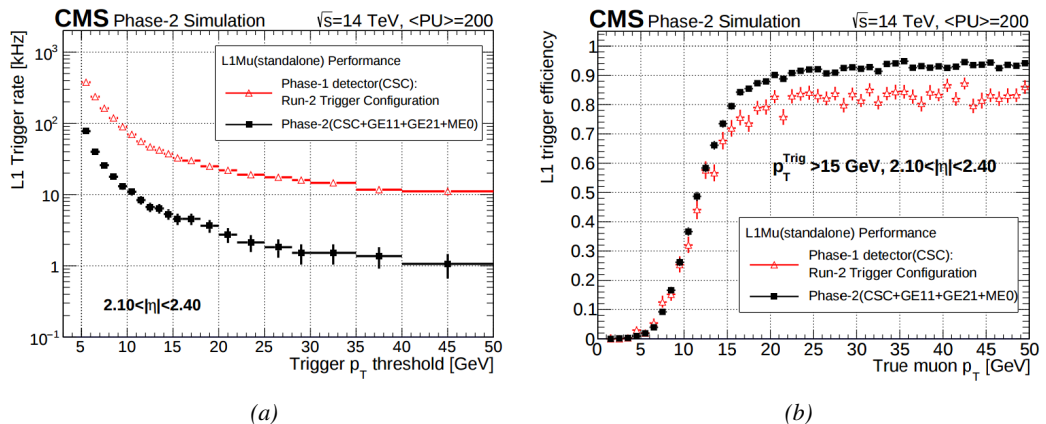


Figure 3.23: Comparison of L1 trigger performances for prompt muons with and without the addition of GEMs in the region $2.1 < |\eta| < 2.4$ at Phase-II conditions. GEMs would allow a reduction of the trigger accept rate by an order of magnitude (Figure 3.23a) while increasing the trigger efficiency (Figure 3.23b).

The addition of GEMs will improve greatly the measured muon momentum resolution by improving the global resolution of the direction of muon tracks, as can be seen in Figure 3.22, which will contribute to lowering the trigger rate and increase the efficiency, as can be seen from Figure 3.23 that focuses especially in the most challenging pseudo-rapidity region. Data from both CSCs and GEMs are combined into the OTMB to build on each station, GEM/CSC primitives matching space and time information from both subsystems.

Finally, the development of a track finder specific to the overlap region was already achieved during the Phase-I upgrade of the L1-Trigger [194]. Nevertheless, the improvements of DT spatial resolution and RPC timing will be carried and implemented into the OMTF.

2017 3.7 Ecofriendly gas studies

2018 Future strict restrictions in the use of certain gases will affect the gaseous detectors of several experiment,
 2019 including CMS. The European Commission adopted a new "F-gas regulation" in 2014 [195]
 2020 with the goal to strongly control and reduce the use of fluorinated gases with high Global Warming
 2021 Potential (GWP). Using CF_4 , $C_2H_2F_4$ and SF_6 , both CSC and RPC subsystems will need to
 2022 address this problem by finding new gas mixture for the operation of their detectors. Finding a re-
 2023 placement for these gas component that were used for very specific reasons will be a great challenge.
 2024 Indeed, CSCs use CF_4 in order to enhance the longevity of the detectors, increase the drift velocity
 2025 of electrons and quench photons with a non-flammable gas mixture. RPCs use a mixture mainly
 2026 composed of $C_2H_2F_4$, or $R134a$, that features a high effective Townsend coefficient and the great
 2027 average fast charge allowing for operations with a high threshold, and contains a small fraction of
 2028 SF_6 that is used for its electronegative properties that prevents the development of delta-rays in the
 2029 gas volume that might trigger multiple ionization and avalanches.

	CSC	RPC
Greenhouse gases used	CF_4	$C_2H_2F_4$ and SF_6
Greenhouse gases fraction in the gas mixture	10%	95.2% and 0.3%
Global Warming Potential (relative to CO_2)	6500	1300 and 23900
Gas mixture re-circulation	Yes, 90%	Yes, 85%
Gas mixture replenishing rate (l/hr)	700	1100
F-gas recuperation	Yes, $\approx 40\%$	No
F-gas venting rate (l/hr)	42	1047 and 3.3
CO_2 -equivalent rate (m^3/h)	273	1440
Relative impact (entire muon system = 100%)	16%	84%

Table 3.1: Details of the greenhouse fluorinated gases used in CMS and of their GWP [177].

2030 Nevertheless, all these gases have a very high GWP, as reported in Table 3.1, and only few options
 2031 are left. The subsystems need to work on strongly decrease the loss of these gases due to leaks in the
 2032 gas system or completely change their gas mixture for more ecofriendly ones. Reducing the amount
 2033 of F-gas released in the atmosphere due to leaks on the current gas system will require installation
 2034 of a F-gas recuperation system on RPCs side and an upgrade of CSCs existing one in addition to
 2035 the repair of existing leaks. With such measures, it is expected that the total rate of greenhouses
 2036 gas vented in the atmosphere would represent only 1.6% of the current levels [177]. In the most
 2037 critical case the F-gas were to be banned, it would be necessary to have replacement mixtures to
 2038 operate CMS. CSC is presently investigating replacement for CF_4 such as CF_3I , C_4F_6 , IC_3F_6 ,
 2039 C_3F_8 or CHF_3 while RPCs, in collaboration with the ATLAS RPC group which uses the same gas
 2040 mixture and, hence, faces similar restrictions, have identified CF_3I ($GWP \leq 1$) and $C_3H_2F_4$ (GWP
 2041 ≤ 1), referred to as HFO-1234ze, as potential candidates with mixtures containing CO_2 but more
 2042 R&D needs to be conducted for both subsystems before concluding on the best alternative. No good
 2043 alternative to the present mixtures will require very efficient abatement system in CMS to burn and
 2044 convert the greenhouse gases into less harmful ones. This way, the air pollution would be strongly
 2045 reduced.

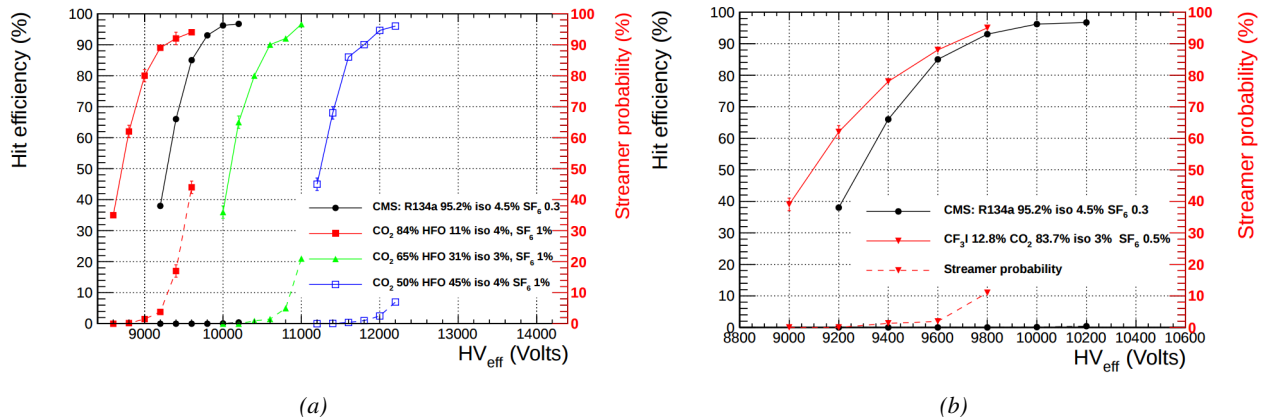


Figure 3.24: The efficiency (solid lines) and streamer probability (dashed lines) of HFO/CO₂ (Figure 3.24a) and CF₃I/CO₂ (Figure 3.24b) based gas mixtures as a function of the effective high-voltage are compared with the present CMS RPC gas mixture represented in black. The detector used for the study is a single gap RPC with similar properties than CMS RPCs. The streamer probability is defined as the proportion of events with a deposited charge greater than 20 pC.

2046 The status of RPC studies are presented in Figure 3.24 in which the performance (efficiency
 2047 and streamer probability) of an RPC operated with alternative gas mixtures is compared to the
 2048 present CMS RPC mixture. Although the efficiency of detectors operated with mixtures containing
 2049 CO₂/CF₃I or CO₂/HFO as a replacement for C₂H₂F₄ seem to reach similar levels than which of
 2050 the detectors operated with the present mixture, the new gas mixtures feature a streamer probability
 2051 (probability to have very large avalanches whose induced charge is greater than 20 pC) that far ex-
 2052 ceeds which of the present fluorinated mixture. The SF₆, being a component of the mixture added
 2053 in order to reduce the probability of large avalanches thanks to its electronegativity, doesn't seem
 2054 to prevent streamers as efficiently even when used at levels more than 3 times higher than with the
 2055 standard CMS RPC mixture. Nevertheless, it is important to note that these results were obtained
 2056 with a single gap RPC while the use of a double gap RPC would reduce the operation voltage by 200
 2057 to 300 V, lowering the induced charge. A compromise in between good efficiency and acceptable
 2058 level of streamer probability and the fine tuned composition of potential replacement gas mixtures
 2059 will be studied using a standard double-gap CMS RPC.

4

2060

2061

Physics of Resistive plate chambers

2062 A Resistive Plate Chamber (RPC) is a gaseous detector used in high-energy physics experiments
2063 as described in Chapter 3. It has been developed in 1981 by Santonico and Cardarelli [196], under
2064 the name of *Resistive Plate Counter*, as an alternative to the local-discharge spark counters pro-
2065 posed in 1978 by Pestov and Fedotovich [197, 198]. Working with spark chambers implied using
2066 high-pressure gas and high mechanical precision which the RPC simplified by formerly using a gas
2067 mixture of argon and butane flowed at atmospheric pressure and a constant and uniform electric
2068 field propagated in between two parallel electrode plates. Moreover, a significant increase in rate
2069 capability was introduced by the use of electrode plate material with high bulk resistivity, preventing
2070 the discharge from growing throughout the whole gas gap. Indeed, the effect of using resistive elec-
2071 trodes is that the constant electric field is locally canceled out by the development of the discharge,
2072 limiting its growth.

2073 Through its development history, different operating modes [199–201], gas mixtures [196, 201–
2074 206] and new detector designs [207–209] have been discovered, leading to further improvement of
2075 the rate capability of such a detector. The low developing costs and easily achievable large detection
2076 areas offered by RPCs, as well as the wide range of possible designs, made them a natural choice
2077 to as muon chambers and/or trigger detectors in multipurpose experiments such as CMS [178] or
2078 ATLAS [210], time-of-flight detectors in ALICE [211], calorimeter with CALICE [212] or even
2079 detectors for volcanic muography with ToMuVol [213].

2080 4.1 Principle

2081 RPCs are ionisation detectors composed of two parallel resistive plate electrodes in between which
2082 a constant electric field is set. The space in between the electrodes, referred to as *gap*, is filled with
2083 a dense gas that is used to generate primary ionization into the gas volume. The free charge carriers
2084 (electrons and cations) created by the ionization of the gas molecules are then accelerated towards the
2085 electrodes by the electric field, as shown in Figure 4.1 [214]. RPCs being passive detectors, a current
2086 on pick-up copper read-out placed outside of the gas volume is induced by the charge accumulation

2087 during the growth of the avalanche resulting from the acceleration of the charge carriers. As a
 2088 consequence, the time resolution of the detector is substantially increased as the output signal is
 2089 generated while the electrons are still in movement. The advantage of a constant electric field, over
 2090 multi-wire proportional chambers, is that the electrons are being fully accelerated from the moment
 2091 charge carriers are freed and feel the full strength of the electric field that doesn't depend on the
 2092 distance to the readout and that the output signal doesn't need for the electrons to be physically
 2093 collected.

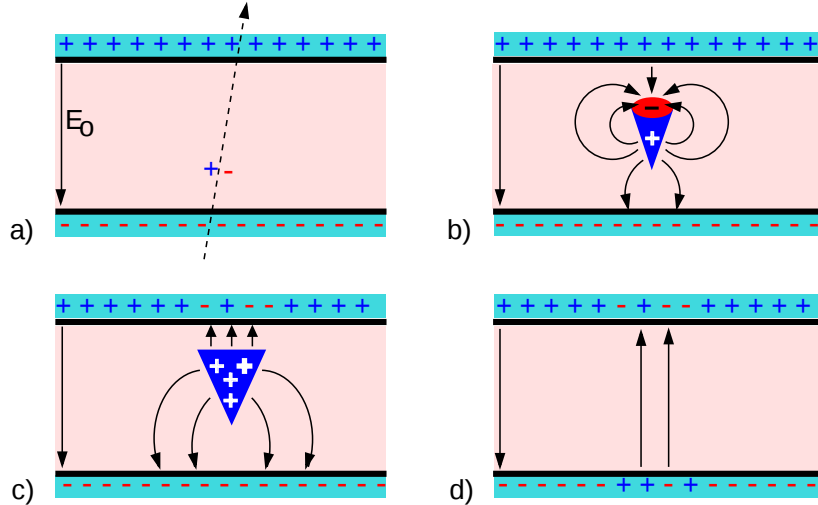


Figure 4.1: Different phases of the avalanche development in the RPC gas volume subjected to a constant electric field E_0 . a) An avalanche is initiated by the primary ionisation caused by the passage of a charged particle through the gas volume. b) Due to its growing size, the avalanche starts to locally influence the electric field. c) The electrons, lighter than the cations reach the anode first. d) The ions reach the cathode. While the charges have not recombined, the electric field in the small region around the avalanche stays affected and locally blinds the detector.

2094 After an avalanche developed in the gas, a time long compared to the development of a discharge
 2095 is needed to recombine the charge carriers in the electrode material due to their resistivity. This
 2096 property has the advantage of affecting the local electric field and avoiding sparks in the detector
 2097 but, on the other hand, the rate capability is intrinsically limited by the time constant τ_{RPC} of the
 2098 detector. Using a quasi-static approximation of Maxwell's equations for weakly conducting media,
 2099 it can be shown that the time constant τ_{RPC} necessary to the charge recombination at the interface
 2100 in between the electrode and the gas volume is given by the Formula 4.1 [215].

$$(4.1) \quad \tau_{RPC} = \frac{\epsilon_{electrode} + \epsilon_{gas}}{\sigma_{electrode} + \sigma_{gas}}$$

2101 A gas can be assimilated to vacuum, leading to $\epsilon_{gas} = \epsilon_0$ and $\sigma_{gas} = 0$, and the electrodes
 2102 permittivity and conductivity can be written as $\epsilon_{electrode} = \epsilon_r \epsilon_0$ and $\sigma_{electrode} = 1/\rho_{electrode}$,
 2103 showing the strong dependence of the time constant to the electrodes resistivity in Formula 4.2.

$$(4.2) \quad \tau_{RPC} = (\epsilon_r + 1)\epsilon_0 \times \rho_{electrode}$$

Very few materials with a low enough resistivity exist in nature. The resistivity targeted to build RPCs ranges from 10^9 to $10^{12} \Omega \cdot \text{cm}$. The most common RPC electrode materials are displayed in Table 4.1. When the doped glass and ceramics can offer short time constants of the order of 1 ms, the developing cost of such materials is quite high due to the very low demand. Thus, High-pressure laminate (HPL) is often the choice for high rate experiments using very large RPC detection areas. Other experiments working at cosmic muon fluxes can safely operate with ordinary float glass.

Material	$\rho_{\text{electrode}} (\Omega \cdot \text{cm})$	ϵ_r	$\tau_{\text{RPC}} (\text{ms})$
Float glass	10^{12}	~7	~700
High-pressure laminate	10^{10} to 10^{12}	~6	~6 to 600
Doped glass (LR S)	10^9 to 10^{11}	~10	~1 to 100
Doped ceramics (SiN/SiC)	10^9	~8.5	~1
Doped ceramics (Ferrite)	10^8 to 10^{12}	~20	~0.2 to 2000

Table 4.1: Properties of the most used electrode materials for RPCs.

4.2 Rate capability and time resolution of Resistive Plate Chambers

The electrode material plays a key role in the maximum intrinsic rate capability of RPCs. R&D is continuously being done to develop at always cheaper costs material with lower resistivity. Nevertheless, the amount of charge released, i.e. the size of the discharge, if reduced leads to a smaller blind area in the detector, increasing the rate capability of the detector. On the other hand, the drift velocity of electrons in the gas volume being quite stable with the applied electric field, the design of a detector and the associated read-out and pulse-processing electronics will be a major component of the time resolution of RPCs. Moreover, the sensitivity of the electronics will also help increasing the rate capability by lowering the gain the gas volume needs to be operated at, increasingly lowering the gas volume in which the signals will develop.

4.2.1 Operation modes

Being a gaseous detector using an accelerating electric field to amplify the signal of primary charge carriers, the RPC can be operated into different modes as the electric field intensity varies. Each mode offers different performances for such a detector, and it will be showed that the operating mode corresponding to the lowest electric field possible is best suited for high rate detectors working in collider experiments.

RPCs where developed early 1980s. At that time it was using an operating mode now referred to as *streamer mode*. Streamers are large discharges that develop in between the 2 electrodes enough to locally discharge the electrodes. If the electric field inside of the gas volume is strong enough, with electrons being fast compared to ions, a large and dense cloud of positive ions will develop nearby the anode and extend toward the cathode while the electrons are being collected, eventually leading to a streamer discharge due to the increase of field seen at the cathode. The field is then strong enough so that electrons are pulled out of the cathode. Electrodes, though they are a unique volume of resistive material, can be assimilated to capacitors. At the moment an electric field is applied in between their outer surfaces, the charge carriers inside of the volume will start moving leading to a situation where there is no voltage across the electrodes and a higher density of negative charges,

i.e. electrons, on the inner surface of the cathode. Finally, when a streamer discharge occurs, these electrons are partially released in the gas volume contributing to increase the discharge strength until the formation of a conductive plasma, the streamer. This can be understood through Figure 4.2 [199]. Streamer signals are very convenient in terms of read-out as no further amplification is required with output pulses amplitudes of the order of a few tens to few hundreds of mV as can be seen on Figure 4.3.

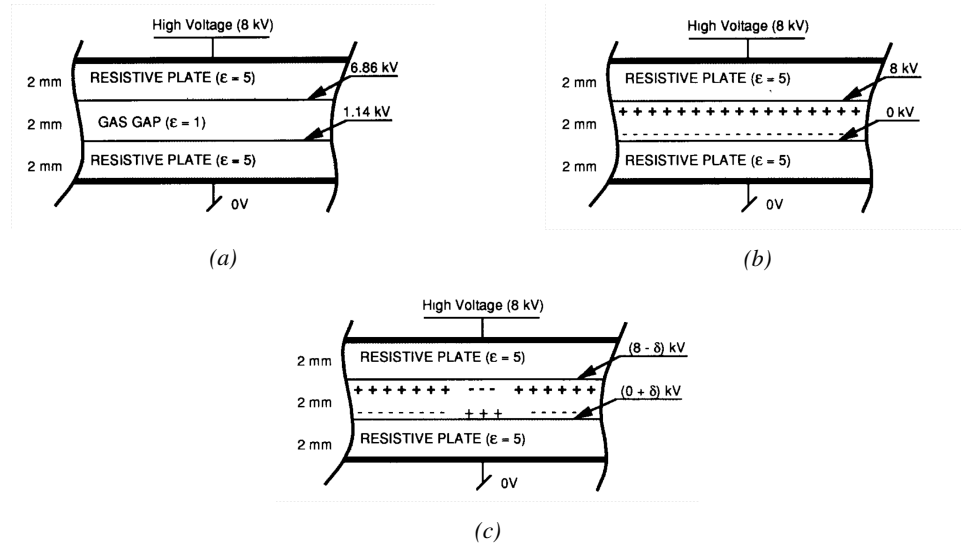


Figure 4.2: Movement of the charge carriers in an RPC. Figure 4.2a: Voltage across an RPC whose electrode have a relative permittivity of 5 at the moment the tension is applied. Figure 4.2b: After the charge carriers moved, the electrodes are charged and there is no voltage drop over the electrodes anymore. The full potential is applied on the gas gap only. Figure 4.2c: The streamer discharge initiated by a charged particle transports electrons and cations towards the anode and cathode respectively.

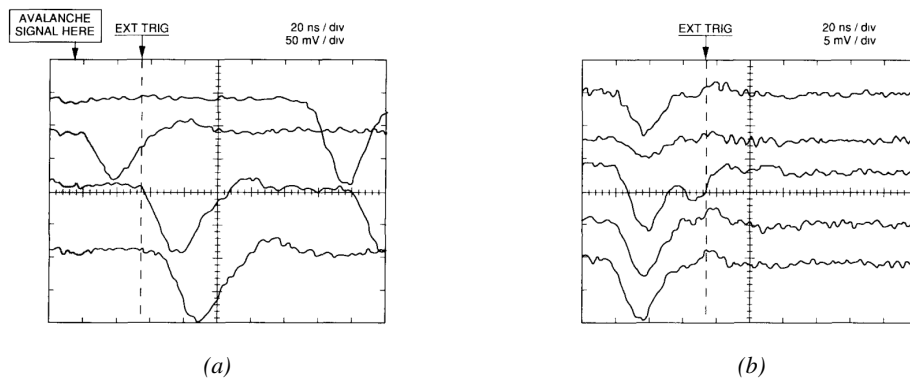


Figure 4.3: Typical oscilloscope pulses in streamer mode (Figure 4.3a) and avalanche mode (Figure 4.3b). In the case of streamer mode, the very small avalanche signal is visible.

When the electric field is reduced though, the electronic gain is small until the electrons get close enough to the anode and the positive ion cloud is much smaller. The electric field cannot rise to the

point a field emission of electrons on the cathode is possible. The resulting signal is weak, of the order of a few mv as shown on Figure 4.3, and requires amplification. This is the *avalanche mode* of RPC operation. This mode offers a higher rate capability by providing smaller discharges that don't affect the electrodes charge and are more locally contained in the gas volume as was demonstrated by Crotty with Figure 4.4 [199]. The detector only stays locally blind the time the charge carriers are recombined and there is no need for electrode recharge which is a long process affecting a large portion of the detector. Another advantage of avalanche signals over streamer is the great time consistency. Figure 4.3 shows very clearly that avalanche signals have a very small time jitter. Thus, using such a mode is a natural choice for experiments in which the detectors are required to have a high detection rate.

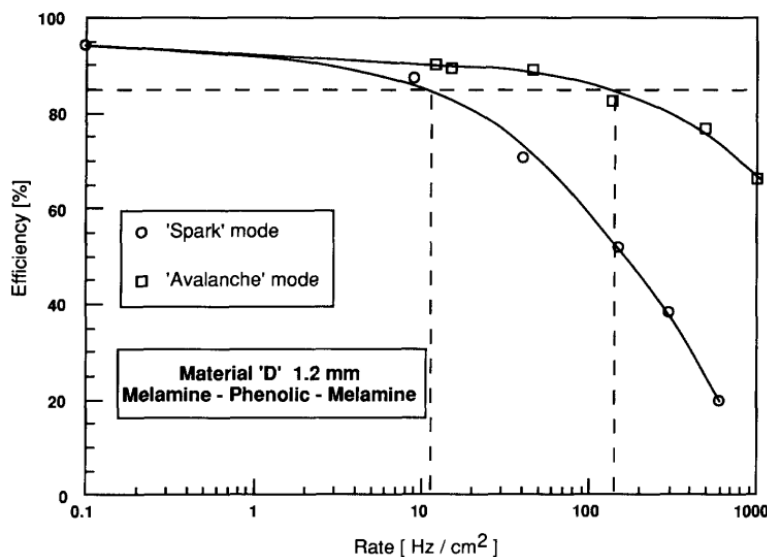


Figure 4.4: Rate capability comparison for the streamer and avalanche mode of operation. An order of magnitude in rate capability for a maximal efficiency drop of 10% is gained by using the avalanche mode over the streamer mode.

4.2.2 Standard gas mixture for RPCs operated in collider experiments

The first RPC working in streamer mode was operated with a 50/50 mixture of argon and butane [196], a standard mixture used at that time in multi-wire proportional chambers, taking profit of the good effective Townsend coefficient of argon to maximize the number of primary charge carriers freed in the gas by ionizing particles and of the quenching properties of butane. Before the discovery of the avalanche mode of RPC operation and concerned about the rate capability of RPCs operated in streamer mode, the performance improvement of the detectors through the increase of fast charge ratio in the signal development ,decreasing the charge induced per avalanche as can be seen through Figure 4.5, was studied by adding Freon based gases, such as CF_3Br , into the typical Ar/C_4H_{10} gas mixture was studied and showed that a lower induced charge could lead to an improvement the rate capability [202]. This consideration lead to the discovery of the avalanche mode which confirmed that the smaller the induced charge, the better the rate capability of the RPCs [199]. This discovery could happen thanks to the increased number of lower induced charge events allowed by adding a

²¹⁶⁸ fraction of strong quencher in the gas mixture.

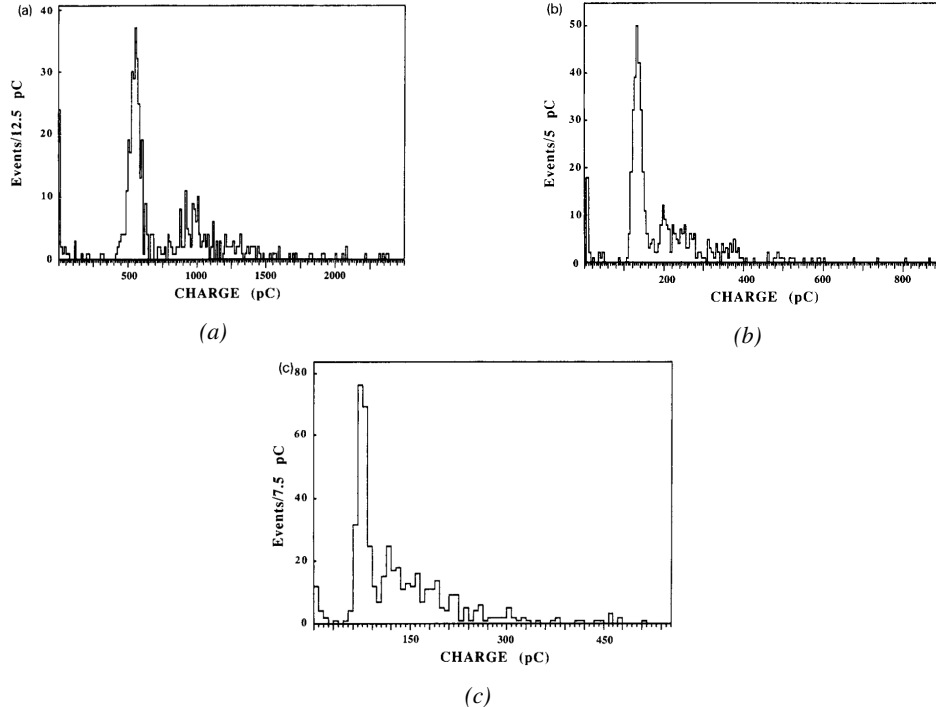


Figure 4.5: Comparison of the charge distribution of signals induced by cosmic muons in an RPC operated with a gas mixture of argon, butane and bromotrifluoromethane (CF_3Br). The Ar/C_4H_{10} is kept constant at 60/40 in volume while the total amount of CF_3Br in the mixture is varied: 0% (Figure 4.5a), 4% (Figure 4.5b) and 8% (Figure 4.5c) [202].

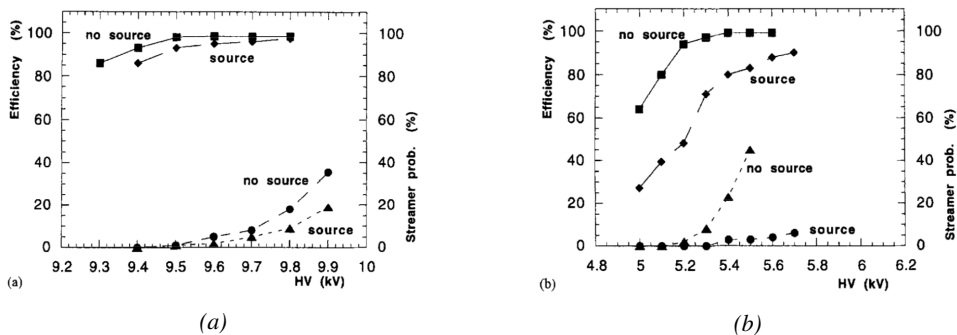


Figure 4.6: Comparison of the efficiency and streamer probability, defined as the fraction of events with an induced charge 10 times larger than that of the average avalanche, with and without irradiation by a 24 GBq ^{137}Cs source of an RPC successively operated with a 90/10 mixture $C_2H_2F_4/i-C_4H_{10}$ (Figure 4.6a) and a 70/5/10/15 mixture of $Ar/i-C_4H_{10}/CO_2/C_2H_2F_4$ (Figure 4.6b) [203].

²¹⁶⁹ From this moment onward, more and more studies were conducted in order to find a gas mixture
²¹⁷⁰ that would allow for the best suppression of streamers for the benefit of low charge avalanches. Most

R&D groups working with narrow gaps started using freon-based gas mixtures while users of wide gap RPCs kept using Ar/CO_2 based mixtures. The differences in between narrow and wide gaps will be later discussed in Section 4.2.3. The CF_3Br having a high GWP, tetrafluoroethane ($C_2H_2F_4$) was preferred to it as more suitable ecofriendly gas in the middle of the 90s. An advantage of this new freon component is that it featured a high primary ionization and a low operating voltage, as reported by Cardarelli [201]. Thus, the new gas mixtures used were mainly composed of tetrafluoroethane alone with lower content of isobutane in order to reduce the flammability of the mixtures in the case it were to be used in accelerator experiments for safety reasons. Performance and models about such mixtures were discussed in papers of Abbrescia [203, 204] and showed a better suitability of such a gas mixture, with respect to argon based ones, for operations with high radiation backgrounds leading to a need for high rate capability of the detectors, as can be seen from Figures 4.6 and 4.7. Indeed, although the operating voltage of a tetrafluoroethane based mixture is higher than which of an argon based mixture but the efficiency under irradiation is more stable, the voltage range with negligible streamer probability is much wider, and the fast charge ratio available is much greater, providing with more stable operation of the detector.

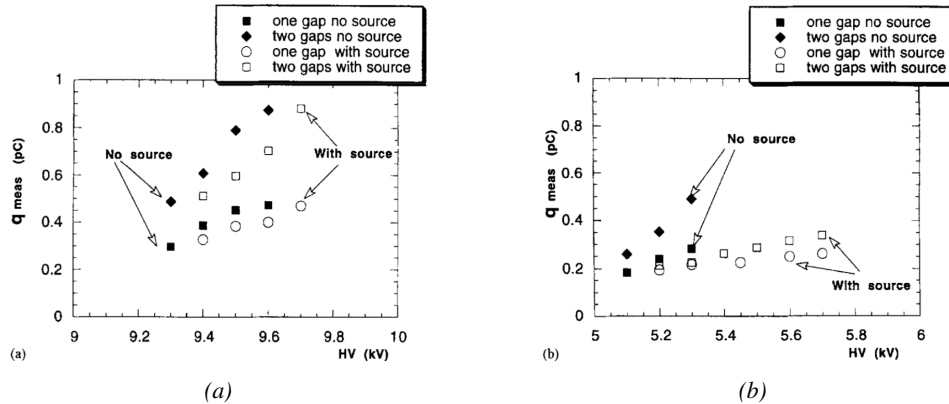


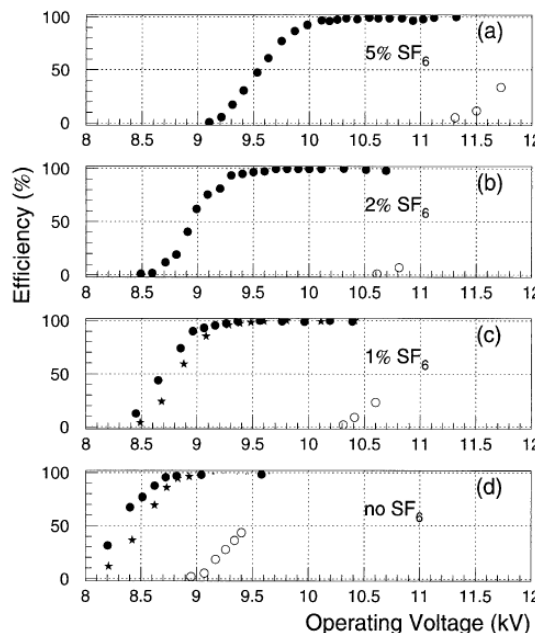
Figure 4.7: Comparison of the fast charge ratio with and without irradiation by a 24 GBq ^{137}Cs source of an RPC successively operated with a 90/10 mixture $C_2H_2F_4/i-C_4H_{10}$ (Figure 4.7a) and a 70/5/10/15 mixture of $Ar/i-C_4H_{10}/CO_2/C_2H_2F_4$ (Figure 4.7b). The results are provided for both single gap and double gap operation [203].

Aside of the improvement of the rate capability through linseed oil surface treatment of HPL electrodes, which allowed for a lower intrinsic noise rate and dark current of the detectors by improving the smoothness of the electrodes surface [216], it was later found that the streamers could be further suppressed by adding an electronegative compound into the gas mixture. The benefits of adding SF_6 in order to push the transitions from avalanche to streamers towards high voltages has been discussed in 1998 [205, 206] and eventually the high rate RPC destined to be used in accelerator physics would unanimously start using this compound into RPC gas mixtures. Being able to control the creation of streamers allows for slower ageing of the detector and lower power consumption as the currents driven by the electrodes consecutively to the induced charges would be smaller. In summary, the typical gas mixture RPCs are operated with is generally composed of the following 3 gas compounds, although, as mentioned in Chapter 3.7, research is being conducted into new more ecofriendly gas mixture using gases with a much lower Global Warming Potential:

- Tetrafluoroethane ($C_2F_4H_2$), also referred to as *Freon* or *R134a*, is the principal compound

2199 of the RPC gas mixtures, with a typical fraction above 90%. It is used for its high effective
 2200 Townsend coefficient and the great average fast charge that allows to operate the detector
 2201 with a high threshold with respect to argon, for example, that has similar effective Townsend
 2202 coefficient but suffers from a lower fast charge. To operate with similar conditions, argon
 2203 would require a higher electric field leading to a higher fraction of streamers, thus limiting the
 2204 rate capability of the detector [203, 204].

- 2205 • Isobutane ($i\text{-C}_4\text{H}_{10}$), only present in a few percent in the gas mixtures, is used for its UV
 2206 quenching properties [217] helping to prevent streamers due to UV photon emission during
 2207 the avalanche growth.
- 2208 • Sulfur hexafluoride, (SF_6), simply referred to as SF_6 , is used in very little quantities for its
 2209 high electronegativity. Excess of electrons are being absorbed by the compound and streamers
 2210 are suppressed [205, 206]. Nevertheless, a fraction of SF_6 higher than 1% will not bring
 2211 any extra benefit in terms of streamer cancelation power but will lead to higher operating
 2212 voltage [205], as can be understood through Figure 4.8.



2213 *Figure 4.8: Efficiency (circles and stars with 30 mV and 100 mV thresholds respectively) and streamer prob-
 2214 ability (open circles) as function of the operating voltage of a 2 mm single gap HPL RPC flushed with a gas
 2215 mixture containing (a) 5%, (b) 2%, (c) 1% and (d) no SF_6 [205].*

2216 In the last steps of R&D, the gas mixture of CMS RPCs was foreseen to be a 96.2/3.5/0.3 compo-
 2217 sition of $\text{C}_2\text{H}_2\text{F}_4$ / $i\text{-C}_4\text{H}_{10}$ / SF_6 [218] but finally it was slightly changed into a 95.2/4.5/0.3 mixture
 2218 of the same gases [219]. A summary of the operation performance of the RPCs since the start of
 LHC and of CMS data taking is given in Figure 4.9 [220]. The performance of the detectors is
 regularly monitored and the operating voltages updated in order to obtain a very stable performance
 through time. Nevertheless, the detectors will face new challenges during Phase-II during which they

will exposed to more extreme radiation conditions. Description of the longevity tests with extreme irradiation and the conclusions regarding the operation of the present RPC system will be given in Chapter 5.

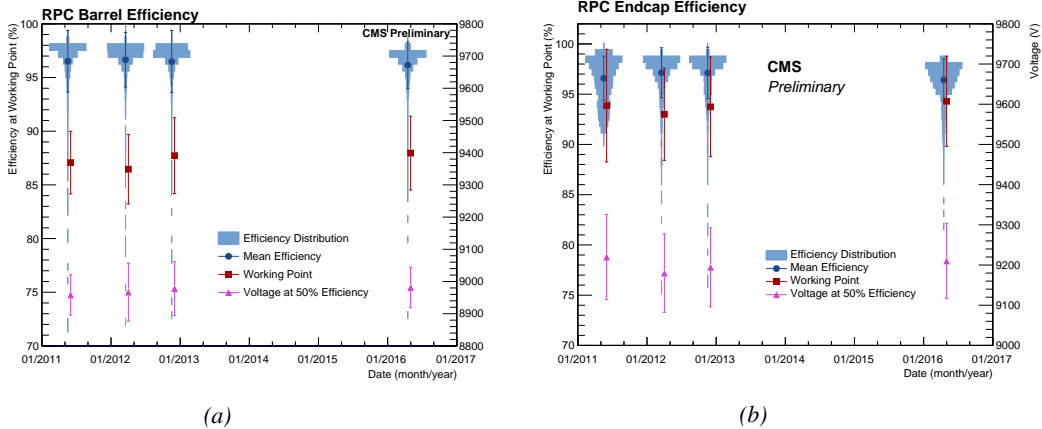


Figure 4.9: Evolution of the efficiency, working voltage, and voltage at 50% of maximum efficiency for CMS Barrel (Figure 4.9a) and Endcap (Figure 4.9b) RPCs obtained through yearly voltage scans since 2011. The working voltage of each RPC is updated after each voltage scan to ensure optimal operation [220].

It was already discussed that in the future, it is likely that the use of freon gases could be banned. As potential replacement for tetrafluoroethane was proposed the trifluoriodomethane (CF_3I), a molecule with similar properties than CF_3Br which was replaced by the tetrafluoroethane, and the 1,3,3,3-tetrafluoropropene ($C_3H_2F_4$ or HFO-1234re), a molecule with similar properties than the actual tetrafluoroethane and proposed as a replacement in refrigerating and air conditioning systems [221]. These 2 gases have stronger quenching properties than $C_2H_2F_4$ which means a much stronger electric field needs to be applied on the parallel electrodes of the RPCs in order to reach full efficiency. But the power supply system of CMS RPC is limited to 15 kV and so is ATLAS power supply system which is participating in a joined R&D. As can be seen from Figure 3.24, reducing the working voltage was achieved by mixing the potential replacements together with CO_2 . Introducing carbon dioxide into the mixture while keeping similar levels of isobutane and SF_6 increases the streamer probability and the best candidate identified for a compromise in between low enough working voltage and acceptable levels of streamers corresponds to a mixture containing 50% of CO_2 , 45% of HFO, 4% of isobutane and 1% of SF_6 but is not yet considered satisfactory. On the other hand, no good replacement for SF_6 has yet been identified. With its very high Global Warming Potential (23900), even small fraction of this gas in the mixture (it only represents 0.3% of CMS standard mixture but more than 5% of its overall GWP) substantially increase the danger for the environment. Although finding a replacement for this gas is less critical than for the tetrafluoroethane composing more than 90% of usual RPC standard mixtures, the problem will need to be addressed.

4.2.3 Detector designs and performance

Different RPC design have been used and each of them present its own advantages. Historically, the first type of RPC to have been developed is what is now referred to as *narrow gap* RPC [196, 222].

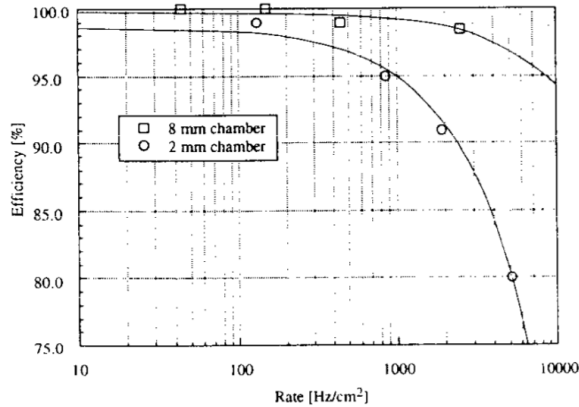


Figure 4.10: Comparison of the rate capability of 8 mm and 2 mm wide RPCs. The lines are linear fits on the data [222].

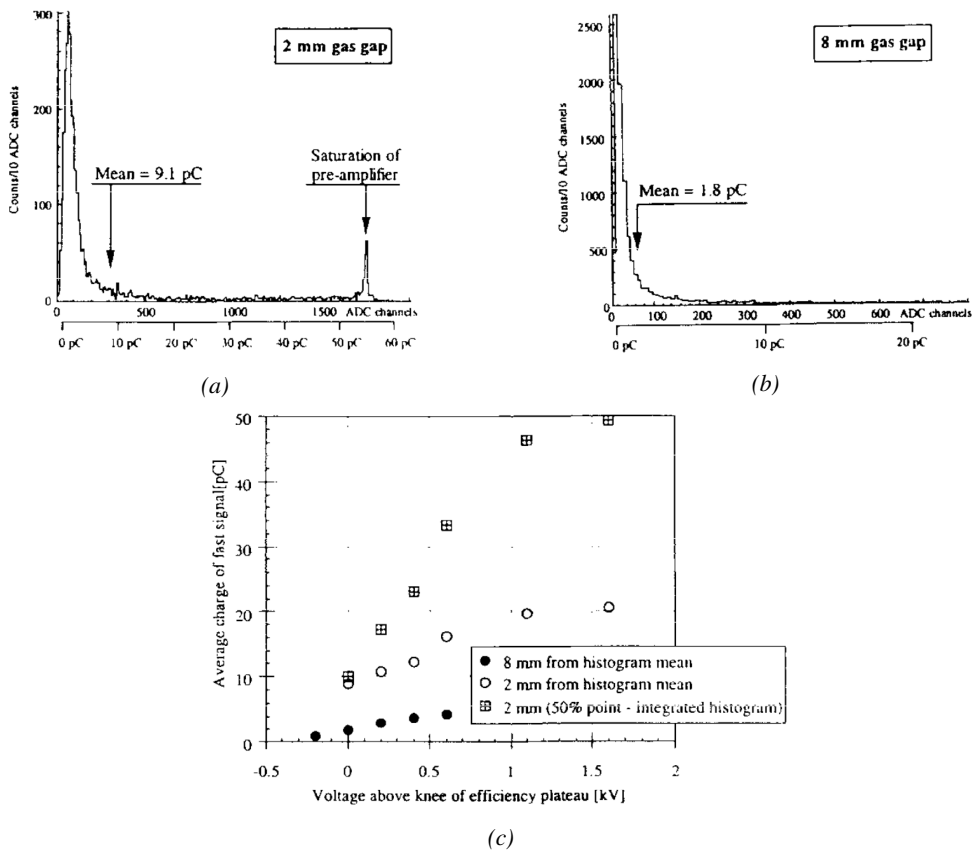


Figure 4.11: Distributions of the induced charge of fast signals on 2 mm (Figure 4.11a) and 8 mm (Figure 4.11b) RPCs exposed to a radiation rate of 100 Hz/cm^2 . Average induced charge of fast signals as a function of the high voltage applied on 2 mm and 8 mm RPCs (Figure 4.11c). In the case of the 2 mm RPC, a saturation of the pre-amplifier was observed. The average of the distribution is underestimated and the median is showed together with the average to account for this bias [222].

After the avalanche mode has been discovered [199], it has been showed that increasing the width of the gas gap lead to higher rate capability, due to lower charge deposition per avalanche, and lower power dissipation [222], as is showed in Figures 4.10 and 4.11. The distance in between the electrode being greater, a weaker electric field can be applied and a lower gain used as a longer gas volume will contribute to the signal induction on the read-out circuit. Nevertheless, by increasing the gas gap width, the time resolution of the detector decreases. This is a natural result if the increase of active gas volume in the detector is taken into account. Indeed, for a given detection threshold on the induced charge per signal, only the small fraction of gas closest to the cathode will provide enough gain to have a detectable signal. In the case of a wider gas volume, the active region is then larger and a larger time jitter is introduced with the variation of starting position of the avalanche, as discussed in [207] and showed in Figure 4.12.

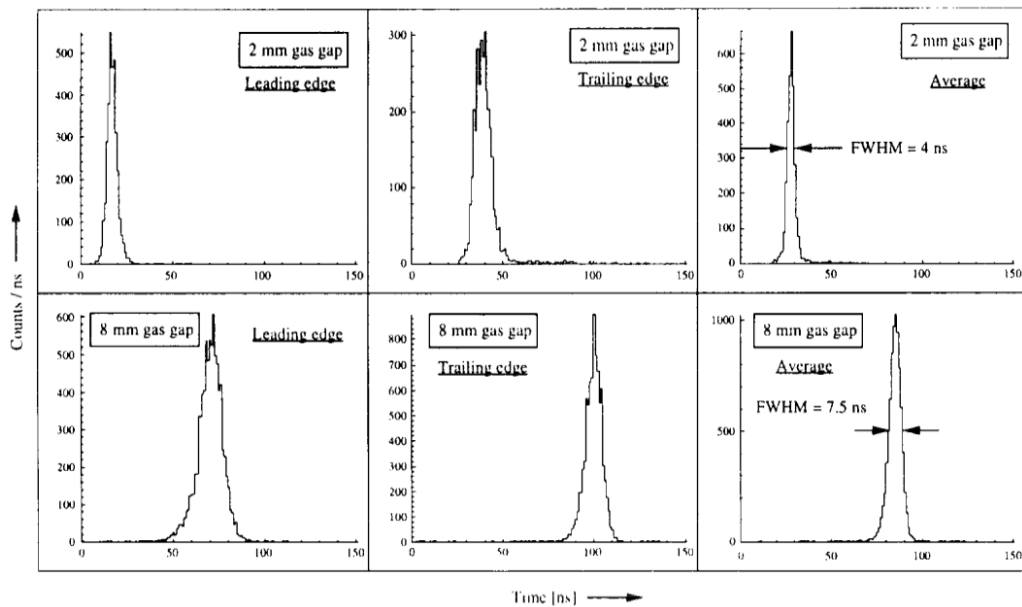


Figure 4.12: Time distributions of the leading, trailing, and average of both leading and trailing edges for 2 mm (top row) and 8 mm (bottom row) RPCs exposed to a 100 Hz/cm² radiation rate. The data was collected with RPCs operated at the voltage corresponding to the knee of the efficiency distribution, defined as the point where 95% of the maximum efficiency is obtained [222].

To improve both the time resolution and the rate capability, different methods were used trying to take advantage of both narrow and wide gap RPCs into a single design. Thus, double gap RPCs, combining two narrow gaps into a single detector to increase the effective sensitive volume, and multigap RPCs, which divided the large volume of a wide gap RPC into thinner sub-gaps by adding intermediate electrodes in between the cathode and anode to improve the time resolution by mimicking narrow gap RPCs, were developed starting from the middle of the 90s.

4.2.3.1 Double gap RPC

Made out of 2 narrow RPC detectors stacked on top of each other as shown in Figure 4.13, this detector layout, popularized by the two multipurpose experiments CMS [178] and ATLAS [210] at LHC, can be used as an OR system in which each individual chamber participates in the output signal

and increases the overall sensitive volume of the detector apparatus. Keeping the copper strip read-out system at the ground, CMS and ATLAS, due to different goals, have chosen different designs as CMS RPCs possess a 1D read-out while ATLAS RPCs offer a 2D read-out. The difference comes from placing the read-out in between the gaps, the anodes facing each other, or to have both RPC gaps in between 2 layers of read-out panels, one along the X-axis and one along the Y-axis, the cathodes facing each other.

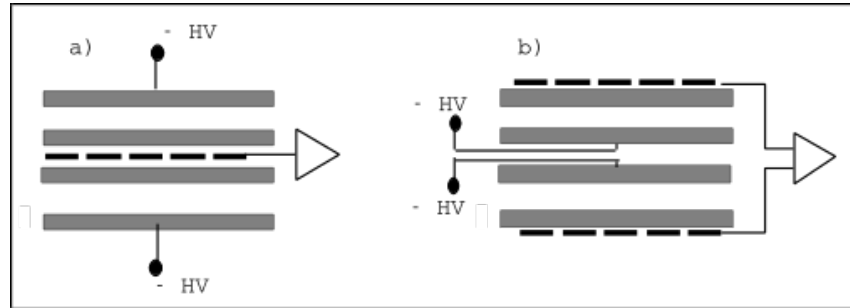


Figure 4.13: Possible double-gap RPC layouts: a) "standard" 1D double-gap RPC, as used in CMS experiment, where the anodes are facing each other and a 1D read-out plane is sandwiched in between them, b) double read-out double-gap RPC as used in ATLAS experiment, where the cathodes are facing each other and 2 read-out planes are used on the outer surfaces. This last layout can offer the possibility to use a 2D reconstruction by using orthogonal read-out planes.

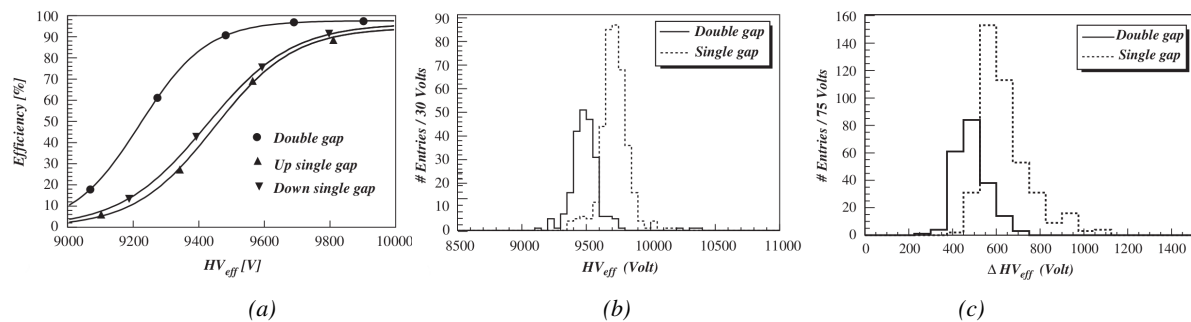


Figure 4.14: Comparison of performance of CMS double and single gap RPCs using cosmic muons [218]. Figure 4.14a: Comparison of efficiency sigmoids. Figure 4.14b: Voltage distribution at 95% of maximum efficiency. Figure 4.14c: $\Delta_{10\%}^{90\%}$ distribution.

The gain of such a detector is reduced by a factor 2 with respect to single-gap RPCs with an efficiency plateau reached at lower voltage, as visible on Figure 4.14, due to the two gas gaps contributing to the signal formation and offering a dynamic range closer to that of a wide gap RPC. A double gap is then fully efficient while the individual RPC gaps composing it are only 70 to 80% efficient. Naturally, by operating the double gap at a lower voltage, the rate capability is found to be increased as the induced charge per gap is then lower than in the case of a single gap detector also leading to a reduction of the streamer probability and a better extraction of the fast charge of the total signal as could be seen through previously presented Figure 4.7.

2280 **4.2.3.2 Multigap RPC (MRPC)**

2281 MRPCs are layouts in which floating sub electrode plates are placed into a wide gap RPC to divide
 2282 the gas volume and create a sum of narrow gaps [207, 208]. Similarly to the double gap RPC for
 2283 which the gain could be reduced by increasing the dynamic range, the multigap reduces the gain
 2284 while keeping a total dynamic range similar to which of a wide gap RPC by reducing the size of
 2285 each individual sub-gap composing the detector. The dynamic range, associated to the sensitive
 2286 volume, and the comparison of each detector layout to the wide gap RPC is showed in Figure 4.15.

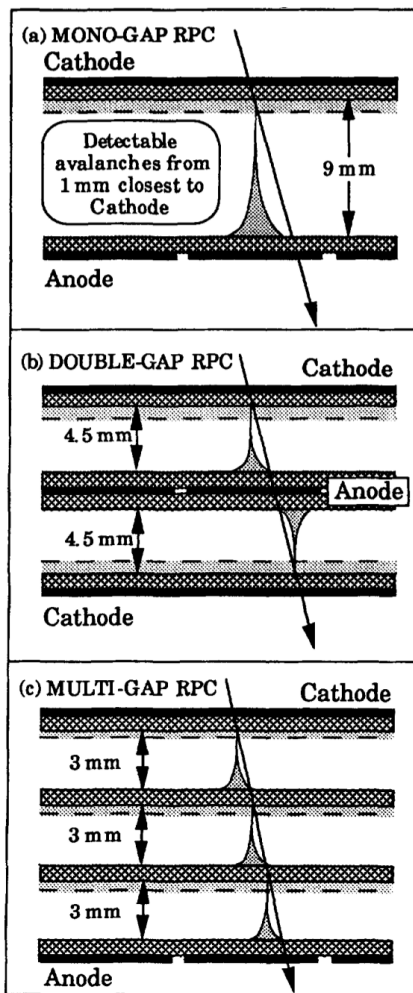


Figure 4.15: Representation of different RPC layouts (wide gap on Figure (a), double gap on Figure (b) and multigap on Figure (c)), of the corresponding sensitive volume in gray, and of the associated avalanche size [208].

2287 By operating the detector with thinner gaps, the time resolution is improved. Comparatively to
 2288 the time resolution presented in Figure 4.12 for the wide gap RPC of 8 mm, a complementary study
 2289 was conducted on multigaps using two 4 mm and four 2 mm subgaps and showed, via Figure 4.16,
 2290 an improvement of the time resolution with the reduction of the gap width and of the number of gaps

2291 while the same sensitive volume was kept [208].

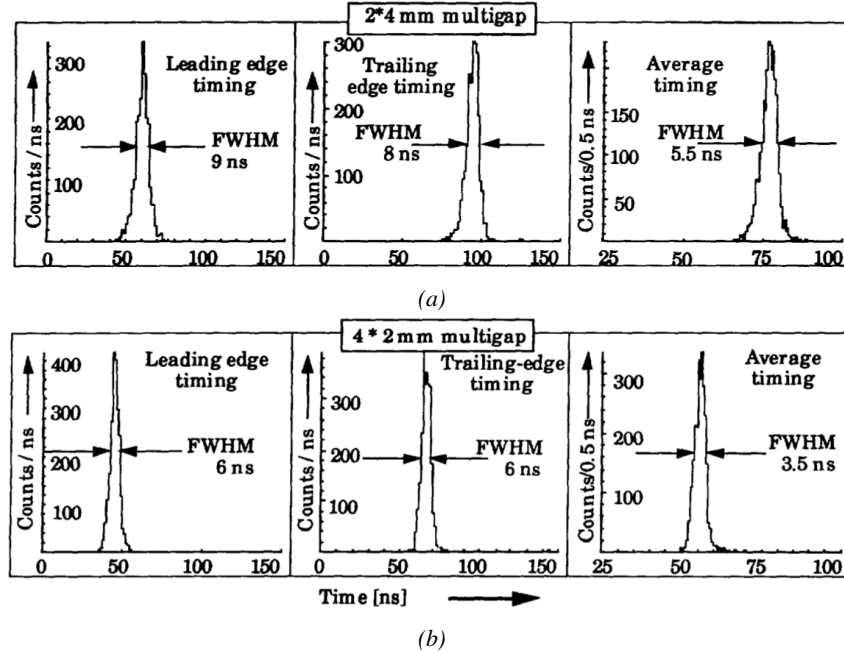


Figure 4.16: Time distributions of the leading, trailing, and average of both leading and trailing edges for multigap RPCs consisting in two 4 mm (Figure 4.16a) and four 2 mm (Figure 4.16b) exposed to a 100 Hz/cm^2 radiation rate. The data was collected with RPCs operated at the voltage corresponding to the knee of the efficiency distribution, defined as the point where 95% of the maximum efficiency is obtained [208].

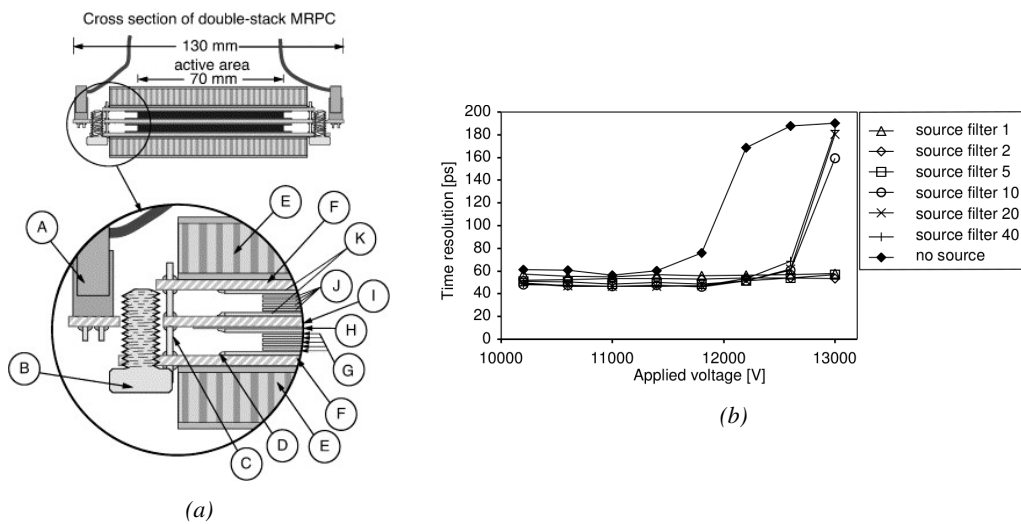


Figure 4.17: Presentation of a study of a possible ALICE MRPC cell using $250 \mu\text{m}$ gas gaps, $620 \mu\text{m}$ outer glass electrodes, and $550 \mu\text{m}$ inner floating electrodes (Figure 4.17a), and of its time resolution performance as a function of the applied high voltage for different radiation levels referred through different filter settings of the $740 \text{ GBq } ^{137}\text{Cs}$ source the former CERN GIF facility [223].

After the problem of streamers was solved by adding SF_6 into the gas mixture, the size of the MRPCs decreased as the research groups started applying the concept of dividing the gas volume into subvolumes to the narrow gap RPCs leading to the now widely used micro gap MRPCs. The time resolution of such a detector can reach of few tens of ps, with gas gaps of the order of a few hundred μm as showed in Figure 4.17 representing a single cell of ALICE Time-of-flight (ToF) system consisting of double MRPCs, as it was studied in the early 2000s [223].

Sometimes used as a double multigap RPC, taking advantage of the OR of double gap RPCs to both be able to operate a higher number of gaps while keeping a reasonable high voltage applied in between the cathode and anode and to further reduce the gain, the MRPC is mainly used as ToF detector [223–227] due to its excellent timing properties that allow to perform particle identification as explained by Williams in [228]. The principle of particle identification using ToF is simply the measurement of the velocity of a particle. Indeed, particles are defined by their mass (for the parameter of interest here, their electric charge being measured using the bending angle of the particles traveling through a magnetic field) and this mass can be calculated by measuring the velocity β and momentum of the particle:

$$(4.3) \quad \beta = \frac{p}{\sqrt{p^2 + m^2}}$$

Intuitively, it is trivial to understand that 2 different particles having the same momentum will have a different velocity due to the mass difference and thus a different flight time T_1 and T_2 through the detector and this is used to separate and identify particles. The better the time resolution of the ToF system used, the stronger will the separation be:

$$(4.4) \quad T = \frac{L}{v} = \frac{L}{c \cdot \beta}, \quad \Delta T = T_1 - T_2 = \frac{L}{c} \left(\sqrt{1 + m_1^2/p^2} - \sqrt{1 + m_2^2/p^2} \right) \cong (m_1^2 - m_2^2) \frac{L}{2cp^2}$$

An example of particle identification is given for the case of STAR experiment in Figure 4.18.

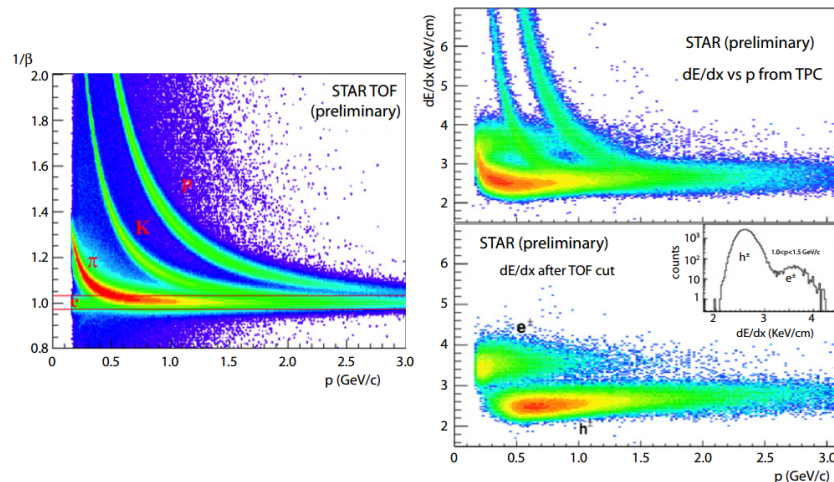


Figure 4.18: Particle identification applied to electrons in the STAR experiment. The identification is performed combining ToF and dE/dx measurements [228].

2312 Taking into account the distortion effect on the electric field inside of a MRPC built using micro
 2313 gaps due to the exposition to irradiation, distortion that can be understood by monitoring the current
 2314 drawn by the detector which should stay constant at constant electric field, another benefice of using
 2315 such small gas gaps is the strong reduction of the average avalanche volume and thus of the blind
 2316 spot on MRPCs leading to an improved rate capability. Multigaps can sustain backgrounds of several
 2317 kHz/cm² as demonstrated in Figure 4.19.

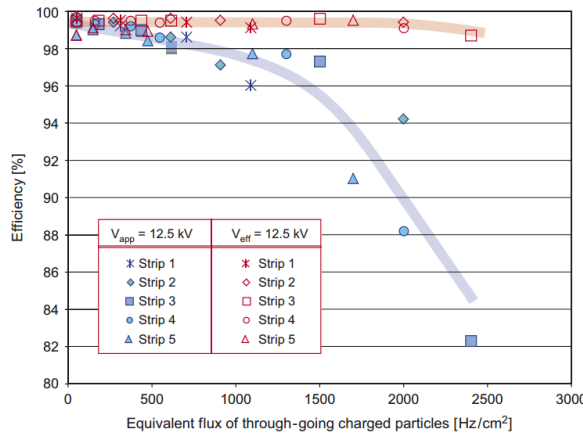


Figure 4.19: Comparison of the detector performance of ALICE ToF MRPC [229] at fixed applied voltage (in blue) and at fixed effective voltage (in red). The effective voltage is kept fixed by increasing the applied voltage accordingly to the current drawn by the detector.

2318 4.2.3.3 Charge distribution and performance limitations

2319 [This part could be moved in the next section of the chapter and deepened using the perspective
 2320 of the avalanche physics.]

2321 The direct consequence of the different RPC layouts is a variation of intrinsic time resolution of
 2322 the RPC as the gap size decreases and of the rate capability when the deposited charge per event is
 2323 spread over a larger number of amplification volumes, allowing for a reduction of the overall gain of
 2324 the detectors which is replaced by an on-electronics pre-amplification of the signals. in this sense,
 2325 an advantage is given to multigaps whose design use sub-millimeter gas volumes providing very
 2326 consistent signals.

2327 From the charge spectrum point of view, each layout has its own advantages. When the double-
 2328 gap has the highest induced over drifting charge ratio, as seen in Figure 4.20, the multigap has a
 2329 charge spectrum strongly detached from the origin, as visible in Figure 4.21. A high induced over
 2330 drifting charge ratio means that the double gap can be safely operated at high threshold or that at
 2331 similar threshold it can be operated with a twice smaller drifting charge, meaning a higher rate
 2332 capability if operated with sensitive enough electronics. On the other hand, the strong detachment
 2333 of the charge spectrum from the origin in the MRPC case allows to reach a higher efficiency with
 2334 increasing threshold as most of the induced charge is not low due to the convolution of several
 2335 single gap spectra. The range of stable efficiency increases with the number of gap, as presented in
 2336 Figure 4.22.

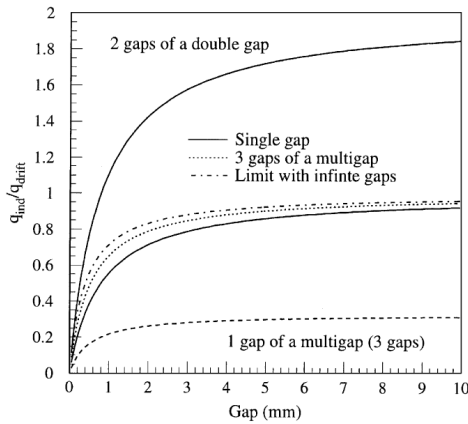


Figure 4.20: Ratio between total induced and drifting charge have been simulated for single gap, double-gap and multigap layouts [230]. The total induced charge for a double-gap RPC is a factor 2 higher than for a multigap.

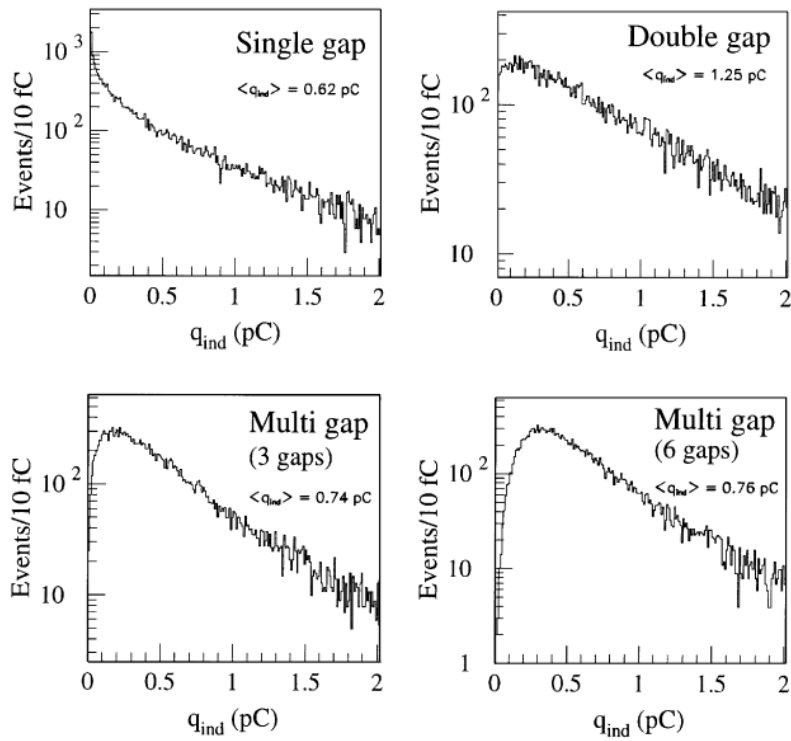


Figure 4.21: Charge spectra have been simulated for single gap, double-gap and multigap layouts [230]. It appears that when single gap shows a decreasing spectrum, double and multigap layouts exhibit a spectrum whose peak is detached from the origin. The detachment gets stronger as the number of gaps increases.

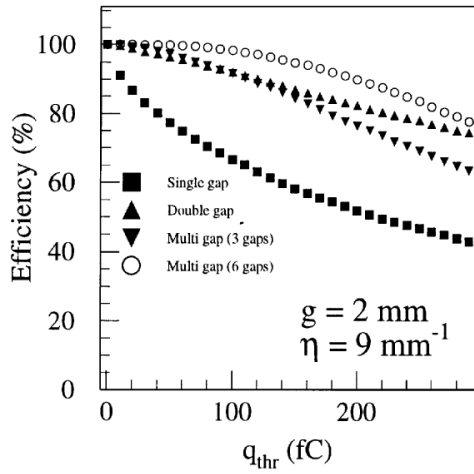


Figure 4.22: The maximal theoretical efficiency is simulated for single gap, double-gap and multigap layouts [230] at a constant gap thickness of 2 mm and using an effective Townsend coefficient of 9 mm^{-1} .

4.3 Signal formation

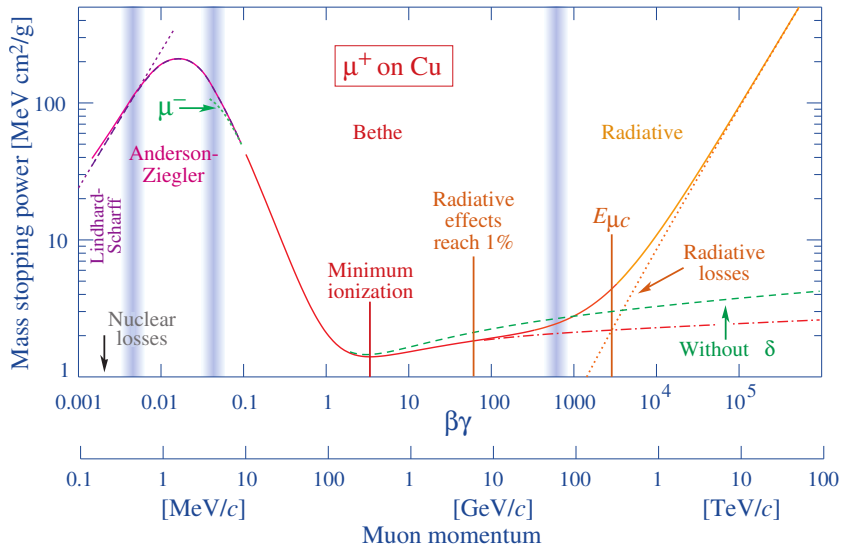


Figure 4.23: Mass stopping power as a function of $\beta\gamma = p/Mc$ for positive muons in copper [115]. The total stopping power is indicated with solid line and local components with dashed lines. The vertical bands are used to indicate boundaries between different approximations used at different energy range.

The physics of Resistive Plate Chambers still is far from being fully understood and work is regularly being accomplished in trying to model these detectors the best way possible by phenomenological models using well-defined physics [214, 231, 232]. These theoretical works have nevertheless lead to a better understanding of the key principles that account for RPCs signal formation. As previously

discussed, the typical mixture of such a detector is in great majority composed by a ionizing gas with some quenching properties and a low ionization potential to easily produce electrons, with the addition of UV quencher and electronegative compounds. The electronic avalanche formation will be triggered by a charged particle passing through the gas, typically a muon in the case of most uses of RPCs. The production of electrons in the gas of a detector is related to the energy lost by the incoming particle traveling through a material medium. The example of the mass stopping power of copper on muons is given in Figure 4.23 on which the different energy loss mechanisms at different energy ranges are visible. Once primary electrons have been freed in the gas volume, the electric field applied in between the electrodes of the RPC will make the charges move and there will be a competition in the gas in between the Townsend and attachment coefficient which describe the evolution of the number of electrons in an avalanche. While drifting through the gas, the electrons are also subjected to diffusion that will affect the evolution of the avalanches. Finally, when the avalanche is big enough, the accumulation of negative (electrons) and positive (ions) charges in the gas volume will start affecting the local electric field. This effect is known as space charge effect.

4.3.1 Energy loss at intermediate energies

Intuitively, a particle traveling through a medium will interact with its components, losing energy. When a muon travels through the gas of a gaseous detector, at the energy range usually observed, it interacts with the molecules of the gas leading to dissipation of the transferred energy in the form of inelastic diffusion or ionization. The photons and electron-ion pairs resulting from these interaction can trigger avalanches in the gas which will contribute to feed the avalanche growth thanks to the strong electric field applied in between the 2 electrodes of a RPC.

The mass stopping power of moderately relativistic ($0.1 \lesssim \beta\gamma \lesssim 1000$) heavy particles ($M \gg m_e$) traveling through a medium via excitation and ionization processes was studied by Bethe in 1930 [233] and is well described by the so called the Bethe Formula given in Equation 4.5.

$$(4.5) \quad \left\langle -\frac{dE}{dx} \right\rangle = K z^2 \frac{Z}{A} \frac{1}{\beta^2} \left(\frac{1}{2} \ln \frac{2m_e c^2 \beta^2 \gamma^2 W_{max}}{I^2} - \beta^2 - \delta(\beta\gamma) \right)$$

The different parameters used in this equation are

E	- incident particle energy γMc^2	MeV
x	- mass per unit area	g cm^{-2}
N_A	- Avogadro's number	$6.022\ 140\ 857(74) \times 10^{23} \text{ mol}^{-1}$
c	- speed of light in vacuum	$299\ 792\ 458 \text{ m s}^{-1}$
μ_0	- permeability of free space	$4\pi \times 10^{-7} \text{ N A}^{-2}$
ϵ_0	- permittivity of free space $\epsilon_0 = 1/\mu_0 c^2$	$8.854\ 187\ 817\dots \times 10^{-12} \text{ F m}^{-1}$
α	- fine structure constant $\alpha = e^2/4\pi\epsilon_0\hbar c$	$1/137.035\ 999\ 139(31)$
r_e	- classical electron radius $r_e = e^2/4\pi\epsilon_0 m_e c^2$	$2.817\ 940\ 3227(19) \text{ fm}$
e	- elementary charge of the electron	$-1.6021766208(98) \times 10^{-19} \text{ C}$
$m_e c^2$	- electron mass $\times c^2$	$0.510\ 998\ 9461(31) \text{ MeV}$
K	- constant defined as $K = 4\pi N_A r_e^2 m_e c^2$	$0.307\ 075 \text{ MeV mol}^{-1} \text{ cm}^2$
z	- charge number of incident particle	
Z	- atomic number of absorbing medium	
A	- atomic mass of absorbing medium	g mol^{-1}
β	- velocity of particle $\beta = v/c$	
γ	- Lorentz factor $\gamma = (1 - \beta^2)^{-1/2}$	

W_{max}	- maximum energy transfer through a single collision	MeV
I	- mean excitation energy of absorbing medium	eV
$\delta(\beta\gamma)$	- density effect correction to ionization energy loss	

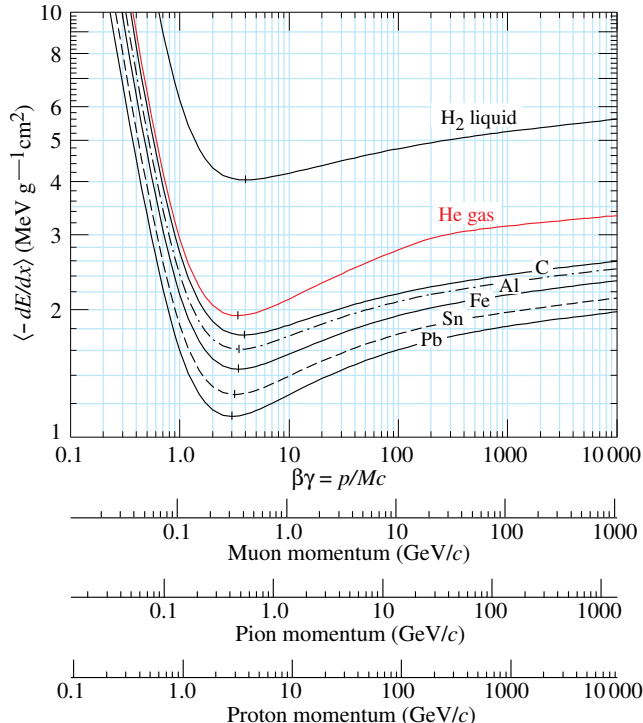


Figure 4.24: Mean mass stopping power for liquid hydrogen, as used in bubble chambers, gaseous helium, carbon, aluminum, iron, tin, and lead without the inclusion of radiative effect at higher $\beta\gamma$ necessary for pions and muons in denser materials [115].

In this equation, the maximum energy transfer W_{max} is defined as function of the incident particle mass M , expressed in MeV/c^2

$$(4.6) \quad W_{max} = \frac{2m_e c^2 \beta^2 \gamma^2}{1 + 2\gamma m_e / M + (m_e / M)^2}$$

and the mean excitation energy I depends on the absorber and its determination is non-trivial but recommendation are given by the International Commission on Radiation Units & Measurements (ICRU) based on experimental measurements and interpolations as showed in Figure 4.25.

For the case of copper, the mean stopping power is visible in Figure 4.23. The mean stopping power corresponding only to the Bethe range for other materials is given in Figure 4.24 and shows that $\langle -dE/dx \rangle$ is similar for each material with a slow decrease with Z . The factor affecting the equation the most is β as the dependence on M is introduced at higher energies in the logarithm via the max transfer energy per single collision but in most practice cases, only the dependence on β is considered as most of the relativistic particles are closed to the lowest mean energy loss rate and are

2378 referred to as minimum ionizing particles (mip's). The almost logarithmic relation in between the
 2379 mean energy loss rate for minimum ionizing particles and Z is showed in Figure 4.26.

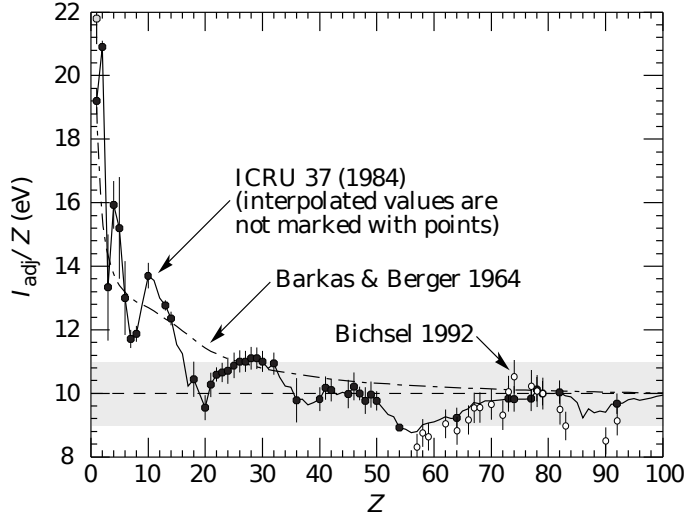


Figure 4.25: Mean excitation energies normalized to the atomic number as adopted by the ICRU [115, 234, 235].

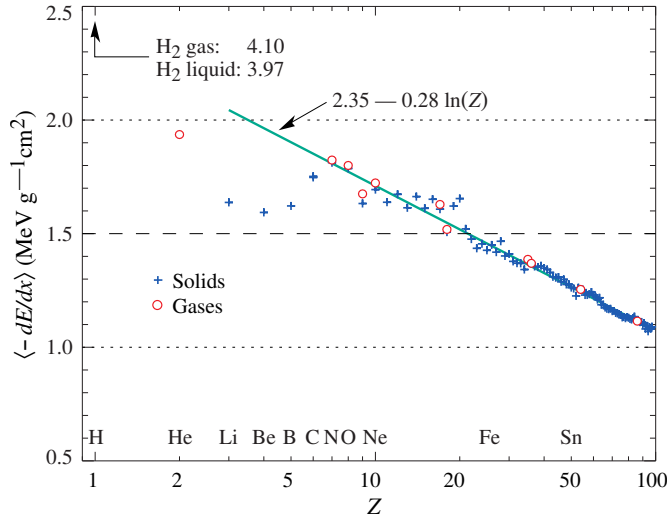


Figure 4.26: Mean mass stopping power at minimum ionization as a function of the atomic number [115].

2380 Finally, the term $\delta(\beta\gamma)/2$ corresponds to the density effect correction introduced to account for
 2381 the polarization of a real media that limits the spatial extension of the electric field of relativistic
 2382 particles. Indeed, as the energy of a particle increases, the associated electric field will flatten and
 2383 extend. Due to this effect, the distant collision contribution to Equation 4.5 will increase as $\ln(\beta\gamma)$
 2384 but the polarization of the media trunc this rise. At high energies, the correction is given by Equa-

2385 tition 4.7

$$(4.7) \quad \delta/2 \longrightarrow \ln(\hbar\omega_p/I) + \ln(\beta\gamma) - 1/2$$

2386 where $\hbar\omega_p$ represents the plasma energy that depends on the electron density of the media and
 2387 the electron mass and can be calculated as $\sqrt{\rho\langle Z/A\rangle} \times 28.816$ eV. The introduction of this cor-
 2388 rection term reduces the increase of the mean stopping power at higher energies as can be seen in
 2389 Figure 4.23. Moreover, due to poorer electron density, the effect is less visible on gases than on
 2390 liquids and solids has van be seen from Figure 4.24.

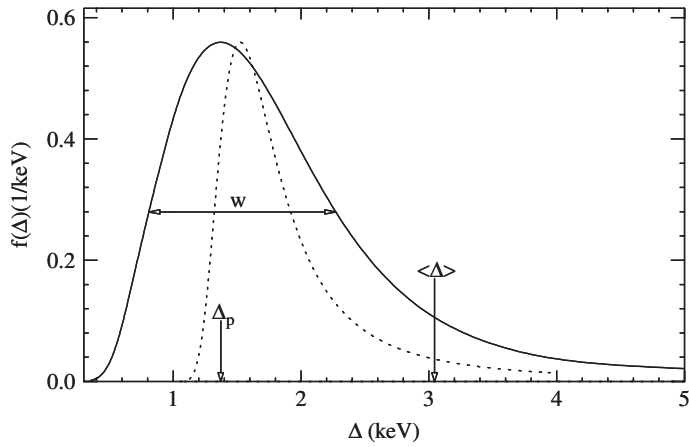


Figure 4.27: Example of straggling function $f(\Delta)$ of particles passing through 1.2 cm of Argon gas with a $\beta\gamma$ of 3.6 and represented with a solid line. The original Landau distribution is showed with a dashed line [236].

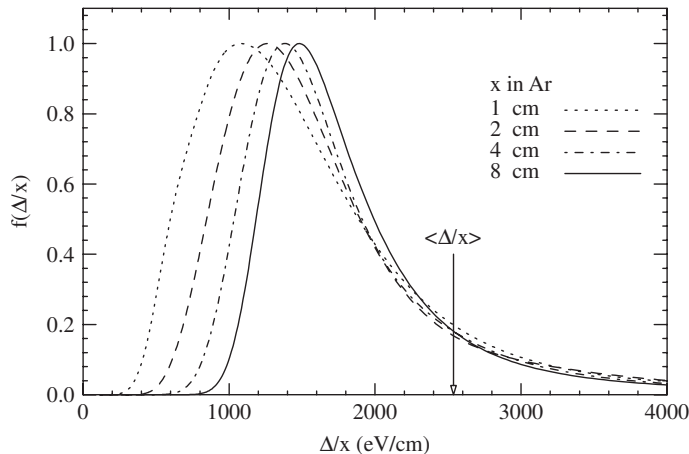


Figure 4.28: Evolution of straggling functions $f(\Delta)$ of particles passing through a volume of Argon gas with a $\beta\gamma$ of 3.6 with increasing thickness x [236].

2391 The mean energy loss per collision can be difficult to measure for low data samples and is not
 2392 always representative of the energy loss distribution for a given incident particle energy. Hence, it is

2393 easier to access the most probable energy loss which is a lower value than than the average loss due
 2394 to the distribution of the energy transfer. This value is well described by a highly skewed Landau
 2395 distribution for detectors with "moderate" thickness x , expressed in g mol⁻¹. But for gas volumes,
 2396 a Landau distribution greatly underestimates the width w of the distribution and only succeeds to
 2397 provide with a correct value for the most probable energy loss, as showed in Figure 4.27. Thus,
 2398 the energy loss distribution is better represented by its most probable energy loss Δ_p and its full-
 2399 width-at-half-maximum (FWHM) w . As showed by Figure 4.28, the distribution is affected by
 2400 the thickness of the gas volume and the most probable energy loss normalized to the thickness is
 2401 increased and the width decreased, converging towards the Landau distribution, whereas the mean
 2402 energy loss is unchanged. Correction are brought to the original Landau equation in order to account
 2403 better for the number of collisions leading to an increased width of the energy loss distribution [236].

2404 In the case of gas mixtures, composed of several elements, using Bragg additivity it can be
 2405 understood that the mean energy loss of the mixture is the sum of the mean energy losses in each
 2406 individual element j layer of weight w_j .

$$(4.8) \quad \left\langle \frac{dE}{dx} \right\rangle = \sum w_j \left\langle \frac{dE}{dx} \right\rangle_j$$

2407 4.3.2 Primary ionization

2408 Using Bethe formula to understand the mean energy transfer of charged particle when traveling
 2409 through a gas volume give an intuition of the physics that affect the particle but doesn't provide a
 2410 detailed enough information about the individual ionizations along its tracks at a microscopic level.
 2411 In order to simulate efficiently an RPC and hence understand the processes governing avalanches
 2412 creation and growth, knowledge on the ionization process is necessary.

2413 To convert the energy loss rate into a number of primary ionizations was developed in 1980 the
 2414 Photo-Absorption Ionisation (PAI) model [237] based on the cross section of ionization of gas atoms
 2415 to real photons and the dielectric constant of the medium through which the charged particles are
 2416 going. Indeed, the interaction of charged particles with the gas molecules being of electromagnetic
 2417 nature, it is mediated by quasi-real photons and, hence, the cross section to photon ionization is
 2418 important to understand. This approach is nevertheless semi-classical as it relies on classical elec-
 2419 trodynamics and it only gives access to the energy transfer to the gas atoms and no information on
 2420 the energy dissipation and secondary emissions is available on the output of the model. The energy
 2421 transferred to the medium is not all used for ionization. For an energy deposition Δ , the number of
 2422 electron-ion pairs produced is:

$$(4.9) \quad \Delta = n_i W$$

2423 W corresponds to the mean work per pair production that depends on the medium and is greater
 2424 than the ionization potential leading to the conclusion that part of the transferred energy is dissipated
 2425 through other processes [232, 238]. In order to understand the energy dissipation and the secondary
 2426 emissions, the fine structure of each atom is taken into account. Through the PAI model, the incident
 2427 charged particle interacts is assumed to interact with the full atom rather than with a single electron.

2428 Although, considering that the particle interacts with a single electron, leads to the possibility
 2429 to study the excited state of the atom once the photo-electron has been emitted with an energy

corresponding to the transferred energy minus the binding energy of the electronic shell. The resulting vacancies in the electronic shell will be filled through emission of photons or Auger electrons and can contribute to further ionization or excitation in the gas volume. Fluorescence photons are usually not considered as they only constitute a very small fraction of secondary emissions [239]. Assuming that the transferred energy is absorbed in its totality by a single electronic shell, the PAI model was modified to include relaxations and constitute the new Photo-Absorption Ionisation with Relaxation (PAIR) model [239]. In this model, the cross section corresponding to the whole atom is re-expressed using a sum of partial cross sections corresponding to the different electronic shells. When one or more electrons are knocked out of the atom, the vacancies are filled by electrons of the shell above with relaxation by Auger electron emission. These processes happen in cascade from the inner shell to the outer one until all the vacancies are filled and the energy has been released.

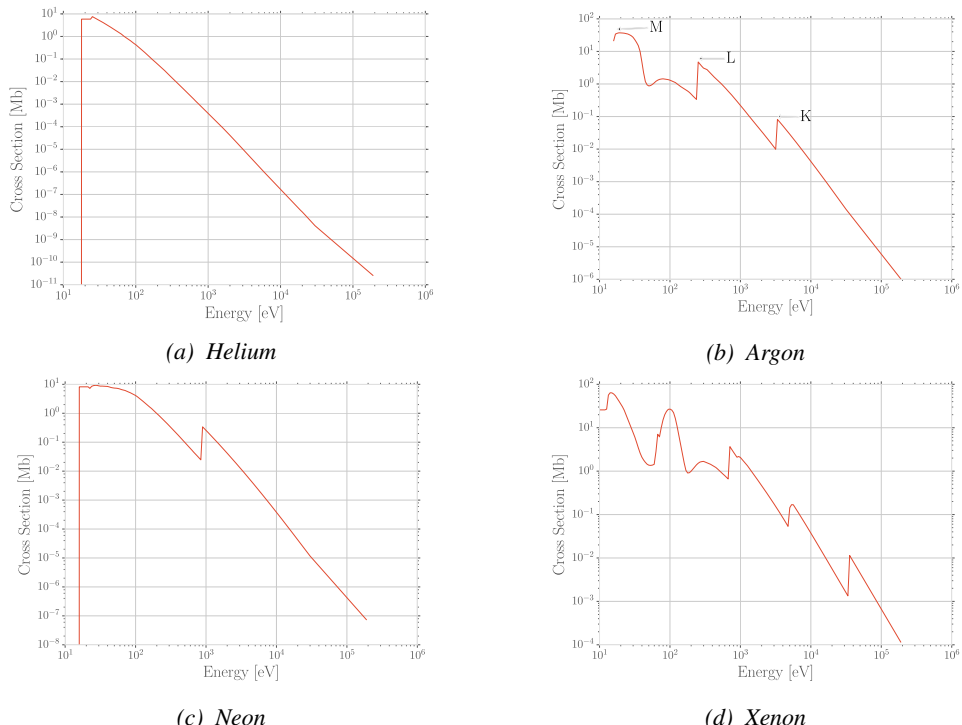


Figure 4.29: Photo-absorption cross section as computed by HEED for nobles gases with different electric shell numbers [232].

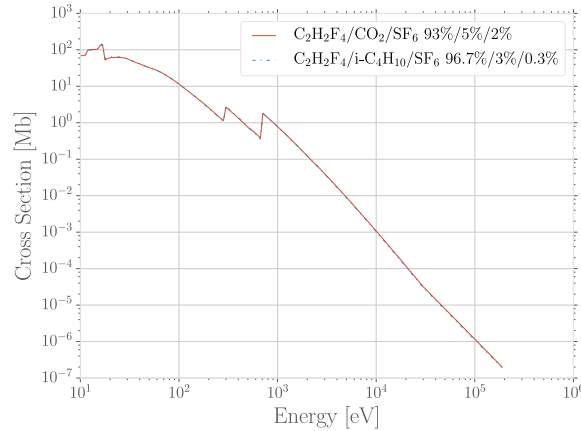


Figure 4.30: Photo-absorption cross section as computed by HEED for typical RPC gas mixtures [232]. The RPC mixture with CO_2 corresponds to the mixture used by CALICE SDHCAL [240] while the other one was foreseen for the experiment ATLAS [241] but has been changed since then.

2441 This model is included in the program HEED developed at CERN [242] and called by Garfield,
 2442 a program developed for the simulation of gaseous detectors. The results for the cross section for a
 2443 few noble gases are given in Figure 4.29. It can be seen that for each shell, the cross section is in-
 2444 creased. More complex patterns are seen with bigger atoms such as Xenon on Figure 4.29d. For gas
 2445 mixtures, like the typical RPC mixtures, the cross section is showed in Figure 4.30. Both mixtures
 2446 being mainly composed of $C_2H_2F_4$, the variations in between the 2 cross section profiles are very
 2447 subtle and depends on the concentration of the other compounds.

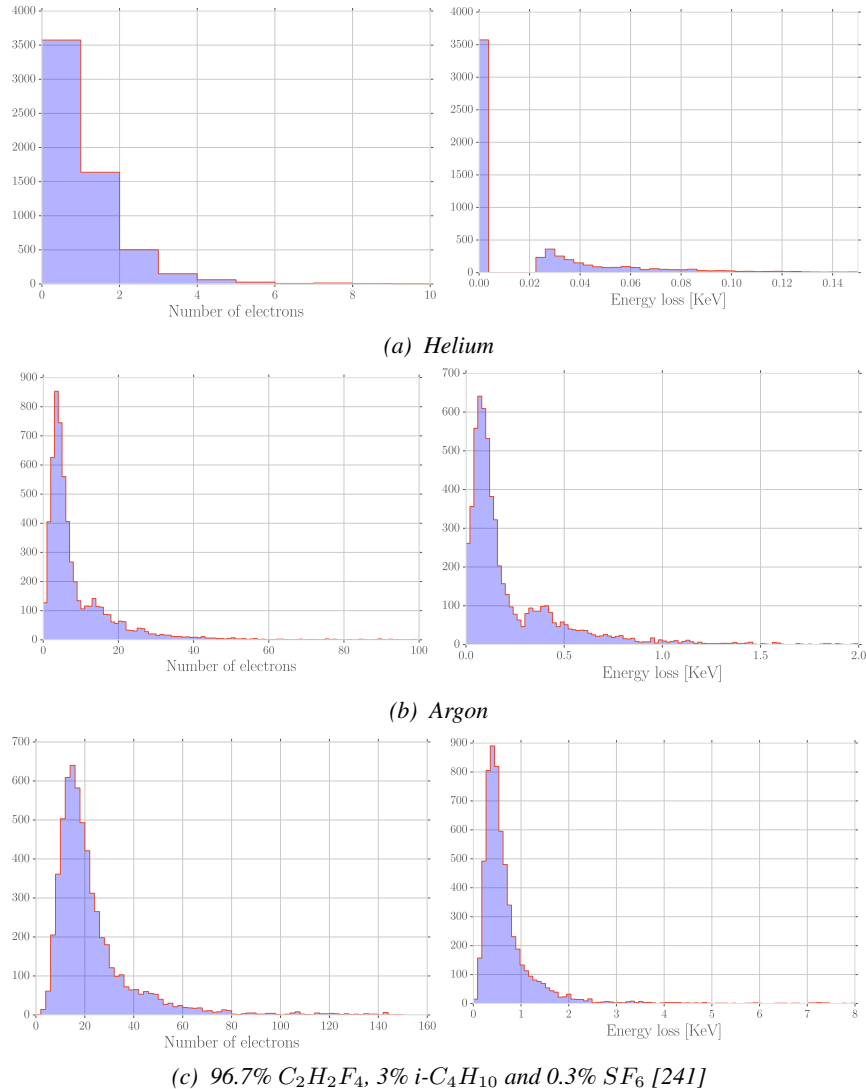


Figure 4.31: Distributions of number of electrons (left) and energy loss (right) for a 5 GeV/c muon passing through 1.2 mm of Helium (Figure 4.31a), Argon (Figure 4.31b) or a typical RPC gas mixture (Figure 4.31c) [232].

Once the cross section of interaction is known, it is possible to extract the distribution of energy loss and of the number of electron produced, as showed in Figure 4.31 for Helium, Argon, which is used in gaseous detectors, and for a typical RPC mixture [232]. The distributions are computed using HEED and show typical straggling function profiles with some complex structures that can be related to interaction of the incoming particle with the different electronic shells. Helium does not have a great photo-absorption cross-section according to Figure 4.29a and a muon will not be likely to lose a lot of energy and to create a lot of electrons whereas in a more complex atom like Argon, the cross-section is greater and will lead to a greater energy loss of muons and more electron produced. Finally, a complex gas mixture used in RPCs will offer an even greater cross-section, a wider energy loss distribution and will be able to produce more electrons. The same information is seen by looking

at the evolution of the mean number of cluster as a function of the lorentz factor associated to muons showed in Figure 4.32a. Indeed, the greater photo-absorption cross-section of RPC mixtures allow for a much greater amount of clusters to be created by charged particles. The size of these clusters is studied through Figure 4.32b which shows that, in most of the cases ($\approx 80\%$), the clusters only are composed of a single electron which is consistent with minimum ionizing particles.

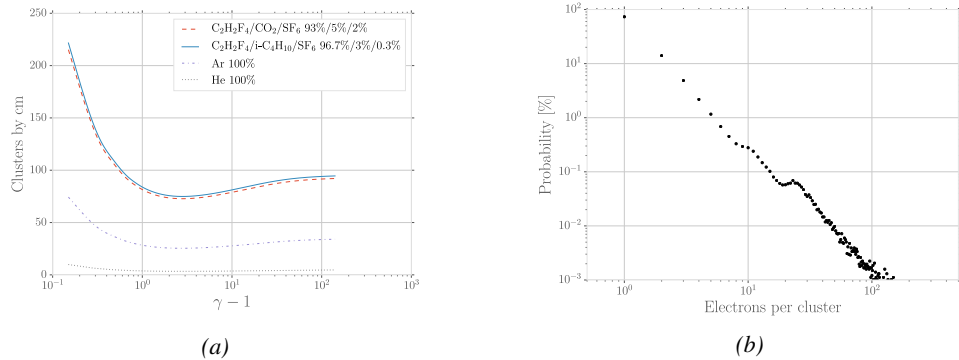


Figure 4.32: Figure 4.32a: Mean cluster density for muons through different gas volumes [232]. Figure 4.32b: Distribution of the number of electrons per cluster for a 5 GeV/c muon traveling through a mixture of 96.7% $C_2H_2F_4$, 3% $i-C_4H_{10}$ and 0.3% SF_6 [232, 241].

4.3.3 Development and propagation of avalanches

From the clusters released in the gas volume by the charged particles, free electrons will start drifting due to the electric applied in between the electrodes of the RPC. Gaining velocity and energy, these electrons in their turn will be able to ionize the gas. This process being repeated by all the produced electrons will trigger an avalanche to develop.

The growth of the avalanche can be intuitively understood as a competition between 2 effects. Due to their increasing energy, electrons have a probability to trigger new ionizations by interacting with gas molecules. On the other hand, before the minimal amount of energy is reached, the electrons can get attached to a gas molecule instead. These two effects can be described using a simple model in which the multiplication and attachment processes are given by the Townsend coefficient α and the attachment coefficient η , assuming that the history of previous interactions in the gas does not influence new interactions. This model simply takes into account probabilities to have at the gas depth z for a given number n of free electrons in the gas $n+1$ or $n-1$ electrons at the depth $z+dz$ (respectively $n\alpha dz$ and $n\eta dz$). Then, the mean number of electrons \bar{n} and cations \bar{p} can be written for single compound gases as

$$(4.10) \quad \frac{d\bar{n}}{dz} = (\alpha - \eta)\bar{n}, \quad \frac{d\bar{p}}{dz} = \alpha\bar{n}$$

which, assuming the initial conditions $\bar{n}(0) = 1$ and $\bar{p}(0) = 0$, lead to the mean number of electrons and cations at a depth z

$$(4.11) \quad \bar{n}(z) = e^{(\alpha-\eta)z}, \quad \bar{p}(z) = \frac{\alpha}{\alpha-\eta} \left(e^{(\alpha-\eta)z} - 1 \right)$$

2480 The Townsend and attachment coefficient as a function of the applied electric field are given in
 2481 Figure 4.33 for a standard RPC gas mixture using Magboltz [243].

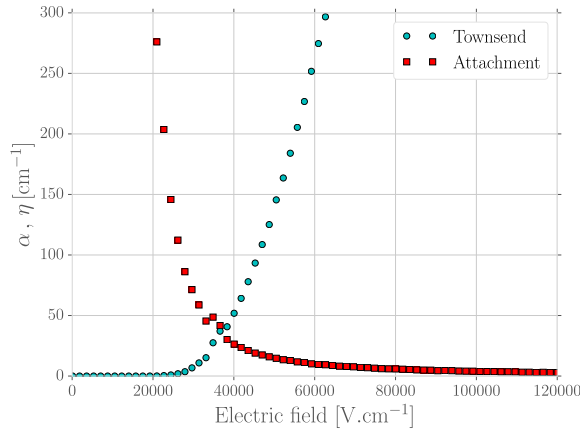


Figure 4.33: Townsend and attachment coefficient for a typical 96.7/3/0.3 mixture of $C_2H_2F_4/i-C_4H_{10}/SF_6$, at a temperature $T = 296.15\text{ K}$ and a pressure $P = 1013\text{ hPa}$ [232, 241].

2482 Nevertheless, there are more to the avalanche growth than simply these two factors. Throughout
 2483 the 20th century, models have been developed to better understand the physics of discharges in gas.
 2484 In 1937, Furry developed a model to describe electromagnetic cascades [244] that would be used for
 2485 electron avalanches in gas during the 1950s. Furry realized that the use of a Poisson law to describe
 2486 the distribution of shower sizes could not be accurate as he understood that the events occurring in
 2487 the development of a cascade are not independent from each other, as a Poisson law would suggest.
 2488 Indeed, part of the particles produce others and this process depends on both their original energy
 2489 and energy lost. Experimental results showed excess of small showers and an under estimate of very
 2490 large ones. To solve this problem, Furry proposed a distribution of sizes of following the likelihood
 2491 described in Equation 4.12, in which $\bar{n} = e^{\alpha z}$, compared with a Poisson law in Figure 4.34.

$$(4.12) \quad P(n, \bar{n}) = \bar{n}^{-1}(1 - \bar{n}^{-1})^{n-1}$$

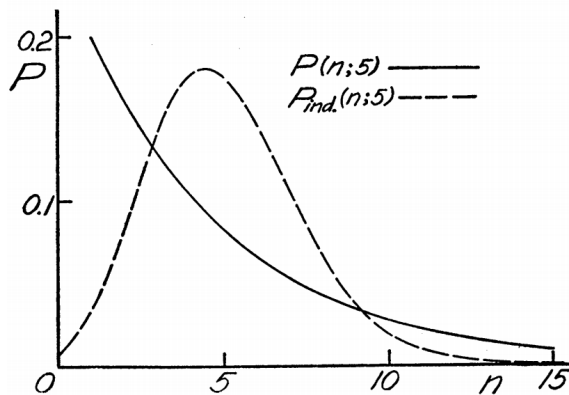


Figure 4.34: Comparison of the distribution law of Furry and the Poisson law for $\bar{n} = 5$ [244].

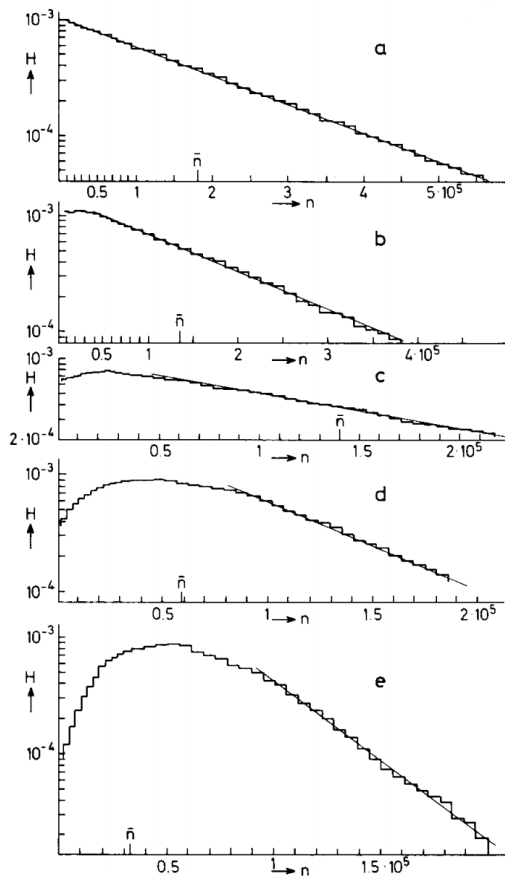


Figure 4.35: Single-electron avalanche size distribution in a proportionnal counter filled with methylal at different E/p values. (a) 70, (b) 76.5, (c) 105, (d) 186.5, (e) 426V/cm torr [245].

In this model, no extra energy is brought to the electrons in the showers, contrary to the case of a gaseous detector such as a RPC where an electric field accelerates them. Using the Furry model, Genz studied the fluctuations in electron avalanches in gaseous detectors [245]. Collisions leading to ionizations leave electrons with an energy much smaller than the ionization energy eU_i , where U_i is the ionization potential of a gas molecule. Hence, the electrons need to travel a distance $s = U_i/E$ along the electric field E to acquire a high enough energy to trigger a new ionization. For the probability of a new ionization to be independent from the path followed by the electrons since the previous ionization, the mean free path $1/\alpha$ of electrons in the gas has to be large compared to s and thus $E/\alpha \gg U_i$. The Townsend coefficient is related to the gas pressure leading to conditions on the value of E/p . Avalanches in gas are large compared to the showers Furry has studied in his original paper. For very large avalanche sizes, Equation 4.12 can be written as an exponential, as showed in Equation 4.13.

$$(4.13) \quad P(n, \bar{n}) = \bar{n}^{-1} e^{-n/\bar{n}}$$

This exponential behaviour is showed through Figure 4.35. In practice, to fully understand the avalanche growth, taking into account the path followed by electrons from one ionization to another

will become necessary. In the same paper, Genz then discusses models using Polya distributions to estimate the multiplication by looking at the size of the avalanche it self. Indeed, the number of charge carriers in the avalanche might become important enough to have an effect on the multiplication process. To account for this, it was proposed to use a varying Townsend coefficient such as described by Equation 4.14 depending on the position x in which θ is an empirical parameter leading to the probability distribution of Equation 4.15. In the limit case where θ goes to 0, the formula describes again the Furry model. But the data deviates from this model as well at large n values. Moreover, the introduction of an empirical parameters makes the model hard to interpret physically.

$$(4.14) \quad \alpha(n, x) = \alpha(x) \left(1 + \frac{\theta}{n}\right), \quad n > 0$$

$$(4.15) \quad P(n, x) = \frac{1 + \theta}{\bar{n}} \frac{1}{\theta!} \left(\frac{n(1 + \theta)}{\bar{n}}\right)^{\theta} e^{-\frac{n(1 + \theta)}{\bar{n}}}$$

In order to have a model that describes reality better, the introduction of the attachment into the model is an important step. Despite its limitations, the Furry model had the advantage to describe well avalanches occurring when the attachment could be ignored. This is only natural that this model was then extended to included attachment. This was done by Riegler, Lippmann and Veenhof [241] which showed that what was important was to consider both the Townsend coefficient describing the multiplication *and* the attachment coefficient, not only the effective multiplication coefficient $\bar{\alpha} = \alpha - \eta$. The probability to see an avalanche started by a single electron grow to a size n after having traveled a distance z through the gas is given by Equation 4.16.

$$(4.16) \quad \begin{aligned} P(n, z) = & P(n - 1, z) (n - 1)\alpha dz (1 - (n - 1)\eta dz) \\ & + P(n, z) (1 - n\alpha dz) (1 - n\eta dz) \\ & + P(n, z) n\alpha dz n\eta dz \\ & + P(n + 1, z) (1 - (n + 1)\alpha dz) (n + 1)\eta dz \end{aligned}$$

The first term of this probability that from a state with $n - 1$ electrons, only 1 multiplies while the others don't get attached. Both the second and third terms describes the probability that from a state with already n electrons the total number of electrons stay the same. On the second term, no electron gets attached nor multiplies while on the third term, 1 electron gets multiplied and 1 gets attached to compensate. Finally, the fourth term describes the probability to fall from a state with $n + 1$ to a state with n electrons due to the attachment of a single electron. At the first order, the evaluation of the previous expression leads to Equation 4.17 which general solution is given in Equation 4.18 in which are introduced the variables $\bar{n}(z)$, defined as in Equation 4.11, and $k = \eta/\alpha$ making explicit the fact that the distribution not only depends on the effective Townsend coefficient.

$$(4.17) \quad \frac{dP(n, z)}{dz} = -P(n, z)n(\alpha + \eta) + P(n - 1, z)(n - 1)\alpha + P(n + 1, z)(n + 1)\eta$$

$$(4.18) \quad P(n, z) = \begin{cases} k^{\frac{\bar{n}(z)-1}{\bar{n}(z)-k}}, & n = 0 \\ \bar{n}(z) \left(\frac{1-k}{\bar{n}(z)-k}\right)^2 \left(\frac{\bar{n}(z)-1}{\bar{n}(z)-k}\right)^{n-1}, & n > 0 \end{cases}$$

The example given through Figure 4.36 shows the importance of each individual process in the growth of avalanches and the fluctuation of their size. The values of α and η will influence the probability distribution, as can be seen from Figure 4.36a. Then, Figure 4.36b shows that the fluctuation really takes place within the very first interactions. Indeed, when the avalanche contains a large enough amount of charge carriers (a few hundreds), its size then increases like $e^{z(\alpha-\eta)}$.

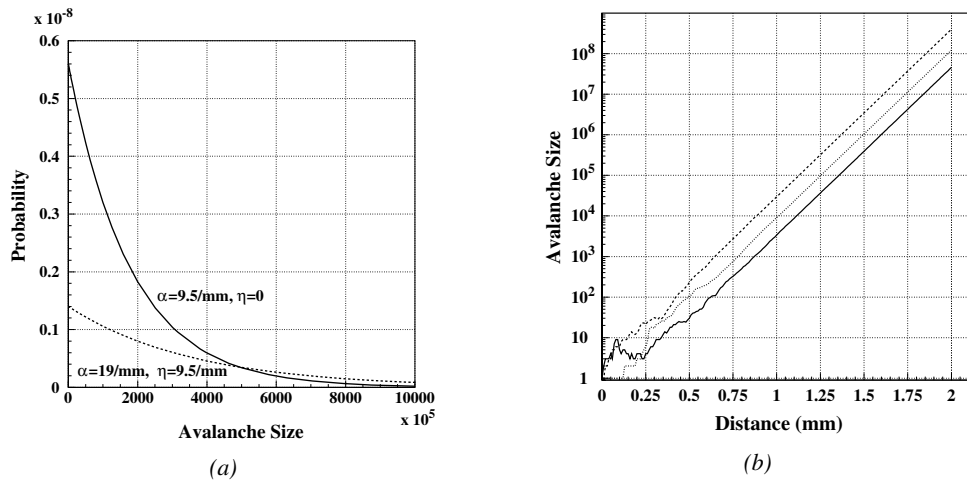


Figure 4.36: Figure 4.36a: Comparison of avalanche size distributions for different values of Townsend and attachment coefficients. The effective Townsend coefficient is the same for both distributions. Figure 4.36b: Fluctuation in avalanche size for avalanche started by a single electron with $\alpha = 13 \text{ mm}^{-1}$ and $\eta = 3.5 \text{ mm}^{-1}$ [241].

4.3.4 Drift and diffusion of the electron cloud

During the growth of avalanches, an electron cloud drifting along the electric field through the gas will undergo thermal diffusion due to random collisions with the gas molecules. This phenomenon can be studied using Maxwell-Boltzmann distribution whose mean is defined by the thermal energy of the cloud $\langle E \rangle = 3/2kT$ with an extra component coming from the constant drift motion. The drift of electrons along the field lines is usually observed on a macroscopic scale through which the speed can be assimilated to a constant v_D which corresponds to the mean drift speed over a large number of collisions in the gas.

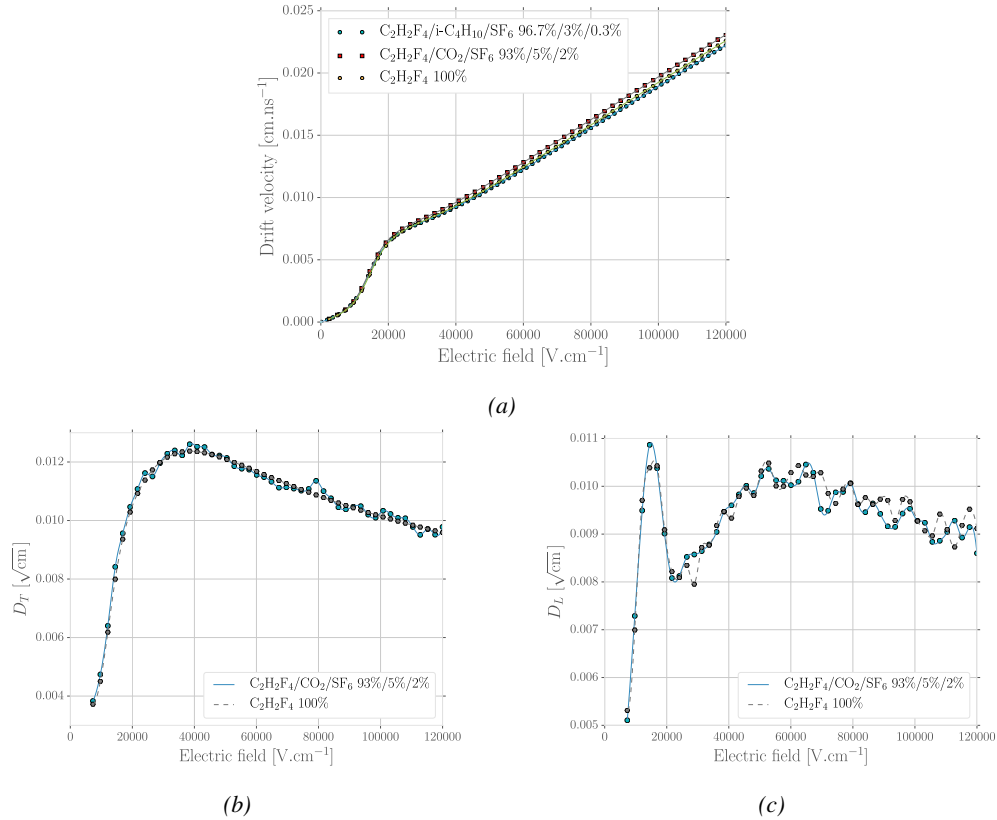


Figure 4.37: Figure 4.37a: Electron mean drift velocity v_D in pure C₂H₂F₄ and typical RPC gas mixtures. Figure 4.37b: Transverse diffusion coefficient in pure C₂H₂F₄ and a typical RPC gas mixture. Figure 4.37c: Longitudinal diffusion coefficient in pure C₂H₂F₄ and a typical RPC gas mixture. All results are given with a pressure $P = 760$ Torr and a temperature $T = 296.15$ K [232].

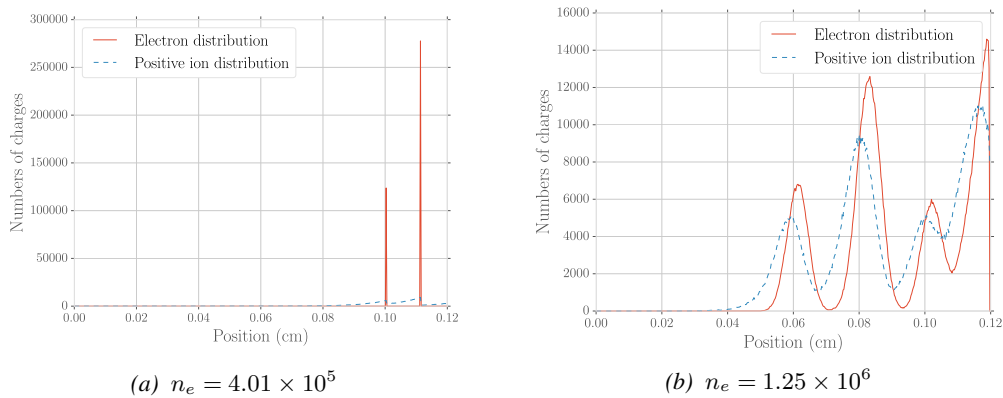


Figure 4.38: Comparison of the free charge carriers in the gas after a time $t = 7.90$ ns in the case where no diffusion is taken into account to simulate the avalanche (Figure 4.38a) and in the case where the diffusion is implemented (Figure 4.38b) [232].

Indeed, at the microscopic scale, the electrons are drifting over a distance δz while acquiring the corresponding kinetic energy $T = e_0 |\vec{E}| \delta z$ until they are slowed down by a collision in which they lose part of their energy. This process is repeated as long as electrons are free carriers. Starting from a point-like electron cloud, the Gaussian density distribution at \vec{r}_0 will be described by Formula 4.19 in which the width of the isotropic distribution is $\sigma = 2\bar{D}t$, with \bar{D} being a diffusion coefficient expressed in m^2/s [214].

$$(4.19) \quad \varphi(\vec{r}, t) = \frac{1}{(\sqrt{2\pi}\sigma(t))^3} \exp\left(-\frac{(\vec{r} - \vec{r}_0)^2}{2\sigma^2(t)}\right)$$

Now, if the constant drifting motion is added, the distribution is anisotropic and can be divided onto transversal (Formula 4.20) and longitudinal (Formula 4.21) terms, $\varphi(r, z, t) = \varphi_T(r, t)\varphi_L(z, t)$, with a cylindrical symmetry around the field axis [214]. The variables t and $\sigma_{T,L}(t)$ can be hidden to the profit of the diffusion coefficients by using the relations $v_D = l/t$ and $\sigma_{T,L}^2(t) = 2\bar{D}_{T,L}l/v_D$ and introducing new diffusion coefficients $D_{T,L} = \sqrt{2\bar{D}_{T,L}/v_D}$ in order to explicitly show the dependence of the Gaussian width in drifted distance l .

$$(4.20) \quad \varphi_T(r, t) = \frac{1}{D_T^2 l} \exp\left(-\frac{(r - r_0)^2}{2D_T^2 l}\right)$$

$$(4.21) \quad \varphi_L(z, t) = \frac{1}{\sqrt{2\pi l} D_L} \exp\left(-\frac{(z - z_0)^2}{2D_L^2 l}\right)$$

These coefficients, as well as the drift velocity of the electrons, can be calculated thanks to Magboltz as showed in Figure 4.37. The influence of the diffusion on the distribution of charge carriers throughout the gas volume is depicted in Figure 4.38. From very localised electron clusters in the gas in Figure 4.38a, a Gaussian diffusion is then visible in Figure 4.38b. Due to the interactions with gas molecules during the drift, diffusions can occur in the forward and backward direction. Electrons diffused backward will effectively drift over a longer distance and multiply more than electrons diffused forward that will see a shorter drift length. As an effect, the avalanche develops over a longer time and extends over a greater gas volume than in the case the electron cloud is considered as point like and without diffusion. Moreover, as a side effect to the longer growth of the avalanche due to backward longitudinal diffusion, the total production of electrons is increased.

4.3.5 Space charge effect & streamers

Now that have been considered the basic processes that influence the development of avalanches in a gaseous detector in the previous sections, it is now important to consider the influence of the charge carriers present in the avalanche on the electric field seen by the avalanche. Indeed, each charged particle induces an electric field and it is only natural that the increasing density of electrons and ions in the detector volume will affect the electric field. Thus, parameters such as the Townsend and attachment coefficients, drift velocity or diffusion coefficients will find themselves to be modified along the gas gap length due to this effect referred to as *space charge effect*. Figure 4.39 is a more detailed version of Figure 4.1 (b) in which three electric regions are distinguished [214]. When compared to the linear electric field of strength E_0 that is developed in between the detector's electrodes, the

2576 accumulation of negative charges (electrons) on the front of the avalanche will reinforce the effective
 2577 electric field in between the anode of the avalanche front. Deeper in the gas volume, the positive
 2578 charges (cations) slowly drift towards the cathode and can induce together with the avalanche front
 2579 opposite electric field loops. Finally, due to the density of positive charges, the electric field seen in
 2580 between the ions tails and the cathode charged with negative charges is on average stronger than E_0
 2581 and compensate for the locally reversed field E_2 . Lippmann roughly estimated by considering that
 2582 10^6 charges were contained in a sphere of radius $r_d = 0.1$ mm that the space charge effect could
 2583 change the electric field by 3% and the Townsend and attachment coefficient up to 14% [214, 232].

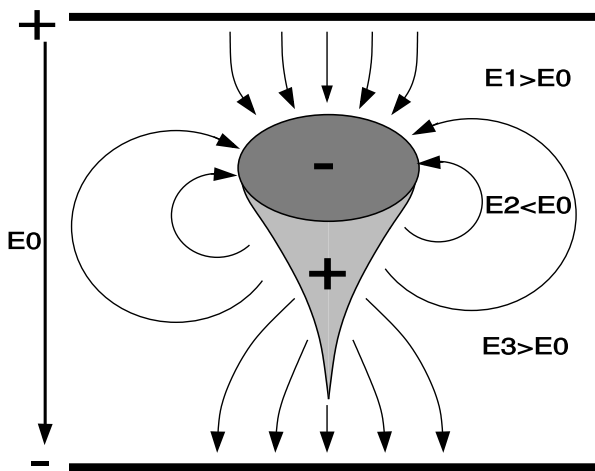


Figure 4.39: Schematic representation of an avalanche and of the electric field deformation it causes due to the local concentration of charge carriers [214].

2584 To account for the space charge effect, the electric potential and field of free charges are solved
 2585 and applied to each charges in the avalanche [214, 232]. As discussed by Français who has been
 2586 working on simulating RPCs similar to that used by the SDHCAL project of ILC, the computation
 2587 of these equations for each individual charge carrier to dynamically know the space charge field at
 2588 every stage of an avalanche development is a difficult task and would require far too much computa-
 2589 tion time and a solution is to pre-compute an interpolation table keeping an adequately large number
 2590 of values of the space charge field for each positions in space thanks to which the values stored in the
 2591 interpolation table become very close to the analytic solution and allow for a much faster simulation.
 2592

2593 The study of space charge effect through simulation shows that it can lead to a saturation of
 2594 the avalanche growth due to the deformation of the electric field, as showed through Figure 4.40.
 2595 Additionnally, a more precise understanding of the space charge effect is given through Figure 4.41
 2596 which looks at the distribution of charges and the distortion of the electric field at different steps of
 2597 the evolution of an avalanche in a RPC. At the moment a 5 GeV muon ionizes the gas, electron-ion
 2598 pairs are created in the gas in different clusters (Figure 4.41a). Later, the first clusters have reached
 2599 the anode while the clusters that where created the closest to the cathode are now big enough to start
 2600 influencing the electric field in the gap (Figure 4.41b). When a cluster is big enough, the electric field
 2601 in front of it locally increases a lot and contributes to a stronger but very localised multiplication. At
 2602 the same moment, the positive ions right behind the cluster avalanche front decrease the electric field,
 2603 saturating the electron multiplication on the tail of the electron cloud (Figure 4.41c). Finally, when

2604 all the electrons have reached the anode and are relaxing, the electric field still is very deformed
 2605 by the distribution of both positive and negative ions in the the gas volume closest to the anode
 2606 (Figure 4.41d).

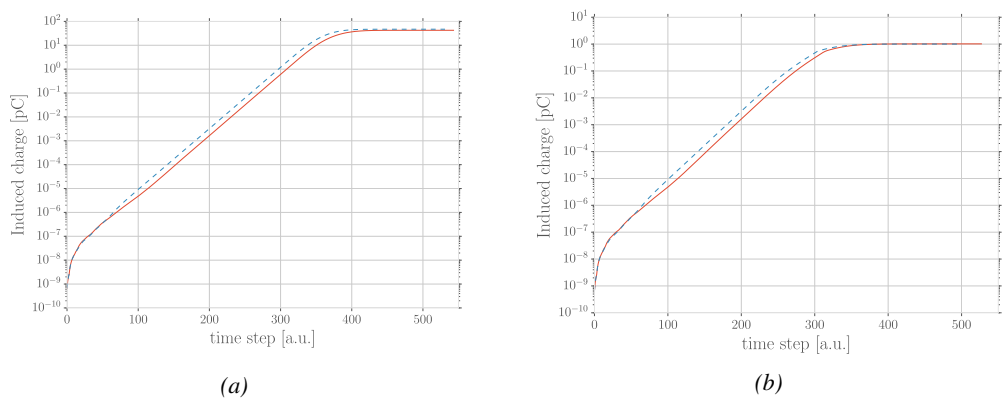


Figure 4.40: Evolution of the charge induced by an avalanche started by a single electron in a 1.2 mm thick RPC with an applied electric field of 54 kV/cm in the case space charge is not taken into account (Figure 4.40a) and in the case it is implemented into the simulation (Figure 4.40b). The total induced charge is correlated to the size of the avalanche [232].

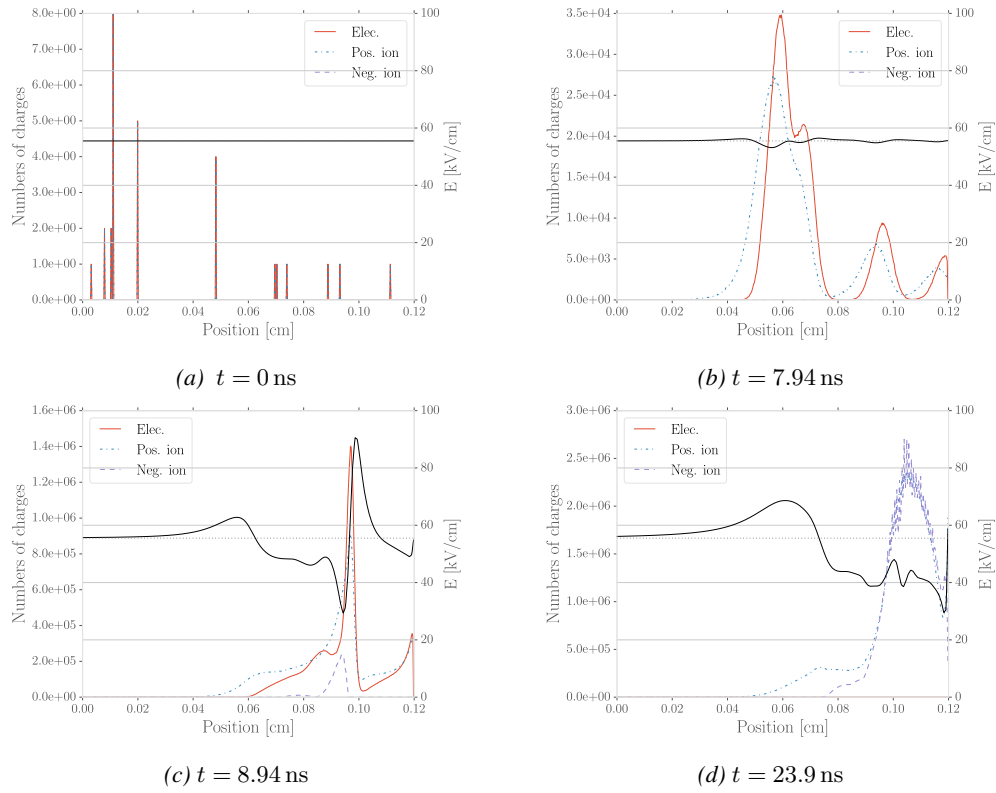


Figure 4.41: Distributions of charge carriers within the gas volume of a 1.2 mm thick RPC and the corresponding deformation of the electric field at different time steps with an applied electric field of 55.5 kV/cm [232].

2607 The electric field following the development of an avalanche can stay perturbed for a long time
 2608 with respect to the avalanche development due to the slow drift of the much heavier ions. This can
 2609 result in powerful secondary avalanches triggered by the fluctuation of the electric field together with
 2610 the emission of UV-photons leading to emission of electrons at the surface of the electrode. This is
 2611 a slow phenomenon compared to the development of avalanches. Experimentally, it is observed that
 2612 the stronger the electric field applied over the gap, the sooner after the avalanche, referred to as *pre-*
 2613 *cursor signal* in this context, and the stronger will the secondary avalanche be, possibly reaching the
 2614 streamer regime. This could be due to the amount of UV-photons emitted by the growing precursor.
 2615 These photons will be able to trigger new avalanches in a radius of a few mm around the precursor
 2616 by knocking electrons from the cathode by photoelectric effect. The strong distortions of the electric
 2617 field due to a large avalanche will be more likely to emit UV-photons as the electric field at the front
 2618 of the precursor avalanche will be large, providing the electrons with a larger energy. Eventually, the
 2619 new avalanches can grow to form streamers.

2620 4.4 Effect of atmospherical conditions on the detector's performance

2621

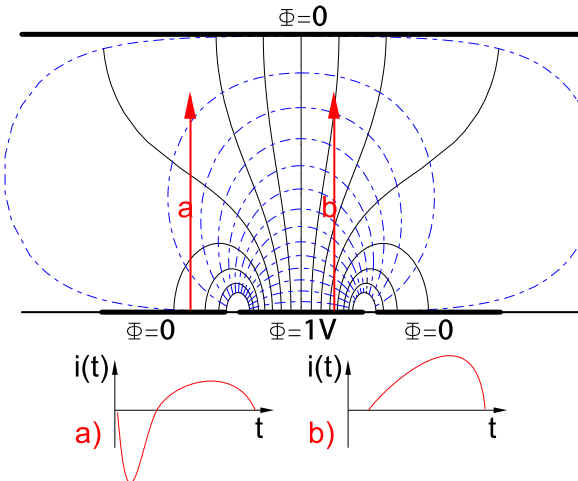


Figure 4.42: Representation of the weighting field in the volume of a RPC and the resulting induced current in the strip placed at 1 V and its neighbour connected to the ground. The induced current corresponds, as can be understood from Formula 4.22 [214].

2622 Accordingly to Ramo's theorem, the movement of charge carriers, and in particular, the movement
 2623 of a dense electron cloud toward the anode induces a current signal on one or more of the readout
 2624 electrodes (strips or pads). The ions on the other hand induce only a very small current as their
 2625 movement is much slower than which of the electrons. The current induced by n_{Cl} clusters of $N_j(t)$
 2626 charge carriers drifting at velocities $\vec{v}_{Dj}(t) = \vec{x}_j(t)$ at a time t is given by Formula 4.22 in which e_0
 2627 is the unit charge and \vec{E}_w is the weighting field.

$$(4.22) \quad i(t) = \sum_{j=1}^{n_{Cl}} \vec{E}_{wj}(\vec{x}_j(t)) \cdot \vec{v}_{Dj}(t) e_0 N_j(t)$$

2628 The weighting field, that has been schematised in Figure 4.42, corresponds to the electric field
 2629 that would be observed in the gas gap if a readout electrode is placed at a potential of 1 V while
 2630 keeping all the other electrodes grounded. Then the induced charge in the readout can be simply
 2631 obtained by integrating Formula 4.22 over the duration T of the signal, as given by Formula 4.23.

$$(4.23) \quad Q(t) = \int_0^T \sum_{j=1}^{n_{Cl}} \vec{E}_{wj}(\vec{x}_j(t)) \cdot \vec{v}_{Dj}(t) e_0 N_j(t)$$

2632 The signal induced in the readout of RPCs operated in avalanche mode is then sent into Front-
 2633 End Electronics in which they will be pre-amplified and discriminated. The discrimination and
 2634 digitization of signals in CMS FEE is described through Figure 4.43. On a first stage, analogic sig-
 2635 nals are amplified, following the curve given on Figure 4.44, and then sent to the Constant Fraction

Discriminator (CFD) described in Figure 4.45. At the end of the chain, 100 ns long pulses are sent in the LVDS output. The digital signals are both used as trigger for CMS and to evaluate the performance of the detectors. The performance will depend on the applied HV, i.e. on the electric field inside of the gas volume, but also on the threshold applied on the CFDs. Indeed, in order to reduce the probability to measure noise, the threshold is set to a level where the noise is strongly suppressed while the signals are not too affected. Typically, CMS FEEs are set to a threshold of 215 mV after pre-amplification, corresponding to an input charge of about 140 fC.

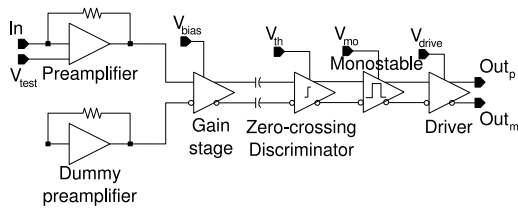


Figure 4.43: Schematics of CMS RPC FEE logic.

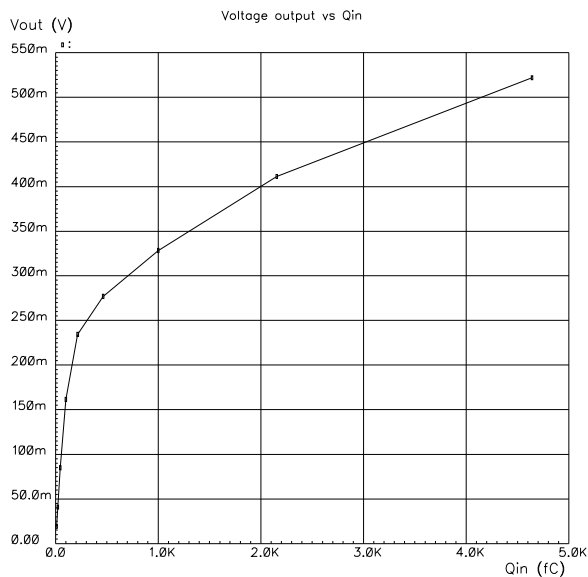


Figure 4.44: Equivalence in between the charge of the induced signal in input of the CMS FEE and the signal strength on the output of the pre-amplifier.

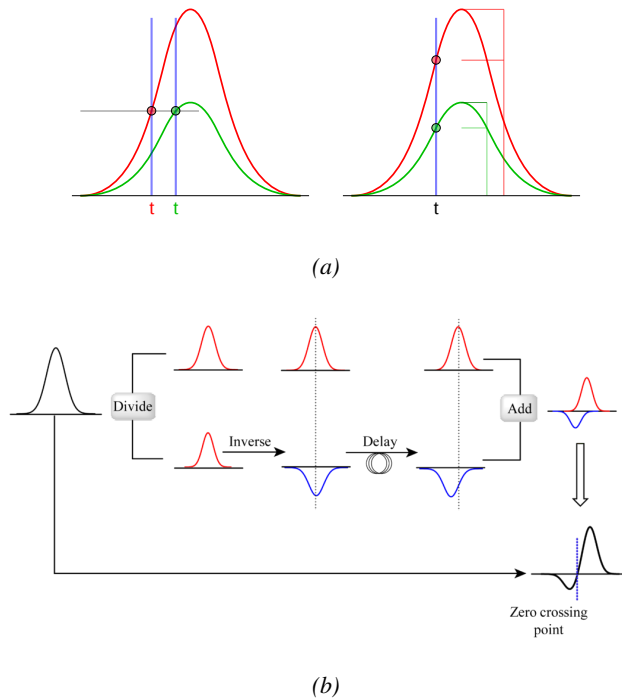


Figure 4.45: Description of the principle of a CFD. A comparison of threshold triggering (left) and constant fraction triggering (right) is shown in Figure 4.45a. Constant fraction triggering is obtained thanks to zero-crossing technique as explained in Figure 4.45b. The signal arriving at the input of the CFD is split into three components. A first one is delayed and connected to the inverting input of a first comparator. A second component is connected to the noninverting input of this first comparator. A third component is connected to the noninverting input of another comparator along with a threshold value connected to the inverting input. Finally, the output of both comparators is fed through an AND gate.

The performance of a detector is then simply measured relatively to which of a reference detector used as trigger as the ratio in between the number of events recorded in coincidence in the detector and the reference and the total amount of trigger events, $\epsilon = n_{events}/n_{triggers}$. An example of efficiency measured as a function of the effective voltage HV_{eff} is given in Figure 4.46 and can be fitted thanks to a sigmoidal function described as in Formula 4.24 and where ϵ_{max} is the maximal efficiency of the detector, λ is proportional to the slope at half maximum and HV_{50} is the value of the voltage when the efficiency reaches half of the maximum.

$$(4.24) \quad \epsilon(HV_{eff}) = \frac{\epsilon_{max}}{1 + e^{-\lambda(HV_{eff} - HV_{50})}}$$

CMS RPC also define two points on this sigmoid that called *knee* and *working point*. The corresponding voltages HV_{knee} is defined as the voltage at 95% of the maximum efficiency, and HV_{WP} is defined as in Formula 4.25.

$$(4.25) \quad HV_{WP} = HV_{knee} + \begin{cases} 100V & (\text{barrel}) \\ 150V & (\text{endcap}) \end{cases}$$

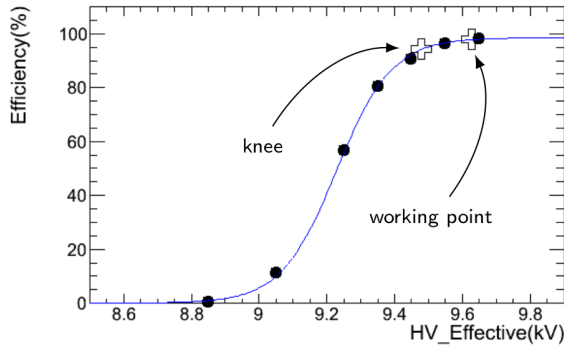


Figure 4.46: Typical efficiency sigmoid of a CMS RPC detector. The black dots correspond to the data, the blue line to the sigmoid fit and the opened cross to the knee and working extracted from the fit line.

Nevertheless, the voltage applied on a detector may vary due to a change in environmental conditions. Indeed, the variation of temperature and/or pressure will have effects on the gas density and the electrodes' resistivity which can be overcome by changing the electric field accordingly. The variation in temperature and pressure are depicted respectively in Figure 4.47 and Figure 4.48. A standard procedure to correct for temperature and pressure variations is to keep the factor $HV \cdot T/P$ constant using Formula 4.26 [246, 247] with reference values for T_0 and P_0 . For example, CMS uses $T_0 = 293.15$ K and $P_0 = 965$ hPa.

$$(4.26) \quad HV_{app} = HV_{eff} \frac{P_0}{P} \frac{T}{T_0}$$

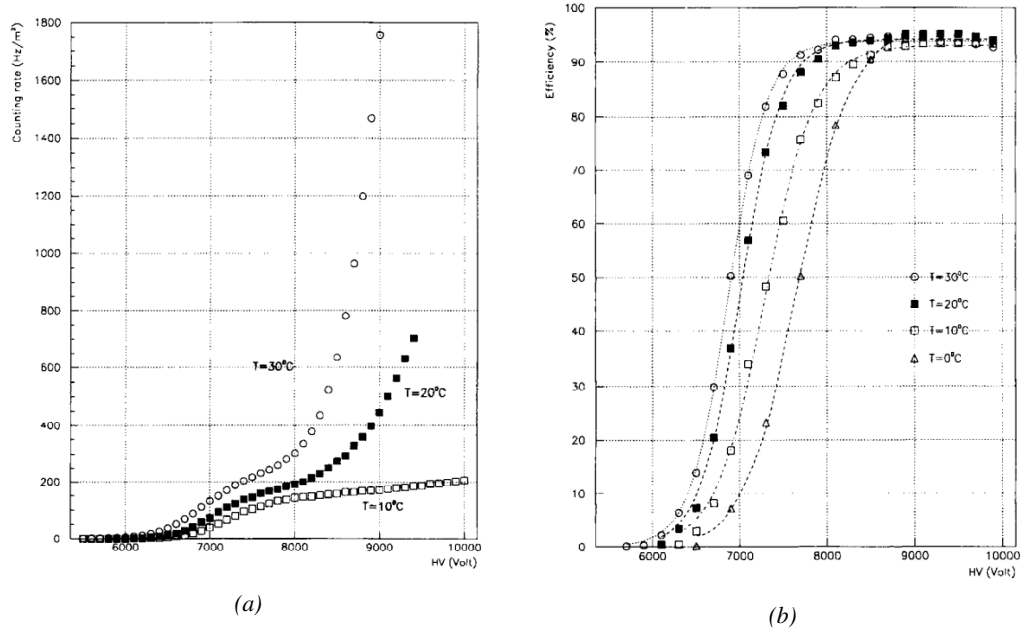


Figure 4.47: Effect of the temperature variation on the rate (Figure 4.47a) and the efficiency (Figure 4.47b) of a RPC [246].

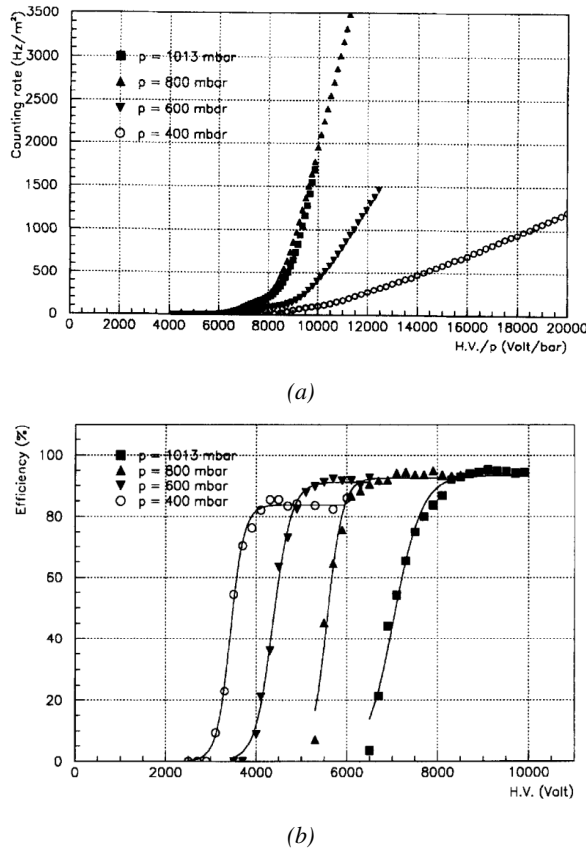


Figure 4.48: Effect of the pressure variation on the rate (Figure 4.48a) and the efficiency (Figure 4.48b) of a RPC [247].

It was actually found that such a simple procedure would overcorrect the applied voltage in the case the variations of temperature or pressure were too important [248–251]. CMS, considering that the temperature variations in the detector cavern were very small, decided only to improve the pressure correction, giving rise to Formula 4.27 [248] while on the other hand, ATLAS decided to have a more robust correction for both parameters and uses Formula 4.28 instead [251]. The coefficients α , in the case of CMS, and α, β , in the case of ATLAS, are extracted from fit on available dataset obtained during the operation of the detectors.

$$(4.27) \quad HV_{app} = HV_{eff} \left(1 - \alpha + \alpha \frac{P_0}{P} \right) \frac{T}{T_0}, \quad \alpha = 0.8$$

$$(4.28) \quad HV_{eff} = HV_{app} \left(1 + \alpha \frac{\Delta T}{T_0} \right) \left(1 - \beta \frac{\Delta P}{P_0} \right), \quad \alpha = 0.5, \beta = 0.71$$

5

2667

2668

2669

Longevity studies and Consolidation of the present CMS RPC subsystem

2670 The RPC system, located in both barrel and endcap regions, provides a fast, independent muon trigger
2671 with a looser p_T threshold over a large portion of the pseudo-rapidity range ($|\eta| < 1.6$). During
2672 HL-LHC operations the expected conditions in terms of background and pile-up will make the iden-
2673 tification and correct p_T assignment a challenge for the muon system. The goal of RPC upgrade is to
2674 provide additional hits to the Muon System with more precise timing. All this information will be
2675 elaborated by the Trigger System in a global way enhancing the performance of the trigger in terms
2676 of efficiency and rate control. The RPC Upgrade is based on two projects: an improved Link Board
2677 System and the extension of the RPC coverage up to $|\eta| = 2.4$.

2678 The Link Board System is responsible for the processing, the synchronization and the zero-
2679 suppression the signals coming from the RPC FEBs. The Link Board components have been pro-
2680 duced between 2006 and 2007 and will be subjected to ageing and failure on a long term scale. An
2681 upgraded Link Board System will overcome the ageing problems and will allow for a more precise
2682 timing information to the RPC hits from 25 to 1.5 ns.

2683 In order to develop an improved RPC that fulfills CMS requirements, an extensive R&D program is
2684 being conducted. The benefits of adding two new RPC layers in the innermost ring of stations 3 and
2685 4 will be mainly observed in the neutron-induced background reduction and efficiency improvement
2686 for both trigger and offline reconstruction.

2687 The coverage of the RPC System up to higher pseudo-rapidity $|\eta| = 2.1$ was part of the original
2688 CMS TDR. Nevertheless, the expected background rates being higher than the certified rate capabili-
2689 ty of the present CMS RPCs in that region and the budget being limited, RPCs were restricted to a
2690 shorter range. Even though the iRPC technology that will equip the extension of the Muon System
2691 will be different than the current CMS RPC technology, it is necessary to certify the rate capability
2692 and longevity of the existing detectors as the radiation level will increase together with the increase
2693 of instantaneous luminosity of the LHC. For this purpose, spare RPC detectors built but not installed
2694 in CMS have been installed in different irradiation facilities, first of all, to certify the detectors to the

new levels of irradiation they will be subjected to and, finally, to study their ageing and certify their good operation throughout the HL-LHC program.

5.1 Testing detectors under extreme conditions

The upgrade from LHC to HL-LHC will increase the peak luminosity from $10^{34} \text{ cm}^{-2} \text{ s}^{-1}$ to reach $5 \times 10^{34} \text{ cm}^{-2} \text{ s}^{-1}$, increasing in the same way the total expected background to which the RPC System will be subjected to. Mainly composed of low energy gammas, neutrons, and electrons and positrons from p - p collisions, but also of low momentum primary and secondary muons, punch-through hadrons from calorimeters, and particles produced in the interaction of the beams with collimators, the background will mostly affect the regions of CMS that are the closest to the beam line, i.e. the RPC detectors located in the endcaps.

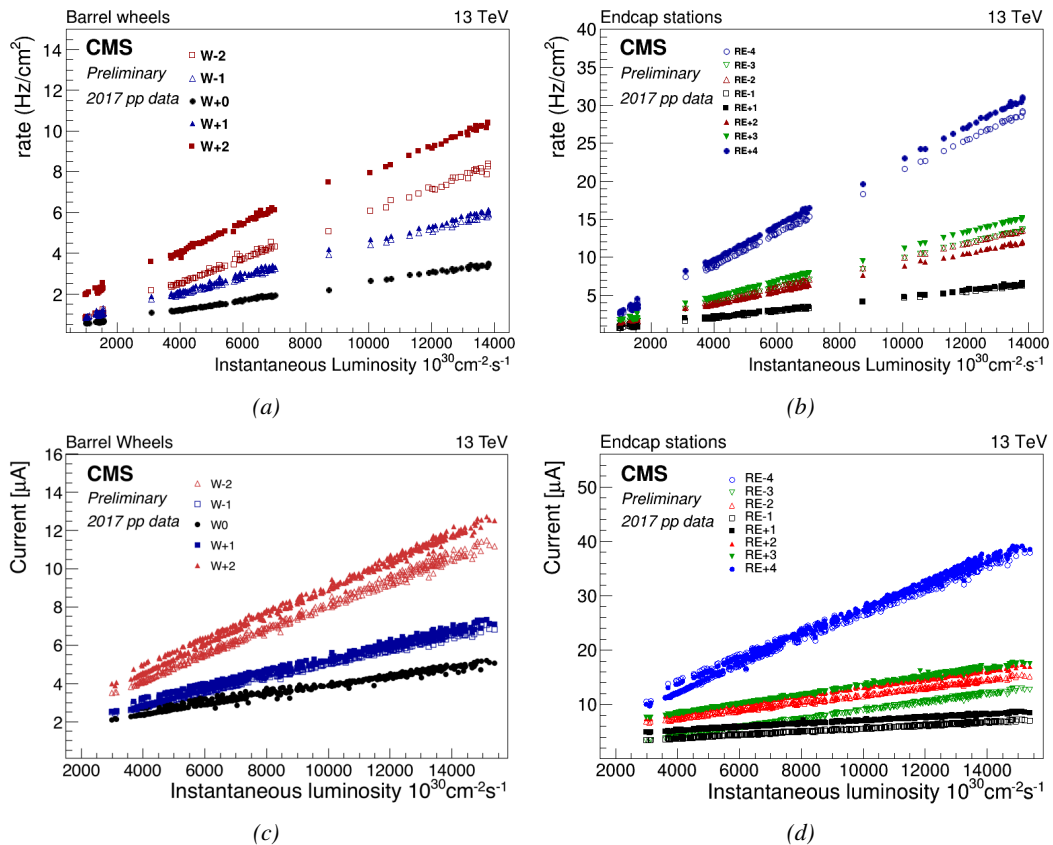


Figure 5.1: Mean RPC Barrel (left column) and Endcap (right column) rate (top row) and current (bottom row) as a function of the instantaneous luminosity as measured in 2017 p - p collision data.

Data collected over 2017, presented through Figure 5.1, allows to study the values of the background rate in all the RPC System. This was achieved thanks to a monitoring of the rates in each RPC rolls, where rolls correspond to the pseudo-rapidity partitioning of the readout electronics, and of the current in each HV channel. A linear dependence is between the mean rate or current with

instantaneous luminosity is showed in selected runs with identical LHC running parameters. In Figure 5.2, a linear extrapolation of the distribution of the background hit rate per unit area as well as the integrated charge is showed at a HL-LHC condition. The maximum rate per unit area in the endcap detectors at HL-LHC conditions is expected to be of the order of 600 Hz/cm^2 while the charge deposition should exceed 800 mC/cm^2 . The detectors will then be certified up to an irradiation of 840 mC/cm^2 . These extrapolations are provided with a required safety factor 3 for the certification study.

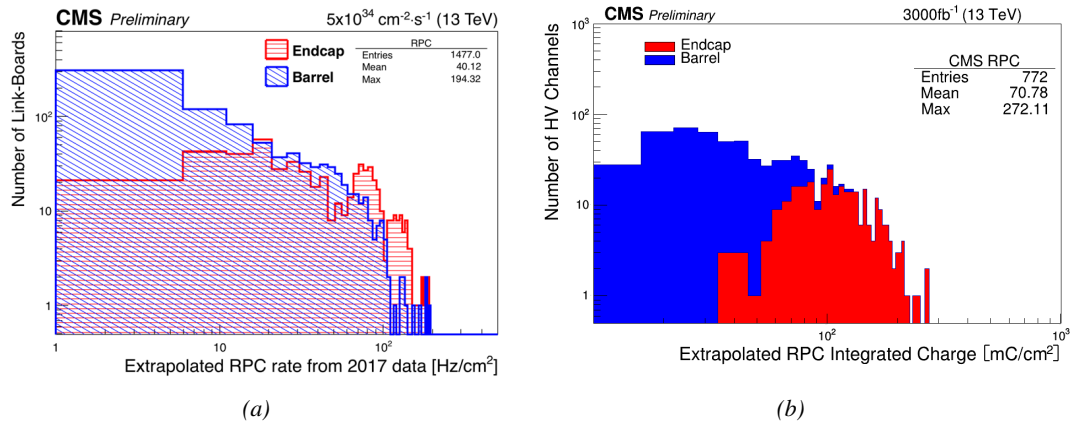


Figure 5.2: Figure 5.2a: The hit rate per region (Barrel, Endcap) is linearly extrapolated to HL-LHC highest instantaneous luminosity ($5 \times 10^{34} \text{ cm}^{-2} \text{ s}^{-1}$) using the rate as a function of instantaneous luminosity recorded by RPCs in 2017 showing a linear dependence. Figure 5.2b: The integrated charge per region (Barrel, Endcap) is extrapolated to HL-LHC integrated luminosity (3000 fb^{-1}) using the data accumulated in 2016 in every HV channels.

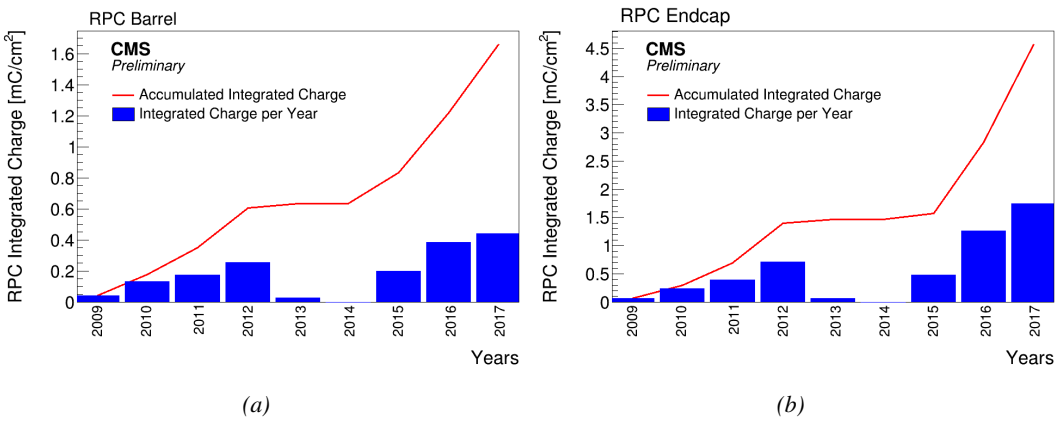


Figure 5.3: CMS RPC mean integrated charge in the Barrel region (Figure 5.3a) and the Endcap region (Figure 5.3b). The integrated charge per year is shown in blue. The red curve shows the evolution of the accumulated integrated charge through time. The blank period in 2013 and 2014 corresponds to LS1. The total integrated charge for the entire operation period (Oct.2009 - Dec.2017) is estimated to be about 1.66 mC/cm^2 in the Barrel and 4.58 mC/cm^2 in the Endcap.

In the past, extensive long-term tests were carried out at several gamma and neutron facilities

certifying the detector performance. Both full size and small prototype RPCs have been irradiated with photons up to an integrated charge of $\sim 0.05 \text{ C/cm}^2$ and $\sim 0.4 \text{ C/cm}^2$ respectively and were certified for rates reaching 200 Hz/cm^2 [252, 253]. Since the beginning of Run-I until December 2017, the RPC system provided stable operation and excellent performance and did not show any ageing effects for a maximum integrated charge in a detector of the order of 0.01 C/cm^2 - the average being of the order of 2 mC/cm^2 in the Barrel and 5 mC/cm^2 in the Endcap, closer to the beam line, as can be seen from Figure 5.3 - and a peak luminosity reaching $1.4 \times 10^{34} \text{ cm}^{-2} \text{ s}^{-1}$ during 2017 data taking period.

To perform the necessary studies on the present CMS RPC detectors, facilities offering the possibility to irradiate the chambers are necessary in order to recreate HL-LHC conditions or stronger and study their performance through time. Such facilities exist at CERN and were exploited to conduct this study. A first series of preliminary studies were conducted in the former gamma facility of CERN (GIF) before its dismantlement. This preliminary study was used as a stepping stone towards the building of a more powerful irradiation fully dedicated to longevity studies of CMS and ATLAS subsystems in the perspective of HL-LHC. The period of preliminary work has also been a key moment in the elaboration and improvement of data acquisition, offline analysis and online monitoring tools that are extensively used in the new gamma irradiation facility.

5.1.1 GIF

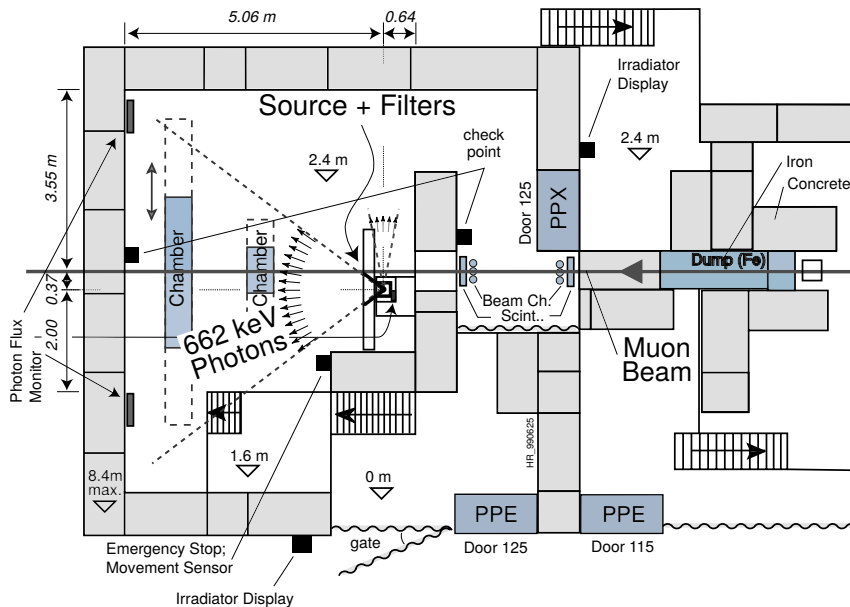


Figure 5.4: Layout of the test beam zone called X5c GIF at CERN. Photons from the radioactive source produce a sustained high rate of random hits over the whole area. The zone is surrounded by 8 m high and 80 cm thick concrete walls. Access is possible through three entry points. Two access doors for personnel and one large gate for material. A crane allows installation of heavy equipment in the area.

Located in the SPS West Area at the downstream end of the X5 test beam, the Gamma Irradiation Facility (GIF) was a test area in which particle detectors were exposed to a particle beam in presence of an adjustable gamma background [254]. Its goal was to reproduce background conditions these

detectors would suffer in their operating environment at LHC. GIF layout is showed in Figure 5.4. Gamma photons are produced by a strong ^{137}Cs source installed in the upstream part of the zone inside a lead container. The source container includes a collimator, designed to irradiate a $6 \times 6 \text{ m}^2$ area at 5 m maximum to the source. A thin lens-shaped lead filter helps providing with a uniform out-coming flux in a vertical plane, orthogonal to the beam direction. The photon rate is controlled by further lead filters allowing the maximum rate to be limited and to vary within a range of four orders of magnitude. Particle detectors under test are then placed within the pyramidal volume in front of the source, perpendicularly to the beam line in order to profit from the homogeneous photon flux. Adjusting the background flux of photons can then be done by using the filters and choosing the position of the detectors with respect to the source.

As described on Figure 5.5, the ^{137}Cs source emits a 662 keV photon in 85% of the decays. An activity of 740 GBq was measured on the 5th of March 1997. To estimate the strength of the flux in 2014, was considered the nuclear decay through time associated to the Cesium source whose half-life is well known ($t_{1/2} = (30.05 \pm 0.08) \text{ y}$). The GIF tests were done in between the 20th and the 31st of August 2014, i.e. at a time $t = (17.47 \pm 0.02) \text{ y}$ resulting in an attenuation of the activity from 740 GBq in 1997 to 494 GBq in 2014.

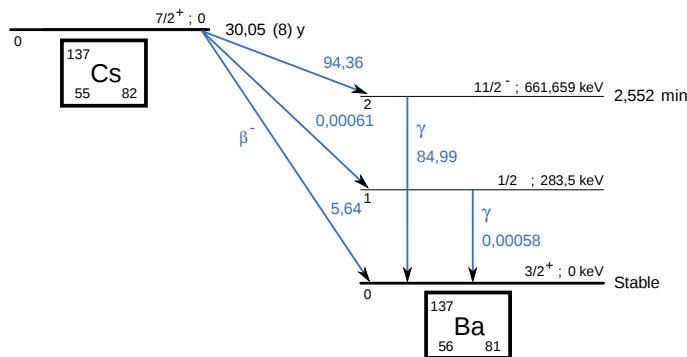


Figure 5.5: ^{137}Cs decays by β^- emission to the ground state of ^{137}Ba (BR = 5.64%) and via the 662 keV isomeric level of ^{137}Ba (BR = 94.36%) whose half-life is 2.55 min.

5.1.2 GIF++

The new Gamma Irradiation Facility (GIF++), located in the SPS North Area at the downstream end of the H4 test beam, has replaced its predecessor during LS1 and has been operational since spring 2015 [255]. Like GIF, GIF++ features a ^{137}Cs source of 662 keV gamma photons, their fluence being controlled with a set of filters of various attenuation factors. The source provides two separated large irradiation areas for testing several full-size muon detectors with homogeneous irradiation, as presented in Figure 5.6.

The source activity was measured to be about 13.5 TBq in March 2016. The photon flux being far greater than HL-LHC expectations, GIF++ provides an excellent facility for accelerated ageing tests of muon detectors. The source is situated in a bunker designed to perform irradiation test along a muon beam line, the muon beam being available during selected periods throughout the year. The H4 beam, providing the area with muons with a maximum momentum of about 150 GeV/c, passes through the GIF++ zone and is used to periodically study the performance of the detectors placed under long term irradiation. Its flux is of $104 \text{ particles/s/cm}^2$ focused in an area similar to

2768 $10 \times 10 \text{ cm}^2$. Therefore, with properly adjusted filters, one can simulate the background expected at
 2769 HL-LHC and study the performance and ageing of muon detectors in HL-LHC environment.

2770

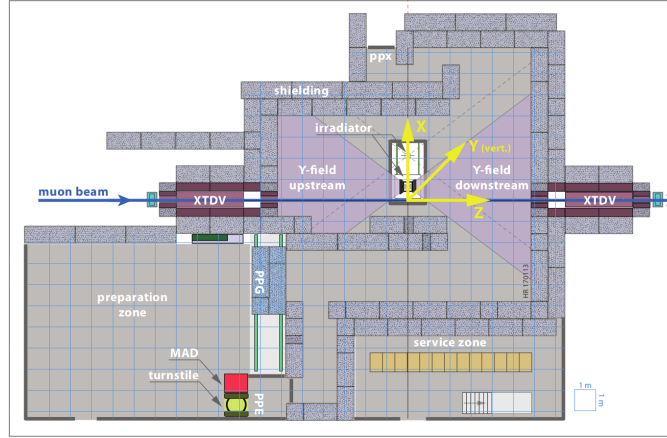


Figure 5.6: Floor plan of the *GIF++* facility. When the facility downstream of the *GIF++* takes electron beam, a beam pipe is installed along the beam line (z -axis). The irradiator can be displaced laterally (its center moves from $x = 0.65 \text{ m}$ to 2.15 m), to increase the distance to the beam pipe.

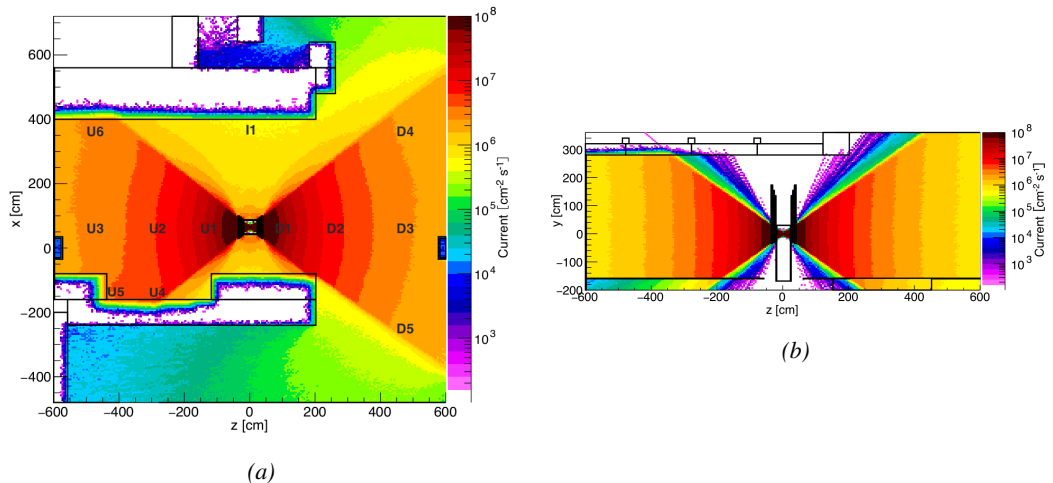


Figure 5.7: Simulated unattenuated current of photons in the xz plane (Figure 5.7a) and yz plane (Figure 5.7b) through the source at $x = 0.65 \text{ m}$ and $y = 0 \text{ m}$ [256]. With angular correction filters, the current of 662 keV photons is made uniform in xy planes.

2771 The gamma current as simulated with GEANT4 is presented in Figure 5.7 in which the labels
 2772 UN, DN, with $N \in [1 : 5]$ and I1 correspond to the position of different Radiation Monitoring
 2773 (RADMON) sensors dedicated to measuring the irradiation in the bunker area [256]. According to
 2774 the simulation results, that agree within 12% to the doses measured with the RADMONs, the RPCs
 2775 that will be tested in *GIF++* can expect a maximal gamma current of the order of 2 to 5×10^6

2776 $\text{cm}^{-2} \text{s}^{-1}$ assuming they will always stay in a region in between sensor U5 and the back wall of the
 2777 upstream area.

2778 5.2 Preliminary studies at GIF

2779 5.2.1 RPC test setup

2780 During summer 2014, preliminary tests have been conducted in the GIF area on an endcap chamber
 2781 of type RE4/2 and labeled RE-4-2-BARC-161 produced for the extension of the endcap with a
 2782 fourth disk in 2013. This chamber has been placed into a trolley covered with a tent. The position
 2783 of the RPC inside the tent and of the tent with respect to the source in the bunker are described in
 2784 Figure 5.8. The goal of the study were to have a preliminary understanding of the rate capability
 2785 of the present technology used in CMS. It was decided to measure the efficiency of the RPC under
 2786 irradiation at detecting cosmic muons as, at the time of the tests, the beam not operational anymore.
 2787 Three different absorber settings were used and compared to the case where the detector was not ir-
 2788 radated in order to study the evolution of the performance of the detector with increasing exposition
 2789 to gamma radiation. First of all, measurements were done with fully opened source. To complete
 2790 this preliminary study, the gamma flux has been attenuated by a factor 2, a factor 5 and finally the
 2791 source was shut down. Was measured the efficiency of the RPC at detecting the cosmic muons in
 2792 coincidence with a cosmic trigger as well as the background rate as seen by the detectors.

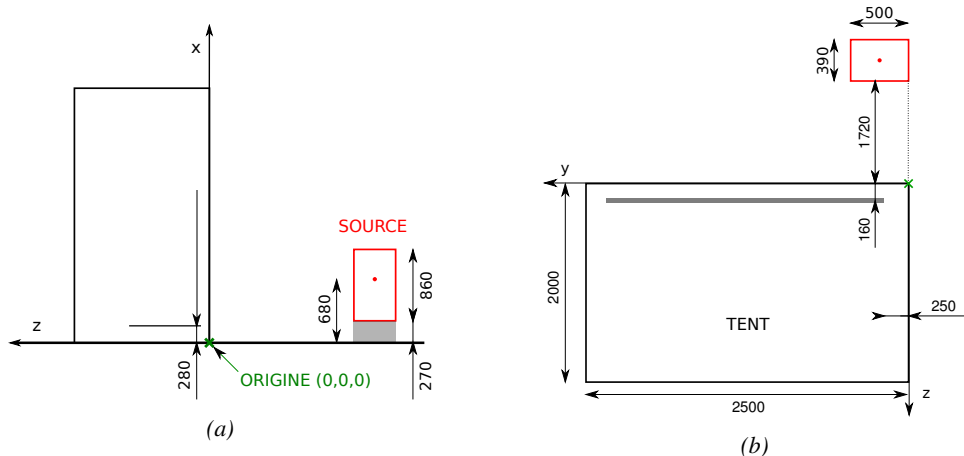


Figure 5.8: Description of the RPC setup. Dimensions are given in mm. A tent containing RPCs is placed at 1720 mm from the source container. The source is situated in the center of the container. RE-4-2-BARC-161 chamber is 160 mm inside the tent. This way, the distance between the source and the chambers plan is 2060 mm. Figure 5.8a provides a side view of the setup in the xz plane while Figure 5.8b shows a top view in the yz plane.

2793 The trigger system was composed of 2 plastic scintillators and was placed in front of the setup
 2794 with an inclination of 10° with respect to the detector plane in order to look at cosmic muons. Using
 2795 this particular trigger layout, showed in Figure 5.9, leads to a cosmic muon hit distribution into the
 2796 chamber similar to the one of Figure 5.10. Measured without gamma irradiation, two peaks can
 2797 be seen on the profile of readout partition B, centered on strips 52 and 59. Section 5.2.2 will help
 2798 us understand that these two peaks are due respectively to forward and backward coming cosmic

2799 particles where forward coming particles are first detected by the scintillators and then the RPC
 2800 while the backward coming muons are first detected in the RPC.



Figure 5.9: RE-4-2-BARC-161 chamber is inside the tent as described in Figure 5.8. In the top right, the two scintillators used as trigger can be seen. This trigger system has an inclination of 10° relative to horizontal and is placed above half-partition B2 of the RPCs. PMT electronics are shielded thanks to lead blocks placed in order to protect them without stopping photons from going through the scintillators and the chamber.

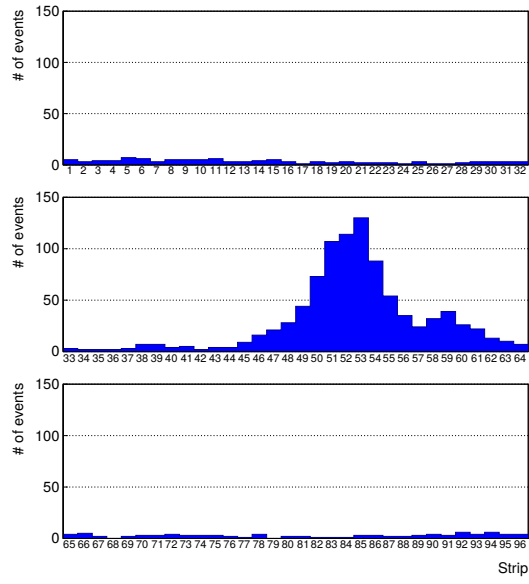


Figure 5.10: Hit distributions over all 3 partitions of RE-4-2-BARC-161 chamber is showed. Top, middle and bottom figures respectively correspond to partitions A, B, and C. The profiles show that some events still occur in other half-partitions than B2, which corresponds to strips 49 to 64, in front of which the trigger is placed, contributing to the inefficiency of detection of cosmic muons. In the case of partitions A and C, the very low amount of data can be interpreted as noise. On the other hand, it is clear that a little portion of muons reach the half-partition B1, corresponding to strips 33 to 48.

2801 The data taking is then performed thanks to a CEAN TDC module of type V1190A [257] to
 2802 which is connected the digitized output of the RPC Front-End Board, as described in Figure 5.11a
 2803 and the trigger signal from the telescope. The communication with the computer is performed thanks
 2804 to a CAEN communication module of type V1718 [258]. In order to control the rates recorded by
 2805 the detector, the digitized RPC signals are also sent to scalers as described in Figure 5.11b. The
 2806 C++ DAQ software used in GIF was developed as an early attempt towards the understanding of
 2807 the CAEN libraries and the data collected by the TDCs was saved into .dat files is analysed with
 2808 an algorithm computing parameters such as efficiency, hit profile, cluster size, or gamma and noise
 2809 rates which was developed with C++ as well. Finally, histograms and curves are produced using
 2810 ROOT.

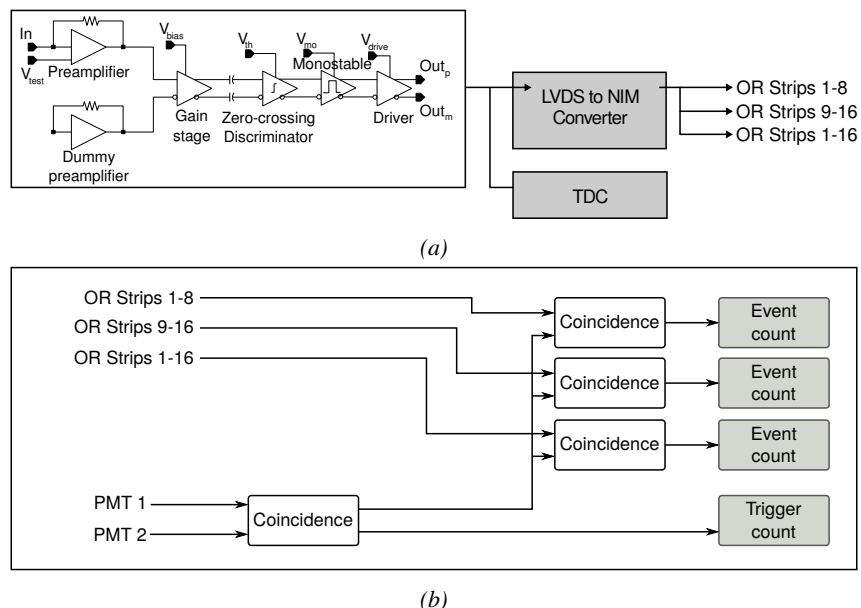


Figure 5.11: Signals from the RPC strips are shaped by the FEE described on Figure 5.11a. Output LVDS signals are then read-out by a TDC module connected to a computer or converted into NIM and sent to scalers. Figure 5.11b describes how these converted signals are put in coincidence with the trigger.

2811 5.2.2 Geometrical acceptance of the setup layout to cosmic muons

2812 In order to profit from a constant gamma irradiation, the detectors inside of the GIF bunker need
 2813 to be placed in a plane orthogonal to the beam line. The muon beam that used to be available was
 2814 meant to test the performance of detectors under test. This beam not being active anymore, an other
 2815 solution to test detector performance had to be used. Thus, it has been decided to use cosmic muons
 2816 detected through a telescope composed of two scintillators. Lead blocks were used as shielding to
 2817 protect the photomultipliers from gammas as can be seen from Figure 5.9.

2818 An inclination of $\sim 10^\circ$ has been given to the cosmic telescope to maximize the muon flux. A
 2819 good compromise had to be found between good enough muon flux and narrow enough hit distribution
 2820 to be sure to contain all the events into only one half partitions as required from the limited
 2821 available readout hardware. It was then foreseen to detect muons and read them out only from
 2822 half-partition B2, the last 16 channels of readout partition B (i.e. strips 49 to 64). Nevertheless,

a consequence of the misplaced trigger, that can be seen as a loss of events in half-partition B1 (strips 33 to 48) in Figure 5.10, is an inefficiency. The observed inefficiency of approximately 20% highlighted in Figure 5.12 by comparing the performance of chamber RE-4-2-BARC-161 as measured prior to the study at GIF and at GIF without irradiation seems too important, compared to the 12.7% of data contained into the first 16 strips observed on Figure 5.10, to only be explained by the geometrical acceptance of the setup itself. Simulations have been conducted to show how the setup brings inefficiency.

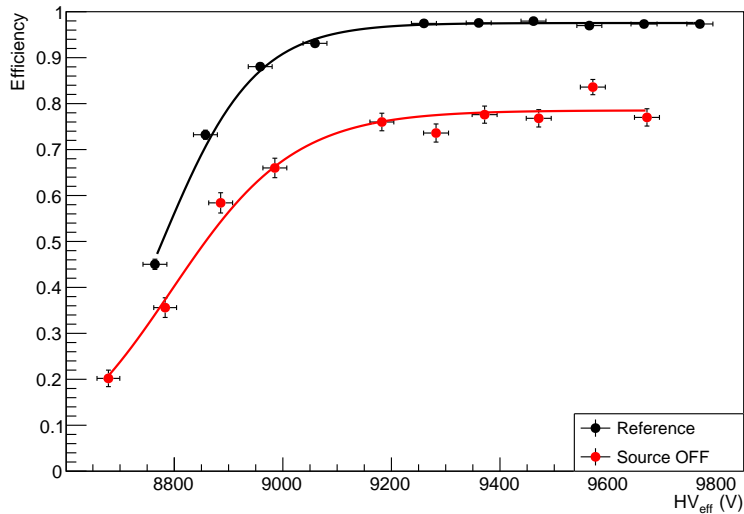


Figure 5.12: Results are derived from data taken on half-partition B2 only. On the 18th of June 2014, data has been taken on chamber RE-4-2-BARC-161 at CERN building 904 (Prevessin Site) with cosmic muons providing us a reference efficiency plateau of $(97.54 \pm 0.15)\%$ represented by a black curve. A similar measurement has been done at GIF on the 21st of July with the same chamber giving a plateau of $(78.52 \pm 0.94)\%$ represented by a red curve.

5.2.2.1 Description of the simulation layout

The layout of GIF setup has been reproduced, only roughly using Figure 5.9 due to the lack of measures, and incorporated into a C++ Monte Carlo (MC) simulation to study the geometrical acceptance of the telescope projected onto the readout strips [259]. A 3D view of the simulated layout is given into Figure 5.13. Muons are generated randomly in a horizontal plane located at a height corresponding to the lowest point of the PMTs. This way, the needed size of the plane in order to simulate events happening at very large azimuthal angles (i.e. $\theta \approx \pi$) can be kept relatively small while the total number of muon tracks to propagate is kept relatively small. The muon flux is designed to follow the usual $\cos^2\theta$ distribution for cosmic particles. The goal of the simulation is to look at muons that pass through the telescope composed of the two scintillators and define their distribution onto the RPC read-out plane. During the reconstruction, the read-out plane is then divided into read-out strips and each muon track is assigned to a strip.

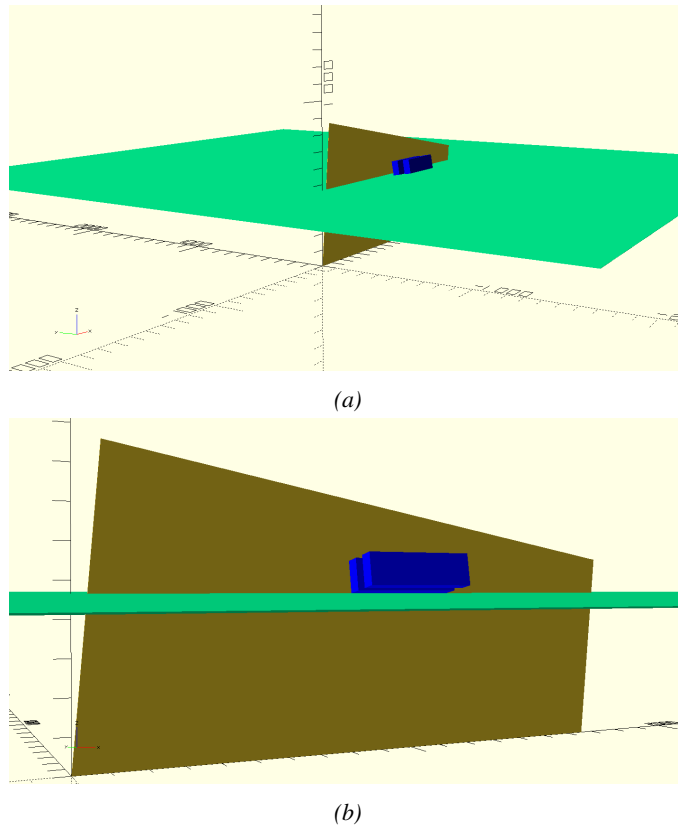


Figure 5.13: Representation of the layout used for the simulations of the test setup. The RPC read-out plane is represented as a yellow trapezoid while the two scintillators as blue cuboids looking at the sky. The green plane corresponds to the muon generation plane within the simulation. Figure 5.8a shows a global view of the simulated setup. Figure 5.8b shows a zoomed view that allows to see the 2 scintillators as well as the full RPC plane.

2842 5.2.2.2 Simulation procedure

2843 $N_\mu = 10^8$ muons are randomly generated inside the muon plane with an azimuthal angle θ chosen
 2844 to follow a $\cos^2\theta$ distribution. Infinite planes are associated to each surface of the scintillators.
 2845 Knowing the muon position into the muon generation plane and its direction allows, by assuming
 2846 that muons travel in a straight line, to compute the intersection of the muon track with these planes.
 2847 Applying conditions to the limits on the contours of the scintillators' faces then gives an answer to
 2848 whether or not the muon passed through the scintillators. In the case the muon was not *detected* into
 2849 both scintillators, the simulation discards the muon and generates a new one.

2850 On the contrary, if the muon is labeled as good, its position within the RPC read-out plane
 2851 is computed and the corresponding strip, determined through geometrical tests, gets a *hit*. Muon
 2852 hits fill different histograms whether they are associated to forward or backward coming muons.
 2853 A discrimination is performed according to their direction components. An (x, y, z) position into
 2854 the generation plane as well as a $(\theta; \phi)$ pair are associated to each generated muon providing with
 2855 information on the direction the track follows. This way, muons satisfying the condition $0 \leq \phi < \pi$
 2856 are labeled as *backward* coming muons while muons satisfying $\pi \leq \phi < 2\pi$ as *forward* coming

2857 muons.

2858 **5.2.2.3 Results and limitations**

2859 The output from the simulation is given in Figure 5.14 in which the distribution is showed for all
 2860 muons but also for the separate contributions of forward and backward coming muons. The strip
 2861 number is here given in a range of 1 to 32 corresponding to the 32 strips contained in each RPC
 2862 read-out partition, without taking into account the fact that partition B of an RPC correponds, by
 2863 convention, to strips 33 to 64. Comparing the number of muons recorded respectively in the first 16
 2864 strips and the in all of the 32 strips of the RPC read-out panel, it can be established than, out of the
 2865 total amount of muons that have passed through the telescope and reached the RPC, 16.8% where to
 2866 be detected in the 16 first strip of the read-out plane corresponding to half partition B1. This brings
 2867 a geometrical inefficiency of the same amount that can then be used to correct the data by scaling up
 2868 by a factor $c_{geo} = 1/(1 - 0.168)$ the maximum efficiency measured during data taking.

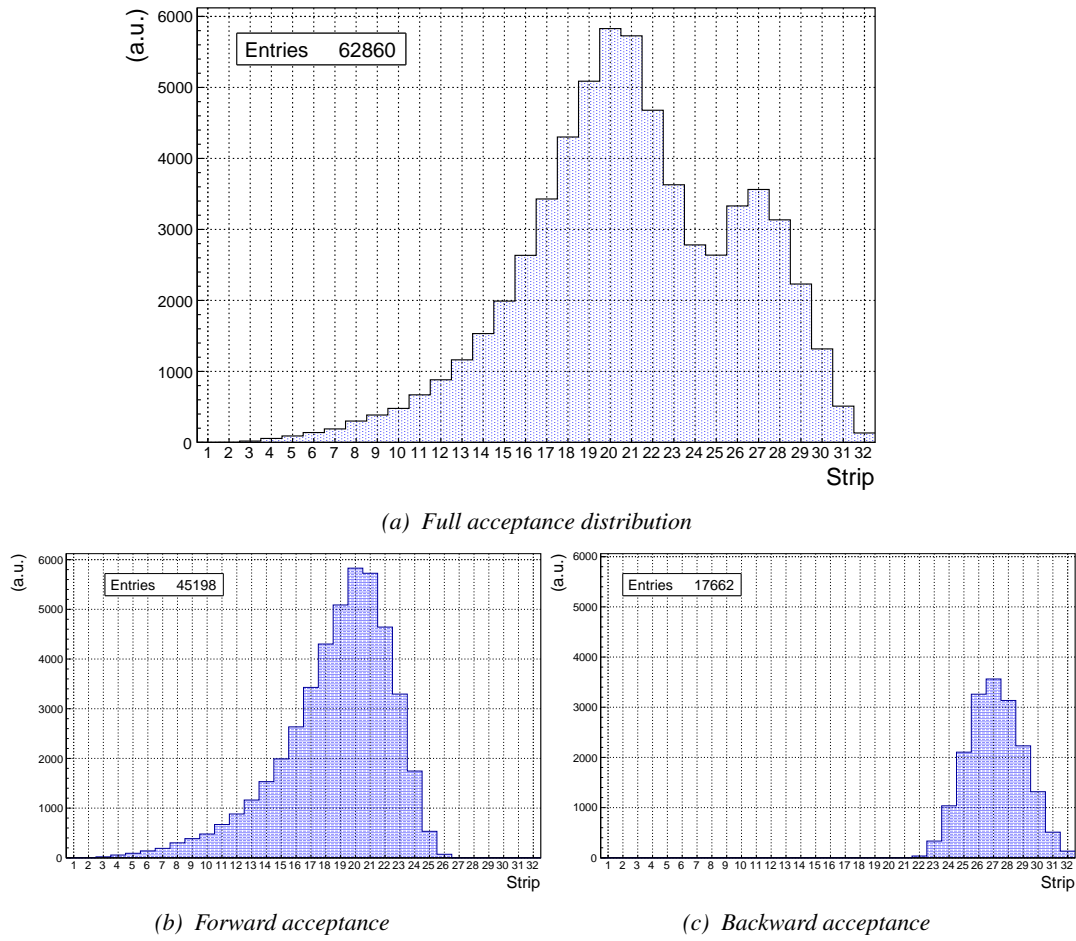


Figure 5.14: Geometrical acceptance distribution as provided by the Monte Carlo simulation.

2869 Nevertheless, it is difficult to evaluate a systematical uncertainty on this geometrical correction

for different reasons. First of all, even though the dimensions of the scintillators and of the RPC are well known, the position of each element of the setup with respect to one another was not measured. It was then necessary, using known dimensions, to extract the positions of each element from Figure 5.9 with unknown uncertainty. The inclination is also roughly measured to be 10° and even if the position of each peak, distant in the simulation of 7 strips, tends to confirm this assumption, the geometrical inefficiency would be affected by a variation of the inclination angle. Introducing in the simulation an error of $\pm 2^\circ$ would lead to a correction factor $c_{geo} = 1.20^{+0.04}_{-0.03}$ that allows for a good improvement of the efficiency measured in GIF, as can be seen from Figure 5.15. GIF measurement is in agreement with the reference curve within statistical errors.

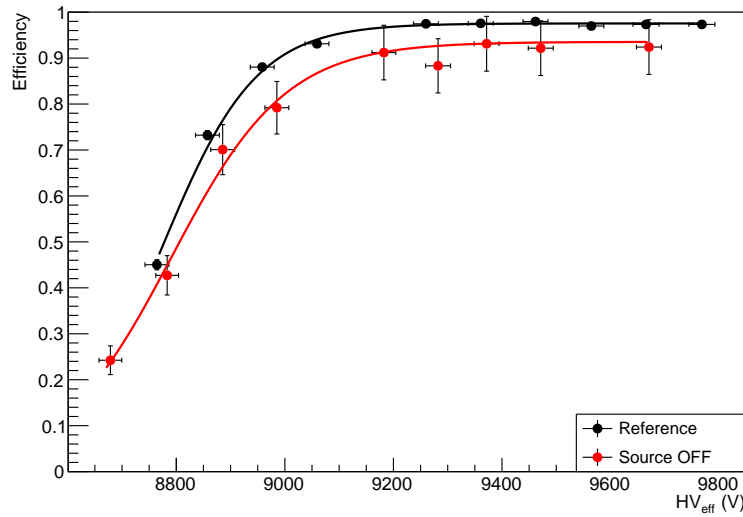


Figure 5.15: Correction of the efficiency without source. The efficiency after correction gets much closer to the Reference measurement performed before the study in GIF by reaching a plateau of $(93.52 \pm 2.64)\%$.

Further corrections could be also be brought as it can easily be understood that the distribution showed through Figure 5.14a differs from the measured hit profile showed in Figure 5.10. The contributions of forward and backward muon indicate that 28.1% of the total geometrical acceptance should contribute to detecting backward muons whereas it is measured that the hit profile contains 22.0% of backward data only. This estimation of the backward versus forward content in the data was done through a fit using a sum of two skew distribution, one acting on the forward muon peak while the other acts on the backward muon fit, as showed in Figure 5.16. Although a skew distribution lacks physical interpretation, it allows to easily fit such kind of data. A description of a skew distribution, as the product of a gaussian and a sigmoid (Formula 5.1), is given through Formula 5.2.

$$(5.1) \quad g(x) = A_g e^{\frac{-(x-\bar{x})^2}{2\sigma^2}}, \quad s(x) = \frac{A_s}{1 + e^{-\lambda(x-x_i)}}$$

$$(5.2) \quad sk(x) = g(x) \times s(x) = A_{sk} \frac{e^{\frac{-(x-\bar{x})^2}{2\sigma^2}}}{1 + e^{-\lambda(x-x_i)}}$$

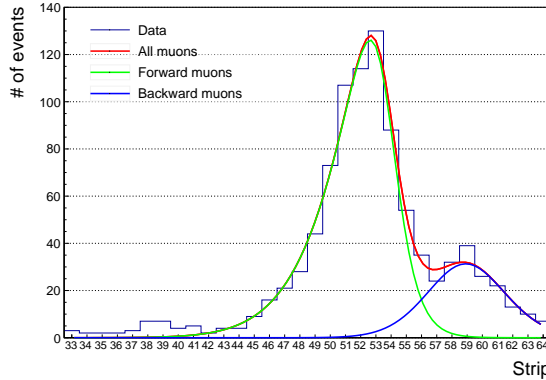


Figure 5.16: Hit distributions over read-out partition B of RE-4-2-BARC-161 chamber together with skew distribution fits corresponding to forward and backward coming muons.

From the obvious difference in between geometrical simulation and data, it is necessary to realize that the geometrical acceptance and the hit profile are two distinct information. When the geometrical acceptance only provides with the information about what the detector can expect to see in a perfect world where all muons are detected in the exact same way independently from their energy, angle of incidence, fluctuation of the detector gain due to complexe avalanche development, thresholds applied on the scintillators and on the RPC FEEs to reduce the noise, the cross-talk and corresponding spread of the induced charge observed on the read-out strips, the hit profile provides the final product of all the previously mentioned contributions and can greatly differ from purely geometrical considerations. A full physics analysis involving softwares such as GEANT would be required to further refine the correction on the measured efficiency at GIF.

5.2.3 Photon flux at GIF

In order to understand and evaluate the γ flux in the GIF area, simulations had been conducted at the time GIF was opened for research purposes [254]. Table 5.1 presented in this article gives the γ flux for different distances D to the source. The simulation was done using GEANT and a Monte Carlo N-Particle (MCNP) transport code, and the flux F is given with the estimated error from these packages expressed in %.

Nominal ABS	Photon flux F [$\text{cm}^{-2} \text{s}^{-1}$]			
	at $D = 50 \text{ cm}$	at $D = 155 \text{ cm}$	at $D = 300 \text{ cm}$	at $D = 400 \text{ cm}$
1	$0.12 \times 10^8 \pm 0.2\%$	$0.14 \times 10^7 \pm 0.5\%$	$0.45 \times 10^6 \pm 0.5\%$	$0.28 \times 10^6 \pm 0.5\%$
2	$0.68 \times 10^7 \pm 0.3\%$	$0.80 \times 10^6 \pm 0.8\%$	$0.25 \times 10^6 \pm 0.8\%$	$0.16 \times 10^6 \pm 0.6\%$
5	$0.31 \times 10^7 \pm 0.4\%$	$0.36 \times 10^6 \pm 1.2\%$	$0.11 \times 10^6 \pm 1.2\%$	$0.70 \times 10^5 \pm 0.9\%$

Table 5.1: Total photon flux ($E\gamma \leq 662 \text{ keV}$) with statistical error predicted considering a ^{137}Cs activity of 740 GBq at different values of the distance D to the source along the x-axis of irradiation field [254].

The simulation does not provide with an estimated flux at the level of the RPC under test. First of all, it is necessary to extract the value of the flux from the available data contained in the original paper and then to estimate the flux in 2014 at the time the experimentation took place. In the case of a pointlike source emitting isotropic and homogeneous gamma radiations, the gamma flux F at a

2908 distance D from the source with respect to a reference point situated at D_0 where a known flux F_0
 2909 is measured will be expressed like in Formula 5.3, assuming that the flux decreases as $1/D^2$, where
 2910 c is a fitting factor that can be written from Formula 5.3 as Formula 5.4. Finally, using Equation 5.4
 2911 and the data of Table 5.1, with $D_0 = 50$ cm as reference point, Table 5.2 can be built. It is interesting
 2912 to note that c for each value of D doesn't depend on the absorption factor.

$$(5.3) \quad F^{ABS} = F_0^{ABS} \times \left(\frac{cD_0}{D} \right)^2$$

$$(5.4) \quad c = \frac{D}{D_0} \sqrt{\frac{F^{ABS}}{F_0^{ABS}}} , \quad \Delta c = \frac{c}{2} \left(\frac{\Delta F^{ABS}}{F^{ABS}} + \frac{\Delta F_0^{ABS}}{F_0^{ABS}} \right)$$

Nominal ABS	Correction factor c		
	at $D = 155$ cm	at $D = 300$ cm	at $D = 400$ cm
1	$1.059 \pm 0.70\%$	$1.162 \pm 0.70\%$	$1.222 \pm 0.70\%$
2	$1.063 \pm 1.10\%$	$1.150 \pm 1.10\%$	$1.227 \pm 0.90\%$
5	$1.056 \pm 1.60\%$	$1.130 \pm 1.60\%$	$1.202 \pm 1.30\%$

Table 5.2: Correction factor c is computed thanks to Formula 5.4 taking as reference $D_0 = 50$ cm and the associated flux F_0^{ABS} for each absorption factor available in table 5.1.

2913 For the range of D/D_0 values available, it is possible to use a simple linear fit to get the evolution
 2914 of c that can be expressed as $c(D/D_0) = aD/D_0 + b$. Using Formula 5.5, but neglecting the
 2915 uncertainty on D that will only be used when extrapolating the values for the position of the RPC
 2916 under test whose position is not perfectly known, the results showed in Figure 5.17 is obtained.
 2917 Figure 5.17b confirms that using only a linear fit to extract c is enough as the evolution of the rate
 2918 that can be obtained superimposes well on the simulation points.

$$(5.5) \quad F^{ABS} = F_0^{ABS} \left(a + \frac{bD_0}{D} \right)^2 , \quad \Delta F^{ABS} = F^{ABS} \left[\frac{\Delta F_0^{ABS}}{F_0^{ABS}} + 2 \frac{\Delta a + \Delta b \frac{D_0}{D} + \Delta D \frac{bD_0}{D^2}}{a + \frac{bD_0}{D}} \right]$$

2919 In the context of the 2014 GIF tests, the RPC read-out plane is located at a distance $D = 206$ cm
 2920 from the source. Moreover, to estimate the strength of the flux in 2014 it is necessary to consider the
 2921 nuclear decay through time assiciated to the Cesium source whose half-life is well known ($t_{1/2} =$
 2922 (30.05 ± 0.08) y). The very first source activity measurement has been done on the 5th of March
 2923 1997 while the GIF tests where done in between the 20th and the 31th of August 2014, i.e. at a time
 2924 $t = (17.47 \pm 0.02)$ y resulting in an attenuation of the activity from 740 GBq in 1997 to 494 GBq in
 2925 2014. All the needed information to extrapolate the expected flux through the detector at the moment
 2926 of GIF preliminary tests has now been assembled, leading to Table 5.3. By assuming a sensitivity of
 2927 the RPC to γ of 2×10^{-3} , the order of magnitude of the expected hit rate per unit area would be of
 2928 the order of the kHz for the fully opened source, as reported in the last column of the table.

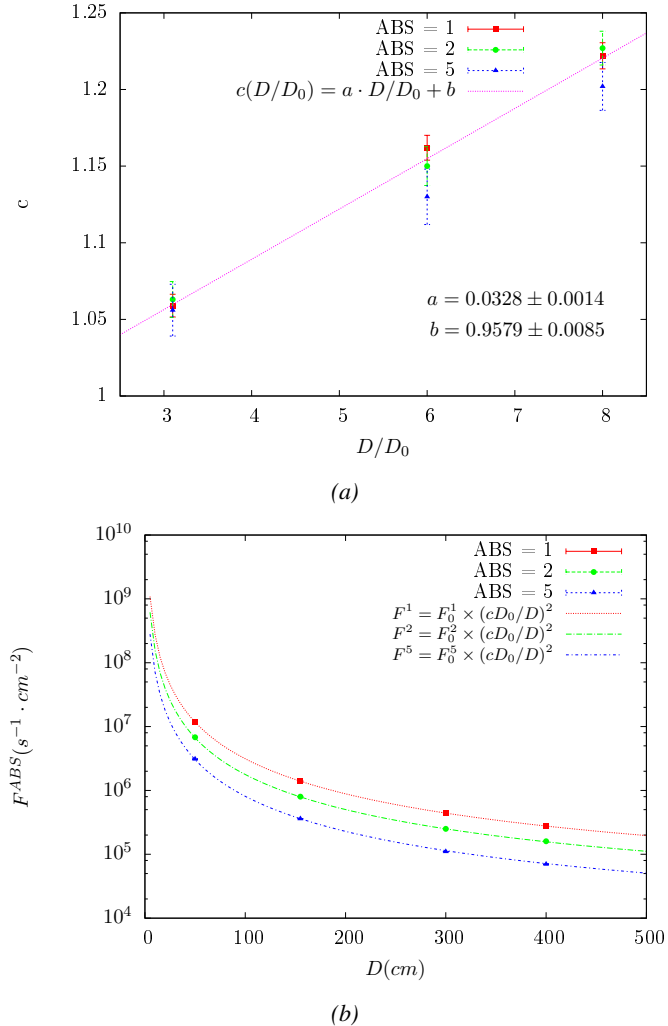


Figure 5.17: Figure 5.17a shows the linear approximation fit performed on data extracted from table 5.2. Figure 5.17b shows a comparison of Formula 5.5 with the simulated flux using a and b given in figure 5.17a in formulae 5.3 and the reference value $D_0 = 50$ cm and the associated flux for each absorption factor F_0^{ABS} from table 5.1

Nominal ABS	Photon flux F [$cm^{-2} s^{-1}$]			Rate [Hz/cm^2] at $D^{2014} = 206$ cm
	at $D_0^{97} = 50$ cm	at $D^{97} = 206$ cm	at $D^{2014} = 206$ cm	
1	$0.12 \times 10^8 \pm 0.2\%$	$0.84 \times 10^6 \pm 1.2\%$	$0.56 \times 10^6 \pm 1.2\%$	1129 ± 14
2	$0.68 \times 10^7 \pm 0.3\%$	$0.48 \times 10^6 \pm 1.2\%$	$0.32 \times 10^6 \pm 1.2\%$	640 ± 8
5	$0.31 \times 10^7 \pm 0.4\%$	$0.22 \times 10^6 \pm 1.2\%$	$0.15 \times 10^6 \pm 1.2\%$	292 ± 4

Table 5.3: The data at D_0 in 1997 is taken from [254]. Using Formula 5.5, the flux at D , including an error of 1 cm, can be estimated in 1997. Then, taking into account the attenuation of the source activity, the flux at D can be estimated at the time of the tests in GIF in 2014. Assuming a sensitivity of the RPC to γ s = 2×10^{-3} , an estimation of the hit rate per unit area is obtained.

2929 The goal of the study will be to have a good measurement of the intrinsic performance without
 2930 source irradiation. Then, taking profit of the two working absorbers, at absorbtion factors 5 (300 Hz)
 2931 and 2 (~ 600 Hz) the goal will be to show that the detectors fulfill the performance certification of
 2932 CMS RPCs. Finally, a first idea of the performance of the detectors at higher background will be
 2933 provided with absorbtion factor 1 (no absorbtion and >1 kHz)).

2934 5.2.4 Results and discussions

2935 The data taking at GIF has been conducted in between the 21st and the 31st of August, 2014. Data
 2936 has been collected with both source OFF and ON using three different absorber settings (ABS 5, 2
 2937 and 1) in order to vary the irradiation on the RPC. For each source setting, two HV scans have been
 2938 performed with two different trigger settings. During a first scan the trigger sent to the TDC module
 2939 was the coincidence of the two scintillators composing the telescope while during a second scan the
 2940 trigger was a pulse coming from a pulse generator in order to measure the noise or gamma rate seen
 2941 by the chamber. Indeed, using a pulse allows to trigger at moments not linked to any physical event
 2942 and, hence, to obtain a *RANDOM* trigger on noise and gamma events to measure the associated rates,
 2943 the probability to have a pulse in coincidence with a cosmic muon being negligible.

2944 From the cosmic trigger scans, a summary of the efficiencies and corresponding cluster sizes is
 2945 showed in Figure 5.18. The efficiency curves with Source ON show a shift with respect to the case
 2946 without irradiation. With ABS 5, the general shape of the efficiency curve stays unchanged whereas
 2947 a clear alteration of the performance is observed at ABS 2 and ABS 1. From the cluster size results,
 2948 a reduction of the cluster size under irradiation can be oberved at equivalent efficiency. This effect
 2949 can be due to the perturbation of the electric field by the strong rate of gamma particles starting
 2950 avalanches in the gas volume of the detector.

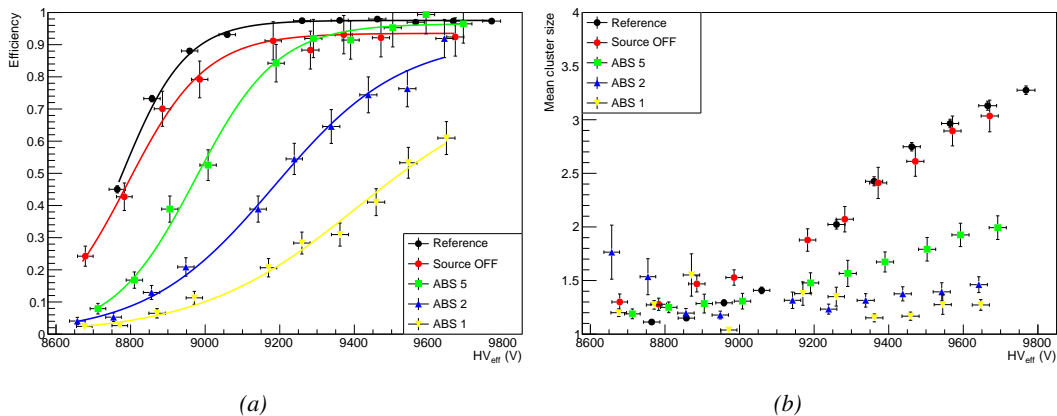


Figure 5.18: Efficiency (Figure 5.18a) and cluster size (Figure 5.18b) of chamber RE-4-2-BARC-161 measured at GIF with Source OFF (red) and Source ON using different absorber settings: ABS 5 (green), ABS 2 (blue) and ABS 1 (yellow). The results are compared to the Reference values obtained with cosmics.

2951 It is necessary to study the evolution of the performance of the chamber with the increasing rate.
 2952 In Figure 5.19a, the noise rate when the source is OFF stays low but increases at voltages above
 2953 9500 V. The rise of the noise rate in the detector can be related to the increased streamer probability
 2954 observed with such a large electric field. The rates with source ON measured at GIF all show a

similar behaviour until a high voltage of approximately 9400 V at which the rate of ABS 5 saturates, corresponding to the chamber reaching full efficiency. It is important to note that, even though the rates look similar independently from the gamma flux, relatively to the efficiency of the chamber, the rate actually increases with increasing flux at equivalent efficiency. A rough way to measure the rate effectively observed by the detector for each source setting would be to normalize the measured rates to the efficiency of the detector. This exercise was done with Figure 5.19b from which constant fits were done on Source ON data in order to extract the rate the chamber was subjected to.

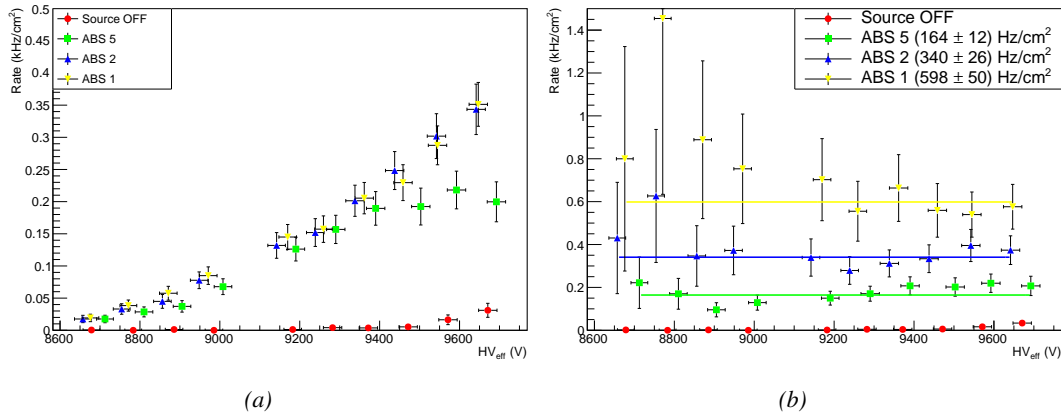


Figure 5.19: Rates in chamber RE-4-2-BARC-161 measured at GIF with Source OFF (red) and Source ON using different absorber settings: ABS 5 (green), ABS 2 (blue) and ABS 1 (yellow). On Figure 5.19b, the rates of Figure 5.19a were normalized to the measured efficiency and constant fits are performed on Source ON data showing the gamma rate in the chamber.

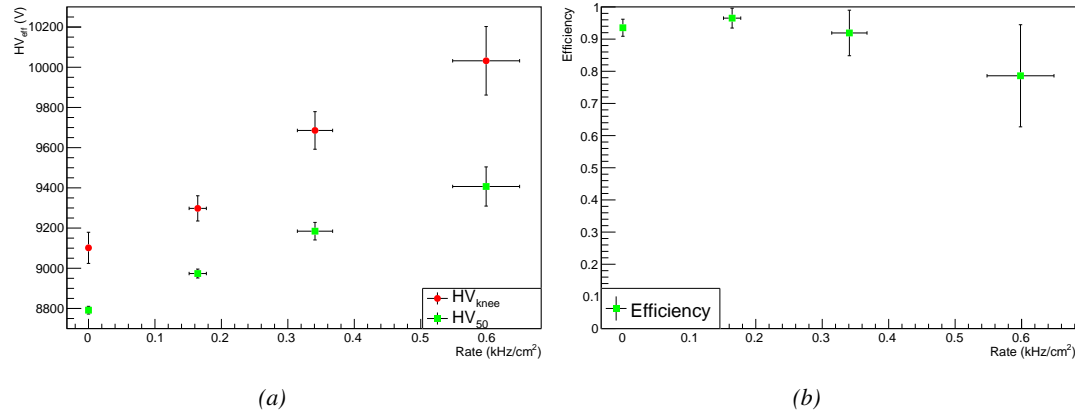


Figure 5.20: Evolution of the voltages at half maximum and at 95% of the maximum efficiency (Figure 5.20a), and of the maximum efficiency (Figure 5.20b) as a function of the rate in chamber RE-4-2-BARC-161. The data is extracted from the fits in Figures 5.18a and 5.19b.

The results need to be taken with care as a better estimation of the rate would have been to push the detector towards higher voltages to reach the efficiency plateau for each absorber configuration

and only then extract the measured rate at working voltage, defined as in Formula 4.25. Nevertheless, using this method to estimate the rate the chamber is subjected to, it is possible to look at the evolution of the HV_{50} and HV_{knee} (the working voltage being defined to be 150 V above the knee in the endcap) as a function of the increasing rate as showed in Figure 5.20. The results from GIF suggest that at a rate of 600 Hz/cm^2 the working voltage of the chamber is increased by a thousand V while the efficiency is reduced to approximately 80%, although the result still is consistent with an efficiency better than 90% due to the large error on the measurement. Moreover, it is likely that the rates obtained through fitting on normalized values is underestimated. Indeed, monitoring the current in the 3 gaps composing a CMS endcap RPC (Figure 5.21) while knowing the rate, the charge deposition per avalanche q_γ can be computed.

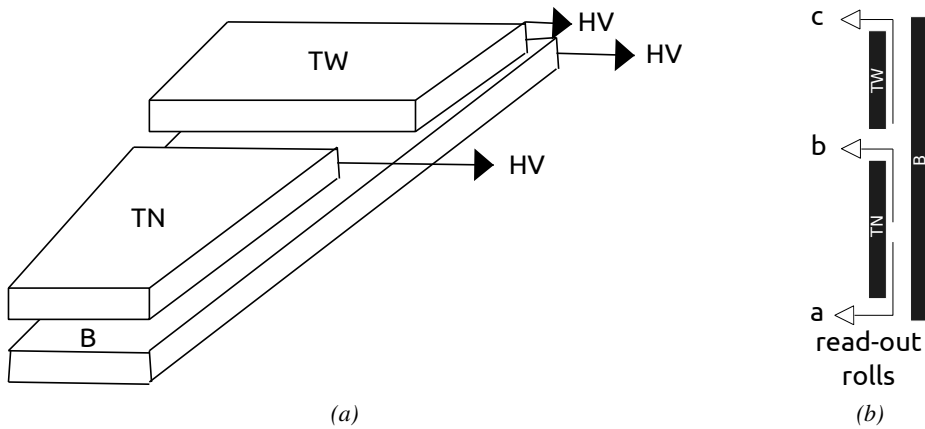


Figure 5.21: Presentation of a double-gap endcap RPC with its 3 RPC gaps. Due to the partitioning of the read-out strips into 3 rolls, the TOP layer of gap is divided into 2 gaps: TOP NARROW (TN) and TOP WIDE (TW). The BOTTOM (B) only consists in 1 gap.

A charge is expressed in C which is consistent with a current density, expressed in A/cm^2 , divided by a rate per unit area, expressed in Hz/cm^2 . The current driven by the RPC is assumed to be due to the irradiation, hence, to the avalanches developing in the gas volume due to the photons of the Cesium source. On the other hand, the rate is supposed to be a measure of the number of photons interacting with the detector. This way, it comes that the charge deposition per avalanche is expressed like $q_\gamma = J_{mon}/R_\gamma$, J_{mon} being the monitored current density and R_γ the measured γ rate. The current density is computed as the sum of the current density measured on the top gap layer and of which measured in the bottom gap layer, $J_{mon} = (I_{mon}^{TW} + I_{mon}^{TN})/(A_{TW} + A_{TN}) + I_{mon}^B/A_B$, $A_{B,TN,TW}$ being the active area and $I_{mon}^{B,TN,TW}$ the monitored currents of the gaps. According to Figure 5.22, the charge deposition per avalanche consistently converges to a value of the order of 50 pC for each absorber setting which corresponds to a value more than twice greater than what reported in literature for CMS detectors [260, 261] indicating that the rates could have been wrongly evaluated during the short study performed at GIF. An increase of the γ rate by a factor 2 would be consistent with the expected rates calculated in Table 5.3, assuming the sensitivity to γ to be of the order of 2×10^{-3} .

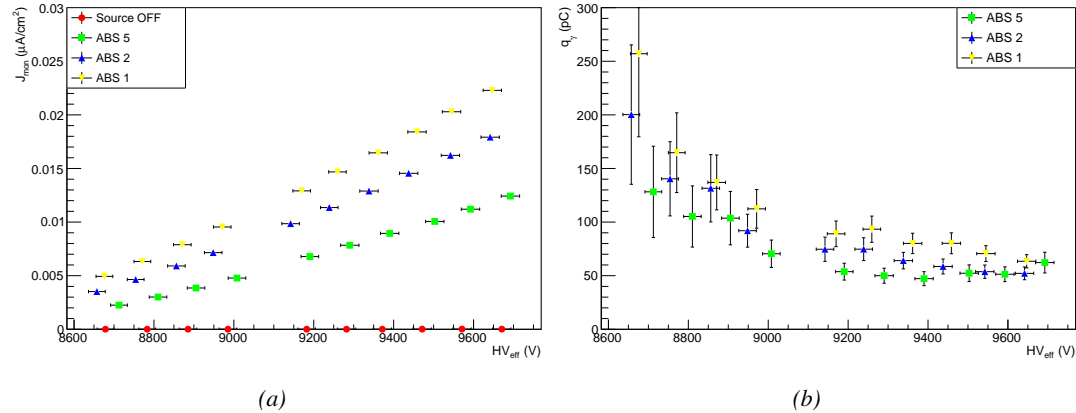


Figure 5.22: Current density and charge deposition per gamma avalanche, defined as the current density normalized to the measured rate taken from Figure 5.19a as a function of the effective high voltage in chamber RE-4-2-BARC-161 measured at GIF with Source ON using different absorber settings: ABS 5 (green), ABS 2 (blue) and ABS 1 (yellow).

Overall, working at GIF has been a rewarding experience as it offered CMS RPC R&D team the possibility to start developing the necessary skills and tools that would become the core of GIF++ experiment. The quality of the results can be argued both due to the little robustness of the experimental setup and the lack of available statistics to draw conclusions from, bringing large errors on the final result. The confrontation of the data to known results pointed to a failure in correctly measuring the γ rate at working voltage and, hence, to an overestimation of the charge per avalanche and of the drift of working voltage with increasing rate. Nevertheless, the prototypes of DAQ and offline analysis tools proved to be reliable.

5.3 Longevity tests at GIF++

5.3.1 Selection and characterization of CMS RPCs for longevity at GIF++

First proposed in 2009 [262], the new Gamma Irradiation Facility of CERN was thought in the perspective of future upgrades of PHC that would bring detectors to be operated in a high irradiation environment. GIF++ would thus provide all LHC R&D teams working on behalf of the different LHC experiment with a facility to perform longevity studies using a very intense Cesium gamma source.

In the specific case of CMS RPC, the longevity studies imply a constant irradiation of selected detectors in order to accumulate a charge equivalent to what is expected during HL-LHC, i.e. a charge of $0.8 \text{ C}/\text{cm}^2$ according to Figure 5.2 including a safety factor 3, while other detectors are left non irradiated to be used as references. Throughout the irradiation campaign, the performance of the irradiated and reference detectors will be periodically probed using the high intensity H4 muon beam. Dedicated test beam periods will be used to measure the efficiency and γ rate at the level of the detectors with different source absorber settings to have access to the rate capability of CMS RPCs, that needs to be certified above $600 \text{ Hz}/\text{cm}^2$, and to identify signs of ageing in the case the performance of the irradiated detectors diverges from those of the reference detectors with increasing accumulated charge. Other than the performance of the detectors, signs of ageing

3014 could come from increasing dark current that would be related to local ageing of the electrodes
 3015 triggered by the fluoridric acid (*HF*) production in an irradiated environment. *HF* is produced
 3016 by the decomposition of $C_2H_2F_4$ molecules during the charge multiplication process and leads to
 3017 increased dark current and noise in Bakelite RPCs treated with linseed oil. This effect is strongly
 3018 reinforced by the presence of UV photons [263, 264]. A close monitoring of the current driven by
 3019 the detectors will then be necessary as well as dedicated periodical electrode resistivity measurement
 3020 and chromatography measurement on the gas exhaust.

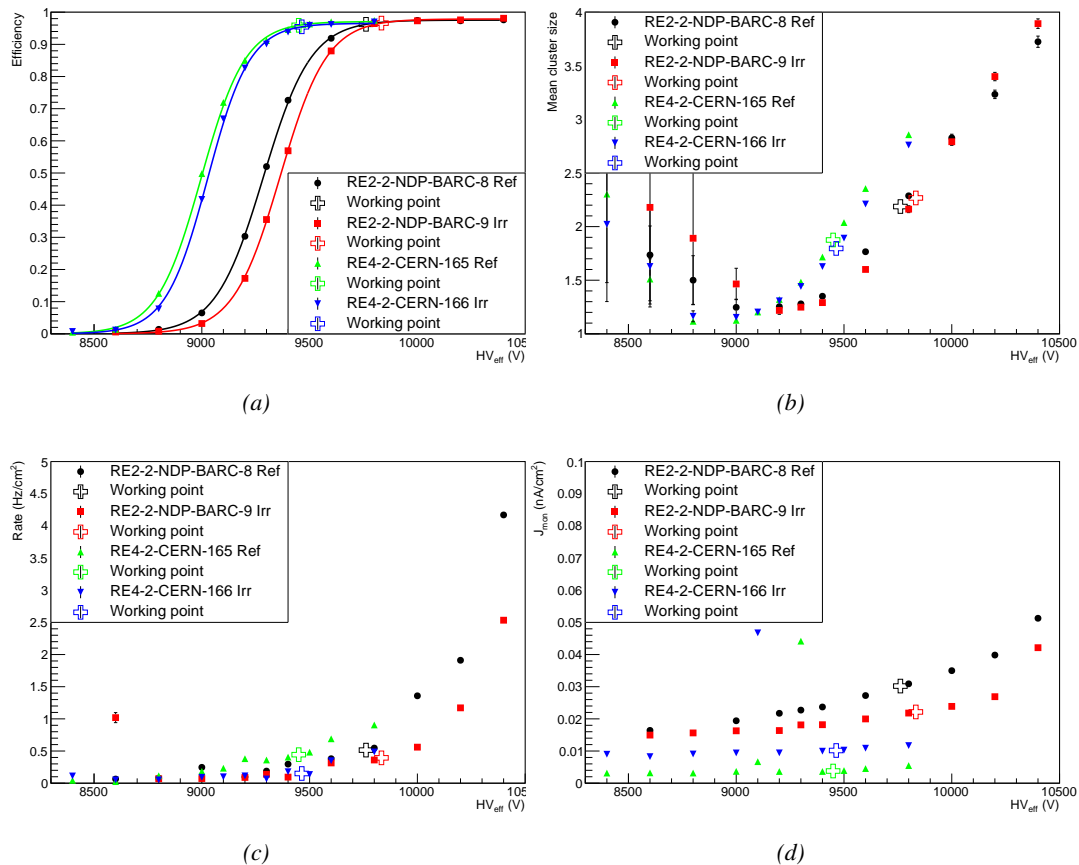


Figure 5.23: Characterization of CMS RPC detectors foreseen to be used at Gif++ for longevity studies of the present system. Using cosmic muons, efficiency (Figure 5.23a) and cluster size (Figure 5.23b) were measured as well as noise rate (Figure 5.23c) and current density (Figure 5.23d). For each detector, the working voltage, defined as in Formula 4.25, was extracted from sigmoid fits performed in Figure 5.23a and the values of efficiency, cluster size, noise rate and current density at this voltage are reported using open crosses.

3021 As the maximum background is found in the endcap, the choice naturally was made to focus
 3022 the Gif++ longevity studies on endcap chambers. Most of the RPC system was installed in 2007.
 3023 Nevertheless, the large chambers in the fourth endcap (RE4/2 and RE4/3) have been installed during
 3024 LS1 in 2014. The Bakelite of these two different productions having different properties, four spare
 3025 chambers of the present system were selected. From the original CMS RPC system, two RE2/2
 3026 spares were selected along two RE4/2 spares from the newest detectors. Having two chambers of

3027 each type allows to always keep one of them non irradiated as reference. Due to the limited gas
 3028 flow in GIF++, the RE4 chamber remained non-irradiated until end of November 2016 where the
 3029 longevity studies could finally be started on those chambers.

3030 The performance of the chambers prior to the start of the longevity campaign has been char-
 3031 acterized in Ghent before being shipped to CERN to be installed in GIF++. The results of the
 3032 characterization are showed in Figure 5.23 and summarized in Table 5.4. A clear difference in per-
 3033 formance for both types of chambers is observed as the working voltages of the newest chambers,
 3034 of type RE4, are 300 to 400 V lower to the older chambers indicating that the gap thickness of RE4
 3035 detectors could be thinner. This conclusion could as well be supported by the lower cluster size at
 3036 working voltages that also are smaller in RE4 chambers. Even though the measured currents are
 3037 low, RE4 detectors draw less current without irradiation than RE2 detectors pointing to a difference
 3038 in electrode resistivity that were produced at different moments. Efficiency and noise rate levels are
 3039 of the same order of magnitude for both type of RPCs.

RPC	RE2-2-NPD-BARC-08	RE2-2-NPD-BARC-09	RE4-2-CERN-165	RE4-2-CERN-166
Used as	Reference	Irradiation	Reference	Irradiation
HV_{WP} [V]	(9762 \pm 6)	(9833 \pm 6)	(9449 \pm 5)	(9464 \pm 5)
Efficiency at WP	(96.2 \pm 0.3)	(96.6 \pm 0.3)	(95.9 \pm 0.3)	(95.5 \pm 0.3)
Cluster size at WP	(2.19 \pm 0.04)	(2.27 \pm 0.05)	(1.88 \pm 0.04)	(1.80 \pm 0.04)
Noise at WP [Hz/cm ²]	(0.51 \pm 0.01)	(0.39 \pm 0.01)	(0.44 \pm 0.00)	(0.15 \pm 0.01)
J^{WP} [pA/cm ²]	(30.1 \pm 0.1)	(22.2 \pm 0.1)	(3.8 \pm 0.0)	(10.2 \pm 0.0)

Table 5.4: Summary of the characterization measurement performed in Ghent on CMS RPC detectors foreseen to be used at GIF++ for longevity studies of the present system. For each detector, the working voltage, defined as in Formula 4.25, was extracted from sigmoid fits performed in Figure 5.23a and the values of efficiency, cluster size, noise rate and current density at this voltage are reported.

5.3.2 RPC test setup

3041 For an easy manipulation of the detectors, a trolley with a structure containing slots in which the
 3042 RPCs can be slid vertically and referred to as T1 was used. In this position, each chamber is in a
 3043 plane perpendicular to the beam line and the source flux as can be seen through Figure 5.24, receiving
 3044 a uniform irradiation. Moreover the trolley allows for easy movement of the system. Indeed, the
 3045 position of trolley varies according to the period of the year.

3046 During the dedicated test beam periods during which GIF++ longevity experiments are in control
 3047 of the muon beam, the trolley is placed in the upstream region of the bunker, in the beam line, as
 3048 described through Figure 5.24a. The CMS RPC detectors are the ones being further away from the
 3049 source on this side of the source as other detectors need to be certified at higher background rates. An
 3050 additional trolley, referred to as T3, containing iRPCs and tracking RPCs is placed in between the
 3051 source and the trolley containing present CMS RPCs. Indeed, iRPCs need to be certified at higher
 3052 rates and thus need to be placed closer to the source to receive a stronger irradiation using the same
 3053 absorber settings. The space on T1 being limited, the tracking RPCs used for extra offline informa-
 3054 tion during the analysis are placed on the same trolley than iRPCs and are kept at full efficiency at
 3055 all time to reconstruct muon tracks in correlate them with hits recorded in T1 chambers. The beam
 3056 trigger system is composed of 2 scintillators placed outside on each side of the bunker and of a third
 3057 scintillator placed in between T1 and the wall of the bunker along the beam line.

3058 However, most of the year, T1 is placed in the so called *ageing position* corresponding to the

furthest position from the source outside of the beam line, which needs to stay clear during periods where GIF++ doesn't have the control of the beam so that a beam tube can be installed through the bunker, as can be seen in Figure 5.24b. The reason for placing the chambers as far as possible from the source comes from the too high irradiation delivered by the source during the irradiation periods where all the other experiment having placed detectors into the bunker requires to integrate as much charge as possible. Hence, the source is operated with any absorbers. On the contrary, during the test beam periods, all the groups working in GIF++ are interested in operating the source using various absorber settings to study the performance of their detectors under different irradiation conditions. The time spent with a source fully opened and during which the RPCs of T1 are kept at a standby voltage of 6500 V much lower than what necessary to grow avalanches in the gas is then small compared to the time spent with other source settings and during which data can be taken.

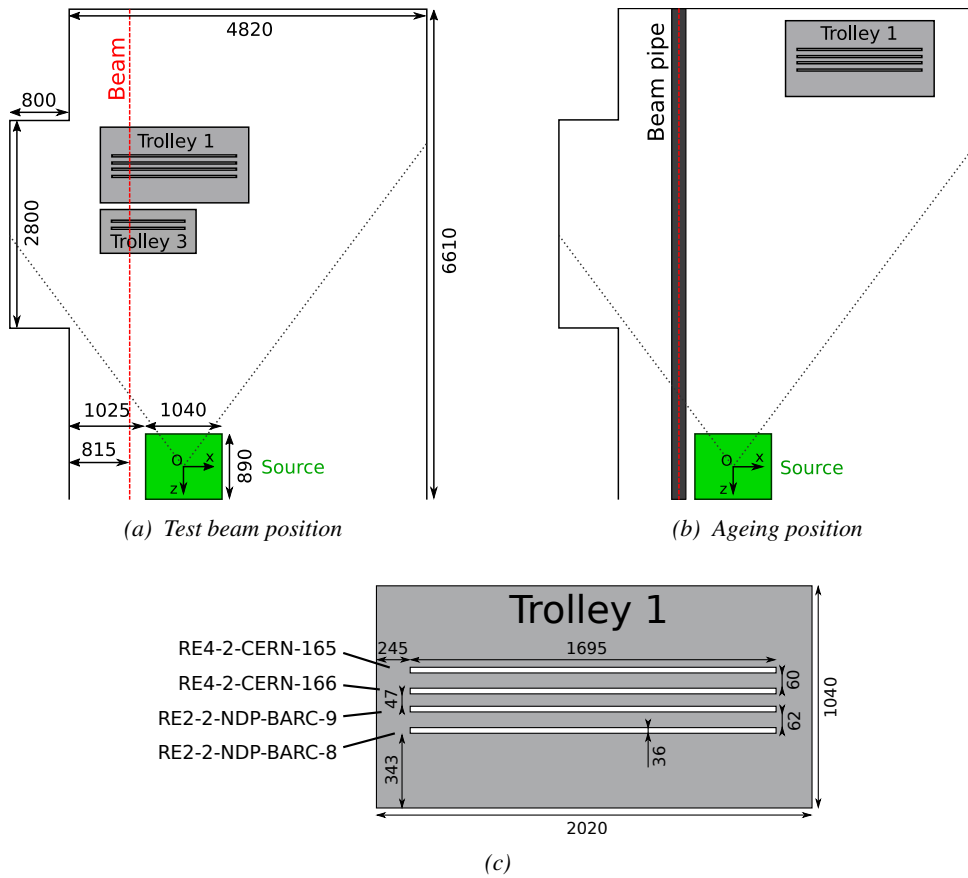


Figure 5.24: CMS RPC setup inside of GIF++ bunker during test beam (Figure 5.24a) and ageing periods (Figure 5.24b). The space in between the RPCs and the source is usually used by other detectors while the space in between T1 and the upstream wall is not filled. Due to the presence of the beam pipe, the trolley is moved away from the beam line during irradiation periods and placed further away from the source for less intense irradiation. The position of the trolley can vary due to the use of the space by other setups and is then not exact. In the contrary, the position of the chambers in the trolley is fixed and given in Figure 5.24c.

From the bunker area, the detectors are connected to the service area, visible in Figure 5.6, through the wooden floor tanks to long cable. The service area hosts all the high and low voltage power

3072 supplies, the TDCs and computers used for data acquisition and preliminary offline analysis used
 3073 to fill the Detector Control Software (DCS) webpage, referred to as WebDCS, with Data Quality
 3074 Monitoring (DQM) histograms useful for the shifters on duty in the control room located further in
 3075 the building, away from the beam lines, as well as the gas system required for the gaseous detectors
 3076 installed in GIF++ [265]. The detectors read-out is, as in the case of GIF, connected to V1190A
 3077 VME TDCs communicating with the DAQ computer thanks to a V1718 VME bridge manufactured
 3078 by CAEN. Moreover, a constant monitoring of all the environmental parameters, in different points
 3079 of the bunker area, gas parameters, to control its composition, temperature and pressure, and of the
 3080 voltages and currents delivered by the power supplies is performed and displayed on the homepage
 3081 of the WebDCS interface.

3082 5.3.3 GIF++ data flow

3083 At GIF++, the CMS RPC R&D experiment collects different types of data coming from the detectors
 3084 monitored parameters, such as voltage and currents, the gas, source, and environmental parameters,
 3085 and, of course, the TDC data in which are collected the actual muon and gamma physics. These
 3086 different data source compose 3 different data flows as presented in Figure 5.25.

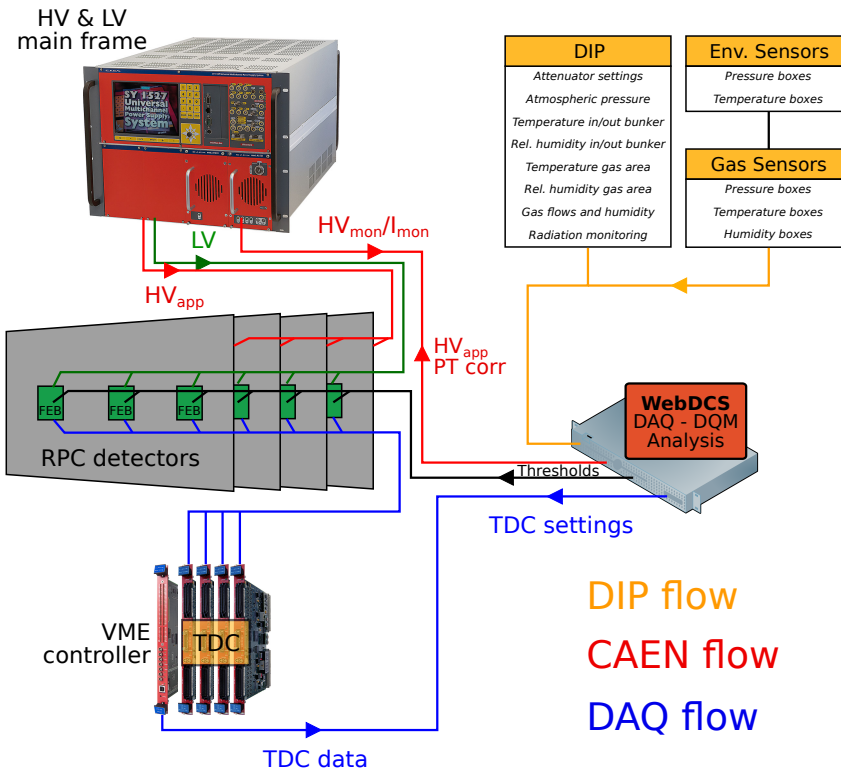


Figure 5.25: Visualtion of the main data flows in GIF++. The yellow flow lines corresponds to the DIP flow used for source, environmental and gas information. The red flow lines are for the CAEN flow through which the WebDCS communicates the voltages to be applied on the detectors using pressure and temperature information and retrieves the monitored voltages and currents. Finally, the blue flow lines corresponds to the DAQ flow through which the RPC data is collected from the TDCs by the computer.

3087 The *DIP flow*, DIP being a communication system allowing for exchange of real-time information
 3088 concerns all the data coming from the gas composition, temperature and humidity, the environmental temperature and pressure, the source settings and the radiation monitoring sensors. The experimental area is in charge of measuring, storing and distributing the data
 3089 of interest for all of the users of the facility (source settings, radiation monitoring, gas composition
 3090 at the exit of the gas mixer and general environmental information). Retrieving this data is done by
 3091 accessing to the database of the experimental hall in which GIF++ is located through DIP communica-
 3092 tion. More specific data such as gas flow, temperature and humidity at the level of the detectors
 3093 (upstream and downstream of the detectors) as well as environmental parameters are at the charge
 3094 of the users. For this reason, several pressure, temperature and humidity sensors were installed on
 3095 the gas distribution system of the RPC trolleys. The corresponding data flow, although not related
 3096 to DIP itself, is saved together with the DIP data into the local CMS RPC database and displayed
 3097 on the front page of the WebDCS together with alerts in the case the values measured are out of
 3098 optimal working range. The data is particularly important to perform the PT correction described in
 3099 Section 4.4 of Chapter 4 and keep stable the effective voltage of the detectors. Monitoring history
 3100 plots are made using JavaScript are also displayed for an easy access to past information, as
 3101 showed in Figure 5.26.
 3102

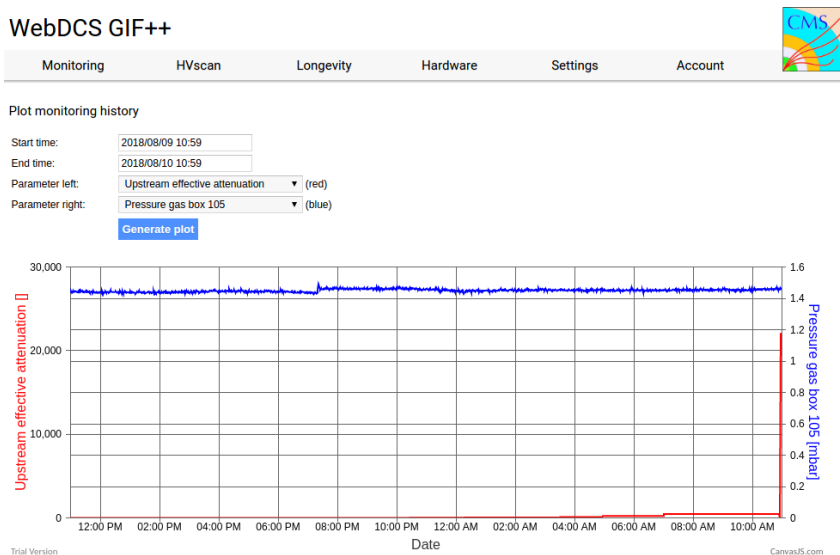


Figure 5.26: *DIP monitoring history accessed through GIF++ WebDCS interface.*

3104 The data flow related to the monitoring of detector high voltages and currents, referred to as
 3105 *CAEN flow* as a reference to the manufacturer of power supplies, is retrieved thanks to computer
 3106 to main frame communications. Indeed, during the operations (irradiation or beam period), these
 3107 values can be accessed directly through the bus of the main frame hosting the high voltage supplies.
 3108 Finally, the DAQ flow concerns all data acquired through the use of the TDCs, i.e. all the muon or
 3109 gamma data recorded by the detectors under test at GIF++.

3110 **5.3.4 Measurements performed during beam periods**

3111 As previously described, two types of measurement are performed on the chambers during beam
 3112 periods. On one hand, it is interesting to measure the efficiency of the RPCs with increasing voltage
 3113 with different source absorber settings but on the other hand, it is important to correlate the efficiency
 3114 information to the gamma rate seen by the chambers at the voltages that were scanned for efficiency.
 3115 The choice was made to separate efficiency measurements from rate measurements to better manage
 3116 time and data volume. In both cases, TDC data recorded during so called *HV scans* is divided into
 3117 *runs*, one for each high voltage point, whose data is stored into ROOT files. The TDC settings
 3118 used during both these scans as well as the ROOT data structure are detailed in Section A.4.2 of
 3119 Appendix A.

3120 The goal of both efficiency and rate scans is to measure the rate capability of the detectors but
 3121 also to monitor any degradation of the performance due to ageing. This way, during test beam
 3122 periods the efficiency and corresponding gamma background are measured to correlate the evolution
 3123 of rate capability at different stages of irradiation. In the absence of other signs of ageing, a reduction
 3124 of the rate capability could be related to an increase of the electrodes resistivity.

3125 **5.3.4.1 Efficiency scans**

3126 The HV scans performed to specifically measure the muon detection efficiency under different ir-
 3127 radiation conditions follow a standardized procedure. Data using the DAQ is taken at the same 12
 3128 HV points for all chambers, ranging from 9 kV to 10.1 kV by steps of 100 V. For each HV run, a
 3129 minimum of 5000 muon beam triggers, provided by the coincidence of the 3 scintillators, is required
 3130 in order to accumulate enough statistics for a reliable computation of the efficiency of the detectors.
 3131 In addition to the 4 RPCs held on T1, 2 tracking RPCs installed on T3 are kept at a fixed voltage of
 3132 9.7 kV to provide the analysis software [266] with beam position information to exclude off-track
 3133 signals. The tracking RPCs, whose design is based on which of CMS RPCs, are double gap detectors
 3134 featuring 2 mm HPL electrodes and 2 mm gas gaps. Finally, the monitored currents and voltages are
 3135 recorded in histograms along the TDC data in a different ROOT file for each run.

3136 HV scans are taken for different source settings as the goal is to irradiate all the detectors with a
 3137 minimal rate of 600 Hz/cm². Usually, a full study of the performance of the detectors is performed
 3138 with Source OFF, and then with 9 absorber settings that attenuate the nominal gamma flux by factors
 3139 from more than 200 to only 3, settings with fully opened source being avoided with RPCs in test
 3140 beam position. Adjusting the gamma flux is possible thanks to the 3 layers of absorbers featured on
 3141 the Cesium source [267].

3142 **5.3.4.2 Rate scans**

3143 These background measurement are performed using a similar HV scan procedure than in the case
 3144 of efficiency measurements. The HV scan in test beam period will be taken fewer HV points than
 3145 for the efficiency scans as the region of interest is located around the knee and efficiency plateau
 3146 of the detectors in order to extract through linear interpolation the value of the rate at the working
 3147 voltage deduced from the efficiency scan. Thus, these scans are performed only on 6 HV points
 3148 ranging from 9.5 kV to 10 kV. Rate scans are substantially heavier than efficiency scans. Indeed, a
 3149 good estimation of the rate requires a long enough integrated time worth of data. The way data is
 3150 collected, detailed in Appendix A, makes the DAQ search for data stored in the TDC buffers prior to
 3151 the trigger signal. The time window from which the data is collected ranges in between only 25 ns

3152 to more than $50\ \mu\text{s}$. The Cesium source delivering a consistent gamma flux, it was decided than a
 3153 total integrated time of 0.2 s would be enough to have a reliable calculation of the γ rate. This is
 3154 achieved by taking 20,000 random trigger pulses delivered by a pulse generator at a frequency of
 3155 300 Hz while extracting $10\ \mu\text{s}$ of data from the buffers for each trigger.

3156 Separating rate measurements from efficiency measurement was motivated by the inconsistency
 3157 of the muon beam provided in GIF++. Using periods without beam to measure rates with a good
 3158 statistics allows for faster study programs. Moreover, depending on the muon strength that can
 3159 strongly vary due to users placed upstream of GIF++ and using magnets, the number of muon de-
 3160 livered per beam spill can make the accumulation of 20,000 events too long for the other users of
 3161 GIF++. Hence, efficiency scans are performed with lower statistics and the time window from which
 3162 the data is extracted is strongly reduced (400ns for efficiency scans versus $10\ \mu\text{s}$ for rate scans) to
 3163 keep the data size to its bare minimum.

3164 5.3.4.3 Offline analysis and Data Quality Monitoring

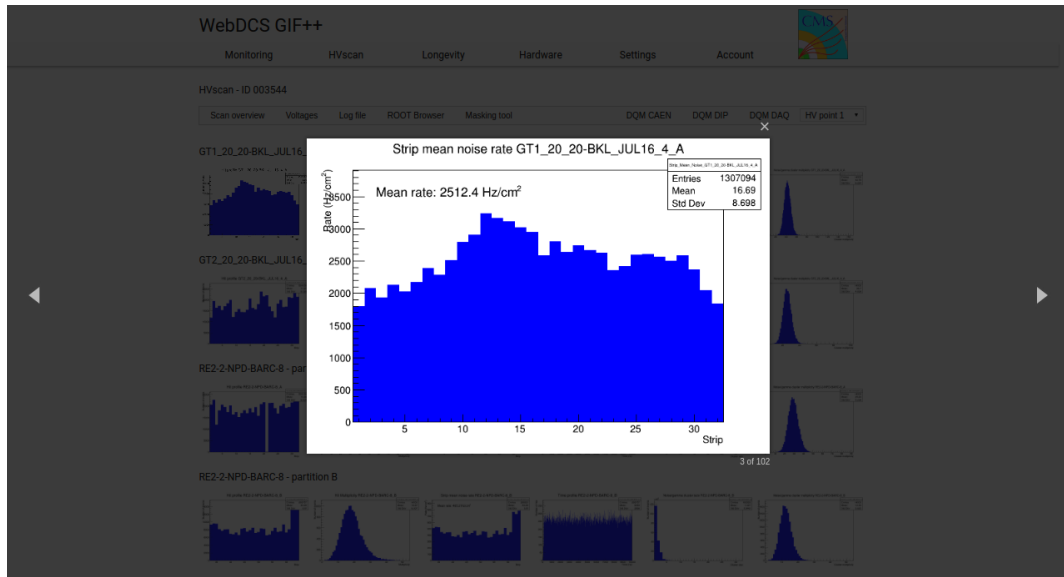


Figure 5.27: Example of DQM page available on CMS WebDCS in GIF++. Here is presented the rate measured in one of the tracking chambers, namely GT1_20_20-BKL_JUL16_4. The DQM page allows to click on each histogram to extend its view and to navigate through the histograms thanks to the left and right arrows.

3165 The data recorded during efficiency and rate scans always consist in two ROOT files per run, a run
 3166 corresponding to a HV point. One of the files corresponds to the TDC data, a collection of hits
 3167 per active channel on the read-out of the RPCs, while the second is the CAEN main frame data,
 3168 offering a monitoring of the currents and high voltages. This data is systematically analysed at the
 3169 end of each scan thanks to the Offline Analysis tool of GIF++, detailed in Appendix B, that produces
 3170 histograms such as hit, rate and time profiles, hit multiplicities, gamma cluster sizes or multiplicities
 3171 for the DQM display of the WebDCS, as showed in Figure 5.27. More histograms can be accessed
 3172 through the ROOT browser included in the WebDCS, as showed in Figure 5.28. Moreover, the
 3173 analysis performed thanks to the Offline tool is definitive in the case of evaluating the rates from rate

3174 scans. On the contrary, the algorithm for efficiency calculation is kept simple and approximative in
 3175 the tool as including traking into the analysis requires manual adjustment for each individual scan.

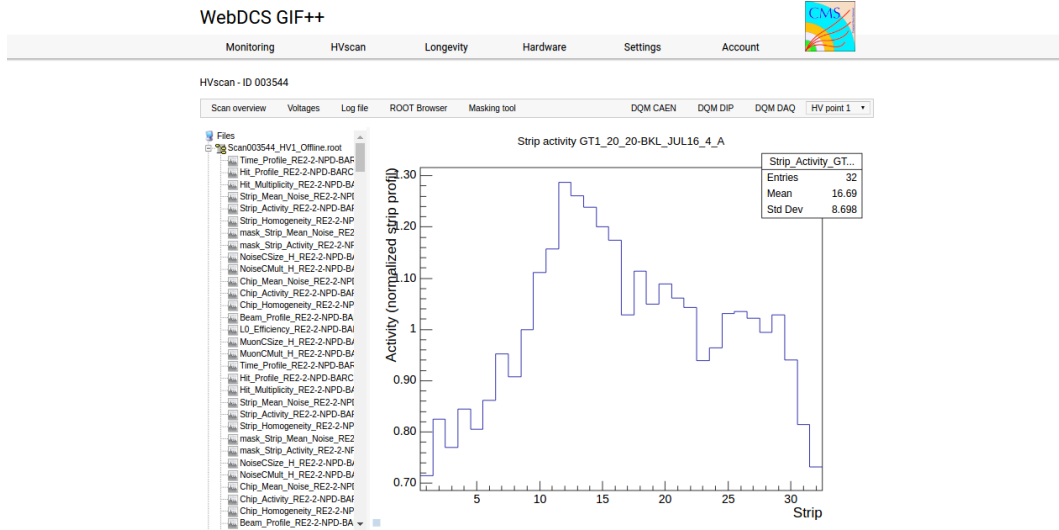


Figure 5.28: Example of DQM ROOT Browser page available on CMS RPC WebDCS in GIF++. Here is presented the strip activity profile, defined as the rate profile normalized to the mean rate, in one of the tracking chabers, namely GT1_20_20-BKL_JUL16_4. Available ROOT files and histograms can be browsed thanks to the left panel showing the directory and files structures.

3176 5.3.5 Measurements performed during irradiation periods

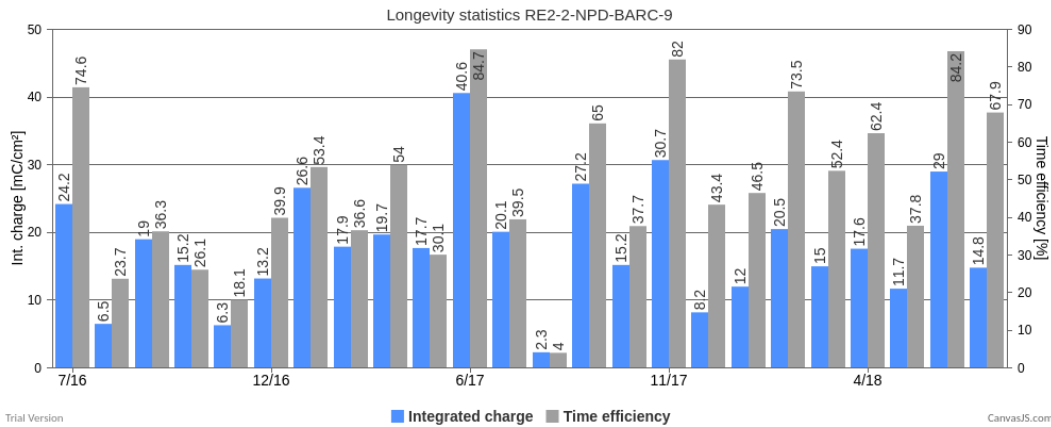


Figure 5.29: Longevity statistics of chamber RE2-2-NPD-BARC-9 in GIF++. For each month since July 2017, the integrated charge (in blue) as well as the time efficiency of irradiation (in gray) is reported.

3177 Even though test beam periods are stressful times has an extensive data taking planing needs to
 3178 be finalized in a short amount of time, the biggest amount of data comes from irradiation periods.

Indeed, when T1 is moved back to its ageing position in between each test beam periods, data is recorded at any time the source can be switched ON for irradiation. Indeed, other experiments in the area might prevent the source from staying opened continuously. As an example, the time efficiency of irradiation of CMS RPC detectors in Gif++ is presented in Figure 5.29.

Several types of measurement are performed throughout the irradiation period. Indeed, as long as the detectors are being irradiated, a monitoring of the currents is performed to evaluate the corresponding integrated charge considering the irradiation time. Moreover, the corresponding gamma rates need to be measured on a regular basis. Ageing signs can be understood through an increase of the detector noise correlated with an increased dark current. For this purpose, HV scans are performed to measure the noise with increasing voltage and the dark currents. Another way to highlight ageing is through the loss of rate capability of the detectors. During irradiation periods this can be looked through thanks to HV scans performed at various source settings, which are referred to as *source scans*. The loss in rate capability could be understood by a saturation of the measured at higher gamma flux. This effect could be correlated with an increase of the electrodes resistivity. The resistivity is then measured periodically during the year, generally before or after test beam periods by the use of Argon breakdown technic.

5.3.5.1 Longevity scans

The main activity of irradiation periods consist in the *longevity scans* during which the currents of the irradiated chambers are continuously monitored. The two irradiated chambers, RE2-2-NPD-BARC-09 and RE4-2-CERN-166, are both brought to a voltage of 9.8 kV while the source flux can vary depending on the need of experiments using the facility. The currents are recorded on each active gas volume and each gap contribution is then translated into the mean chamber integrated charge as can be seen from Figure 5.30. At the end of each longevity scan the integrated charge accumulated in each chamber is used to update the summary plots providing the collaboration with official results to be spread.

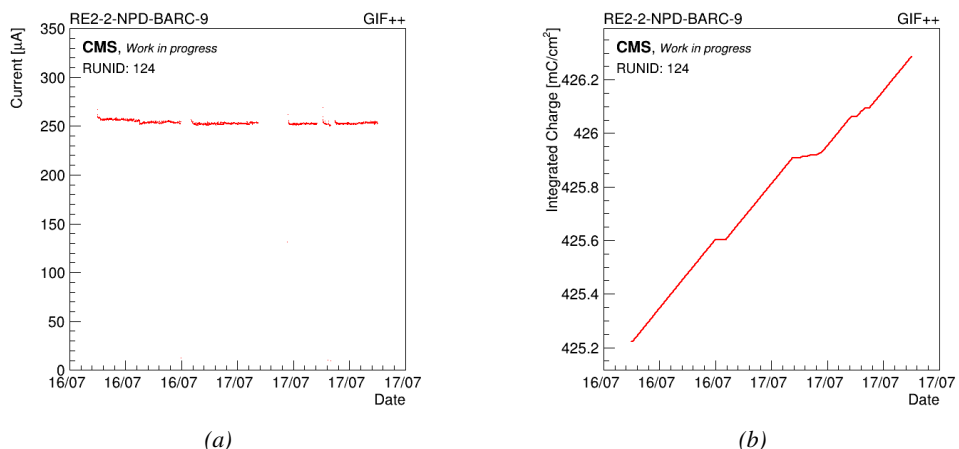


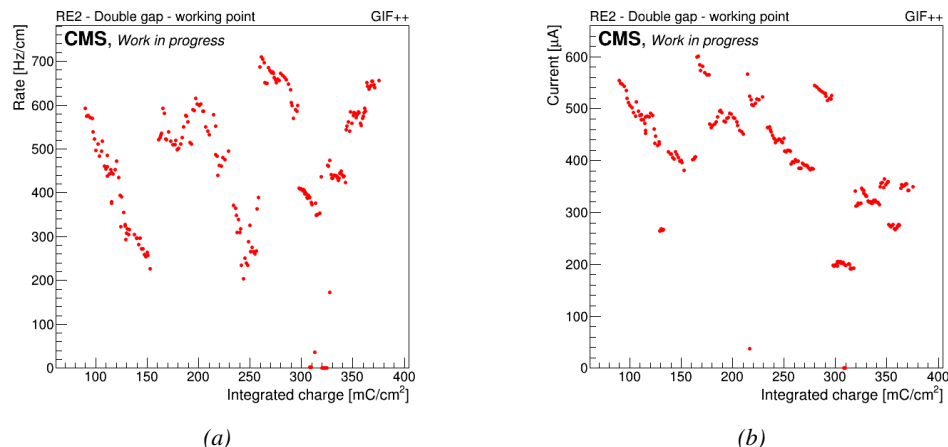
Figure 5.30: Example of current monitoring (Figure 5.30a) and of corresponding integrated charge (Figure 5.30b) of chamber RE2-2-NPD-BARC-09. The decrease of current are related to a decrease of the voltage due to the daily rate scan procedure or to periods during which the source was turned OFF.

5.3.5.2 Daily rate monitoring scans

3205 Every night during longevity scans, the DAQ is used to perform *daily rate scans*. These scans aim
 3206 at keeping track of the gamma rate measured in the irradiated RPCs during longevity but is also
 3207 measured the noise rate at standby voltage and this, for each gap individually. The procedure for
 3208 these HV scans consist in 9 runs for which 50,000 random triggers are requested, corresponding to
 3209 0.5 s of total integrated time.

- 3210 1- All gaps are first left at the irradiation voltage of 9.8 kV to measure the γ rate.
- 3211 2- Then all gaps are brought to the standby voltage of 6.5 kV to measure the noise rate of the full
 detectors.
- 3213 3- Both top gaps (TW and TN) are brought to a voltage equivalent to an OFF status, i.e. 1 kV so
 3214 that the noise contribution of only the bottom gap at standby voltage can be measured.
- 3215 4- The bottom gaps are ramped up toward the working voltage of 9.8 kV to measure their contri-
 3216 bution to the gamma rate estimation.
- 3217 5-8 The steps 3 and 4 are repeated on TN and then on TW, keeping the bottom and the top gap
 3218 which is not of interest at a voltage of 1 kV. This way, the individual contribution to the noise
 3219 and gamma rates are known.
- 3220 9- Finally, both TW and TN are brought to working voltage while the bottom gap is left at 1 kV
 3221 to measure the gamma rate for the full top layer at once.

3222 Finally, the voltages of all gaps are brought back to working voltage for the longevity program
 3223 to continue until the next daily scan.



3224 *Figure 5.31: Example of rate (Figure 5.31a) and current (Figure 5.31b) monitoring of chamber
 3225 RE2-2-NPD-BARC-09 with increasing integrated charge. The variations of rate and current are correlated
 3226 and corresponds to change of source irradiation, gas flow, gas humidity, or environmental conditions.*

3224 Naturally, as this data is taken using Gif++ DAQ, 2 ROOT files containing the DAQ data and
 3225 CAEN data are created for each runs in the exact same way than for efficiency or rate scans taken
 3226 during test beam periods but while the currents are still monitored by the longevity scan and saved

3227 into GIFT++ database for an easy evaluation of the currents to the integrated charge. The Offline
 3228 Analysis tool provides then the DQM page with histograms and daily values can be assembled in
 3229 long term monitoring plots to study the variations of rate and current with increasing integrated
 3230 charge, as presented in Figure 5.31. The rates on every single read-out channel is also tracked to
 3231 control their activity with increasing integrated charge and, this way, understand the appearance of
 3232 hot spots through noisy channels, as showed in Figure 5.32.

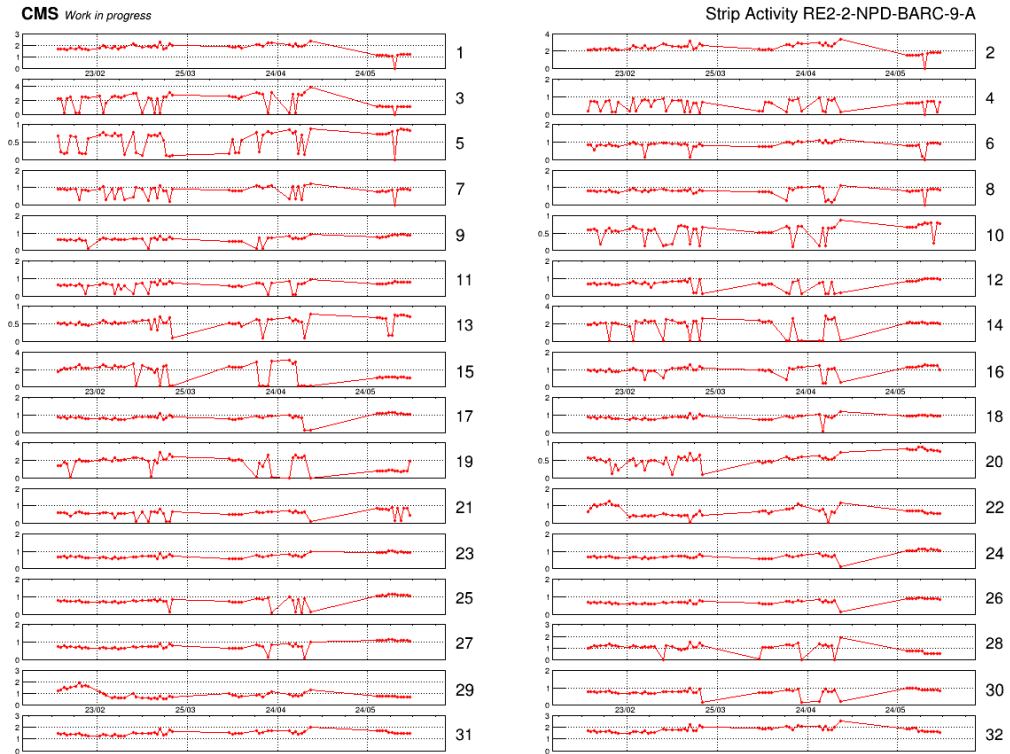


Figure 5.32: Example of strip activity of chamber RE2-2-NPD-BARC-09 monitoring through time. The activity of a strip is defined as the rate of the individual channel normalized to the mean rate measured in the corresponding read-out partition.

3233 5.3.5.3 Weekly noise monitoring scans

3234 Once a week, the source is turned OFF for the CMS RPC to make a noise scan, which consist into
 3235 a HV scan composed of 7 runs and involving both the irradiated but also the reference chambers,
 3236 providing with a weekly monitoring of the evolution of the irradiated chambers noise and dark
 3237 current. The first run is taken at standby voltage for all chambers while the next 6 runs are taken
 3238 with voltages ranging from 9.4 to 9.9 kV in order to have for both type of chambers, RE2 and RE4, a
 3239 coverage of the noise rate in the voltage region in which the efficiency rises and reaches the plateau.

3240 5.3.5.4 Weekly source scans

3241 Directly following the weekly noise scans, HV rate scans are organised at 3 different source settings,
 3242 usually corresponding to ABS 6.8, 4.6 and 3.3. The procedure of these HV scans is strictly similar to

3243 which of weekly noise scans, involving the four RPCs in order to have a weekly comparison of the
 3244 values recorded in every chambers. Measuring with all detectors at the same time allows to get rid
 3245 of potential systematics that might make the rates (noise or gamma) vary from one measurement to
 3246 another. If such systematic effect occurs, it will be observed in all detectors.

3247 **5.3.5.5 Weekly current scans**

3248 The previously detailed daily rate scans, but also the weekly noise and source scans are interesting
 3249 tools to look at an increase of noise rates and dark currents or at a loss of rate capability and point
 3250 to an increase of surface resistivity of the electrodes through the absorption of fluoridric acid. Nev-
 3251 ertheless, periodically measuring the currents on wider high voltage ranges allows to have access
 3252 to the ohmic part of the current driven by the detectors related to the electrodes resistance. This is
 3253 why precise current scans, consisting only in measuring the current driven through the 4 detectors,
 3254 are performed each week. The scan procedure consists in 131 high voltage steps in between 500 V
 3255 and 10 kV by steps of 100 V until the standby voltage of 6.5 kV is reached and then by steps of
 3256 50 V. The current increase in between 500 V and the voltage where charge multiplication starts to
 3257 occur is only driven by the resistance of the detector to current and thus increases linearly. A fit on
 3258 this linear increase of the currents in the range before charge multiplication occurs gives access to
 3259 the resistance of the system electrodes/gas. If any variation of the electrode resistance occurs, the
 3260 global resistance will increase and so will the current. Technically, these scans will record a ROOT
 3261 file per HV step that will have the same format than the CAEN ROOT file saved during other HV
 3262 scans and is also analysed using the Offline Analysis tool to provide with DQM histograms as well
 3263 as standardised I/V tables.

3264 **5.3.5.6 Resistivity measurements**

3265 Aside of the parameters monitored to spot ageing, the resistivity of the HPL planes is measured
 3266 regularly before or after test beam periods through high voltage scans of the detectors operated
 3267 with pure Argon. The electric field strength at which Argon breaks down being well known, the
 3268 breakdown voltage in the detectors is measured and gives an information about the resistance of the
 3269 electrodes, as above the breakdown voltage Argon turns into a conductive plasma and thus does not
 3270 offer electric resistance anymore, which then can be used to calculate the resistivity of the electrode
 3271 material. The Argon line in GIF++ are not kept humid and thus this measurement is not performed
 3272 too often to make sure the electrodes don't dry out, leading to an increase of the electrode resistivity.

3273 **5.3.6 Results and discussions**

3274 Since 2015, CMS RPCs have been irradiated in GIF++ with the goal to reach a total integrated
 3275 charge per irradiated detector of 0.84 C/cm^2 while certifying the detectors to a rate capability of
 3276 600 Hz/cm^2 . As of today, the RE2 and RE4 chambers respectively achieved 51 and 26% of the
 3277 total irradiation program. A few years of irradiation are expected before reaching the end of the
 3278 longevity study and a final answer on whether the detector will be able to live through HL-LHC or
 3279 not. A negative answer to this question would probably lead to solutions to replace the detectors
 3280 before HL-LHC or to improve the shielding of these detectors against background radiation in CMS
 3281 cavern, which could be a more sustainable solution.

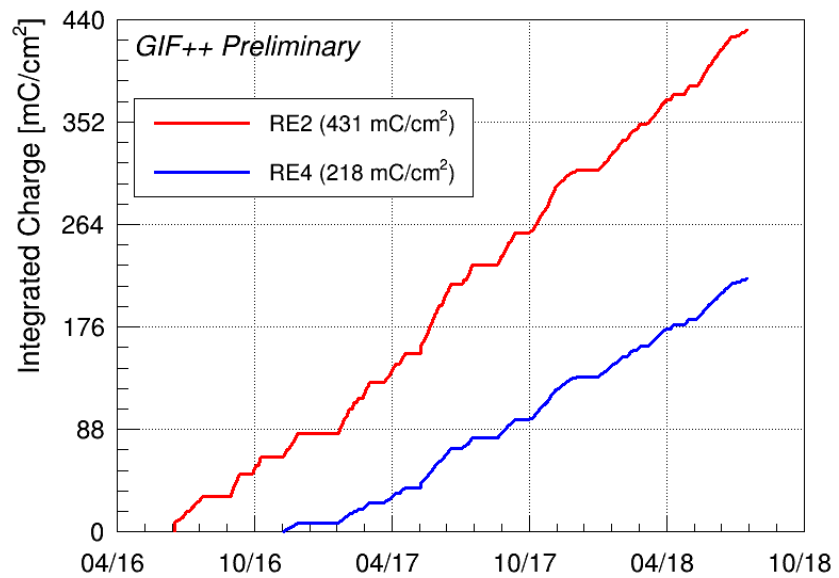


Figure 5.33: Total integrated charge in the irradiated RPCs, RE2–2–NPD–BARC–9 and RE4–2–CERN–165, before starting August 2018 test beam period. The irradiation of the RE2 chamber started in June 2016 while the RE4 chamber couldn't be irradiated before November 2016.

6

3282

3283

3284

Improved RPC investigation and preliminary electronics studies

3285 The extension in the endcap of the RPC sub-system towards higher pseudo-rapidity will bring the
3286 new detectors to be exposed to much more intense background radiations due to the proximity of
3287 the detectors with the beam line. The challenge will be to produce high counting rate detectors
3288 with limited ageing rate to ensure a stable operation of the detector over a period longer than 10
3289 years. In Chapter 4 was discussed the influence of the detector design (number and thickness of
3290 gas volumes, OR system, etc...) on the charge deposition and rate capability. Nevertheless, this
3291 question can also be addressed from the electronics point of view as a better signal to noise ratio
3292 would also mean the possibility to greatly lower the charge threshold on the signals to be detected,
3293 allowing to use the detector at lower gain, hence lowering the charge deposition per avalanche in the
3294 gas volume. Cardarelli showed that the production of low-noise fast FEE could help decreasing the
3295 charge deposition per avalanche at working voltage by an order of magnitude virtually increasing
3296 the life expectancy of such a detector in the same way [268].

3297 **6.1 FEE candidate for the production of iRPCs**

3298 The extension of the third or fourth endcap disks with improved RPCs has been presented in
3299 Chapter 3 together with the expected background levels and the needed requirements from such
3300 detectors to bring out the full potential of the CMS detector by strongly reducing the detection rate
3301 thanks to a more precise reconstruction of the events of interest. An important piece of these iRPCs
3302 will be the Front-End Electronics that will be equipped on the chambers. A fast, low-jitter and low
3303 charge sensitive electronics will help in further reducing the charge deposition in the detector by
3304 making it possible to operate at lower gain.

3305 In the context of the CMS Muon Upgrade, two FEE solutions have been considered to equip the
3306 iRPCs. The baseline for the RPC upgrade is based on the PETIROC ASIC, initially for Time-of-
3307 flight (ToF) applications. A back-up solution is also under study and focuses on a new low-noise

3308 preamplifier designed in INFN laboratories in Rome to replace the preamplification stage of the
 3309 already existing CMS RPC Front-End Board.

3310 The FEEs that are foreseen to equip the new RPCs need to be able to detect charges as small as
 3311 10 fC. Not only the new electronics need to be fast and reliable, they also should be able to sustain
 3312 the high radiation the detectors will be subjected to in the region closest to the beam.

3313 6.1.1 CMS RPCROC: the RPC upgrade baseline

3314 Designed by Weeroc, a spin-off company from the french OMEGA laboratory, the PETIROC 2A
 3315 consists in a fast and low jitter 32-channel ASIC originally developed to read-out Silicon Photomul-
 3316 tiplier (SiPM) in ToF applications and that allows for precise time measurements [269, 270]. The
 3317 ASIC uses an AMS 350 ns SiGe technology. The block diagram of the ASIC is showed on Fig-
 3318 ure 6.1. A 10-bit DAC allows to adjust the trigger level in a dynamical range spanning from 0.5 to
 3319 a few tens of photoelectrons and a 6-bit DAC to adjust the response of each individual channel to
 3320 similar a level.

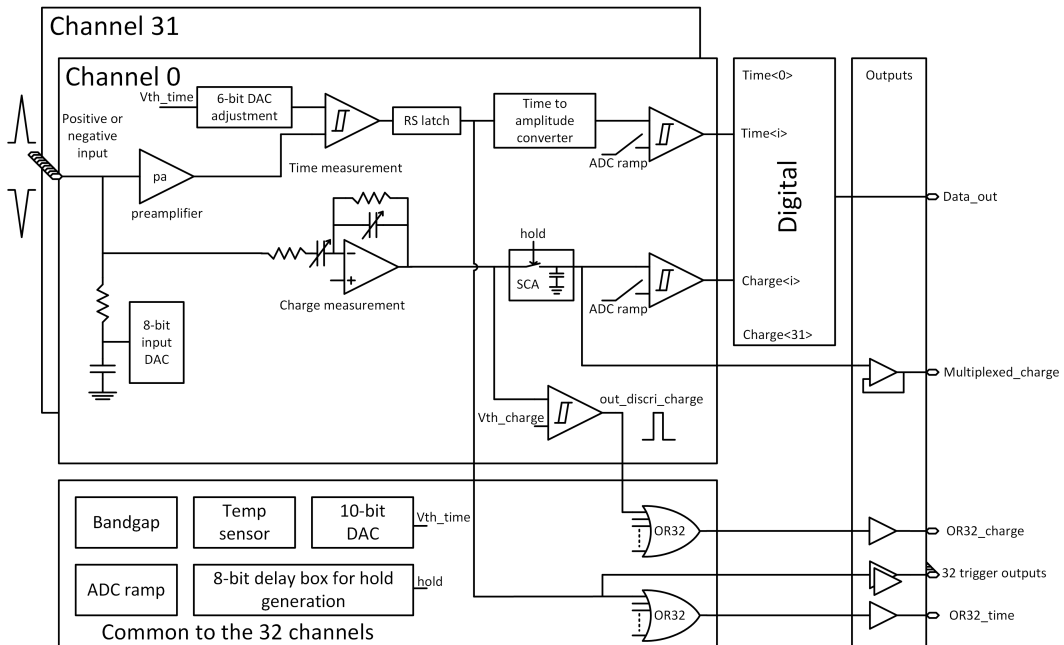


Figure 6.1: PETIROC 2A block diagram.

3321 Nevertheless, in order to adapt this ASIC to CMS, modifications were brought to the PETIROC [177].
 3322 In the new CMS RPCROC, the measurement of the charge will be performed by a TimeOverTech-
 3323 nique, taking profit of the capacity the ASIC has in measuring both the leading and trailing edges of the
 3324 input signals. The dynamic range will be expanded towards lower values to allow for the detection
 3325 of charges as low as 10 fC. Due to the radiation levels that are foreseen at the level of the iRPCs, the
 3326 SiGe technology will be replaced by the Taiwan Semiconductor Manufacturing Company (TSMC)
 3327 130 nm CMOS, to increase its radiation hardness while keeping fast pre-amplification and discrimi-
 3328 nation with a very low jitter that can reach less than 20 ps if no internal clock is used, as can be seen
 3329 from Figure 6.2. The ASIC is associated with an FPGA which purpose is to measure time thanks to

3330 a TDC with a time resolution of 50-100 ps developed by Tsinghua University and that will provide
 3331 a measurement of the signal position along the strip with a precision of a few cm by measuring the
 3332 signal timing on both ends of the strips. In order to read-out all 96 strips, 3 ASICs and 3 TDCs, each
 3333 having an increased number of 64-channels, are hosted on a FEB attached to the chamber.

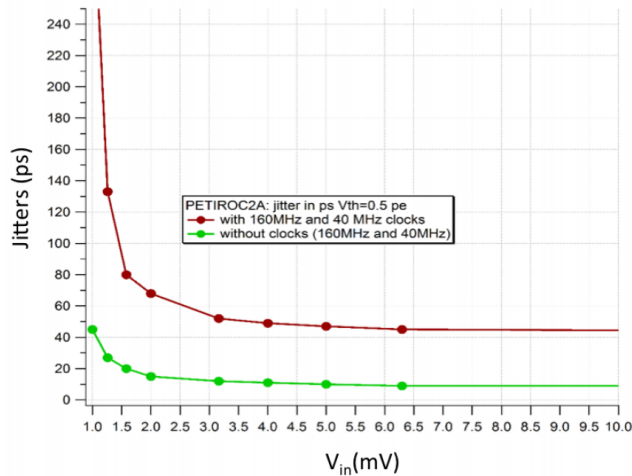


Figure 6.2: The PETIROC time jitter as a function of the input signal amplitude, measured with and without internal clocks.

3334 6.1.2 INFN Front-End Electronics: a robust back-up solution

3335 6.2 Preliminary tests at CERN

7

3336

3337

Conclusions and outlooks

3338 **7.1 Conclusions**

3339 **7.2 Outlooks**

A

3340

3341

A data acquisition software for CAEN VME TDCs

3342

3343 Certifying detectors in the perspective of HL-LHC required to develop tools for the GIF++ experi-
3344 ment. Among them was the C++ Data Acquisition (DAQ) software that allows to make the commu-
3345 nications in between a computer and TDC modules in order to retrieve the RPC data [271]. In this
3346 appendix, details about this software, as of how the software was written, how it functions and how
3347 it can be exported to another similar setup, will be given.

3348 A.1 GIF++ DAQ file tree

3349 GIF++ DAQ source code is fully available on github at [https://github.com/afagot/GIF_](https://github.com/afagot/GIF_DAQ)
3350 DAQ. The software requires 3 non-optional dependencies:

- 3351 • CAEN USB Driver, to mount the VME hardware,
3352 • CAEN VME Library, to communicate with the VME hardware, and
3353 • ROOT, to organize the collected data into a TTree.

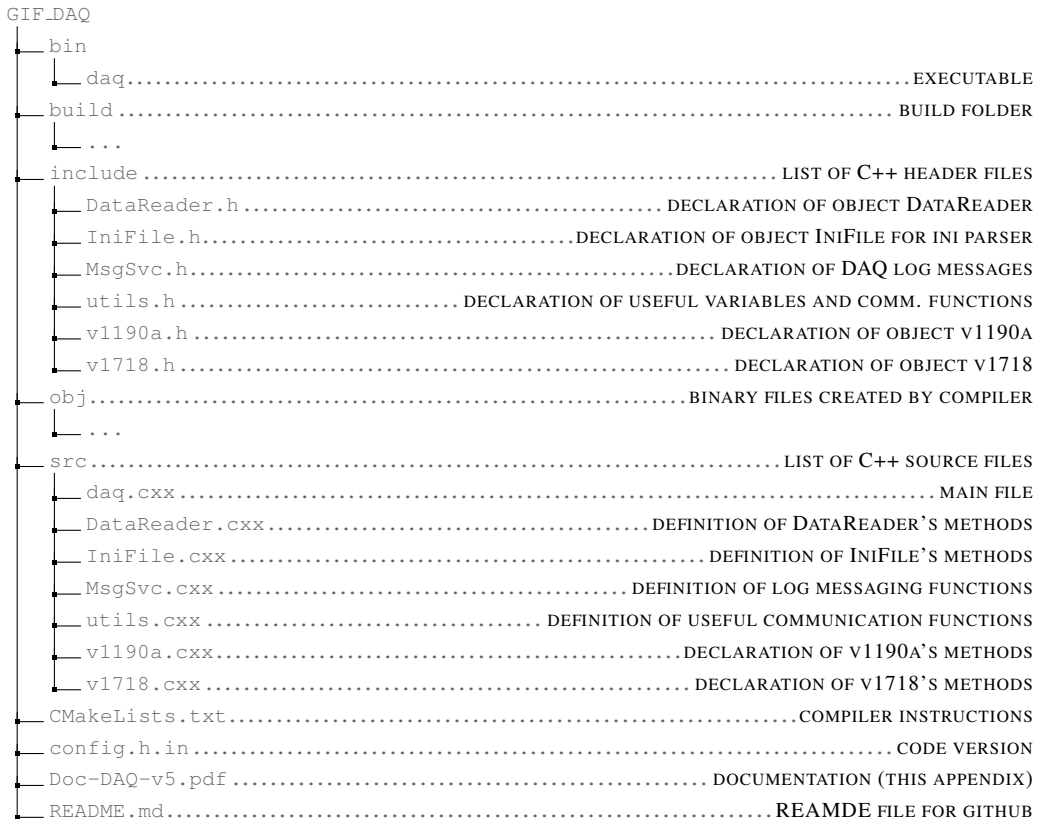
3354 The CAEN VME library will not be packaged by distributions and will need to be installed man-
3355 ually. To compile the GIF++ DAQ project via a terminal, from the DAQ folder use the command:

```
3356 mkdir build  
3357 cd build  
3358 cmake ..  
3359 make install
```

3358 The source code tree is provided below along with comments to give an overview of the files' con-
3359 tent. The different objects created for this project (`v1718`, `v1190a`, `IniFile` & `DataReader`) will be

3360 described in details in the following sections.

3361



3362 A.2 Usage of the DAQ

3363 GIF++ DAQ, as used in GIF++, is not a standalone software. Indeed, the system being more com-
 3364 plexe, the DAQ only is a sub-layer of the software architecture developped to control and monitor
 3365 the RPCs that are placed into the bunker for performance study in an irradiated environment. The top
 3366 layer of GIF++ is a Web Detector Control System (webDCS) application. The DAQ is only called
 3367 by the webDCS when data needs to be acquired. The webDCS operates the DAQ through command
 3368 line. To start the DAQ, the webDCS calls:

3369

3370 bin/daq /path/to/the/log/file/in/the/output/data/folder

3371 where /path/to/the/log/file/in/the/output/data/folder is the only argument required. This
 3372 log file is important for the webDCS as this file contains all the content of the communication of the
 3373 webDCS and the different systems monitored by the webDCS. Its content is constantly displayed
 3374 during data taking for the users to be able to follow the operations. The communication messages
 3375 are normally sent to the webDCS log file via the functions declared in file `MsgSvc.h`, typically
 3376 `MSG_INFO(string message)`.

3377

3378 A.3 Description of the readout setup

3379 The CMS RPC setup at GIF++ counts 5 V1190A Time-to-Digital Converter (TDC) manufactured
 3380 by CAEN [257]. V1190A are VME units accepting 128 independent Multi-Hit/Multi-Event TDC
 3381 channels whose signals are treated by 4 100 ps high performance TDC chips developed by CERN
 3382 / ECP-MIC Division. The communication between the computer and the TDCs to transfer data is
 3383 done via a V1718 VME master module also manufactured by CAEN and operated from a USB
 3384 port [258]. These VME modules are all hosted into a 6U VME 6021 powered crate manufactured by
 3385 W-Ie-Ne-R than can accommodate up to 21 VME bus cards [272]. These 3 components of the DAQ
 3386 setup are shown in Figure A.1.

3387

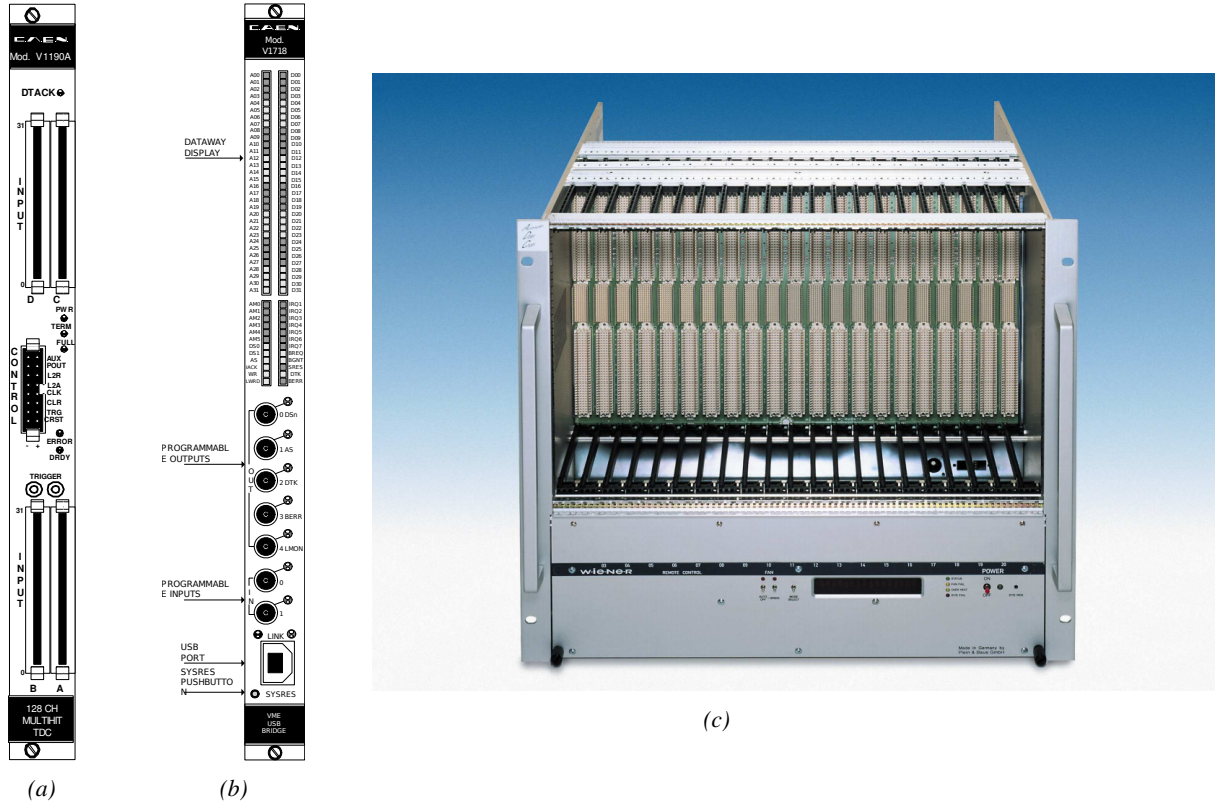


Figure A.1: (A.1a) View of the front panel of a V1190A TDC module [257]. (A.1b) View of the front panel of a V1718 Bridge module [258]. (A.1c) View of the front panel of a 6U 6021 VME crate [272].

3388 A.4 Data read-out

3389 To efficiently perform a data readout algorithm, C++ objects to handle the VME modules (TDCs
 3390 and VME bridge) have been created along with objects to store data and read the configuration file
 3391 that comes as an input of the DAQ software.

3392

A.4.1 V1190A TDCs

3394 The DAQ used at GIF takes profit of the *Trigger Matching Mode* offered by V1190A modules.
 3395 This setting is enabled through the method `v1190a::SetTrigMatching (int ntdcs)` where `ntdcs`
 3396 is the total number of TDCs in the setup this setting needs to be enabled for (Source Code A.1). A
 3397 trigger matching is performed in between a trigger time tag, a trigger signal sent into the TRIGGER
 3398 input of the TDC visible on Figure A.1a, and the channel time measurements, signals recorded from
 3399 the detectors under test in our case. Control over this data acquisition mode, explained through
 3400 Figure A.2, is offered via 4 programmable parameters:

- 3401 • **match window:** the matching between a trigger and a hit is done within a programmable time
 3402 window. This is set via the method
`void v1190a::SetTrigWindowWidth(Uint windowHeight, int ntdcs)`
- 3404 • **window offset:** temporal distance between the trigger tag and the start of the trigger matching
 3405 window. This is set via the method
`void v1190a::SetTrigWindowWidth(Uint windowHeight, int ntdcs)`
- 3407 • **extra search margin:** an extended time window is used to ensure that all matching hits are
 3408 found. This is set via the method
`void v1190a::SetTrigSearchMargin(Uint searchMargin, int ntdcs)`
- 3410 • **reject margin:** older hits are automatically rejected to prevent buffer overflows and to speed
 3411 up the search time. This is set via the method
`void v1190a::SetTrigRejectionMargin(Uint rejectMargin, int ntdcs)`

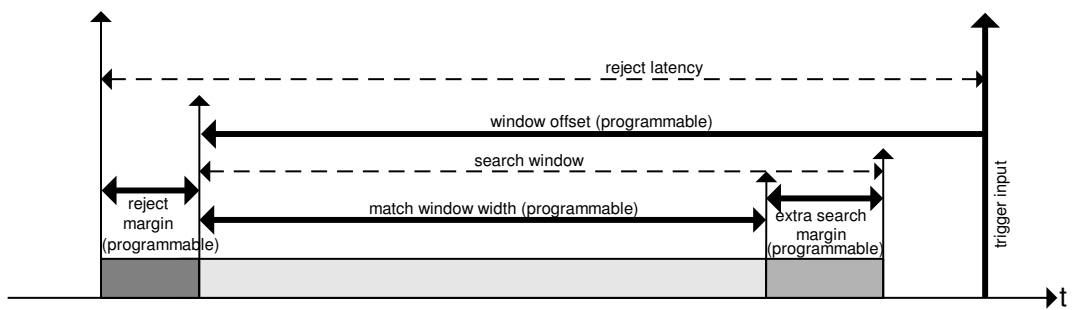


Figure A.2: Module V1190A Trigger Matching Mode timing diagram [257].

3413 Each of these 4 parameters are given in number of clocks, 1 clock being 25 ns long. It is easy to
 3414 understand at this level that there are 3 possible functioning settings:

- 3415 • **1:** the match window is entirely contained after the trigger signal,
- 3416 • **2:** the match window overlaps the trigger signal, or
- 3417 • **3:** the match window is entirely contained before the trigger signal as displayed on Figure A.2.

3418 In both the first and second cases, the sum of the window width and of the offset can be set to
 3419 a maximum of 40 clocks, which corresponds to 1 μ s. Evidently, the offset can be negative, allowing

3420 for a longer match window, with the constraint of having the window ending at most 1 μ s after the
3421 trigger signal. In the third case, the maximum negative offset allowed is of 2048 clocks (12 bit) cor-
3422 responding to 51.2 μ s, the match window being strictly smaller than the offset. In the case of GIF++,
3423 the choice has been made to use this last setting by delaying the trigger signal. During the studies
3424 performed in GIF++, both the efficiency of the RPCs, probed using a muon beam, and the noise or
3425 gamma background rate are monitored. The extra search and reject margins are left unused.

3426 To probe the efficiency of RPC detectors, the trigger time tag is provided by the coïncidence of
3427 scintillators when a bunch of muons passes through GIF++ area is used to trigger the data acquisi-
3428 tion. For this measurement, it is useful to reduce the match window width only to contain the muon
3429 information. Indeed, the delay in between a trigger signal and the detection of the corresponding
3430 muon in the RPC being very contant (typically a few tens of ns due to jitter and cable length), the
3431 muon signals are very localised in time. Thus, due to a delay of approximalety 325 ns in between
3432 the muons and the trigger, the settings were chosen to have a window width of 24 clocks (600 ns)
3433 centered on the muon peak thanks to a negative offset of 29 clocks (725 ns).

3434 On the otherhand, monitoring the rates don't require for the DAQ to look at a specific time window.
3435 It is important to integrate enough time to have a robust measurement of the rate as the number of
3436 hits per time unit. The triggering signal is provided by the pulse generator integrated into the com-
3437 munication module V1718 at a frequency of 100 Hz to ensure that the data taking occurs in a random
3438 way, uncorrelated with beam physics, to probe only the irradiation spectrum on the detectors. The
3439 match window is set to 400 clocks (10 μ s) and the negative offset to 401 clocks as it needs to exceed
3440 the value of the match window.

3441

3442 The v1190a object, defined in the DAQ software as in Source Code A.1, offers the possi-
3443 bility to store all TDCs in the readout setup into a single object containing a list of hardware ad-
3444 dresses (addresses to access the TDCs' buffer through the VME crate) and each constructor and
3445 method acts on the list of TDCs to set the different acquisition parameters as describe above.
3446 The type of trigger matching is chosen with `v1190a::SetTrigMatching()` and the time substrac-
3447 tion, used to have a time measurement referring to the beggining of the time window, is set by
3448 `v1190a::SetTrigTimeSubtraction()`. Then, the wiwdow width and offset are respectively set
3449 thanks to `v1190a::SetTrigWindowWidth()` and `v1190a::SetTrigWindowOffset()`. The rejection
3450 and extra search margin, even if left unused and hence set to a default value of 0, can be set through
3451 `v1190a::SetTrigRejectionMargin()` and `v1190a::SetTrigSearchMargin()`. These methods are
3452 then called in `v1190a::SetTrigConfiguration()` that uses the information contained in the config-
3453 uration file `IniFile *iniFile` to set the different TDC parameters. A thorough explaination of the
3454 content of the configuration file is provided in Section A.5.2.

3455

3456 Among the other methods of class `v1190a` can be found a set of the detection mode (`v1190a::SetTDC`
3457 `DetectionMode()`), of the TDC time resolution (`v1190a::SetTDCResolution()`), of the dead time
3458 in between two consecutive signals recorded into a single channel (`v1190a::SetTDCDeadTime()`) or
3459 of the maximal number of signals that can be recorded per event (`v1190a::SetTDCEventSize()`). To
3460 help with setting these parameters, `enum` were used (`EdgeMode`, `Resolution`, `DeadTime` and `HitMax`
3461 are defined in `include/v1190a.h`).

```

3462
class v1190a
{
    private :
        long             Handle;
        vector<Data32>   Address;
        CVDataWidth      DataWidth;
        CVAAddressModifier AddressModifier;

    public:

        v1190a(long handle, IniFile *inifile, int ntdcs);
        ~v1190a();
        Data16 write_op_reg(Data32 address, int code, string error);
        Data16 read_op_reg(Data32 address, string error);
        void Reset(int ntdcs);
        void Clear(int ntdcs);
        void TestWR(Data16 value,int ntdcs);
        void CheckTDCStatus(int ntdcs);
        void CheckCommunication(int ntdcs);
        void SetTDCTestMode(Data16 mode,int ntdcs);
        void SetTrigMatching(int ntdcs);
        void SetTrigTimeSubtraction(Data16 mode,int ntdcs);
        void SetTrigWindowWidth(Uint windowHeight,int ntdcs);
        void SetTrigWindowOffset(Uint windowOffset,int ntdcs);
        void SetTrigSearchMargin(Uint searchMargin,int ntdcs);
        void SetTrigRejectionMargin(Uint rejectMargin,int ntdcs);
        void GetTrigConfiguration(int ntdcs);
        void SetTrigConfiguration(IniFile *inifile,int ntdcs);
        void SetTDCDetectionMode(Data16 mode,int ntdcs);
        void SetTDCResolution(Data16 lsb,int ntdcs);
        void SetTDCDeadTime(Data16 time,int ntdcs);
        void SetTDCHeadTrailer(Data16 mode,int ntdcs);
        void SetTDCEventSize(Data16 size,int ntdcs);
        void SwitchChannels(IniFile *inifile,int ntdcs);
        void SetIRQ(Data32 level, Data32 count,int ntdcs);
        void SetBlockTransferMode(Data16 mode,int ntdcs);
        void Set(IniFile *inifile,int ntdcs);
        void CheckStatus(CVErrorCodes status) const;
        int ReadBlockD32(Uint tdc, const Data16 address,
                         Data32 *data, const Uint words, bool ignore_berr);
        Uint Read(RAWData *DataList,int ntdcs);
};

3463

```

3464 *Source Code A.1: Description of C++ object v1190a.*

3465 The detection mode corresponds to the type of edge detection the TDC will be using to
 3466 record the data. The TDCs can record the time stamp of the leading edge alone, of the trailing edge
 3467 alone, of both or they can operate in pair mode, meaning that the leading edge is recorded together
 3468 with the time difference in between leading and trailing edges. This last mode is not very practical
 3469 for the case of GIFT++ measurements as the information is coded into a single words in the TDC's
 3470 buffer, putting strong constraints on the time window and duration of the input signals. Indeed,
 3471 when recording the edges individually (single edge or both edges), a 32-bit word, of which 18 are
 3472 used to provide the time information alone, is stored into memory for each signal edge. With the
 3473 pair mode, instead of having one 32-bit word per edge, only a single 32-bit word is written of which
 3474 12 are used for the leading edge time information and 6 for the width of the pulse, as described on
 3475 p73 of reference [257]. This way, even though the pair mode is convenient to use as it automatically

3476 correlates a leading edge with the corresponding signal width in a single word, it is advised to be
 3477 careful when using it and to be aware of the extra time constraints (for both leading time and signal
 3478 width) that will come for choosing this setting. If it is necessary to work with large input signals,
 3479 the mode recording both edges will be preferred to the pair mode and the association of a leading
 3480 and trailing edges pair will then be performed offline by the user. Then, the time resolution is to be
 3481 chosen in a range from 100 to 800 ps, the dead time in a range from 5 to 100 ns, and the maximal
 3482 number of hits per event in a range from 0 to 128 with the possibility to choose to have no limits.

3483 A.4.2 DataReader

3484 Enabled thanks to `v1190a::SetBlockTransferMode()`, the data transfer is done via Block Transfer
 3485 (BLT). Using BLT allows to transfer a fixed number of events called a *block*. This is used together
 3486 with an Almost Full Level (AFL) of the TDCs' output buffers, defined through `v1190a::SetIRQ()`.
 3487 This AFL gives the maximum amount of 32735 words (16 bits, corresponding to the depth of a TDC
 3488 output buffer) that can be written in a buffer before an Interrupt Request (IRQ) is generated and seen by
 3489 the VME Bridge V1718, which sends a `BUSY` signal intended to stopping the data acquisition during
 3490 the transfer of the content of each TDC buffers before resuming. For each trigger, 6 words or more
 3491 are written into the TDC buffer:

- 3492 • **a global header** providing information of the event number since the beginning of the data
 3493 acquisition,
- 3494 • **a TDC header** which is enabled thanks to `v1190a::SetTDCHeadTrailer()`,
- 3495 • **the TDC data (if any)**, 1 for each hit recorded during the event, providing the channel and the
 3496 time stamp associated to the hit,
- 3497 • **a TDC error** providing error flags,
- 3498 • **a TDC trailer** which is enabled thanks to `v1190a::SetTDCHeadTrailer()`,
- 3499 • **a global trigger time tag** that provides the absolute trigger time relatively to the last reset,
 3500 and
- 3501 • **a global trailer** providing the total word count in the event.

3502 CMS RPC FEEs provide with 100 ns long LVDS output signals that are injected into the TDCs'
 3503 input. Any avalanche signal that gives a signal above the FEEs threshold is thus recorded by the
 3504 TDCs as a hit within the match window. Each hit is assigned to a specific TDC channel with a time
 3505 stamp, with a precision of 100 ps. The reference time, $t_0 = 0$, is provided by the beginning of the
 3506 match window. Thus for each trigger, coming from a scintillator coincidence or the pulse generator,
 3507 a list of hits is stored into the TDCs' buffers and will then be transferred into a ROOT Tree.
 3508 When the BLT is used, it is easy to understand that the maximum number of words that have been set
 3509 as AFL will not be a finite number of events or, at least, the number of events that would be recorded
 3510 into the TDC buffers will not be a multiple of the block size. In the last BLT cycle to transfer data,
 3511 the number of events to transfer will most probably be lower than the block size. In that case, the
 3512 TDC can add fillers at the end of the block but this option requires to send more data to the computer
 3513 and is thus a little slower. Another solution is to finish the transfer after the last event by sending a
 3514 bus error that states that the BLT reached the last event in the pile. This method has been chosen in

3515 GIF++.

3516 Due to irradiation, an event in GIF++ can count up to 300 words per TDC. A limit of 4096 words
 3517 (12 bits) has been set to generate IRQ which represent from 14 to almost 700 events depending on
 3518 the average of hits collected per event. Then the block size has been set to 100 events with enabled
 3519 bus errors. When an AFL is reached for one of the TDCs, the VME bridge stops the acquisition by
 3520 sending a BUSY signal.

3521

3522 The data is then transferred one TDC at a time into a structure called `RAWData` (Source Code A.2).
 3523 Note that the structure as presented here is used when a single edge detection is used as there is only
 3524 one time stamp list associated to the hits. When using detection on both edges, a second time stamp
 3525 list could be added and when using pair detection, a list with the signal width could be added instead.
 3526

```
3527   struct RAWData {
      vector<int>           *EventList;
      vector<int>           *NHitsList;
      vector<int>           *QFlagList;
      vector<vector<int> >  *ChannelList;
      vector<vector<float> > *TimeStampList;
    };
```

3528

Source Code A.2: Description of data holding C++ structure `RAWData`.

```
3529 class DataReader
{
  private:
    bool      StopFlag;
    IniFile  *iniFile;
    Data32   MaxTriggers;
    v1718    *VME;
    int       nTDCs;
    v1190a   *TDCs;
    RAWData  TDCData;

  public:
    DataReader();
    virtual ~DataReader();
    void     SetIniFile(string inifilename);
    void     SetMaxTriggers();
    Data32   GetMaxTriggers();
    void     SetVME();
    void     SetTDC();
    int      GetQFlag(UINT it);
    void     Init(string inifilename);
    void     FlushBuffer();
    void     Update();
    string   GetFileName();
    void     WriteRunRegistry(string filename);
    void     Run();
};
```

3530

Source Code A.3: Description of C++ object `DataReader`.

3531

In order to organize the data transfer and the data storage, an object called `DataReader` was
 3532 created (Source Code A.3). On one hand, it has `v1718` and `v1190a` objects as private members for
 3533 communication purposes, such as VME modules settings via the configuration file `*iniFile` or data

3534 read-out through `v1190a::Read()` and on the other hand, it contains the structure `RAWData` that allows
 3535 to organise the data in vectors reproducing the tree structure of a ROOT file.
 3536 Each event is transferred from `TDCData` and saved into branches of a ROOT `TTree` as 3 integers
 3537 that represent the event ID (`EventCount`), the number of hits read from the TDCs (`nHits`), and the
 3538 quality flag that provides information for any problem in the data transfer (`qflag`), and 2 lists of
 3539 `nHits` elements containing the fired TDC channels (`TDCCh`) and their respective time stamps (`TDCTS`),
 3540 as presented in Source Code A.4. The ROOT file file is named using information contained into
 3541 the configuration file, presented in section A.5.2. The needed information is extracted using method
 3542 `DataReader::GetFileName()` and allow to build the output filename format `ScanXXXXXX_HVX_DAQ.root`
 3543 where `ScanXXXXXX` is a 6 digit number representing the scan number into GIF++ database and `HVX`
 3544 the HV step within the scan that can be more than a single digit. An example of ROOT data file is
 3545 provided with Figure A.3.

```
3546
RAWData TDCData;
TFile *outputFile = new TFile(outputFileName.c_str(), "recreate");
TTree *RAWDataTree = new TTree("RAWData", "RAWData");

int EventCount = -9;
int nHits = -8;
int qflag = -7;
vector<int> TDCCh;
vector<float> TDCTS;

RAWDataTree->Branch("EventNumber", &EventCount, "EventNumber/I");
RAWDataTree->Branch("number_of_hits", &nHits, "number_of_hits/I");
RAWDataTree->Branch("Quality_flag", &qflag, "Quality_flag/I");
RAWDataTree->Branch("TDC_channel", &TDCCh);
RAWDataTree->Branch("TDC_TimeStamp", &TDCTS);

//...
//Here read the TDC data using v1190a::Read() and place it into
//TDCData for as long as you didn't collect the requested amount
//of data.
//...

for(Uint i=0; i<TDCData.EventList->size(); i++) {
    EventCount = TDCData.EventList->at(i);
    nHits = TDCData.NHitsList->at(i);
    qflag = TDCData.QFlagList->at(i);
    TDCCh = TDCData.ChannelList->at(i);
    TDCTS = TDCData.TimeStampList->at(i);
    RAWDataTree->Fill();
}
```

3548 *Source Code A.4: Highlight of the data transfer and organisation within `DataReader::Run()` after the data
 has been collected into `TDCData`.*

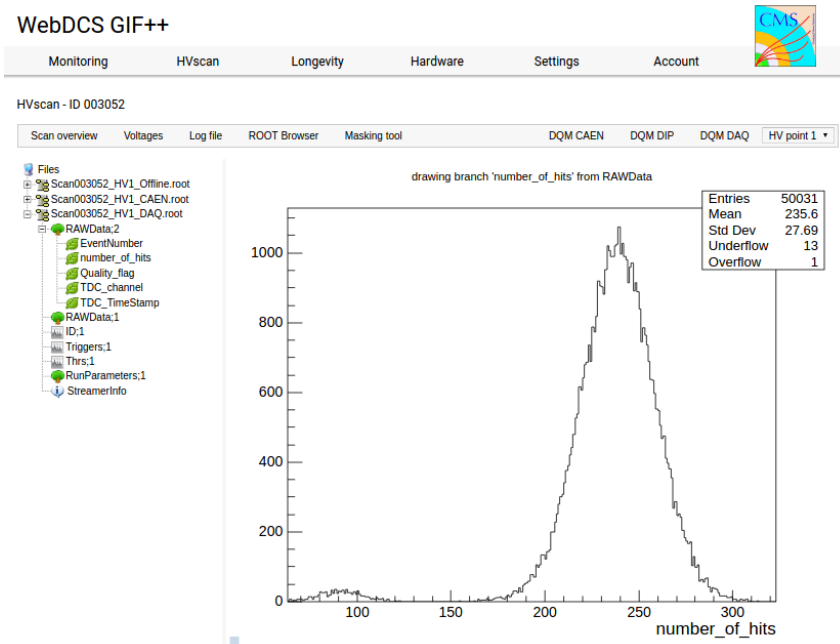


Figure A.3: Structure of the ROOT output file generated by the DAQ. The 5 branches (EventNumber, number_of_hits, Quality_flag, TDC_channel and TDC_TimeStamp) are visible on the left panel of the ROOT browser. On the right panel is visible the histogram corresponding to the variable nHits. In this specific example, there were approximately 50k events recorded to measure the gamma irradiation rate on the detectors. Each event is stored as a single entry in the TTree.

3549 A.4.3 Data quality flag

3550 Among the parameters that are recorded for each event, the quality flag is determined on the fly
 3551 by checking the data recorded by every single TDC. An `enum` called `QualityFlag` was written to
 3552 associate the key `GOOD` to the integer 1 and `CORRUPTED` to 0. From method `v1190a::Read()`, it can
 3553 be understood that the content of each TDC buffer is readout one TDC at a time. Entries are created
 3554 in the data list for the first TDC and then, when the second buffer is readout, events corresponding
 3555 to entries that have already been created to store data for the previous TDC are added to the existing
 3556 list element. On the contrary, when an event entry has not been yet created in the data list, a new
 3557 entry is created.

3558 It is possible that each TDC buffer contains a different number of events. In cases where the first
 3559 element in the buffer list is an event for corresponds to a new entry, the difference in between the
 3560 entry from the buffer and the last entry in the data list is recorded and checked. If it is greater than 1,
 3561 what should never be the case, the quality flag is set to `CORRUPTED` for this TDC and an empty entry
 3562 is created in the place of the missing ones. Missing entries are believe to be the result of a bad hold
 3563 on the TDC buffers at the moment of the readout. Indeed, the software hold is effective only on 1
 3564 TDC at a time and no solution as been found yet to completely block the writting in the buffers when
 3565 an IRQ is received.

3566 At the end of each BLT cycle, the ID of the last entry stored for each TDC buffer is not recorded.
 3567 When starting the next cycle, if the first entry in the pile corresponds to an event already existing
 3568 in the list, the readout will start from this list element and will not be able to check the difference

3569 in between this entry's ID and the one of the last entry that was recorded for this TDC buffer in
 3570 the previous cycle. In the case events were missing, the flag stays at its initial value of 0, which is
 3571 similar to CORRUPTED and it is assumed that then this TDC will not contribute to number_of_hits,
 3572 TDC_channel or TDC_TimeStamp. Finally, since there will be 1 RAWData entry per TDC for each event
 3573 (meaning nTDCs entries, referring to DataReader private attribute), the individual flags of each TDC
 3574 will be added together. The final format is an integer composed nTDCs digits where each digit is the
 3575 flag of a specific TDC. This is constructed using powers of 10 like follows:

3576 TDC 0: QFlag = $10^0 \times \text{QualityFlag}$

3577 TDC 1: QFlag = $10^1 \times \text{QualityFlag}$

3578 ...

3579 TDC N: QFlag = $10^N \times \text{QualityFlag}$

3580 and the final flag to be with N digits:

3581 QFlag = n....3210

3582 each digit being 1 or 0. Below is given an example with a 4 TDCs setup.

3583 If all TDCs were good : QFlag = 1111,

3584 but if TDC 2 was corrupted : QFlag = 1011.

3585 When data taking is over and the data contained in the dynamical RAWData structure is transferred
 3586 to the ROOT file, all the 0s are changed into 2s by calling the method DataReader::GetQFlag().
 3587 This will help translating the flag without knowing the number of TDCs beforehand. Indeed, a flag
 3588 111 could be due to a 3 TDC setup with 3 good individual TDC flags or to a more than 3 TDC setup
 3589 with TDCs those ID is greater than 2 being CORRUPTED, thus giving a 0.

3590 The quality flag has been introduced quite late, in October 2017 only, to the list of GIFT++ DAQ
 3591 parameters to be recorded into the output ROOT file. Before this addition, the missing data, corrupting
 3592 the quality for the offline analysis, was contributing to artificially fill data with lower multiplicity.
 3593 Looking at TBranch number_of_hits provides an information about the data of the full GIFT++
 3594 setup. When a TDC is not able to transfer data for a specific event, the effect is a reduction of the
 3595 total number of hits recorded in the full setup, this is what can be seen from Figure A.4. After offline
 3596 reconstruction detector by detector, the effect of missing events can be seen in the artificially filled
 3597 bin at multiplicity 0 shown in Figure A.5. Nonetheless, for data with high irradiation levels, as it is
 3598 the case for Figure A.5a, discarding the fake multiplicity 0 data can be done easily during the offline
 3599 analysis. At lower radiation, the missing events contribution becomes more problematic as the mul-
 3600 tiplicity distribution overlaps the multiplicity 0 and that in the same time the proportion of missing
 3601 events decreases. Attempts to fit the distribution with a Poisson or skew distribution function were
 3602 not conclusive and this very problem has been at the origin of the quality flag that allows to give a
 3603 non ambiguous information about each event quality.

3604

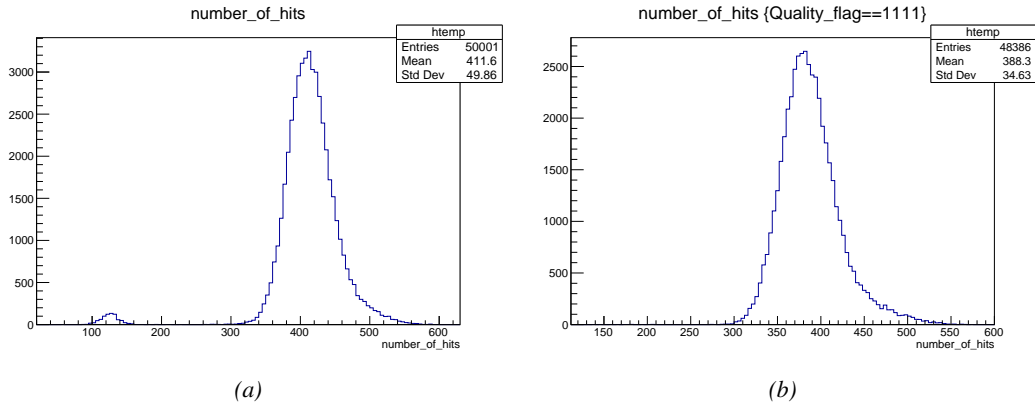


Figure A.4: The effect of the quality flag is explained by presenting the content of TBranch `number_of_hits` of a data file without `Quality_flag` in Figure A.4a and the content of the same TBranch for data corresponding to a `Quality_flag` where all TDCs were labelled as `GOOD` in Figure A.4b taken with similar conditions. It can be noted that the number of entries in Figure A.4b is slightly lower than in Figure A.4a due to the excluded events.

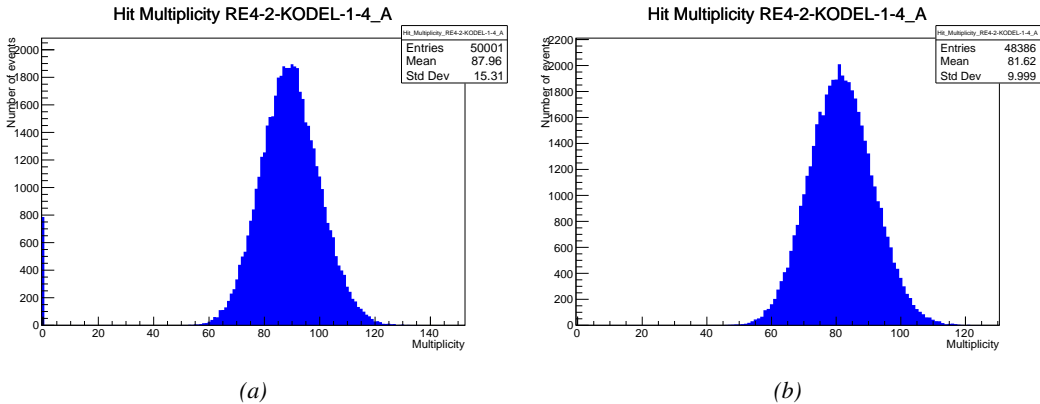


Figure A.5: Using the same data as previously showed in Figure A.4, the effect of the quality flag is explained by presenting the reconstructed hit multiplicity of a data file without `Quality_flag` in Figure A.5a and the reconstructed content of the same RPC partition for data corresponding to a `Quality_flag` where all TDCs were labelled as `GOOD` in Figure A.5b taken with similar conditions. The artificial high content of bin 0 is completely suppressed.

3605 A.5 Communications

3606 To ensure data readout and dialog in between the machine and the TDCs or in between the webDCS
 3607 and the DAQ, different communication solutions were used. First of all, it is important to have a
 3608 module to allow the communication in between the TDCs and the computer from which the DAQ
 3609 operates. When this communication is effective, shifters using the webDCS to control data taking
 3610 can thus send instructions to the DAQ.

3612 **A.5.1 V1718 USB Bridge**

3613 In the previous section, the data transfer as been discussed. The importance of the `v1718` object
 3614 (Source Code A.5), used as private member of `DataReader`, was not explicited. VME master
 3615 modules are used for communication purposes as they host the USB port that connects the pow-
 3616 ered crate buffer to the computer were the DAQ is installed. From the source code point of view,
 3617 this object is used to control the communication status, by reading the returned error codes with
 3618 `v1718::CheckStatus()`, or to check for IRQs coming from the TDCs through `v1718::CheckIRQ()`.
 3619 To ensure that triggers are blocked at the hardware level, a NIM pulse is sent out of one of the two
 3620 first programmable outputs of the module (`v1718::SendBUSY()`) to the VETO of the coincidence
 3621 module where the trigger signals originate. As long as this signal is ON, no trigger can reach the
 3622 TDCs anymore. Finally, used in the case of noise and background measurements in which the trig-
 3623 ger needs not to be provided by the muon beam but by an uncorrelated source, a pulse generator
 3624 is enabled with `v1718::RDMTriggerPulse()`. The "random" pulse is sent through the third and
 3625 fourth outputs of the module. Both the BUSY signal and the random pulse are shaped in the method
 3626 `v1718::SetPulsers()` where the number of pulses to be generated, their width, as well as the period
 3627 of the pulse generator is defined.

3628

```
class v1718{
    private:
        int             Handle;
        Data32          Data;           // Data
        CVIRQLevels     Level;         // Interrupt level
        CVAddressModifier AM;          // Addressing Mode
        CVDataWidth     DataSize;       // Data Format
        Data32          BaseAddress;   // Base Address

    public:
        v1718(IniFile *inifile);
        ~v1718();
        long            GetHandle(void) const;
        int             SetData(Data16 data);
        Data16          GetData(void);
        int             SetLevel(CVIRQLevels level);
        CVIRQLevels     GetLevel(void);
        int             SetAM(CVAddressModifier am);
        CVAddressModifier GetAM(void);
        int             SetDataSize(CVDataWidth datasize);
        CVDataWidth     GetDataSize(void);
        int             SetBaseAddress(Data16 baseaddress);
        Data16          GetBaseAddress(void);
        void            CheckStatus(CVErrorCodes status) const;
        bool            CheckIRQ();
        void            SetPulsers(UINT RDM_Frequency);
        void            SendBUSY(PulserLevel level);
        void            RDMTriggerPulse(PulserLevel level);
};
```

3630

Source Code A.5: Description of C++ object v1718.

3631 A.5.2 Configuration file

3632 The DAQ software takes as input a configuration file written using INI standard [273]. This file is
 3633 partly filled with the information provided by the shifters when starting data acquisition using the
 3634 webDCS, as shown by Figure A.6. This information is written in section **[General]** and will later
 3635 be stored in the ROOT file that contains the DAQ data as can be seen from Figure A.3. Indeed,
 3636 another `TTree` called `RunParameters` as well as the 2 histograms `ID`, containing the scan number,
 3637 start and stop time stamps, and `Triggers`, containing the number of triggers requested by the shifter,
 3638 are available in the data files. Moreover, `ScanID` and `HV` are then used to construct the file name
 3639 thanks to the method `DataReader::GetFileName()`.

Chamber	RE2-2-NPD-BARC-8	RE2-2-CERN-105	RE2-2-NPD-BARC-9	RE2-2-CERN-105	RE4-2-KODEL-1-4	Max triggers
HV _{eff} 1	8600	8500	8600	8500	6500	
HV _{eff} 2	8700	8600	8700	8600	6600	
HV _{eff} 3	8800	8700	8800	8700	6700	
HV _{eff} 4	8900	8800	8900	8800	6800	
HV _{eff} 5	9000	8900	9000	8900	6900	
HV _{eff} 6	9100	9000	9100	9000	7000	
HV _{eff} 7	9200	9100	9200	9100	7100	
HV _{eff} 8	9300	9200	9300	9200	7200	
HV _{eff} 9	9400	9300	9400	9300	7300	
HV _{eff} 10	9500	9400	9500	9400	7400	

Figure A.6: WebDCS DAQ scan page. On this page, shifters need to choose the type of scan (Rate, Efficiency or Noise Reference scan), the gamma source configuration at the moment of data taking, the beam configuration, and the trigger mode. These information will be stored in the DAQ ROOT output. Are also given the minimal measurement time and waiting time after ramping up of the detectors is over before starting the data acquisition. Then, the list of HV points to scan and the number of triggers for each run of the scan are given in the table underneath.

3640 The rest of the information is written beforehand in the configuration file template, as explicated
 3641 in Source Code A.6, and contains the hardware addresses to the different VME modules in the
 3642 setup as well as settings for the TDCs. As the TDC settings available in the configuration file are not
 3643 supposed to be modified, an improvement would be to remove them from the configuration file and
 3644 to hardcode them inside of the DAQ code itself or to place them into a different INI file that would
 3645 host only the TDC settings to lower the probability for a bad manipulation of the configuration file
 3646 that can be modified from one of webDCS' menus.

3647

```
[General]
TdcS=4
ScanID=$scanid
HV=$HV
RunType=$runtype
MaxTriggers=$maxtriggers
Beam=$beam
[VMEInterface]
Type=V1718
BaseAddress=0xFF0000
Name=VmeInterface
int_trig_freq=100
[TDC0]
Type=V1190A
BaseAddress=0x00000000
Name=Tdc0
StatusA00-15=1
StatusA16-31=1
StatusB00-15=1
StatusB16-31=1
StatusC00-15=1
StatusC16-31=1
StatusD00-15=1
StatusD16-31=1
[TDC1]
Type=V1190A
BaseAddress=0x11110000
Name=Tdc1
StatusA00-15=1
StatusA16-31=1
StatusB00-15=1
StatusB16-31=1
StatusC00-15=1
StatusC16-31=1
StatusD00-15=1
StatusD16-31=1
3648
[TDC2]
Type=V1190A
BaseAddress=0x22220000
Name=Tdc2
StatusA00-15=1
StatusA16-31=1
StatusB00-15=1
StatusB16-31=1
StatusC00-15=1
StatusC16-31=1
StatusD00-15=1
StatusD16-31=1
[TDC3]
Type=V1190A
BaseAddress=0x44440000
Name=Tdc3
StatusA00-15=1
StatusA16-31=1
StatusB00-15=1
StatusB16-31=1
StatusC00-15=1
StatusC16-31=1
StatusD00-15=1
StatusD16-31=1
[TDCErrors]
TriggerExtraSearchMargin=0
TriggerRejectMargin=0
TriggerTimeSubtraction=0b1
TdcDetectionMode=0b01
TdcResolution=0b10
TdcDeadTime=0b00
TdcHeadTrailer=0b1
TdcEventSize=0b1001
TdcTestMode=0b0
BLTMode=1
```

Source Code A.6: INI configuration file template for 4 TDCs. In section [General], the number of TDCs is explicitated and information about the ongoing run is given. Then, there are sections for each and every VME modules. There buffer addresses are given and for the TDCs, the list of channels to enable is given. Finally, in section [TDCSettings], a part of the TDC settings are given.

```

3649 typedef map< const string, string > IniFileData;

3650 class IniFile{
3651     private:
3652         bool          CheckIfComment(string line);
3653         bool          CheckIfGroup(string line, string& group);
3654         bool          CheckIfToken(string line, string& key, string& value);
3655         string        FileName;
3656         IniFileData  FileData;
3657         int           Error;

3658     public:
3659         IniFile();
3660         IniFile(string filename);
3661         virtual      ~IniFile();

3662         // Basic file operations
3663         void          SetFileName(string filename);
3664         int           Read();
3665         int           Write();
3666         IniFileData GetFileData();

3667         // Data readout methods
3668         Data32 addressType(string groupname, string keyname, Data32 defaultvalue);
3669         long intType(string groupname, string keyname, long defaultvalue);
3670         long long longType(string groupname, string keyname, long long
3671         defaultvalue);
3672         string stringType(string groupname, string keyname, string defaultvalue);
3673         float floatType(string groupname, string keyname, float defaultvalue);

3674         // Error methods
3675         string GetErrorMsg();
3676     };

```

3651 *Source Code A.7: Description of C++ object IniFile used as a parser for INI file format.*

3652 In order to retrieve the information of the configuration file, the object `IniFile` has been developed
 3653 to provide an INI parser, presented in Source Code A.7. It contains private methods returning a
 3654 boolean to check the type of line written in the file, whether a comment, a group header or a key line
 3655 (`IniFile::CheckIfComment()`, `IniFile::CheckIfGroup()` and `IniFile::CheckIfToken()`). The
 3656 key may sometimes be referred to as *token* in the source code. Moreover, the private element
 3657 `FileData` is a map of `const` string to string that allows to store the data contained inside the
 3658 configuration file via the public method `IniFile::GetFileData()` following the formatting (see
 3659 method `IniFile::Read()`):

```

3660
3661         string group, token, value;
3662         // Get the field values for the 3 strings.
3663         // Then concatenate group and token together as a single string
3664         // with a dot separation.
3665         token = group + "." + token;
3666         FileData[token] = value;

```

3662 More methods have been written to translate the different keys into the right variable format
 3663 when used by the DAQ. For example, to get a **float** value out of the configuration file data, knowing
 3664 the group and the key needed, the method `IniFile::floatType()` can be used. It takes 3 arguments
 3665 being the group name and key name (both `string`), and a default **float** value used as exception in
 3666 the case the expected combination of group and key cannot be found in the configuration file. This
 3667 default value is then used and the DAQ continues on working after sending an alert in the log file for
 3668 further debugging.

3669

3670 A.5.3 WebDCS/DAQ intercommunication

3671 When shifters send instructions to the DAQ via the configuration file, it is the webDCS itself that
 3672 gives the start command to the DAQ and then the 2 softwares use inter-process communication
 3673 through file to synchronise themselves. This communication file is represented by the variable `const`
 3674 `string __runstatuspath`.

3675 On one side, the webDCS sends commands or status that are readout by the DAQ:

- 3676 • INIT, status sent when launching a scan and read via function `CtrlRunStatus(...)`,
- 3677 • START, command to start data taking and read via function `CheckSTART()`,
- 3678 • STOP, command to stop data taking at the end of the scan and read via function `CheckSTOP()`,
 3679 and
- 3680 • KILL, command to kill data taking sent by user and read via function `CheckKILL()`. Note that
 3681 the DAQ doesn't stop before the current ROOT file is safely written and saved.

3682 and on the other, the DAQ sends status that are controled by the webDCS:

- 3683 • DAQ_RDY, sent with `SendDAQReady()` to signify that the DAQ is ready to receive commands
 3684 from the webDCS,
- 3685 • RUNNING, sent with `SendDAQRunning()` to signify that the DAQ is taking data,
- 3686 • DAQ_ERR, sent with `SendDAQError()` to signify that the DAQ didn't receive the expected com-
 3687 mand from the webDCS or that the launch command didn't have the right number of argu-
 3688 ments,
- 3689 • RD_ERR, sent when the DAQ wasn't able to read the communication file, and
- 3690 • WR_ERR, sent when the DAQ wasn't able to write into the communication file.

3691 A.5.4 Example of inter-process communication cycle

3692 Under normal conditions, the webDCS and the DAQ processes exchange commands and status via
 3693 the file hosted at the address `__runstatuspath`, as explained in subsection A.5.3. An example of
 3694 cycle is given in Table A.1. In this example, the steps 3 to 5 are repeated as long as the webDCS tells
 3695 the DAQ to take data. A data taking cycle is the equivalent as what is called a *Scan* in GIFT++ jargon,

3696 referring to a set a runs with several HV steps. Each repetition of steps 3 to 5 is then equivalent to a
 3697 single *Run*.

3698 At any moment during the data taking, for any reason, the shifter can decide that the data taking
 3699 needs to be stopped before it reached the end of the scheduled cycle. Thus at any moment on the
 3700 cycle, the content of the inter-process communication file will be changed to `KILL` and the DAQ will
 3701 shut down right away. The DAQ checks for `KILL` signals every 5s after the TDCs configuration is
 3702 over. So far, the function `CheckKILL()` has been used only inside of the data taking loop of method
 3703 `DataReader::Run()` and thus, if the shifter decides to KILL the data taking during the TDC con-
 3704 figuration phase or the HV ramping in between 2 HV steps, the DAQ will not be stopped smoothly
 3705 and a *force kill* command will be sent to stop the DAQ process that is still awake on the computer.
 3706 Improvements can be brought on this part of the software to make sure that the DAQ can safely
 3707 shutdown at any moment.

3708

step	actions of webDCS	status of DAQ	<code>__runstatuspath</code>
1	launch DAQ ramp voltages ramping over wait for currents stabilization	readout of IniFile configuration of TDCs	INIT
2		configuration done send DAQ ready wait for <code>START</code> signal	DAQ_RDY
3	waiting time over send <code>START</code>		START
4	wait for run to end monitor DAQ run status	data taking ongoing check for <code>KILL</code> signal	RUNNING
5		run over send <code>DAQ_RDY</code> wait for next DCS signal	DAQ_RDY
6	ramp voltages ramping over wait for currents stabilization		DAQ_RDY
3	waiting time over send <code>START</code>		START
4	wait for run to end monitor DAQ run status	update IniFile information data taking ongoing check for <code>KILL</code> signal	RUNNING
5		run over send <code>DAQ_RDY</code> wait for next DCS signal	DAQ_RDY
7	send command <code>STOP</code>	DAQ shuts down	STOP

Table A.1: Inter-process communication cycles in between the webDCS and the DAQ through file string signals.

A.6 Software export

3709 In section A.2 was discussed the fact that the DAQ as written in its last version is not a standalone
 3710 software. It is possible to make it a standalone program that could be adapted to any VME setup

3712 using V1190A and V1718 modules by creating a GUI for the software or by printing the log messages
3713 that are normally printed in the webDCS through the log file, directly into the terminal. This
3714 method was used by the DAQ up to version 3.0 moment where the webDCS was completed. Also, it
3715 is possible to check branches of DAQ v2.X to have example of communication through a terminal.
3716 DAQ v2.X is nonetheless limited in its possibilities and requires a lot of offline manual interventions
3717 from the users. Indeed, there is no communication of the software with the detectors' power
3718 supply system that would allow for a user a predefine a list of voltages to operate the detectors at
3719 and loop over to take data without any further manual intervention. In v2.X, the data is taken for a
3720 single detector setting and at the end of each run, the softwares asks the user if he intends on taking
3721 more runs. If so, the software invites the user to set the operating voltages accordingly to what is
3722 necessary and to manual update the configuration file in consequence. This working mode can be a
3723 very first approach before an evolution and has been successfully used by colleagues from different
3724 collaborations.

3725 For a more robust operation, it is recommended to develop a GUI or a web application to interface
3726 the DAQ. Moreover, to limit the amount of manual interventions, and thus the probability to make
3727 mistakes, it is also recommended to add an extra feature into the DAQ by installing the HV Wrapper
3728 library provided by CAEN of which an example of use in a similar DAQ software developped by a
3729 master student of UGent, and called TinyDAQ, is provided on UGent's github. Then, this HV Wrapper
3730 will help you communicating with and give instructions to a CAEN HV powered crate and can
3731 be added into the DAQ at the same level where the communication with the user was made in DAQ
3732 v2.X. In case you are using another kind of power system for your detectors, it is stringly adviced to
3733 use HV modules or crates that can be remotely controloled via a using C++ libraries.

3734

B

3735

3736

Details on the offline analysis package

3737 The data collected in GIF++ thanks to the DAQ described in Appendix A is difficult to interpret by
3738 a human user that doesn't have a clear idea of the raw data architecture of the ROOT data files. In
3739 order to render the data human readable, a C++ offline analysis tool was designed to provide users
3740 with detector by detector histograms that give a clear overview of the parameters monitored during
3741 the data acquisition [266]. In this appendix, details about this software in the context of GIF++, as
3742 of how the software was written and how it functions will be given.

3743 B.1 GIF++ Offline Analysis file tree

3744 GIF++ Offline Analysis source code is fully available on github at https://github.com/afagot/GIF_OfflineAnalysis. The software requires ROOT as non-optionnal dependency
3745 as it takes ROOT files in input and write an output ROOT file containing histograms. To compile the
3746 GIF++ Offline Analysis project is compiled with cmake. To compile, first a build/ directory must
3747 be created to compile from there:

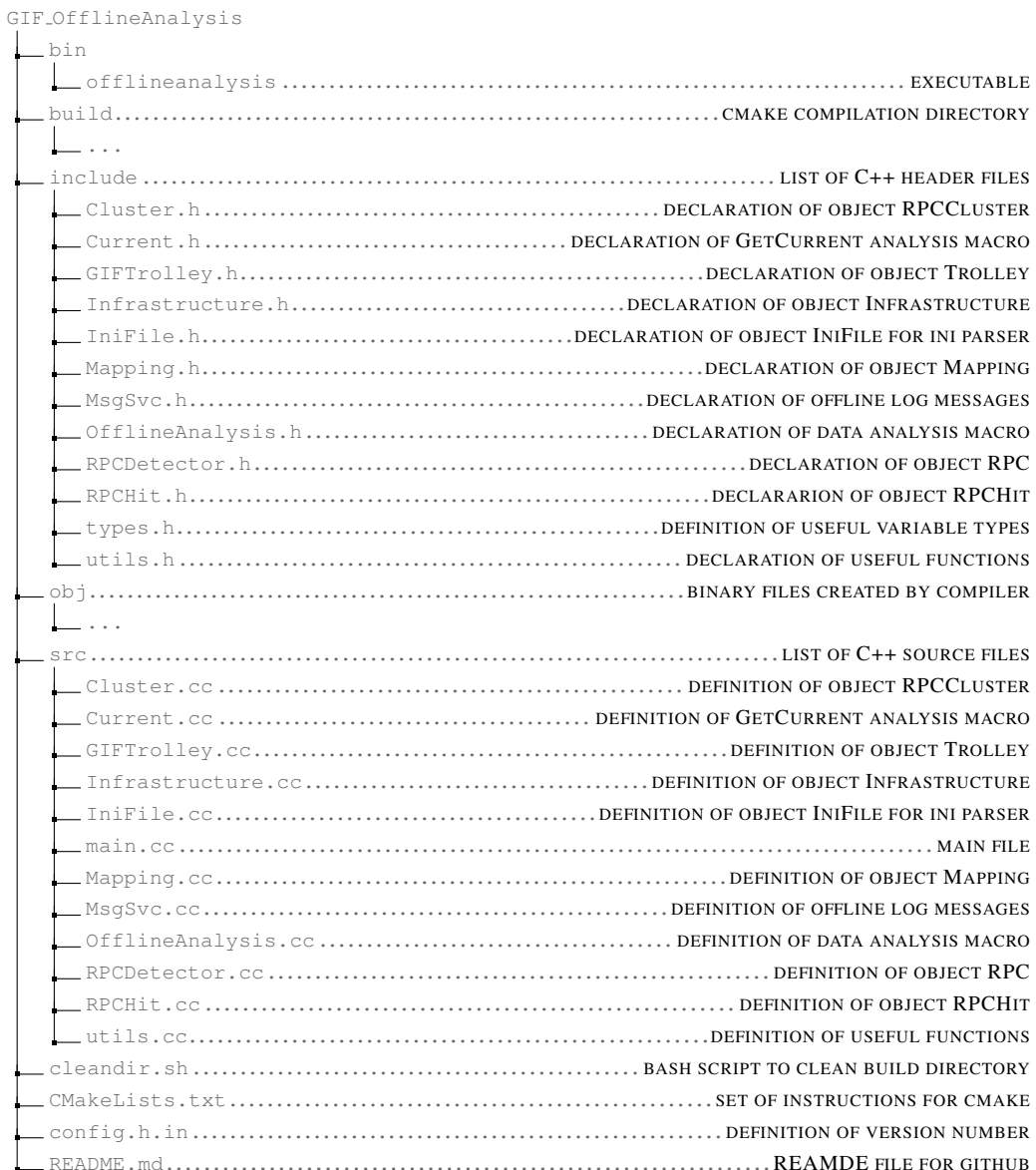
```
3749 mkdir build
3750 cd build
3751 cmake ..
3752 make
3753 make install
```

3751 To clean the directory and create a new build directory, the bash script cleandir.sh can be used:

```
3752
3753 ./cleandir.sh
```

3754 The source code tree is provided below along with comments to give an overview of the files' con-
3755 tent. The different objects created for this project (`Infrastructure`, `Trolley`, `RPC`, `Mapping`, `RPCHit`,
3756 `RPCCluster` and `Inifile`) will be described in details in the following sections.

3757



3758

B.2 Usage of the Offline Analysis

3759

In order to use the Offline Analysis tool, it is necessary to know the Scan number and the HV Step of the run that needs to be analysed. This information needs to be written in the following format:

3761

3762

```
Scan00XXXX_HVY
```

3763

where XXXX is the scan ID and Y is the high voltage step (in case of a high voltage scan, data will be taken for several HV steps). This format corresponds to the base name of data files in the database

3764

3765 of the Gif++ webDCS. Usually, the offline analysis tool is automatically called by the webDCS at
 3766 the end of data taking or by a user from the webDCS panel if an update of the tool was brought.
 3767 Nonetheless, an expert can locally launch the analysis for tests on the Gif++ computer, or a user can
 3768 get the code on its local machine from github and download data from the webDCS for its own anal-
 3769 ysis. To launch the code, the following command can be used from the `GIF_OfflineAnalysis` folder:

3770

```
3771 bin/offlineanalysis /path/to/Scan00XXXX_HVY
```

3772 where, `/path/to/Scan00XXXX_HVY` refers to the local data files. Then, the offline tool will by itself
 3773 take care of finding all available ROOT data files present in the folder, as listed below:

3774

- `Scan00XXXX_HVY_DAQ.root` containing the TDC data as described in Appendix A.4.2 (events,
 hit and timestamp lists), and
- `Scan00XXXX_HVY_CAEN.root` containing the CAEN mainframe data recorded by the monitor-
 ing tool webDCS during data taking (HVs and currents of every HV channels). This file is
 created independently of the DAQ.

3779

B.2.1 Output of the offline tool

3780

B.2.1.1 ROOT file

3781

The analysis gives output ROOT datafiles that are saved into the data folder and called using the
 3782 naming convention `Scan00XXXX_HVY_Offline.root`. Inside those, a list of `TH1` histograms can be
 3783 found. Its size will vary as a function of the number of detectors in the setup as each set of histograms
 3784 is produced detector by detector. For each partition of each chamber, can be found:

3785

3786

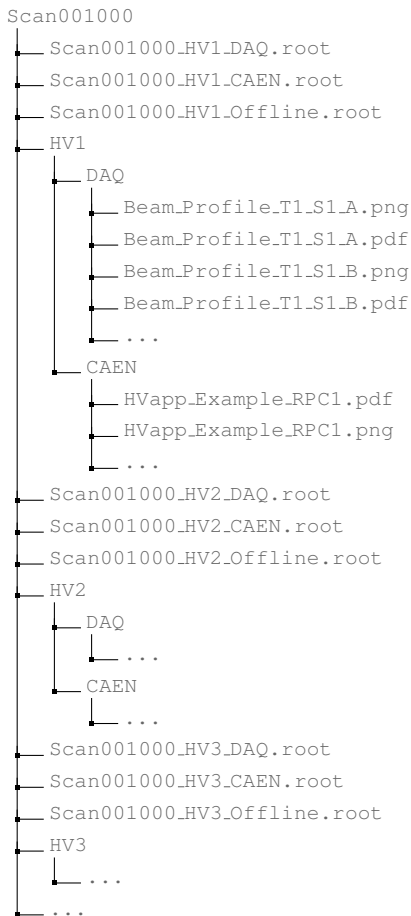
- `Time_Profile_Tt_Sc_p` shows the time profile of all recorded events (number of events per
 time bin),
- `Hit_Profile_Tt_Sc_p` shows the hit profile of all recorded events (number of events per chan-
 nel),
- `Hit_Multiplicity_Tt_Sc_p` shows the hit multiplicity (number of hits per event) of all recorded
 events (number of occurrences per multiplicity bin),
- `Time_vs_Strip_Profile_Tt_Sc_p` shows the 2D time vs strip profile of all recorded events
 (number of events per time bin per strip),
- `Strip_Mean_Noise_Tt_Sc_p` shows noise/gamma rate per unit area for each strip in a se-
 lected time range. After filters are applied on `Time_Profile_Tt_Sc_p`, the filtered version
 of `Hit_Profile_Tt_Sc_p` is normalised to the total integrated time and active detection area
 of a single channel,
- `Strip_Activity_Tt_Sc_p` shows noise/gamma activity for each strip (normalised version of
 previous histogram - strip activity = strip rate / average partition rate),
- `Strip_Homogeneity_Tt_Sc_p` shows the *homogeneity* of a given partition ($\text{homogeneity} = \exp(-\text{strip rates standard deviation}(\text{strip rates in partition}/\text{average partition rate}))$),

- 3801 ● `mask_Strip_Mean_Noise_Tt_Sc_p` shows noise/gamma rate per unit area for each masked
 3802 strip in a selected time range. Offline, the user can control the noise/gamma rate and decide to
 3803 mask the strips that are judged to be noisy or dead. This is done via the *Masking Tool* provided
 3804 by the webDCS,
- 3805 ● `mask_Strip_Activity_Tt_Sc_p` shows noise/gamma activity per unit area for each masked
 3806 strip with respect to the average rate of active strips,
- 3807 ● `NoiseCSize_H_Tt_Sc_p` shows noise/gamma cluster size, a cluster being constructed out of
 3808 adjacent strips giving a signal at the *same time* (hits within a time window of 25 ns),
- 3809 ● `NoiseCMult_H_Tt_Sc_p` shows noise/gamma cluster multiplicity (number of reconstructed
 3810 clusters per event),
- 3811 ● `Chip_Mean_Noise_Tt_Sc_p` shows the same information than `Strip_Mean_Noise_Tt_Scp` us-
 3812 ing a different binning (1 chip corresponds to 8 strips),
- 3813 ● `Chip_Activity_Tt_Sc_p` shows the same information than `strip_Activity_Tt_Scp` using
 3814 chip binning,
- 3815 ● `Chip_Homogeneity_Tt_Sc_p` shows the homogeneity of a given partition using chip binning,
- 3816 ● `Beam_Profile_Tt_Sc_p` shows the estimated beam profile when taking efficiency scan. This
 3817 is obtained by filtering `Time_Profile_Tt_Sc_p` to only consider the muon peak where the
 3818 noise/gamma background has been subtracted. The resulting hit profile corresponds to the
 3819 beam profile on the detector channels,
- 3820 ● `Efficiency_Fake_Tt_Ss_p` shows the efficiency given by fake hits by probing outside the
 3821 peak in an uncorrelated window as wide as the peak window,
- 3822 ● `Efficiency_Peak_Tt_Ss_p` shows the efficiency given by hits contained in the peak window,
- 3823 ● `PeakCSize_H_Tt_Sc_p` shows the cluster size that was estimated using all the hits in the peak
 3824 window,
- 3825 ● `PeakCMult_H_Tt_Sc_p` shows the cluster multiplicity that was estimated using all the hits in
 3826 the peak window,
- 3827 ● `L0_Efficiency_Tt_Sc_p` shows the level 0 muon efficiency that was estimated **without** muon
 3828 tracking after correction,
- 3829 ● `MuonCSize_H_Tt_Sc_p` shows the level 0 muon cluster size that was estimated **without** muon
 3830 tracking after correction, and
- 3831 ● `MuonCMult_H_Tt_Sc_p` shows the level 0 muon cluster multiplicity that was estimated **without**
 3832 muon tracking after correction.

3833 In the histogram labels, *t* stands for the trolley number (1 or 3), *c* for the chamber slot label in
 3834 trolley *t* and *p* for the partition label (A, B, C or D depending on the chamber layout) as explained
 3835 in Chapter 5.3.

3837 In the context of GIF++, an extra script called by the webDCS is called to extract the histograms
 3838 from the ROOT files. The histograms are then stored in PNG and PDF formats into the corresponding
 3839 folder (a single folder per HV step, so per ROOT file). An example of histogram organisation is
 3840 given bellow for an hypothetical scan 001000 with at least 3 HV steps and whose chamber located in
 3841 slot 1 of trolley 1 is called *Example_RPC1* and has at least 2 read-out partitions A and B. The goal is
 3842 to then display the histograms graphs on the Data Quality Monitoring (DQM) page of the webDCS,
 3843 as presented in Figure 5.27, in order for the users to control the quality of the data taking at the end
 3844 of data taking.

3845



3846

B.2.1.2 CSV files

3847

Moreover, up to 4 CSV files can be created depending on which ones of the 3 input files were in the
 3848 data folder:

3849

- `Offline-Corrupted.csv`, is used to keep track of the amount of data that was corrupted and removed from old data format files that don't contain any data quality flag.

3850

- 3851 ● `Offline-Current.csv`, contains the summary of the currents and voltages applied on each
3852 RPC HV channel.
- 3853 ● `Offline-L0-EffCl.csv`, is used to write the efficiencies, cluster size and cluster multiplicity
3854 of efficiency runs. Note that `L0` refers here to *Level 0* and means that the results of efficiency and
3855 clusterization are a first approximation calculated without performing any muon tracking in
3856 between the different detectors. This offline tool provides the user with a preliminar calcula-
3857 tion of the efficiency and of the muon event parameters. Another analysis software especially
3858 dedicated to muon tracking is called on selected data to retrieve the results of efficiency and
3859 muon clusterization using a tracking algorithm to discriminate noise or gamma from muons
3860 as muons are the only particles that pass through the full setup, leaving hits than can be used
3861 to reconstruct their tracks.
- 3862 ● `Offline-Rate.csv`, is used to write the noise or gamma rates measured in the detector readout
3863 partitions.

3864 Note that these 4 CSV files are created along with their *headers* (`Offline-[...]-Header.csv`
3865 containing the names of each data columns) and are automatically merged together when the offline
3866 analysis tool is called from the webDCS, contrary to the case where the tool is runned locally from
3867 the terminal as the merging bash script is then not called. Thus, the resulting files, used to make
3868 official plots, are:

- 3869 ● `Corrupted.csv`,
- 3870 ● `Current.csv`,
- 3871 ● `L0-EffCl.csv`.
- 3872 ● `Rate.csv`.

3873 **B.3 Analysis inputs and information handling**

3874 The usage of the Offline Analysis tool as well as its output have been presented in the previous sec-
3875 tion. It is now important to dig further and start looking at the source code and the inputs necessary
3876 for the tool to work. Indeed, other than the raw ROOT data files that are analysed, more information
3877 needs to be imported inside of the program to perform the analysis such as the description of the
3878 setup inside of GIFT++ at the time of data taking (number of trolleys, of RPCs, dimensions of the
3879 detectors, etc...) or the mapping that links the TDC channels to the coresponding RPC channels in
3880 order to translate the TDC information into human readable data. Two files are used to transmit all
3881 this information:

- 3882
- 3883 ● `Dimensions.ini`, that provides the necessary setup and RPC information, and
- 3884 ● `ChannelsMapping.csv`, that gives the link between the TDC and RPC channels as well as the
3885 *mask* for each channel (masked or not?).

3886 B.3.1 Dimensions file and IniFile parser

3887 GIF++ CMS RPC setup consists in detectors held into trolleys inside of the GIF++ bunker. Each of
 3888 these detector may have a read-out segmented to cover different pseudo-rapidity range once intalled
 3889 in CMS. The segmentation of the read-out is referred to as "partitions". This input file, present in
 3890 every data folder, allows the analysis tool to know of the number of active trolleys, the number of
 3891 active RPCs in those trolleys, and the details about each RPCs such as the number of RPC gaps, the
 3892 number of pseudo-rapidity partitions, the number of strips per partion or the dimensions. To do so,
 3893 there are 3 types of groups in the INI file architecture. Groups are sections of the INI file content
 3894 starting with a title encapsulated in between square brackets. A first general group, appearing only
 3895 once at the head of the document, gives information about the number of active trolleys as well
 3896 as their IDs, as presented in Source Code B.1. For each active trolley, a group similar to Source
 3897 Code B.2 can be found containing information about the number of active detectors in the trolley
 3898 and their IDs. Each trolley group as a `Tt` name format, where `t` is the trolley ID. Finally, for each
 3899 detector stored in slots of an active trolley, there is a group providing information about their names
 3900 and dimensions, as shown in Source Code B.3. Each slot group as a `TtSs` name format, where `s` is
 3901 the slot ID of trolley `t` where the active RPC is hosted.

```
3902    [General]
3903    nTrolleys=2
3904    TrolleysID=13
```

3904 *Source Code B.1: Example of `[General]` group as might be found in `Dimensions.ini`. In GIF++, only 2 trolleys are available to hold RPCs and place them inside of the bunker for irradiation. The IDs of the trolleys are written in a single string as "13" and then read character by character by the program.*

```
3905    [T1]
3906    nSlots=4
3907    SlotsID=1234
```

3906 *Source Code B.2: Example of trolley group as might be found in `Dimensions.ini`. In this example, the file tells that there are 4 detectors placed in the holding slots of the trolley `T1` and that their IDs, written as a single string variable, are 1, 2, 3 and 4.*

```
3908    [T1S1]
3909    Name=RE2-2-NPD-BARC-8
3910    Partitions=3
3911    Gaps=3
3912    Gap1=BOT
3913    Gap2=TN
3914    Gap3=TW
3915    AreaGap1=11694.25
3916    AreaGap2=6432
3917    AreaGap3=4582.82
3918    Strips=32
3919    ActiveArea-A=157.8
3920    ActiveArea-B=121.69
3921    ActiveArea-C=93.03
```

3921 *Source Code B.3: Example of slot group as might be found in `Dimensions.ini`. In this example, the file provides information about a detector named `RE2-2-NPD-BARC-8`, having 3 pseudo-rapidity readout partitions and stored in slot `S1` of trolley `T1`. This is a CMS RE2-2 type of detector. This information will then be used for example to compute the rate per unit area calculation.*

3909 This information is read-out and stored in a C++ object called `IniFile`, that parses the information
 3910 of the INI input file and stores it into a local buffer for later use. This INI parser is the exact
 3911 same one that was previously developed for the GIF++ DAQ and described in Appendix A.5.2.

3912 B.3.2 TDC to RPC link file and Mapping

3913 The same way the INI dimension file information is stored using `map`, the channel mapping and
 3914 mask information making the link in between TDC channels and RPC strips is stored and accessed
 3915 through `map`. First of all, the mapping CSV file is organised into 3 columns separated by tabulations:

3917 RPC_channel	TDC_channel	mask
---------------------	-------------	------

3918 using as formatting for each field:

3919 TSCCC	TCCC	M
------------------	------	---

3921 `TSCCC` is a 5-digit integer where `T` is the trolley ID, `s` the slot ID in which the RPC is held inside
 3922 the trolley `T` and `ccc` is the RPC channel number, or *strip* number, that can take values up to
 3923 3-digits depending on the detector,

3924 `TCCC` is a 4 digit integer where `T` is the TDC ID to which the RPC is connected, `ccc` is the TDC
 3925 channel number linked to the RPC strip that can take values in between 0 and 127, and

3926 `M` is a 1-digit integer indicating if the channel should be considered (`M = 1`) or discarded (`M = 0`)
 3927 during analysis. Note that the absence of a third column is interpreted by the mapping file
 3928 parser as `M = 1` by default.

3929 This mapping and masking information is readout and stored thanks to the object `Mapping`, presented in Source Code B.4. Similarly to `IniFile` objects, this class has private methods to provide with parser rules. The first one, `Mapping::CheckIfNewLine()` is used to find the newline character
 3930 '`\n`' or return character '`\r`' (depending on which kind of operating system interacted with the file).
 3931 Finding and identifying a newline or return character is used for the simple reason that the masking
 3932 information has been introduced only during the year 2017 but the channel mapping files exist since
 3933 2015 and the very beginning of data taking at GIF++. This means that in the older data folders,
 3934 before the upgrade, the channel mapping file only had 2 columns, the RPC channel and the TDC
 3935 channel. For compatibility reasons, this method helps controlling the character following the readout
 3936 of the 2 first fields of a line. In case any end of line character is found, no mask information is present
 3937 in the file and the default `M = 1` is used. On the contrary, if the next character was a tabulation or a
 3938 space, the mask information is present.
 3939

3940 Once the 3 fields have been readout, the second private method `Mapping::CheckIfTDCCh()` is
 3941 used to control that the TDC channel is an existing TDC channel by checking its format. Finally,
 3942 the information is stored into 3 different maps (`Link`, `ReverseLink` and `Mask`) thanks to the public
 3943 method `Mapping::Read()`. `Link` allows to get the RPC channel by knowing the TDC channel while
 3944 `ReverseLink` does the opposite by returning the TDC channel by knowing the RPC channel. Finally,
 3945 `Mask` returns the mask associated to a given RPC channel.

```

3947 typedef map<Uint,Uint> MappingData;

3948 class Mapping {
3949     private:
3950         bool          CheckIfNewLine(char next);
3951         bool          CheckIfTDCCh(Uint channel);
3952         string        FileName;
3953         MappingData  Link;
3954         MappingData  ReverseLink;
3955         MappingData  Mask;
3956         int           Error;
3957
3958     public:
3959         Mapping();
3960         Mapping(string baseName);
3961         ~Mapping();
3962
3963         void SetFileName(const string filename);
3964         int  Read();
3965         Uint GetLink(Uint tdcchannel);
3966         Uint GetReverse(Uint rpcchannel);
3967         Uint GetMask(Uint rpcchannel);
3968     };

```

3949 *Source Code B.4: Description of C++ object Mapping used as a parser for the channel mapping and mask file.*

3950 **B.4 Description of GIF++ setup within the Offline Analysis tool**

3951 In the previous section, the tool input files have been discussed. The dimension file information is
 3952 stored in a map hosted by the `IniFile` object. But this information is then used to create a series of
 3953 new objects that helps defining the GIF++ infrastructure directly into the Offline Analysis. Indeed,
 3954 from the `RPC`, to the more general `Infrastructure`, every element of the GIF++ infrastrucutre is
 3955 recreated for each data analysis based on the information provided in input. All this information
 3956 about the infrastructure will be used to assign each hit signal to a specific strip channel of a specific
 3957 detector, and having a specific active area. This way, rate per unit area calculation is possible.
 3958

3959 **B.4.1 RPC objects**

3960 `RPC` objects have been developped to represent physical active detectors in GIF++ at the moment
 3961 of data taking. Thus, there are as many `RPC` objects created during the analysis than there were
 3962 active `RPCs` tested during a run. Each `RPC` hosts the information present in the corresponding INI
 3963 slot group, as showed in B.3, and organises it using a similar architecture. This can be seen from
 3964 Source Code B.5.

3965 To make the object more compact, the lists of gap labels, of gap active areas and strip active
 3966 areas are stored into `vector` dynamical containers. `RPC` objects are always contructed thanks to the
 3967 dimension file information stored into the `IniFILE` and their ID, using the format `TtSs`. Using the
 3968 `RPC` ID, the constructor calls the methods of `IniFILE` to initialise the `RPC`. The other constructors
 3969 are not used but exist in case of need. Finally, some getters have been written to access the different
 3970 private parameters storing the detector information.

3971

3972 B.4.2 Trolley objects

3973 Trolley objects have been developed to represent physical active trolleys in GIF++ at the moment
 3974 of data taking. Thus, there are as many trolley objects created during the analysis than there were
 3975 active trolleys hosting RPCs under test during a run. Each Trolley hosts the information present in
 3976 the corresponding INI trolley group, as shown in B.2, and organises it using a similar architecture.
 3977 In addition to the information hosted in the INI file, these objects have a dynamical container of `RPC`
 3978 objects, representing the active detectors the active trolley was hosting at the time of data taking.
 3979 This can be seen from Source Code B.6.

3980 Trolley objects are always constructed thanks to the dimension file information stored into the
 3981 `IniFILE` and their ID, using the format `Tt`. Using the Trolley ID, the constructor calls the methods
 3982 of `IniFILE` to initialise the Trolley. Retrieving the information of the RPC IDs via `SlotsID`, a new
 3983 `RPC` is constructed and added to the container `RPCs` for each character in the ID string. The other
 3984 constructors are not used but exist in case of need. Finally, some getters have been written to access
 3985 the different private parameters storing the trolley and detectors information.

3986

3987 B.4.3 Infrastructure object

3988 The `Infrastructure` object has been developed to represent the GIF++ bunker area dedicated to
 3989 CMS RPC experiments. With this very specific object, all the information about the CMS RPC
 3990 setup within GIF++ at the moment of data taking is stored. It hosts the information present in the
 3991 corresponding INI general group, as shown in B.1, and organises it using a similar architecture. In
 3992 addition to the information hosted in the INI file, this object has a dynamical container of `Trolley`
 3993 objects representing the active trolleys in GIF++ area, themselves containing `RPC` objects. This can
 3994 be seen from Source Code B.7.

3995 The `Infrastructure` object is always constructed thanks to the dimension file information stored
 3996 into the `IniFILE`. Retrieving the information of the trolley IDs via `TrolleysID`, a new `Trolley` is
 3997 constructed and added to the container `Trolleys` for each character in the ID string. By extension,
 3998 it is easy to understand that the process described in Section B.4.2 for the construction of RPCs
 3999 takes place when a trolley is constructed. The other constructors are not used but exist in case of
 4000 need. Finally, some getters have been written to access the different private parameters storing the
 4001 infrastructure, trolleys and detectors information.

```

4002 class RPC{
    private:
        string      name;           //RPC name as in webDCS database
        UInt       nGaps;          //Number of gaps in the RPC
        UInt       nPartitions;    //Number of partitions in the RPC
        UInt       nStrips;         //Number of strips per partition
        vector<string> gaps;       //List of gap labels (BOT, TOP, etc...)
        vector<float>  gapGeo;     //List of gap active areas
        vector<float>  stripGeo;   //List of strip active areas

    public:
        RPC();
        RPC(string ID, IniFile* geofile);
        RPC(const RPC& other);
        ~RPC();
        RPC& operator=(const RPC& other);

        string GetName();
        UInt   GetNGaps();
        UInt   GetNPartitions();
        UInt   GetNStrips();
        string GetGap(UInt g);
        float  GetGapGeo(UInt g);
        float  GetStripGeo(UInt p);
    };

```

4004 *Source Code B.5: Description of C++ objects RPC that describe each active detectors used during data taking.*

```

class Trolley{
    private:
        UInt       nSlots;        //Number of active RPCs in the considered trolley
        string    SlotsID;       //Active RPC IDs written into a string
        vector<RPC*> RPCs;      //List of active RPCs

    public:
        Trolley();
        Trolley(string ID, IniFile* geofile);
        Trolley(const Trolley& other);
        ~Trolley();
        Trolley& operator=(const Trolley& other);

        UInt   GetNSlots();
        string GetSlotsID();
        UInt   GetSlotID(UInt s);
        RPC*   GetRPC(UInt r);
        void   DeleteRPC(UInt r);

        //Methods to get members of RPC objects stored in RPCs
        string GetName(UInt r);
        UInt   GetNGaps(UInt r);
        UInt   GetNPartitions(UInt r);
        UInt   GetNStrips(UInt r);
        string GetGap(UInt r, UInt g);
        float  GetGapGeo(UInt r, UInt g);
        float  GetStripGeo(UInt r, UInt p);
    };

```

4006 *Source Code B.6: Description of C++ objects Trolley that describe each active trolley used during data taking.*

```

class Infrastructure {
    private:
        Uint             nTrolleys;   //Number of active Trolleys in the run
        string          TrolleysID;  //Active trolley IDs written into a string
        vector<Trolley*> Trolleys;  //List of active Trolleys (struct)

    public:
        Infrastructure();
        Infrastructure(IniFile* geofile);
        Infrastructure(const Infrastructure& other);
        ~Infrastructure();
        Infrastructure& operator=(const Infrastructure& other);

        Uint    GetNTrolleys();
        string GetTrolleysID();
        Uint    GetTrolleyID(Uint t);

4007        Trolley* GetTrolley(Uint t);
        void    DeleteTrolley(Uint t);

        //Methods to get members of GIFTrolley objects stored in Trolleys
        Uint    GetNSlots(Uint t);
        string GetSlotsID(Uint t);
        Uint    GetSlotID(Uint t, Uint s);
        RPC*   GetRPC(Uint t, Uint r);

        //Methods to get members of RPC objects stored in RPCs
        string GetName(Uint t, Uint r);
        Uint    GetNGaps(Uint t, Uint r);
        Uint    GetNPartitions(Uint t, Uint r);
        Uint    GetNStrips(Uint t, Uint r);
        string GetGap(Uint t, Uint r, Uint g);
        float  GetGapGeo(Uint t, Uint r, Uint g);
        float  GetStripGeo(Uint t, Uint r, Uint p);
    };

```

Source Code B.7: Description of C++ object Infrastructure that contains the full information about CMS RPC experiment in GIF++.

4009 B.5 Handeling of data

4010 As discussed in Appendix A.4.2, the raw data uses a `TTree` architecture where every entry is related
4011 to a trigger signal provided by a muon or a random pulse, whether the goal of the data taking was to
4012 measure the performance of the detector or the noise/gamma background respectively. Each of these
4013 entries, referred also as events, contain a more or less full list of hits in the TDC channels to which
4014 the detectors are connected. To this list of hits corresponds a list of time stamps, marking the arrival
4015 of the hits within the TDC channel.

4016 The infrastructure of the CMS RPC experiment within `GIF++` being defined, combining the raw
4017 data information with the information provided by both the mapping/mask file and the dimension
4018 file allows to build new physical objects that will help in computing efficiency or rates.

4019 **B.5.1 RPC hits**

4020 The raw data stored in the ROOT file as output of the GIFT++ DAQ, is readout by the analysis tool
 4021 using the structure `RAWData` presented in Source Code B.9 that differs from the structure presented
 4022 in Appendix A.4.2 as it is not meant to hold all of the data contained in the ROOT file. In this sense,
 4023 this structure is in the case of the offline analysis tool not a dynamical object and will only be storing
 4024 a single event contained in a single entry of the `TTree`.

4025

```
4026 class RPCHit {
    private:
        Uint Channel;      //RPC channel according to mapping (5 digits)
        Uint Trolley;     //0, 1 or 3 (1st digit of the RPC channel)
        Uint Station;     //Slot where is held the RPC in Trolley (2nd digit)
        Uint Strip;       //RPC strip where the hit occurred (last 3 digits)
        Uint Partition;   //Readout partition along eta segmentation
        float TimeStamp; //Time stamp of the arrival in TDC

    public:
        RPCHit();
        RPCHit(Uint channel, float time, Infrastructure* Infra);
        RPCHit(const RPCHit& other);
        ~RPCHit();
        RPCHit& operator=(const RPCHit& other);

        Uint GetChannel();
        Uint GetTrolley();
        Uint GetStation();
        Uint GetStrip();
        Uint GetPartition();
        float GetTime();
};

4027 typedef vector<RPCHit> HitList;
typedef struct GIFHitList {HitList rpc[NTROLLEYS][NSLOTS][NPARTITIONS];}
                           ↪ GIFHitList;

bool SortHitbyStrip(RPCHit h1, RPCHit h2);
bool SortHitbyTime(RPCHit h1, RPCHit h2);
```

4028

Source Code B.8: Description of C++ object `RPCHit`.

4029

```
4030 struct RAWData{
    int iEvent;           //Event i
    int TDCNHits;        //Number of hits in event i
    int QFlag;            //Quality flag list (1 flag digit per TDC)
    vector<Uint> *TDCCh; //List of channels giving hits per event
    vector<float> *TDCTS; //List of the corresponding time stamps
};
```

4031

Source Code B.9: Description of C++ structure `RAWData`.

4032

4033 Each member of the structure is then linked to the corresponding branch of the ROOT data tree,
 4034 as shown in the example of Source Code B.10, and using the method `GetEntry(int i)` of the ROOT
 4035 class `TTree` will update the state of the members of `RAWData`.

4036

4037 The data is then analysed entry by entry and to each element of the TDC channel list, a `RPCHit` is
 4038 constructed by linking each TDC channel to the corresponding RPC channel thanks to the Mapping

4035 object. The information carried by the RPC channel format allows to easily retrieve the trolley and
 4036 slot from which the hit was recorded (see section B.3.2). Using these 2 values, the readout partition
 4037 can be found by knowing the strip channel and comparing it with the number of partitions and strips
 4038 per partition stored into the `Infrastructure` object.

```
4039 TTree* dataTree = (TTree*)dataFile.Get("RAWData");
4040   RAWData data;
4041
4042   dataTree->SetBranchAddress("EventNumber", &data.iEvent);
4043   dataTree->SetBranchAddress("number_of_hits", &data.TDCNHits);
4044   dataTree->SetBranchAddress("Quality_flag", &data.QFlag);
4045   dataTree->SetBranchAddress("TDC_channel", &data.TDCCh);
4046   dataTree->SetBranchAddress("TDC_TimeStamp", &data.TDCTS);
```

4041 *Source Code B.10: Example of link in between RAWData and TTree.*

4042 Thus `RPCHit` objects are then stored into 3D dynamical list called `GIFHitList` (Source Code B.8)
 4043 where the 3 dimensions refer to the 3 layers of the readout in `GIF++` : in the bunker there are *trolleys*
 4044 (τ) holding detectors in *slots* (s) and each detector readout is divided into 1 or more pseudo-rapidity
 4045 *partitions* (p). Using these 3 information allows to assign an address to each readout partition and
 4046 this address will point to a specific hit list.

4047

4048 B.5.2 Clusters of hits

4049 All the hits contained in the ROOT file have been sorted into the different hit lists through the
 4050 `GIFHitList`. At this point, it is possible to start looking for clusters. A cluster is a group of adjacent
 4051 strips getting hits within a time window of 25 ns. These strips are then assumed to be part of the same
 4052 physical avalanche signal generated by a muon passing through the chamber or by the interaction of
 4053 a gamma stopping into the electrodes of the RPCs.

4054 To keep the cluster information, `RPCCluster` objects have been defined as shown in Source
 4055 Code B.11. Using the information of each individual `RPCHit` taken out of the hit list, it stores
 4056 the cluster size (number of adjacent strips composing the cluster), the first and last hit, the center for
 4057 spatial reconstruction and finally the start and stop time stamps as well as te time spread in between
 4058 the first and last hit.

4059

4060 To investigate the hit list of a given detector partition, the function `Clusterization()` defined
 4061 in `include/Cluster.h` needs the hits in the list to be time sorted. This is achieved by calling func-
 4062 tion `sort()` of library `<algorithm>` using the comparator `SortHitbyTime(RPCHit h1, RPCHit h2)`
 4063 defined in `include/RPCHit.h` that returns `true` if the time stamp of hit `h1` is lower than that of `h2`.
 4064 A first isolation of strips is made only based on time information. All the hits within the 25 ns win-
 4065 dows are taken separately from the rest. Then, this sub-list of hits is sorted this time by ascending
 4066 strip number, using this time the comparator `SortHitbyStrip(RPCHit h1, RPCHit h2)`. Finally, the
 4067 groups of adjacent strips are used to construct `RPCCluster` objects that are then stored in a temporary
 4068 list of clusters that is at the end of the process used to know how many clusters were reconstructed
 4069 and to fill their sizes into an histogram that will allows to know the mean size of muon or gamma
 4070 clusters. This method to group hits together into clusters is limited as no systematic study of the
 4071 average avalanche time development into TDC hits was performed and that there is no correlation

4072 of both spatial and time information to make the first selection of hits. Due to this, two clusters
 4073 developping consecutively next to each other during a total time longer to 25 ns could be wrongly
 4074 grouped as a cluster composed of the first developed cluster plus a part of the second cluster while
 4075 the rest of the second cluster would be placed in a second truncated cluster. This kind of event
 4076 is not likely but needs to be taken into account nonetheless. A possible improvement would be to
 4077 identify clusters in a 2D space whose dimensions are time and strip. In this 2D space, the cluster
 4078 could be geometrically identified as isolated groups of adjacent strips receiving a hit at a similar time.
 4079

```

class RPCCluster{
    private:
        Uint ClusterSize; //Size of cluster #ID
        Uint FirstStrip; //First strip of cluster #ID
        Uint LastStrip; //Last strip of cluster #ID
        float Center; //Center of cluster #ID ((first+last)/2)
        float StartStamp; //Time stamp of the earliest hit of cluster #ID
        float StopStamp; //Time stamp of the latest hit of cluster #ID
        float TimeSpread; //Time difference between earliest and latest hits
                           //of cluster #ID
    public:
        RPCCluster();
        RPCCluster(HitList List, Uint cID, Uint cSize, Uint first, Uint firstID);
        RPCCluster(const RPCCluster& other);
        ~RPCCluster();
        RPCCluster& operator=(const RPCCluster& other);

        Uint GetID();
        Uint GetSize();
        Uint GetFirstStrip();
        Uint GetLastStrip();
        float GetCenter();
        float GetStart();
        float GetStop();
        float GetSpread();
    };

typedef vector<RPCCluster> ClusterList;

//Other functions to build cluster lists out of hit lists
void BuildClusters(HitList &cluster, ClusterList &clusterList);
void Clusterization(HitList &hits, TH1 *hcSize, TH1 *hcMult);

```

4081

Source Code B.11: Description of C++ object Cluster.

4082 B.6 DAQ data Analysis

4083 All the ingredients to analyse GIFT++ data have been introduced. This section will focus on the
 4084 different part of the analysis performed on the data, from determining the type of data the tool is
 4085 dealing with to calculate the hit and cluster rate per unit area in each detector or reconstructing
 4086 muon or gamma clusters.

4087 B.6.1 Determination of the run type

4088 In GIF++, both the performance of the detectors in detecting muons in an irradiated environment
 4089 and the gamma or noise background can be independantly measured. These correspond to different
 4090 run types and hence, to different TDC settings giving different data to look at.

4091 In the case of performance measurements, the trigger for data taking is provided by the coin-
 4092 cidence of several scintillators when muons from the beam passing through the area are detected.
 4093 Data is collected in a 600 ns wide window centered around the arrival of muons in the RPCs. The
 4094 expected time distribution of hits is shown in Figure B.1a. The muon peak is clearly visible in the
 4095 center of the distribution and is to be extracted from the gamma background that composes the flat
 4096 part of the distribution.

4097 On the other hand, gamma background or noise measurements are focussed on the non muon
 4098 related physics and the trigger needs to be independant from the muons to give a good measurement
 4099 of the gamma/noise distribution as seen by the detectors. The trigger is then provided by a pulse
 4100 generated by the DAQ at a frequency of 100 Hz whose pulse is not likely to be on time with a muon.
 4101 In order to increase the integrated time without increasing proportionnaly the acquisition time, the
 4102 width of the acquisition windows are increased to 10 μ s. The time distribution of the hits is expected
 4103 to be flat, as shown by Figure B.1b.

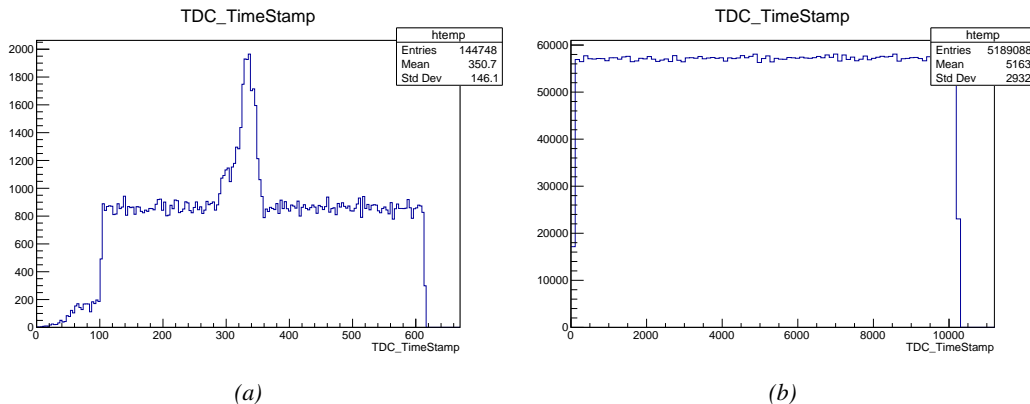


Figure B.1: Example of expected hit time distributions in the cases of efficiency (Figure B.1a) and noise/gamma rate per unit area (Figure B.1b) measurements as extracted from the raw ROOT files. The unit along the x-axis corresponds to ns. The fact that "the" muon peak is not well defined in Figure B.1a is due to the contribution of all the RPCs being tested at the same time that don't necessarily have the same signal arrival time. Each individual peak can have an offset with the ones of other detectors. The inconsistancy in the first 100 ns of both time distributions is an artefact of the TDCs and are systematically rejected during the analysis.

4104 The ROOT files include a `TTree` called `RunParameters` containing, among other things, the infor-
 4105 mation related to the run type. The run type can then be accessed as described by Source Code B.12
 4106 and the function `IsEfficiencyRun()` is then used to determine if the run file is an efficiency run or,
 4107 on the contrary, another type of run (noise or gamma measurement).

4108 Finally, the data files will have a slightly different content whether it was collected before or after
 4109 October 2017 and the upgrade of the DAQ software that brought a new information into the ROOT
 4110 output. This is discussed in Appendix A.4.3 and implies that the analysis will differ a little depending
 4111 on the data format. Indeed, as no information on the data quality is stored, in older data files, the cor-
 4112 rections for missing events has to be done at the end of the analysis. The information about the type

4113 of data format is stored in the variable **bool** `isNewFormat` by checking the list of branches contained
 4114 in the data tree via the methods `TTree::GetListOfBranches()` and `TCollection::Contains()`.

```
4115
4116     TTree* RunParameters = (TTree*)dataFile.Get("RunParameters");
4117     TString* RunType = new TString();
4118     RunParameters->SetBranchAddress("RunType", &RunType);
4119     RunParameters->GetEntry(0);
```

4117 *Source Code B.12: Access to the run type contained in `TTree* RunParameters`.*

4118 **B.6.2 Beam time window calculation for efficiency runs**

4119 Knowing the run type is important first of all to know the width of the acquisition window to be used
 4120 for the rate calculation and finally to be able to seek for muons. Indeed, the peak that appears in the
 4121 time distribution for each detectors is then fitted to extract the most probable time window in which
 4122 the tool should look for muon hits. The data outside of this time window is then used to evaluate the
 4123 noise or gamma background the detector was subjected to during the data taking. Computing the
 4124 position of the peak is done calling the function `SetBeamWindow()` defined in file `src/RPCHit.cc` that
 4125 loops a first time on the data. The data is first sorted in a 3D array of 1D histograms (`GIFH1Array`, see
 4126 `include/types.h`). Then the location of the highest bin is determined using `TH1::GetMaximumBin()`
 4127 and is used to define a window in which a gaussian fit will be applied to compute the peak width.
 4128 This window is a 80 ns defined by Formula B.1 around the central bin.

$$(B.1a) \quad t_{center}(ns) = bin \times width_{bin}(ns)$$

$$(B.1b) \quad [t_{low}; t_{high}] = [t_{center} - 40; t_{center} + 40]$$

4129 Before the fit is performed, the average number of noise/gamma hits per bin is evaluated using
 4130 the data outside of the fit window. Excluding the first 100 ns, the average number of hits per bin
 4131 due to the noise or gamma is defined by Formula B.2 after extracting the amount of hits in the time
 4132 windows $[100; t_{low}]$ and $[t_{high}; 600]$ thanks to the method `TH1::Integral()`. This average number
 4133 of hits is then subtracted to every bin of the 1D histogram, in order to *clean* it from the noise or
 4134 gamma contribution as much as possible to improve the fit quality. Bins where $\langle n_{hits} \rangle$ is greater
 4135 than the actual bin content are set to 0.

$$(B.2a) \quad \Delta t_{noise}(ns) = 600 \overbrace{-t_{high} + t_{low}}^{-80ns} - 100 = 420ns$$

$$(B.2b) \quad \langle n_{hits} \rangle = width_{bin}(ns) \times \frac{\sum_{t=100}^{t_{low}} + \sum_{t=t_{high}}^{600}}{\Delta t_{noise}(ns)}$$

4136 Finally, the fit parameters are extracted and saved for each detector in 3D arrays of **float**
 4137 (`muonPeak`, see `include/types.h`), a first one for the mean arrival time of the muons, `PeakTime`,
 4138 a second for the height or strength of the peak, `PeakHeight`, and a third one for the width of the
 4139 peak, `PeakWidth`. The width is on purpose chosen to be wider than the peak and defined as 6σ of the
 4140 gaussian fit, for a peak range being as given by Formula B.3.

$$(B.3) \quad [t_{low}^{peak}; t_{high}^{peak}] = [t_{center}^{peak} - 3\sigma; t_{center}^{peak} + 3\sigma]$$

4141 For a finer analysis, it is advised to determine more precisely the width of the peak to exclude
 4142 as much noise or background hits as possible. The same settings are applied to every partitions of
 4143 the same detector. To determine which one of the detector's partitions is directly illuminated by the
 4144 beam, the peak height of each partition is compared and the highest one is then used to define the
 4145 peak settings.

4146 It is not possible to identify the particles causing the hits, hence muons, background gamma
 4147 particles or even noise could be responsible of hits within the time window. To be able to account
 4148 for this effect, the peak width extracted from the fit on the peak will also be used to define a fake
 4149 time window, uncorrelated to the muon peak and in which a fake efficiency, contribution from both
 4150 background and noise, will be measured. This window corresponds to the time range described in
 4151 Formula B.4.

$$(B.4) \quad [t_{low}^{fake}; t_{high}^{fake}] = [600 - 6\sigma; 600]$$

4152 B.6.3 Data loop and histogram filling

4153 3D arrays of histogram are created to store the data and display it on the DQM of GIF++ webDCS
 4154 for the use of shifters. The dimensions correspond to the different layers held into the GIF++ infras-
 4155 tructure (trolleys `T` containing RPCs or *slots* `s` each being divided into read-out partitions `p`). These
 4156 histograms, presented in section B.2.1.1, are filled while looping on the data. Before starting the
 4157 analysis loop, it is necessary to control the entry quality for the new file formats featuring `QFlag`. If
 4158 the `QFlag` value for this entry shows that 1 TDC or more have a `CORRUPTED` flag, then this event is
 4159 discarded. The loss of statistics is low enough to be neglected. `QFlag` is controlled using the func-
 4160 tion `IsCorruptedEvent()` defined in `src/utils.cc`. As explained in Appendix A.4.3, each digit of
 4161 this integer represent a TDC flag that can be either 1 or 2. Each 2 is the sign of a `CORRUPTED` state.
 4162 Then, the data is accessed entry by entry in the ROOT `TTree` using `RAWData` and each hit in the hit
 4163 list is assigned to a detector channel and saved in the corresponding histograms. As described in
 4164 Source Code B.13, in the first part of the analysis, in which the loop over the ROOT file's content is
 4165 performed, the different steps are:

4166 **1- RPC channel assignment and control:** a check is done on the RPC channel extracted thanks
 4167 to the mapping via the method `Mapping::GetLink()`. If the channel is not initialised and is 0, or if
 4168 the TDC channel is not contained in a range in between X000 and X127, X being the TDC ID, the
 4169 hit is discarded. This means there was a problem in the mapping. Often a mapping problem leads to
 4170 the failure of the offline tool.

4171 **2- Creation of a `RPCHit` object:** to easily get the trolley, slot and partition in which the hit has
 4172 been assigned, this object is particularly helpful.

4173 **3- General histograms are filled:** the hit is filled into the time distribution, global hit distribution
 4174 and time versus strip histograms, and if the arrival time is within the first 100 ns, it is discarded and
 4175 nothing else happens and the loop proceeds with the next hit in the list, going back to step 1.

4176

```

for(int h = 0; h < data.TDCCh->size(); h++) {
    UInt tdcchannel = data.TDCCh->at(h);
    UInt rpcchannel = RPCChMap->GetLink(tdcchannel);
    float timestamp = data.TDCTS->at(h);
    //Get rid of the hits in channels not considered in the mapping
    if(rpcchannel != NOCHANNELLINK) {
        RPCHit hit(rpcchannel, timestamp, GIFInfra);
        UInt T = hit.GetTrolley();
        UInt S = hit.GetStation()-1;
        UInt P = hit.GetPartition()-1;
        //Fill the time and hit profiles
        TimeProfile_H.rpc[T][S][P]->Fill(hit.GetTime());
        HitProfile_H.rpc[T][S][P]->Fill(hit.GetStrip());
        TimeVSChanProfile_H.rpc[T][S][P]->Fill(hit.GetStrip(), hit.GetTime());
        //Reject the 100 first ns due to inhomogeneity of data
        if(hit.GetTime() >= TIMEREJECT) {
            Multiplicity.rpc[T][S][P]++;
            if(IsEfficiencyRun(RunType)) {
                //Define peak time range for efficiency calculation
                float lowlimit_eff = PeakTime.rpc[T][S][P]
                    - PeakWidth.rpc[T][S][P];
                float highlimit_eff = PeakTime.rpc[T][S][P]
                    + PeakWidth.rpc[T][S][P];
                bool peakrange = (hit.GetTime() >= lowlimit_eff
                    && hit.GetTime() < highlimit_eff);
                //Fill hits inside of the defined peak and noise range
                if(peakrange) {
                    BeamProfile_H.rpc[T][S][P]->Fill(hit.GetStrip());
                    PeakHitList.rpc[T][S][P].push_back(hit);
                } else {
                    StripNoiseProfile_H.rpc[T][S][P]->Fill(hit.GetStrip());
                    NoiseHitList.rpc[T][S][P].push_back(hit);
                }
                //Then define time range for fake efficiency
                float highlimit_fake = BMTDCWINDOW;
                float lowlimit_fake = highlimit_fake
                    - (highlimit_eff-lowlimit_eff);
                bool fakerange = (hit.GetTime() >= lowlimit_fake
                    && hit.GetTime() < highlimit_fake);
                //Fill the hits inside of the fake window
                if(fakerange) {
                    FakeHitList.rpc[T][S][P].push_back(hit);
                }
            } else {
                //Fill the hits inside of the defined noise range
                StripNoiseProfile_H.rpc[T][S][P]->Fill(hit.GetStrip());
                NoiseHitList.rpc[T][S][P].push_back(hit);
            }
        }
    }
}

```

4177

Source Code B.13: For each entry of the raw ROOT data file, the code loops over the list of channels and corresponding time stamps contained in branches `TDC_channel` and `TDC_TimeStamp` and constructs `RPCHit` objects that are filled in the peak, noise and fake hit lists and also fills the time, hit, beam and noise profiles.

4178

4- Multiplicity counter: the hit multiplicity counter of the corresponding detectors is incremented.

4180 **5-a-1 Efficiency runs - Is the hit within the peak window? :** if the hit is contained in the peak
 4181 window previously defined by Formula B.3, it is filled into the beam hit profile histogram of the
 4182 corresponding chamber, added into the list of peak hits and increments the counter of *in time* hits.
 4183 The term *in time* here refers to the hits that are likely to be muons by arriving in the expected time
 4184 window. If the hit is outside of the peak window, it is filled into the noise profile histogram of
 4185 the corresponding detector, added into the list of noise/gamma hits and increments the counter of
 4186 noise/gamma hits.

4187 **5-a-2 Efficiency runs - Is the hit within the fake window? :** if the hit is contained in the fake
 4188 window previously defined by Formula B.4, it is added into the list of fake hits. Counting the fake
 4189 hits outside the peak window allows to estimate the probability to detect in time background or noise.

4190 **5-b- Noise/gamma rate runs - Noise histograms are filled:** the hit is filled into the noise profile
 4191 histogram of the corresponding detector, added into the list of noise/gamma hits and increments the
 4192 counter of noise/gamma hits.

```
4193
  for(UInt tr = 0; tr < GIFInfra->GetNTrolleys(); tr++) {
    UInt T = GIFInfra->GetTrolleyID(tr);
    for(UInt sl = 0; sl < GIFInfra->GetNSlots(tr); sl++) {
      UInt S = GIFInfra->GetSlotID(tr,sl) - 1;
      UInt nStripsPart = GIFInfra->GetNStrips(tr,sl);
      string rpcID = GIFInfra->GetName(tr,sl);
      for (UInt p = 0; p < GIFInfra->GetNPartitions(tr,sl); p++) {
        //Clusterize noise/gamma data
        sort(NoiseHitList.rpc[T][S][p].begin(),
              NoiseHitList.rpc[T][S][p].end(),SortHitbyTime);
        Clusterization(NoiseHitList.rpc[T][S][p],
                       NoiseCSize_H.rpc[T][S][p],NoiseCMult_H.rpc[T][S][p]);
        //Clusterize muon data and fill efficiency histograms based on
        //the content of peak and fake hit vectors if efficiency run
        if(IsEfficiencyRun(RunType)){
          //Peak data
          sort(PeakHitList.rpc[T][S][p].begin(),
                PeakHitList.rpc[T][S][p].end(),SortHitbyTime);
          Clusterization(PeakHitList.rpc[T][S][p],
                         PeakCSize_H.rpc[T][S][p],PeakCMult_H.rpc[T][S][p]);
          if(PeakHitList.rpc[T][S][p].size() > 0)
            EfficiencyPeak_H.rpc[T][S][p]->Fill(DETECTED);
          else EfficiencyPeak_H.rpc[T][S][p]->Fill(MISSED);

          //Fake data
          if(FakeHitList.rpc[T][S][p].size() > 0)
            EfficiencyFake_H.rpc[T][S][p]->Fill(DETECTED);
          else EfficiencyFake_H.rpc[T][S][p]->Fill(MISSED);
        }
        //Save and reinitialise the hit multiplicity
        HitMultiplicity_H.rpc[T][S][p]->Fill(Multiplicity.rpc[T][S][p]);
        Multiplicity.rpc[T][S][p] = 0;
      }
    }
  }
```

4195 *Source Code B.14: Loops to clusterize the hit lists and fill efficiency and multiplicity histograms.*

4196 After the loop on the hit list of the entry is over, the next step is to clusterize the 3D lists filled

4197 in the previous steps, as displayed in Source Code B.14. A 3D loop is then started over the active
 4198 trolley, slot and RPC partitions to access these objects. Each `NoiseHitList` and `PeakHitList`, in
 4199 case of efficiency run, are clusterized as described in section B.5.2. There corresponding cluster size
 4200 and multiplicity histograms are filled at the end of the clustering process.

4201 Then, the peak and fake efficiency histograms are filled in case of efficiency run. The selection is
 4202 simply made by checking whether the RPC detected signals in the peak window or/and fake window
 4203 during this event. In the case a hit is recorded in either of both time windows, the histogram is
 4204 filled with 1. On the contrary, the histogram is filled with 0. Finally, it is useful to remind that
 4205 at this level, it is not possible yet to discriminate in between a muon hit and noise or gamma hit.
 4206 the histograms `PeakCSize_H`, `PeakCMult_H` and `EfficiencyPeak_H` are then subjected to noise and
 4207 background contamination. This contamination is estimated thanks to the fake efficiency histogram
 4208 `EfficiencyFake_H` and corrected at the moment the results will be written into output CSV files and
 4209 the histograms `MuonCSize_H`, `MuonCMult_H` and `Efficiency0_H` will be filled. The correction will be
 4210 explained in Section B.6.4.3.

4211 Finally, the loop ends on the filling of the general hit multiplicity histogram of each detector
 4212 partitions.

4213 **B.6.4 Results calculation**

4214 As mentioned in section B.2.1, the analysis of DAQ data provides the user with 3 CSV files and
 4215 a ROOT file associated to each and every ROOT data file. The fourth CSV file is provided by the
 4216 extraction of the CEAN main frame data monitored during data taking and will be discussed later.
 4217 After looping on the data in the previous part of the analysis macro, the output files are created and a
 4218 3D loop on each RPC readout partitions is started to extract the histograms parameters and compute
 4219 the final results.

4220

4221 **B.6.4.1 Rate normalisation**

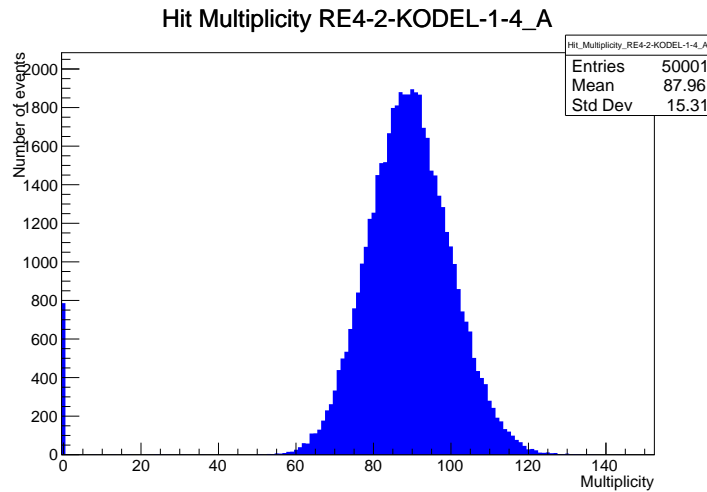


Figure B.2: The effect of the quality flag is explained by presenting the reconstructed hit multiplicity of a data file without `Quality_flag`. The artificial high content of bin 0 is the effect of corrupted data.

4222 The hit rate normalization corresponds to translating a number of hits recorded during the full duration
4223 of data taking into a rate per unit area value. In order to achieve such result, it is first needed
4224 to know the total integrated time and the active area of the read-out partition on which the hits are
4225 counted. The total integrated is simply the noise window used for each event multiplied by the total
4226 number of events stored in the data file.

```

4227
if (!isNewFormat) {
    TF1* GaussFit = new TF1("gaussfit","[0]*exp(-0.5*((x-[1])/[2])**2)",0,Xmax);
    GaussFit->SetParameter(0,100);
    GaussFit->SetParameter(1,10);
    GaussFit->SetParameter(2,1);
    HitMultiplicity_H.rpc[T][S][p]->Fit(GaussFit,"LIQR","",0.5,Xmax);

    TF1* SkewFit = new TF1("skewfit","[0]*exp(-0.5*((x-[1])/[2])**2) / (1 +
→   exp(-[3]*(x-[4])))",0,Xmax);
    SkewFit->SetParameter(0,GaussFit->GetParameter(0));
    SkewFit->SetParameter(1,GaussFit->GetParameter(1));
    SkewFit->SetParameter(2,GaussFit->GetParameter(2));
    SkewFit->SetParameter(3,1);
    SkewFit->SetParameter(4,1);
    HitMultiplicity_H.rpc[T][S][p]->Fit(SkewFit,"LIQR","",0.5,Xmax);

    double fitValue = SkewFit->Eval(1,0,0,0);
    double dataValue = (double)HitMultiplicity_H.rpc[T][S][p]->GetBinContent(2);
    double difference = TMath::Abs(dataValue - fitValue);
    double fitTOdataVSentries_ratio = difference / (double)nEntries;
    bool isFitGOOD = fitTOdataVSentries_ratio < 0.01;
    double nSinglehit = (double)HitMultiplicity_H.rpc[T][S][p]->GetBinContent(1);
    double lowMultRatio = nSinglehit / (double)nEntries;
    bool isMultLOW = lowMultRatio > 0.4;
    if(isFitGOOD && !isMultLOW){
        nEmptyEvent = HitMultiplicity_H.rpc[T][S][p]->GetBinContent(1);
        nPhysics = (int)SkewFit->Eval(0,0,0,0);
        if(nPhysics < nEmptyEvent)
            nEmptyEvent = nEmptyEvent-nPhysics;
    }
}
double corrupt_ratio = 100.*(double)nEmptyEvent / (double)nEntries;
outputCorrCSV << corrupt_ratio << '\t';
float rate_norm = 0.;
float stripArea = GIFIInfra->GetStripGeo(tr,sl,p);

if(IsEfficiencyRun(RunType)){
    float noiseWindow = BMTDCWINDOW - TIMEREJECT - 2*PeakWidth.rpc[T][S][p];
    rate_norm = (nEntries-nEmptyEvent)*noiseWindow*1e-9*stripArea;
} else
    rate_norm = (nEntries-nEmptyEvent)*RDMNOTSEWDW*1e-9*stripArea;

```

4229 *Source Code B.15: Definition of the rate normalisation variable. It takes into account the number of non corrupted entries and the time window used for noise and background calculation, to estimate the total integrated time, and the strip active area to express the result as rate per unit area.*

4230 Nevertheless, to analyse old data format files, not containing any quality flag, it is needed to
4231 estimate the amount of corrupted data via a fit as the corrupted data will always fill events with a
4232 fake "0 multiplicity". Indeed, as no hits were stored in the DAQ ROOT files, these events artificially
4233 contribute to fill the bin corresponding to a null multiplicity, as shown in Figure B.2. In the case the
4234 mean of the hit multiplicity distribution is high, the contribution of the corrupted data can easily be

evaluated for later correction by comparing the level of the bin at multiplicity 0 and of a skew fit curve that should indicate a value consistent with 0. A skew fit has been chosen over a Poisson fit as it was giving better results for lower mean multiplicity values. Nevertheless, for low irradiation cases, as explained in Appendix A.4.3, the hit multiplicity distribution mean is, on the contrary, rather small and the probability to record events without hits can't be considered small anymore, leading to a difficult and non-reliable estimation of the corruption.

As can be seen in Source Code B.15, conditions have been applied to prevent bad fits and wrong corruption estimation in cases where :

- The difference in between the data for multiplicity 1 and the corresponding fit value should be lower than 1% of the total amount of data : $\frac{|n_{m=1} - sk(1)|}{N_{tot}} < 0.01$ where $n_{m=1}$ is the number of entries with multiplicity 1, $sk(1)$ the value of the skew fit, as defined by Formula 5.2, for multiplicity 1 and N_{tot} the total number of entries.
- The amount of data contained in the multiplicity 0 bin should not exceed 40% of the total data content: $\frac{n_{m=0}}{N_{tot}} \leq 0.4$ where $n_{m=0}$ is the number of entries with multiplicity 0. This number has been determined to be the maximum to be able to separate the excess of data due to corruption from the hit multiplicity distribution.

Those 2 conditions need to be fulfilled to estimate the corruption of old data format files. If the fit was successful, the level of corruption is written in `Offline-Corrupted.csv` and the number of corrupted entries, refered as the integer `nEmptyEvent`, is subtracted from the total number of entries when the rate normalisation factor is computed as explicitated in Source Code B.15. Note that for new data format files, the number of corrupted entries being set to 0, the definition of `rate_norm` stays valid.

B.6.4.2 Rate and activity

At this point, the strip rate histograms, `StripNoiseProfile_H.rpc[T][S][p]`, only contain an information about the total number of noise or background rate hits each channel received during the data taking. As described in Source Code B.16, a loop on the strip channels will be used to normalise the content of the rate distribution histogram for each detector partitions. The initial number of hits recorded for a given bin will be extracted and 2 values are computed.

- The strip hit rate, defined as the number of hits recorded in the bin normalised like described in the previous section, using the variable `rate_norm` and the corresponding bin in histogram `StripNoiseProfile_H.rpc[T][S][p]` is updated, and
- the strip activity, defined as the number of hits recorded in the bin normalised to the average number of hits per bin contained in the partition histogram, using the variable `averageNhit`. This value provides an information on the homogeneity of the detector response to the gamma background or of the detector noise. An activity of 1 corresponds to an average response. Above 1, the channel is more active than the average and bellow 1, the channel is less active. This value is filled in the histograms `StripActivity_H.rpc[T][S][p]`.

```

int nNoise = StripNoiseProfile_H.rpc[T][S][p]->GetEntries();
float averageNhit = (nNoise>0) ? (float) (nNoise/nStripsPart) : 1.;

for(UInt st = 1; st <= nStripsPart; st++){
    float stripRate =
        StripNoiseProfile_H.rpc[T][S][p]->GetBinContent(st)/rate_norm;
    float stripAct =
        StripNoiseProfile_H.rpc[T][S][p]->GetBinContent(st)/averageNhit;

    StripNoiseProfile_H.rpc[T][S][p]->SetBinContent(st,stripRate);
    StripActivity_H.rpc[T][S][p]->SetBinContent(st,stripAct);
}

```

Source Code B.16: Description of the loop that allows to set the content of each strip rate and strip activity channel for each detector partition.

On each detector partitions, which are read-out by a single FEE, all the channels are not processed by the same chip. Each chip can give a different noise response and hence, histograms using a chip binning are used to investigate chip related noise behaviours. The average values of the strip rate or activity grouped into a given chip are extracted using the using the function `GetChipBin()` and stored in dedicated histograms as described in Source Codes B.17 and B.18 respectively.

```

float GetChipBin(TH1* H, UInt chip){
    UInt start = 1 + chip*NSTRIPSCHIP;
    int nActive = NSTRIPSCHIP;
    float mean = 0.;

    for(UInt b = start; b <= (chip+1)*NSTRIPSCHIP; b++) {
        float value = H->GetBinContent(b);
        mean += value;
        if(value == 0.) nActive--;
    }

    if(nActive != 0) mean /= (float)nActive;
    else mean = 0.;

    return mean;
}

```

Source Code B.17: Function used to compute the content of a bin for an histogram using chip binning.

```

for(UInt ch = 0; ch < (nStripsPart/NSTRIPSCHIP); ch++) {
    ChipMeanNoiseProf_H.rpc[T][S][p]->
        SetBinContent(ch+1,GetChipBin(StripNoiseProfile_H.rpc[T][S][p],ch));
    ChipActivity_H.rpc[T][S][p]->
        SetBinContent(ch+1,GetChipBin(StripActivity_H.rpc[T][S][p],ch));
}

```

Source Code B.18: Description of the loop that allows to set the content of each chip rate and chip activity bins for each detector partition knowing the information contained in the corresponding strip distribution histograms.

The activity variable is then used to evaluate the homogeneity of the detector response to background or of the detector noise. The homogeneity h_p of each detector partition can be evaluated

4286 using the formula $h_p = \exp(-\sigma_p^R / \langle R \rangle_p)$, where $\langle R \rangle_p$ is the partition mean rate and σ_p^R is the
 4287 rate standard deviation calculated over the partition channels. The more homogeneously the rates
 4288 are distributed and the smaller will σ_p^R be, and the closer to 1 will h_p get. On the contrary, if the
 4289 standard deviation of the channel's rates is large, h_p will rapidly get to 0. This value is saved into
 4290 histograms as shown in Source Code B.19 and could in the future be used to monitor through time,
 4291 once extracted, the evolution of every partition homogeneity. This could be of great help to under-
 4292 stand the apparition of eventual hot spots due to ageing of the chambers subjected to high radiation
 4293 levels. The monitored homogeneity information could then be combined with a monitoring of the
 4294 activity of each individual channel in order to have a finer information. Monitoring tools have been
 4295 suggested and need to be developed for this purpose.

```
4296 float MeanPartSDev = GetTH1StdDev(StripNoiseProfile_H.rpc[T][S][p]);
float strip_homog = (MeanPartRate==0)
    ? 0.
    : exp(-MeanPartSDev/MeanPartRate);
StripHomogeneity_H.rpc[T][S][p]->Fill("exp -#left(#frac{\#sigma_{Strip}
    \rightarrow Rate}{\#mu_{Strip Rate}}\#right)",strip_homog);
StripHomogeneity_H.rpc[T][S][p]->GetYaxis()->SetRangeUser(0.,1.);

4297 float ChipStDevMean = GetTH1StdDev(ChipMeanNoiseProf_H.rpc[T][S][p]);
float chip_homog = (MeanPartRate==0)
    ? 0.
    : exp(-ChipStDevMean/MeanPartRate);
ChipHomogeneity_H.rpc[T][S][p]->Fill("exp -#left(#frac{\#sigma_{Chip}
    \rightarrow Rate}{\#mu_{Chip Rate}}\#right)",chip_homog);
ChipHomogeneity_H.rpc[T][S][p]->GetYaxis()->SetRangeUser(0.,1.);
```

4298 *Source Code B.19: Storage of the homogeneity into dedicated histograms.*

4299 B.6.4.3 Correction of muon performance parameters

4300 By previously filling the peak and fake efficiency histograms as well as the peak and noise cluster
 4301 size and cluster multiplicity it is possible to compute the efficiency of muon detection, the muon
 4302 cluster size, as well as the muon cluster multiplicity. This calculation is based on independent
 4303 event probabilities. The independent events that can be measured in the data are, " μ : A muon was
 4304 detected" and " γ : noise or background was detected". It is trivial to realize that the data in the peak
 4305 window corresponds to the intersection of both events, " $\mu \cup \gamma$: a muon or noise or background was
 4306 detected". This way, the efficiency measured in the peak window is actually the probability of the
 4307 event $\mu \cup \gamma$ while the efficiency in the fake window is then the probability of the event γ alone.
 4308 Assuming that μ and γ are independent, the probability of their intersection can be written as in
 4309 Formula B.5.

$$(B.5) \quad P(\mu \cup \gamma) = P(\mu) + P(\gamma) - P(\mu)P(\gamma)$$

4310 Isolating the probability of the event μ alone, actually corresponding to the muon detection
 4311 efficiency, can be then calculated with the quantities that are contained in the peak and fake histogram
 4312 as in Formula B.6.

$$(B.6) \quad P(\mu) = \frac{P(\mu \cup \gamma) - P(\gamma)}{1 - P(\gamma)} \quad \Leftrightarrow \quad \epsilon_\mu = \frac{\epsilon_{peak} - \epsilon_{fake}}{1 - \epsilon_{fake}}$$

```

if(IsEfficiencyRun(RunType)){  

    //Evaluate the probabilities for each detection case with errors  

    float P_peak = EfficiencyPeak_H.rpc[T][S][p]->GetMean();  

    float P_fake = EfficiencyFake_H.rpc[T][S][p]->GetMean();  

    float P_muon = (P_peak-P_fake)/(1-P_fake);  

    float P_both = P_muon*P_fake;  

    float P_peak_err = sqrt(P_peak*(1.-P_peak)/nEntries);  

    float P_fake_err = sqrt(P_fake*(1.-P_fake)/nEntries);  

    float P_muon_err = sqrt(P_muon*(1.-P_muon)/nEntries);  

    float P_both_err = sqrt(P_both*(1.-P_both)/nEntries);  

    Efficiency0_H.rpc[T][S][p]->Fill("muon efficiency",P_muon);  

    Efficiency0_H.rpc[T][S][p]->Fill("muon efficiency error",P_muon_err);  

    //For each case get the fraction of events it represents  

    float F_both = P_both/P_peak;  

    float F_muon = (P_muon-P_both)/P_peak;  

    float F_fake = (P_fake-P_both)/P_peak;  

    float F_both_err = F_both*(P_both_err/P_both+P_peak_err/P_peak);  

    float F_muon_err = (P_muon_err+F_both_err+F_muon*P_peak_err)/P_peak;  

    float F_fake_err = (P_fake_err+F_both_err+F_fake*P_peak_err)/P_peak;  

    //Get the measured cluster sizes correcting using the fractions  

    float CS_peak = PeakCSIZE_H.rpc[T][S][p]->GetMean();  

    float CS_fake = NoiseCSIZE_H.rpc[T][S][p]->GetMean();  

    float CS_peak_err = 2*PeakCSIZE_H.rpc[T][S][p]->GetStdDev()  

        /sqrt(PeakCSIZE_H.rpc[T][S][p]->GetEntries());  

    float CS_fake_err = 2*NoiseCSIZE_H.rpc[T][S][p]->GetStdDev()  

        /sqrt(NoiseCSIZE_H.rpc[T][S][p]->GetEntries());  

    float CS_muon = (CS_peak-CS_fake*(F_fake+F_both/2.))/(F_muon+F_both/2.);  

    float CS_muon_err = (CS_peak_err  

        +(F_fake+F_both/2.)*CS_fake_err  

        +CS_muon*F_muon_err  

        +CS_fake*(F_fake_err+F_both_err/2.))  

        /(F_muon+F_both/2.);  

    MuonCSIZE_H.rpc[T][S][p]->Fill("muon cluster size",CS_muon);  

    MuonCSIZE_H.rpc[T][S][p]->Fill("muon cluster size error",CS_muon_err);  

    //Finally get the muon cluster multiplicity as peak-fake  

    float noiseWindow = BMTDCWINDOW - TIMEREJECT - 2*PeakWidth.rpc[T][S][p];  

    float peakWindow = 2*PeakWidth.rpc[T][S][p];  

    float CM_peak = PeakCMult_H.rpc[T][S][p]->GetMean();  

    float CM_fake = NoiseCMult_H.rpc[T][S][p]->GetMean()*peakWindow/noiseWindow;  

    float CM_muon = CM_peak-CM_fake;  

    float CM_peak_err = 2*PeakCMult_H.rpc[T][S][p]->GetStdDev()  

        /sqrt(PeakCMult_H.rpc[T][S][p]->GetEntries());  

    float CM_fake_err = 2*NoiseCMult_H.rpc[T][S][p]->GetStdDev()  

        /sqrt(NoiseCMult_H.rpc[T][S][p]->GetEntries())  

        * peakWindow/noiseWindow;  

    float CM_muon_err = CM_peak_err + CM_fake_err;  

    MuonCMult_H.rpc[T][S][p]->Fill("muon cluster multiplicity",CM_muon);  

    MuonCMult_H.rpc[T][S][p]->Fill("muon cluster multiplicity  

    ↳ error",CM_muon_err);  

    //Write in the output CSV file  

    outputEffCSV << P_muon << '\t' << P_muon_err << '\t'  

        << CS_muon << '\t' << CS_muon_err << '\t'  

        << CM_peak << '\t' << CM_peak_err << '\t';
}

```

4314 Source Code B.20: Analysis algorithm to compute muon efficiency, cluster size and multiplicity knowing the peak and fake efficiency, cluster size and multiplicity.

When it comes to the computation of the muon cluster size, a similar reasoning than for the muon detection efficiency computation can be used. Indeed, using Formula B.5, out of the total number of events where a muon or noise or background can be expressed as a sum of fractions of events μ , γ and $\mu \cap \gamma$, the later being the event corresponding to the detection of both events simultaneously, as showed in Formula B.7. The fractions can be expressed as a ratio of the probabilities already known, using this time the notation $P(\mu \cap \gamma)$ instead of $P(\mu)P(\gamma)$. This choice was made to make the code a little clearer.

$$(B.7) \quad 1 = F_\mu + F_\gamma + F_{\mu \cap \gamma} = \frac{P(\mu) - P(\mu \cap \gamma)}{P(\mu \cup \gamma)} + \frac{P(\gamma) - P(\mu \cap \gamma)}{P(\mu \cup \gamma)} + \frac{P(\mu \cap \gamma)}{P(\mu \cup \gamma)}$$

Each ones of these events have an associated cluster size. The cluster size of the noise or background already is measured thanks to the clusterization of the noise hit list. In the same way, the peak cluster size corresponds to the cluster measured for the event $\mu \cup \gamma$. Nevertheless, the cluster of the event $\mu \cap \gamma$ is not known but it can be assumed that the probability of having more than 1 noise or background cluster contained in the peak window is very low if the peak wondow duration is compared to the background rate that rarely seen to go beyond 2000 Hz/cm² [to be confirmed]. Hence, the cluster size that is likely to be measured in such kind of event where both a muon and a background or noise cluster was recorded is the average of the muon cluster size and the background cluster size. The cluster size $C_{\mu \cup \gamma}$ probed in the peak can then be written as in Formula B.8 and leads to the expression for the muon cluster size C_μ written in Formula B.9.

$$(B.8) \quad C_{\mu \cup \gamma} = C_\mu F_\mu + C_\gamma F_\gamma + \frac{C_\mu + C_\gamma}{2} \times F_{\mu \cap \gamma}$$

$$(B.9) \quad C_\mu = \frac{C_{\mu \cup \gamma} - C_\gamma \times (F_\gamma + F_{\mu \cap \gamma}/2)}{F_\mu + F_{\mu \cap \gamma}/2}$$

Finally, the computation of the muon cluster multiplicity comes quite naturally as the cluster multiplicity measured in the peak to which is subtracted the background cluster multiplpicity taken in a window of similar width. These calculations, as well as the error propagation that was not explicitated here, can be seen going through Source Code B.20.

B.6.4.4 Strip masking tool

The offline tool is automatically called at the end of each data taking to analyse the data and offer the shifter DQM histograms to control the data quality. After the histograms have been published online in the DQM page, the shifter can decide to mask noisy or dead channels that will contribute to bias the final rate calculation by editing the mask column of `ChannelsMapping.csv` as can be seen in Figure B.3.

From the code point of view, the function `GetTH1Mean()` is used to retrieve the mean rate partition by partition after the rates have been calculated strip by strip and filled into the histograms `StripNoiseProfile_H.rpc[T][S][p]`, as described through Source Code B.21.

Once the mask for each rejected channel has been updated, the shifter can manually run the offline tool again to update the DQM plots, now including the masked strips, as well the rate results written in the output CSV file `Offline-Rate.csv`. If not done during the shifts, the strip masking

- 4348 procedure needs to be carefully done by the person in charge of data analysis on the scans that were
 4349 selected to produce the final results.

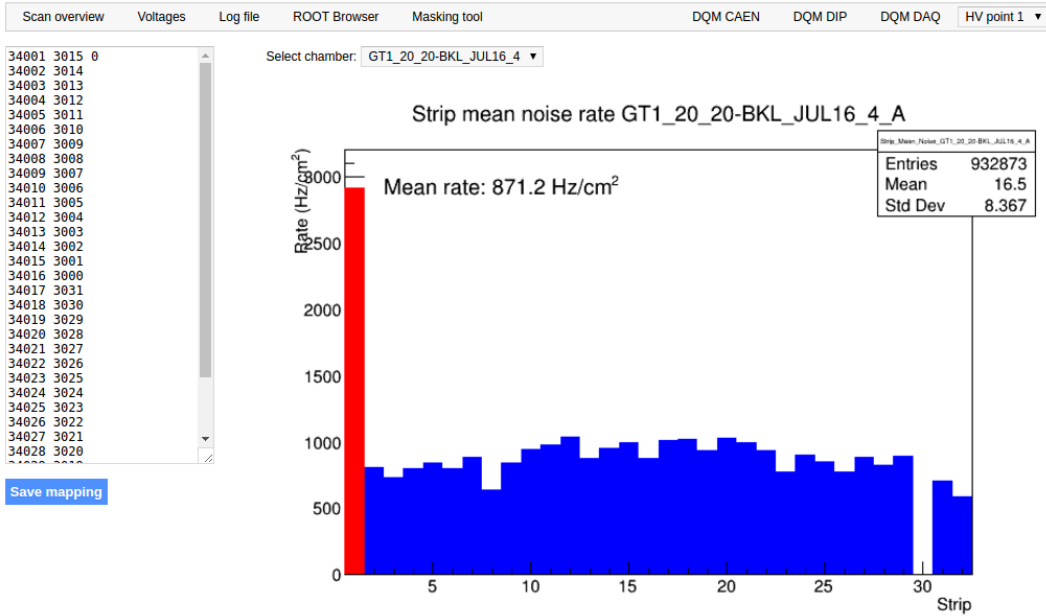


Figure B.3: Display of the masking tool page on the webDCS. The window on the left allows the shifter to edit ChannelsMapping.csv. To mask a channel, it only is needed to set the 3rd field corresponding to the strip to mask to 0. It is not necessary for older mapping file formats to add a 1 for each strip that is not masked as the code is versatile and the default behaviour is to consider missing mask fields as active strips. The effect of the mask is directly visible for noisy channels as the corresponding bin turns red. The global effect of masking strips will be an update of the rate value showed on the histogram that will take into consideration the rejected channels.

```

float GetTH1Mean (TH1* H){
    int nBins = H->GetNbinsX();
    int nActive = nBins;
    float mean = 0.;

    for(int b = 1; b <= nBins; b++){
        float value = H->GetBinContent (b);
        mean += value;
        if(value == 0.) nActive--;
    }

    if(nActive != 0) mean /= (float)nActive;
    else mean = 0.;

    return mean;
}

```

Source Code B.21: The function GetTH1Mean() is used to return the mean along the y-axis of TH1 histograms containing rate information. In order to take into account masked strips whose rate is set to 0, the function looks for masked channels and decrement the number of active channels for each null value found.

4352 **B.6.4.5 Output CSV files filling**

```

for (UInt tr = 0; tr < GIFInfra->GetNTrolleys(); tr++) {
    UInt T = GIFInfra->GetTrolleyID(tr);
    for (UInt sl = 0; sl < GIFInfra->GetNSlots(tr); sl++) {
        UInt S = GIFInfra->GetSlotID(tr,sl) - 1;
        float MeanNoiseRate = 0.;
        float ClusterRate = 0.;
        float ClusterSDev = 0.;

        for (UInt p = 0; p < GIFInfra->GetNPartitions(tr,sl); p++) {
            float MeanPartRate = GetTH1Mean(StripNoiseProfile_H.rpc[T][S][p]);
            float cSizePart = NoiseCSize_H.rpc[T][S][p]->GetMean();
            float cSizePartErr = (NoiseCSize_H.rpc[T][S][p]->GetEntries()==0)
                ? 0.
                : 2*NoiseCSize_H.rpc[T][S][p]->GetStdDev() /
                    sqrt(NoiseCSize_H.rpc[T][S][p]->GetEntries());
            float cMultPart = NoiseCMult_H.rpc[T][S][p]->GetMean();
            float cMultPartErr = (NoiseCMult_H.rpc[T][S][p]->GetEntries()==0)
                ? 0.
                : 2*NoiseCMult_H.rpc[T][S][p]->GetStdDev() /
                    sqrt(NoiseCMult_H.rpc[T][S][p]->GetEntries());
            float ClustPartRate = (cSizePart==0) ? 0.
                : MeanPartRate/cSizePart;
            float ClustPartRateErr = (cSizePart==0) ? 0.
                : ClustPartRate * cSizePartErr/cSizePart;

            outputRateCSV << MeanPartRate << '\t'
                << cSizePart << '\t' << cSizePartErr << '\t'
                << cMultPart << '\t' << cMultPartErr << '\t'
                << ClustPartRate << '\t' << ClustPartRateErr << '\t';

            RPCArea += stripArea * nStripsPart;
            MeanNoiseRate += MeanPartRate * stripArea * nStripsPart;
            ClusterRate += ClustPartRate * stripArea * nStripsPart;
            ClusterSDev += (cSizePart==0)
                ? 0.
                : ClusterRate*cSizePartErr/cSizePart;
        }
        MeanNoiseRate /= RPCArea;
        ClusterRate /= RPCArea;
        ClusterSDev /= RPCArea;
        outputRateCSV << MeanNoiseRate << '\t' << ClusterRate << '\t'
            << ClusterSDev << '\t';
    }
}

```

4354 *Source Code B.22: Description of rate result calculation and writing into the CSV output Offline-Rate.csv. Are saved into the file for each detector, the mean partition rate, cluster size and cluster mutiplicity, along with their errors, for each partition and as well as a detector average.*

4355 All the histograms have been filled. Parameters will then be extracted from them to compute the
 4356 final results that will later be used to produce plots. Once the results have been computed, the very
 4357 last step of the offline macro is to write these values into the corresponding CSV outputs. Aside of
 4358 the file Offline-Corrupted.csv, 2 CSV files are being written by the macro OfflineAnalysis(),
 4359 Offline-Rates.csv and Offline-L0-EffCl.csv that respectively contain information about noise
 4360 or gamma rates, cluster size and multiplicity, and about level 0 reconstruction of the detector effi-
 4361 ciency, muon cluster size and multiplicity. Details on the computation and file writing are respec-

4362 tively given in Sources Codes B.22 and B.20.

4363 **Noise/gamma background variables** are computed and written in the output file for each detector
 4364 partitions. A detector average of the hit and cluster rate is also provided, as shown through Sources
 4365 Code B.22. The variables that are written for each partition are:

- 4366 • The mean partition hit rate per unit area, `MeanPartRate`, that is extracted from the histogram
`StripNoiseProfile_H` as the mean value along the y-axis, as described in section B.6.4.4. No
 4368 error is recorded for the hit rate as this is considered a single measurement. No statistical error
 4369 can be associated to it and the systematics are unknown.
- 4370 • The mean cluster size, `cSizePart`, is extracted from the histogram `NoiseCSize_H` and it's
 4371 statistical error, `cSizePartErr`, is taken to be 2σ of the total distribution.
- 4372 • The mean cluster multiplicity per trigger, `cMultPart`, is extracted from the histogram `NoiseCMult_H`
 4373 and it's statistical error, `cMultPartErr`, is taken to be 2σ of the total distribution. It is impor-
 4374 tant to point to the fact that this variable gives an information that is dependent on the buffer
 4375 window width used for each trigger for the calculation.
- 4376 • The mean cluster rate per unit area, `ClustPartRate`, is defined as the mean hit rate normalised
 4377 to the mean cluster size and it's statistical error, `ClustPartRateErr`, is then obtained using the
 4378 relative statistical error on the mean cluster size.

4379 **Muon performance variables** are computed as discussed in the Section B.6.4.3 and written in
 4380 the output file for each detector partitions as shown through Sources Code B.20. It is reminded that
 4381 this offline tool doesn't include any tracking algorithm to identify muons from the beam and only
 4382 relies on the hits arriving in the time window corresponding to the beam time and is corrected thanks
 4383 to the estimation of the contribution of the background and noise to the efficiency of the detector.
 4384 Assuming that the detection of background and muons were independent events, a probabilistic
 4385 approach was then used to correct efficiency, muon cluster size and muon cluster multiplicity. The
 4386 variables that are written for each partition are:

- 4387 • The muon efficiency, referred to as the probability to detect a muon in the peak window
`P_muon`, also filled in histogram `Efficiency0_H`. The statistical error related to the efficiency,
 4388 `P_muon_err`, is computed using a binomial distribution, as the efficiency measures the proba-
 4389 bility of "success" and "failure" to detect muons.
- 4391 • The mean muon cluster size, `CS_muon`, and its related statistical error, `CS_muon_err`, also filled
 4392 in the histogram `MuonCSize_H`.
- 4393 • The mean muon cluster multiplicity, `CM_muon`, and its related statistical error, `CM_muon_err`,
 4394 also filled in the histogram `MuonCMult_H`.

4395 In addition to these 2 CSV files, the histograms are saved in ROOT file `Scan00XXXX_HVY_Offline.root`
 4396 as explained in section B.2.1.1.

4397 B.7 Current information extraction

4398 Detectors under test at GIF++ are connected both to a CAEN HV power supply and to a CAEN
4399 ADC that reads the currents inside of the RPC gaps bypassing the supply cable. During data tak-
4400 ing, the webDCS records into a ROOT file called `Scan00XXXX_HVY_CAEN.root` histograms with the
4401 monitored parameters of both CAEN devices. Are recorded for each RPC channels (in most cases,
4402 a channel corresponds to an RPC gap):

- 4403 • the effective voltage, HV_{eff} , set by the webDCS using the PT correction on the CAEN power
4404 supply,
- 4405 • the applied voltage, HV_{app} , monitored by the CAEN power supply, and the statistical error
4406 related to the variations of this value through time to follow the variation of the environmental
4407 parameters defined as the RMS of the histogram divided by the square root of the number of
4408 recorded points,
- 4409 • the monitored current, I_{mon} , monitored by the CAEN power supply, and the statistical error
4410 related to the variations of this value through time to follow the variation of the environmental
4411 parameters defined as the RMS of the histogram divided by the square root of the number of
4412 recorded points,
- 4413 • the corresponding current density, J_{mon} , defined as the monitored current per unit area,
4414 $J_{mon} = I_{mon}/A$, where A is the active area of the corresponding gap,
- 4415 • the ADC current, I_{ADC} , recorded through the CAEN ADC module that monitors the dark
4416 current in the gap itself. First of all, the resolution of such a module is better than that of
4417 CAEN power supplies and moreover, the current is not read-out through the HV supply line
4418 but directly at the chamber level giving the real current inside of the detector. The statistical
4419 error is defined as the RMS of the histogram distribution divided by the square root of the
4420 number of recorded points.

4421 Once extracted through a loop over the element of GIF++ infrastructure via the C++ macro
4422 `GetCurrent()`, these parameters, organised in 9 columns per detector HV supply line, are written in
4423 the output CSV file `Offline-Current.csv`. The macro can be found in the file `Current.cc`.

References

- [1] K. Ruedenberg & W.H.E. Schwarz. “Three Millennia of Atoms and Molecules”. In: *Pioneers of Quantum Chemistry*. Ed. by Angela K. Wilson E. Thomas Strom. Vol. 1122. ACS Symposium Series, 2013, pp. 1–45.
- [2] A. Lavoisier. *Traité élémentaire de chimie*. Éditions la Bibliothèque Digitale, 2014 (first published 1789).
- [3] J. Dalton. *A New System of Chemical Philosophy*. William Dawson & Sons, 1808.
- [4] J. von Fraunhofer. “Bestimmung des Brechungs- und des Farben-Zerstreuungs - Vermögens verschiedener Glasarten, in Bezug auf die Vervollkommnung achromatischer Fernröhre”. In: *Denkschriften der Königlichen Akademie der Wissenschaften zu München*. Die Akademie, 1817, pp. 193–226.
- [5] J.J. Thomson. “XL. Cathode Rays”. In: *The London, Edinburgh, and Dublin Philosophical Magazine and Journal of Science* 44:269 (1897), pp. 293–316.
- [6] J.B. Perrin. “Nouvelles propriétés des rayons cathodiques”. In: *Comptes Rendus Hebdomadaires des Séances de L'Académie des Sciences*. Vol. 121. Académie des Sciences, 1895, pp. 1130–1134.
- [7] H. Becquerel. “Déviation du rayonnement du radium dans un champ électrique”. In: *Comptes Rendus Hebdomadaires des Séances de L'Académie des Sciences*. Vol. 130. Académie des Sciences, 1900, p. 809.
- [8] J.J. Thomson. “XXIV. On the structure of the atom: an investigation of the stability and periods of oscillation of a number of corpuscles arranged at equal intervals around the circumference of a circle; with application of the results to the theory of atomic structure”. In: *The London, Edinburgh, and Dublin Philosophical Magazine and Journal of Science* 7:39 (1904), pp. 237–265.
- [9] E. Rutherford & T. Royds. “XXIV. Spectrum of the radium emanation”. In: *The London, Edinburgh, and Dublin Philosophical Magazine and Journal of Science* 16:92 (1904), pp. 313–317.
- [10] H. Geiger. “On the scattering of the α -particles by matter”. In: *Proceedings of the Royal Society A* 81 (1908), pp. 174–177.
- [11] H. Geiger & E. Marsden. “On a diffuse reflection of the α -particles”. In: *Proceedings of the Royal Society A* 82 (1909), pp. 495–500.
- [12] H. Geiger. “The scattering of α -particles by matter”. In: *Proceedings of the Royal Society A* 83 (1910), pp. 492–504.
- [13] H. Geiger & E. Marsden. “LXI. The laws of deflexion of a particles through large angles”. In: *The London, Edinburgh, and Dublin Philosophical Magazine and Journal of Science* 25:148 (1913), pp. 604–623.

- 4460 [14] E. Rutherford. "LXXIX. The Scattering of α and β Particles by Matter and the Structure of
4461 the Atom". In: *The London, Edinburgh, and Dublin Philosophical Magazine and Journal of*
4462 *Science* 21:125 (1911), pp. 669–688.
- 4463 [15] E. Rutherford. "LIV. Collision of α particles with light atoms. IV. An anomalous effect in
4464 nitrogen". In: *The London, Edinburgh, and Dublin Philosophical Magazine and Journal of*
4465 *Science* 37:222 (1919), pp. 581–587.
- 4466 [16] O. Masson. "XXIV. The constitution of atoms". In: *The London, Edinburgh, and Dublin*
4467 *Philosophical Magazine and Journal of Science* 41:242 (1921), pp. 281–285.
- 4468 [17] W. Prout. "On the Relation between the Specific Gravities of Bodies in their Gaseous State
4469 and the Weights of their Atoms." In: *Annals of Philosophy* 6 (1815), pp. 321–330.
- 4470 [18] W. Prout. "Correction of a Mistake in the Essay on the Relation between the Specific Gravities
4471 of Bodies in their Gaseous State and the Weights of their Atoms". In: *Annals of Philosophy*
4472 7 (1816), pp. 111–113.
- 4473 [19] E. Rutherford. "Bakerian Lecture: Nuclear constitution of atoms". In: *Proceedings of the*
4474 *Royal Society A* 97 (1920), pp. 374–400.
- 4475 [20] W. Bothe & H. Becker. "Künstliche Erregung von Kern- γ -Strahlen". In: *Zeitschrift für Physik*
4476 66 (1930), pp. 289–306.
- 4477 [21] H. Becker & W. Bothe. "Die in Bor und Beryllium erregten γ -Strahlen". In: *Zeitschrift für*
4478 *Physik* 76 (1932), pp. 421–438.
- 4479 [22] I. Curie & F. Joliot. "Émission de protons de grande vitesse par les substances hydrogenées
4480 sous l'influence de rayons γ très pénétrants". In: *Comptes Rendus Hebdomadaires des Séances*
4481 *de L'Académie des Sciences*. Vol. 194. Académie des Sciences, 1932, pp. 273–275.
- 4482 [23] J. Chadwick. "Possible Existence of a Neutron". In: *Nature* 129 (1932), p. 312.
- 4483 [24] J. Chadwick. "Bakerian lecture. The neutron". In: *Proceedings of the Royal Society A* 142
4484 (1933), pp. 1–25.
- 4485 [25] Max Plank. "Ueber das Gesetz der Energieverteilung im Normalspectrum". In: *Annalen Der*
4486 *Physik* 309 (1901), pp. 553–563.
- 4487 [26] A. Einstein. "Über einen die Erzeugung und Verwandlung des Lichtes betreffenden heuristischen
4488 Gesichtspunkt". In: *Annalen Der Physik* 322 (1905), pp. 132–148.
- 4489 [27] N. Bohr. "I. On the constitution of atoms and molecules". In: *The London, Edinburgh, and*
4490 *Dublin Philosophical Magazine and Journal of Science* 26:151 (1913), pp. 1–25.
- 4491 [28] H.G.J. Moseley. "XCIII. The high-frequency spectra of the elements". In: *The London, Edinburgh,*
4492 *and Dublin Philosophical Magazine and Journal of Science* 26:156 (1913), pp. 1024–
4493 1034.
- 4494 [29] A. Sommerfeld. "Zur Quantentheorie der Spektrallinien". In: *Annalen Der Physik* 356 (1916),
4495 pp. 1–94.
- 4496 [30] P. Zeeman. "XXXII. On the influence of magnetism on the nature of the light emitted by a
4497 substance". In: *The London, Edinburgh, and Dublin Philosophical Magazine and Journal of*
4498 *Science* 43:262 (1897), pp. 226–239.
- 4499 [31] P. Zeeman. "VII. Doublets and triplets in the spectrum produced by external magnetic forces".
4500 In: *The London, Edinburgh, and Dublin Philosophical Magazine and Journal of Science*
4501 44:266 (1897), pp. 55–60.
- 4502 [32] P. Zeeman. "VII. Doublets and triplets in the spectrum produced by external magnetic forces.—(II.)"
4503 In: *The London, Edinburgh, and Dublin Philosophical Magazine and Journal of Science*
4504 44:268 (1897), pp. 255–259.

BIBLIOGRAPHY

- 4505 [33] P. Zeeman. "XXI. Measurements concerning radiation-phenomena in the magnetic field.—(I.)"
4506 In: *The London, Edinburgh, and Dublin Philosophical Magazine and Journal of Science*
4507 45:273 (1898), pp. 197–201.
- 4508 [34] W. Gerlach & O. Stern. "Der experimentelle Nachweis der Richtungsquantelung im Mag-
4509 netfeld". In: *Zeitschrift für Physik* 9 (1922), pp. 349–352.
- 4510 [35] W. Pauli. "Über den Einfluß der Geschwindigkeitsabhängigkeit der Elektronenmasse auf den
4511 Zeeman-Effekt". In: *Zeitschrift für Physik* 31 (1925), 373–385.
- 4512 [36] W. Pauli. "Über den Zusammenhang des Abschlusses der Elektronengruppen im Atom mit
4513 der Komplexstruktur der Spektren". In: *Zeitschrift für Physik* 31 (1925), 765–783.
- 4514 [37] G.E. Uhlenbeck & S. Goudsmit. "Spinning Electrons and the Structure of Spectra". In: *Nature*
4515 117 (1926), pp. 264–265.
- 4516 [38] W. Pauli. "Zur Quantenmechanik des magnetischen Elektrons". In: *Zeitschrift für Physik* 43
4517 (1927), 601–623.
- 4518 [39] L. De Broglie. "Recherches sur la théorie des Quanta". PhD thesis. University of Paris, 1924.
- 4519 [40] E. Schrödinger. "An Undulatory Theory of the Mechanics of Atoms and Molecules". In:
4520 *Phys. Rev.* 28 (1927), pp. 1049–1070.
- 4521 [41] P. Dirac. "The quantum theory of the emission and absorption of radiation". In: *Proceedings
4522 of the Royal Society A* 114 (1928), pp. 243–265.
- 4523 [42] P. Dirac. "The quantum theory of the electron". In: *Proceedings of the Royal Society A* 117
4524 (1928), pp. 610–624.
- 4525 [43] J. R. Oppenheimer. "On the Theory of Electrons and Protons". In: *Phys. Rev.* 35 (1930),
4526 pp. 562–563.
- 4527 [44] P. Dirac. "Quantised singularities in the electromagnetic field". In: *Proceedings of the Royal
4528 Society A* 133 (1931), pp. 60–72.
- 4529 [45] J. R. Oppenheimer. "Note on the Theory of the Interaction of Field and Matter". In: *Phys.
4530 Rev.* 35 (1930), pp. 461–477.
- 4531 [46] H.A. Bethe. "The Electromagnetic Shift of Energy Levels". In: *Phys. Rev.* 72 (1947), pp. 339–
4532 341.
- 4533 [47] H.F.J. Dyson. "The Radiation Theories of Tomonaga, Schwinger, and Feynman". In: *Phys.
4534 Rev.* 75 (1949), pp. 486–502.
- 4535 [48] H. Yukawa. "On the Interaction of Elementary Particles. I". In: *Proc. Phys. Math. Soc. Jap.*
4536 17 (1935), pp. 48–57.
- 4537 [49] C.D. Anderson & S.H. Neddermeyer. "Cloud Chamber Observations of Cosmic Rays at 4300
4538 Meters Elevation and Near Sea-Level". In: *Phys. Rev.* 50 (1936), pp. 263–271.
- 4539 [50] S.H. Neddermeyer & C.D. Anderson. "Note on the Nature of Cosmic-Ray Particles". In:
4540 *Phys. Rev.* 51 (1937), pp. 884–886.
- 4541 [51] J.C. Street & E.C. Stevenson. "New Evidence for the Existence of a Particle of Mass Inter-
4542 mediate Between the Proton and Electron". In: *Phys. Rev.* 52 (1937), pp. 1003–1004.
- 4543 [52] C.M.G. Lattes et al. "Processes involving charged mesons". In: *Nature* 159 (1947), pp. 694–
4544 697.
- 4545 [53] C.M.G. Lattes et al. "Observations on the Tracks of Slow Mesons in Photographic Emulsions
4546 (Part 1)". In: *Nature* 160 (1947), pp. 453–456.

- 4547 [54] C.M.G. Lattes et al. “Observations on the Tracks of Slow Mesons in Photographic Emulsions
4548 (Part 2)”. In: *Nature* 160 (1947), 486–492.
- 4549 [55] R. Blokland et al. “High Energy Photons from Proton-Nucleon Collisions”. In: *Phys. Rev.*
4550 77 (1950), pp. 213–218.
- 4551 [56] G.D. Rochester & C.C. Butler. “Evidence for the Existence of New Unstable Elementary
4552 Particles”. In: *Nature* 160 (1947), 855–857.
- 4553 [57] A. Pais. “Some Remarks on the V-Particles”. In: *Phys. Rev.* 86 (1952), pp. 663–672.
- 4554 [58] M. Gell-Mann. “Symmetries of Baryons and Mesons”. In: *Phys. Rev.* 125 (1962), pp. 1067–
4555 1084.
- 4556 [59] K. Nishijima & T. Nakano. “Charge Independence for V-particles”. In: *Progress of Theoretical
4557 Physics* 10 (1953), 581–582.
- 4558 [60] K. Nishijima. “Charge Independence Theory of V-Particles”. In: *Progress of Theoretical
4559 Physics* 13 (1955), pp. 285–304.
- 4560 [61] M. Gell-Mann. “The interpretation of the new particles as displaced charge multiplets”. In:
4561 *Il Nuovo Cimento* 4 (1956), 848–866.
- 4562 [62] W. Heisenberg. “Über den Bau der Atomkerne. I”. In: *Zeitschrift für Physik* 77 (1932), 1–11.
- 4563 [63] V.E. Barnes et al. “Observation of a Hyperon with Strangeness Minus Three”. In: *Phys. Rev.
4564 Lett.* 12 (1964), pp. 204–206.
- 4565 [64] M. Gell-Mann. “A schematic model of baryons and mesons”. In: *Physics Letters* 8 (1964),
4566 pp. 214–215.
- 4567 [65] G. Zweig. *An SU(3) Model for Strong Interaction Symmetry and its Breaking*. Tech. rep.
4568 CERN-TH-401. CERN, 1964.
- 4569 [66] G. Zweig. *An SU(3) Model for Strong Interaction Symmetry and its Breaking (II)*. Tech. rep.
4570 CERN-TH-412. CERN, 1964.
- 4571 [67] E.D. Bloom et al. “High-Energy Inelastic $e - p$ Scattering at 6° and 10° ”. In: *Phys. Rev. Lett.*
4572 23 (1969), pp. 930–934.
- 4573 [68] M. Breidenbach et al. “Observed Behavior of Highly Inelastic Electron-Proton Scattering”.
4574 In: *Phys. Rev. Lett.* 23 (1969), pp. 935–939.
- 4575 [69] B.J. Bjørken & S.L. Glashow. “Elementary particles and SU(4)”. In: *Physics Letters* 11
4576 (1964), pp. 255–257.
- 4577 [70] J. Iliopoulos & L. Maiani S. Glashow. “Weak Interactions with Lepton-Hadron Symmetry”.
4578 In: *Phys. Rev. D* 2 (1970), pp. 1285–1292.
- 4579 [71] J.H. Christenson et al. “Evidence for the 2π Decay of the K_2^0 Meson”. In: *Phys. Rev. Lett.* 13
4580 (1964), pp. 138–140.
- 4581 [72] M. Kobayashi & T. Maskawa. “CP-Violation in the Renormalizable Theory of Weak Inter-
4582 action”. In: *Progress of Theoretical Physics* 49 (1973), pp. 652–657.
- 4583 [73] H. Harari. “A new quark model for hadrons”. In: *Physics Letters B* 57 (1975), pp. 265–269.
- 4584 [74] B. Richter et al. “Discovery of a Narrow Resonance in e^+e^- Annihilation”. In: *Phys. Rev.
4585 Lett.* 33 (1974), pp. 1406–1408.
- 4586 [75] S. Ting et al. “Experimental Observation of a Heavy Particle J ”. In: *Phys. Rev. Lett.* 33
4587 (1974), pp. 1404–1405.
- 4588 [76] S.W. Herb et al. “Observation of a Dimuon Resonance at 9.5 GeV in 400 GeV Proton-
4589 Nucleus Collisions”. In: *Phys. Rev. Lett.* 39 (1977), pp. 252–255.

BIBLIOGRAPHY

- 4590 [77] S. Abashi et al. “Search for High Mass Top Quark Production in $\bar{p}p$ Collisions at $\sqrt{s} =$
4591 1.8 TeV”. In: *Phys. Rev. Lett.* 74 (1995), pp. 2422–2426.
- 4592 [78] F. Abe et al. “Observation of Top Quark Production in $\bar{p}p$ Collisions with the Collider De-
4593 tector at Fermilab”. In: *Phys. Rev. Lett.* 74 (1995), pp. 2626–2631.
- 4594 [79] F. Tkachov. “A contribution to the history of quarks: Boris Struminsky’s 1965 JINR publi-
4595 cation”. In: (2009).
- 4596 [80] O.W. Greenberg. “Spin and Unitary-Spin Independence in a Paraquark Model of Baryons
4597 and Mesons”. In: *Phys. Rev. Lett.* 13 (1964), pp. 598–602.
- 4598 [81] M.Y. Han & Y. Nambu. “Three-Triplet Model with Double $SU(3)$ Symmetry”. In: *Phys.*
4599 *Rev.* 139 (1965), B1006–B1010.
- 4600 [82] R.P. Feynman. “The behavior of hadron collisions at extreme energies”. In: *Conf. Proc.*
4601 C690905 (1969), pp. 237–258.
- 4602 [83] J.D. Bjorken & E.A. Paschos. “Inelastic Electron-Proton and γ -Proton Scattering and the
4603 Structure of the Nucleon”. In: *Phys. Rev.* 185 (1969), pp. 1975–1982.
- 4604 [84] M. Gell-Mann & H. Leutwyler H. Fritzsch. “Advantages of the color octet gluon picture”.
4605 In: *Physics Letters B* 47 (1973), pp. 365–368.
- 4606 [85] D.J. Gross & F. Wilczek. “Ultraviolet Behavior of Non-Abelian Gauge Theories”. In: *Phys.*
4607 *Rev. Lett.* 30 (1973), pp. 1343–1346.
- 4608 [86] H.D. Politzer. “Reliable Perturbative Results for Strong Interactions?” In: *Phys. Rev. Lett.* 30
4609 (1973), pp. 1346–1349.
- 4610 [87] S. Bethke. “ α_s 2002”. In: *Nuclear Physics B* 121 (2003), pp. 74–81.
- 4611 [88] E. Fermi. “Versuch einer Theorie der β -Strahlen. I”. In: *Zeitschrift für Physik* 88 (1934),
4612 pp. 161–177.
- 4613 [89] W. Pauli. “Dear radioactive ladies and gentlemen”. In: *Phys. Today* 31N9 (1978), p. 27.
- 4614 [90] C.L. Cowan Jr. et al. “Detection of the Free Neutrino: a Confirmation”. In: *Science* 20 (1956),
4615 pp. 103–104.
- 4616 [91] E.J. Konopinski & H.M. Mahmoud. “The Universal Fermi Interaction”. In: *Phys. Rev.* 92
4617 (1953), pp. 1045–1049.
- 4618 [92] J. Steinberger et al. L.M. Lederman M. Schwartz. “Observation of High-Energy Neutrino Re-
4619 actions and the Existence of Two Kinds of Neutrinos”. In: *Phys. Rev. Lett.* 9 (1962), pp. 36–
4620 44.
- 4621 [93] T.D. Lee & C.N. Yang. “Question of Parity Conservation in Weak Interactions”. In: *Phys.*
4622 *Rev.* 104 (1956), pp. 254–258.
- 4623 [94] G. Gamow & E. Teller. “Selection Rules for the β -Disintegration”. In: *Phys. Rev.* 49 (1936),
4624 pp. 895–899.
- 4625 [95] C.S. Wu et al. “Experimental Test of Parity Conservation in Beta Decay”. In: *Phys. Rev.* 105
4626 (1957), pp. 1413–1415.
- 4627 [96] S. Weinberg. “A Model of Leptons”. In: *Phys. Rev. Lett.* 19 (1967), pp. 1264–1266.
- 4628 [97] Y. Nambu & G. Jona-Lasinio. “Dynamical Model of Elementary Particles Based on an Anal-
4629 ogy with Superconductivity. I”. In: *Phys. Rev.* 122 (1961), pp. 345–358.
- 4630 [98] Y. Nambu & G. Jona-Lasinio. “Dynamical Model of Elementary Particles Based on an Anal-
4631 ogy with Superconductivity. II”. In: *Phys. Rev.* 124 (1961), pp. 246–254.

- 4632 [99] & J. R. Schrieffer J. Bardeen L.N. Cooper. “Microscopic Theory of Superconductivity”. In: *Phys. Rev.* 106 (1957), pp. 162–164.
- 4633
- 4634 [100] Y. Nambu. “Quasi-Particles and Gauge Invariance in the Theory of Superconductivity”. In: *Phys. Rev.* 117 (1960), pp. 648–663.
- 4635
- 4636 [101] J. Goldstone. “Quasi-Particles and Gauge Invariance in the Theory of Superconductivity”. In: *Il Nuovo Cimento* 19 (1961), pp. 154–164.
- 4637
- 4638 [102] P.W. Anderson. “Plasmons, Gauge Invariance, and Mass”. In: *Phys. Rev.* 130 (1963), pp. 439–442.
- 4639
- 4640 [103] J. Schwinger. “Gauge Invariance and Mass”. In: *Phys. Rev.* 125 (1962), pp. 397–398.
- 4641 [104] F. Englert & R. Brout. “Broken Symmetry and the Mass of Gauge Vector Mesons”. In: *Phys. Rev. Lett.* 13 (1964), pp. 321–323.
- 4642
- 4643 [105] P.W. Higgs. “Broken Symmetries and the Masses of Gauge Bosons”. In: *Phys. Rev. Lett.* 13 (1964), pp. 508–509.
- 4644
- 4645 [106] & T.W.B. Kibble G.S. Guralnik C.R. Hagen. “Global Conservation Laws and Massless Particles”. In: *Phys. Rev. Lett.* 13 (1964), pp. 585–587.
- 4646
- 4647 [107] Wikipedia. *Standard Model*. 2018. URL: https://en.wikipedia.org/wiki/Standard_Model.
- 4648
- 4649 [108] UA1 Collaboration. “Experimental observation of isolated large transverse energy electrons with associated missing energy at $s = 540 \text{ GeV}$ ”. In: *Physics Letters B* 122 (1983), pp. 103–116.
- 4650
- 4651
- 4652 [109] UA2 Collaboration. “Observation of single isolated electrons of high transverse momentum in events with missing transverse energy at the CERN pp collider”. In: *Physics Letters B* 122 (1983), pp. 476–485.
- 4653
- 4654
- 4655 [110] UA1 Collaboration. “Experimental observation of lepton pairs of invariant mass around $95 \text{ GeV}/c^2$ at the CERN SPS collider”. In: *Physics Letters B* 126 (1983), pp. 398–410.
- 4656
- 4657 [111] UA2 Collaboration. “Evidence for $Z_0 \rightarrow e^+e^-$ at the CERN pp collider”. In: *Physics Letters B* 129 (1983), pp. 130–140.
- 4658
- 4659 [112] ATLAS Collaboration. “Observation of a new particle in the search for the Standard Model Higgs boson with the ATLAS detector at the LHC”. In: *Physics Letters B* 716 (2012), pp. 1–29.
- 4660
- 4661
- 4662 [113] CMS Collaboration. “Observation of a new boson at a mass of 125 GeV with the CMS experiment at the LHC”. In: *Physics Letters B* 716 (2012), pp. 30–61.
- 4663
- 4664 [114] CMS Collaboration ATLAS Collaboration. “Combined Measurement of the Higgs Boson Mass in pp Collisions at $\sqrt{s} = 7$ and 8 TeV with the ATLAS and CMS Experiments”. In: *Physical Review Letters* 114 (2015). 191803.
- 4665
- 4666
- 4667 [115] M. Tanabashi et al. (Particle Data Group). “Review of Particle Physics”. In: *Phys. Rev. D* 98 (2018), p. 030001.
- 4668
- 4669 [116] A.A. Arkhipov. “Proton proton total cross-sections from the window of cosmic ray experiments”. In: *Elastic and diffractive scattering. Proceedings, 9th Blois Workshop, Pruhonice, Czech Republic*. 2001, pp. 293–304.
- 4670
- 4671
- 4672 [117] H. Pointcaré. “The Milky Way and the Theory of Gases”. In: *Popular Astronomy* 14 (1906), pp. 475–488.
- 4673
- 4674 [118] J.C. Kapteyn. “First Attempt at a Theory of the Arrangement and Motion of the Sidereal System”. In: *Astrophysical Journal* 55 (1922), p. 302.
- 4675

BIBLIOGRAPHY

- 4676 [119] F. Zwicky. “Republication of: The redshift of extragalactic nebulae (First published in
4677 1933)”. In: *General Relativity and Gravitation* 41 (2009), pp. 207–224.
- 4678 [120] F. Zwicky. “On the Masses of Nebulae and of Clusters of Nebulae”. In: *Astrophysical Journal* 86 (1937), p. 217.
- 4680 [121] H.W. Babcock. “The rotation of the Andromeda Nebula”. In: *Lick Observatory bulletin* 498 (1939), pp. 41–51.
- 4682 [122] V.C. Rubin & W.K. Ford Jr. “Rotation of the Andromeda Nebula from a Spectroscopic Survey of Emission Regions”. In: *Astrophysical Journal* 159 (1970), p. 379.
- 4684 [123] D.H. Rogstad & G.S. Shostak. “Gross Properties of Five Scd Galaxies as Determined from 21-CENTIMETER Observations”. In: *Astrophysical Journal* 176 (1972), p. 315.
- 4686 [124] Planck Collaboration. “Planck 2015 results. XIII. Cosmological parameters”. In: *A&A* 594.A13 (2016).
- 4688 [125] N. Jarosik et al. “Seven-year Wilkinson Microwave Anisotropy Probe (WMAP*) observations: Sky maps, Systematic errors, and Basic Results”. In: *ApJS* 192.14 (2011).
- 4690 [126] E. Verlinde. “Emergent Gravity and the Dark Universe”. In: *SciPost Phys.* 2 (2017), p. 016.
- 4691 [127] A. Maeder. “An alternative to the Λ CDM model: the case of scale invariance”. In: *ApJ* 834.194 (2017).
- 4693 [128] E. Corbelli & P. Salucci. “The extended rotation curve and the dark matter halo of M33”. In: *Monthly Notices of the Royal Astronomical Society* 311 (2000), pp. 441–447.
- 4695 [129] S. Dimopoulos & H. Georgi. “Softly broken supersymmetry and SU(5)”. In: *Nuclear Physics B* 193 (1981), pp. 150–162.
- 4697 [130] F. Tanedo. *The Hierarchy Problem: why the Higgs has a snowball’s chance in hell*. 2012.
4698 URL: [https://www.quantumdiaries.org/2012/07/01/the-hierarchy-
4699 problem-why-the-higgs-has-a-snowballs-chance-in-hell/](https://www.quantumdiaries.org/2012/07/01/the-hierarchy-problem-why-the-higgs-has-a-snowballs-chance-in-hell/).
- 4700 [131] M. Kamionkowski & K. Griest G. Jungman. “Supersymmetric dark matter”. In: *Physics Reports* 267 (1996), pp. 10–14.
- 4702 [132] & P. Nath A.H. Chamseddine R. Arnowitt. “Locally Supersymmetric Grand Unification”. In: *Phys. Rev. Lett.* 49 (1982), pp. 970–974.
- 4704 [133] A. Askew et al. “Searching for dark matter at hadron colliders”. In: *International Journal of Modern Physics A* 29 (2014), p. 1430041.
- 4706 [134] S. Dimopoulos & G. Dvali N. Arkani-Hamed. “The hierarchy problem and new dimensions at a millimeter”. In: *Physics Letters B* 429 (1998), pp. 263–272.
- 4708 [135] S. Dimopoulos & G. Dvali N. Arkani-Hamed. “Phenomenology, astrophysics, and cosmology of theories with submillimeter dimensions and TeV scale quantum gravity”. In: *Phys. Rev. D* 59 (1999), p. 086004.
- 4711 [136] T. Kaluza. “Zum Unitsproblem der Physik”. In: *Sitzungsber. Preuss. Akad. Wiss. Berlin (Math. Phys.)* 1921 (1921), pp. 966–972.
- 4713 [137] O. Klein. “The Atomicity of Electricity as a Quantum Theory Law”. In: *Nature* 118 (1926), p. 516.
- 4715 [138] L. Randall & R. Sundrum. “Large Mass Hierarchy from a Small Extra Dimension”. In: *Phys. Rev. Lett.* 83 (1999), pp. 3370–3373.
- 4717 [139] L. Randall & R. Sundrum. “An Alternative to Compactification”. In: *Phys. Rev. Lett.* 83 (1999), pp. 4690–4693.

- 4719 [140] M. Strassler & K. Zurek. “Echoes of a hidden valley at hadron colliders”. In: *Phys. Let. B*
4720 651 (2007), pp. 374–379.
- 4721 [141] A. Sakharov. “Violation of CP i variance, C asymmetry, and baryon asymmetry of the uni-
4722 verse”. In: *JETP Letters* 5 (1967), pp. 24–27.
- 4723 [142] M.E. Shaposhnikov & G. Farrar. “Baryon asymmetry of the Universe in the minimal stan-
4724 dard model”. In: *Phys. Rev. Lett.* 70 (1993), pp. 2833–2836.
- 4725 [143] V.A.Rubakov & M.E. Shaposhnikov V.A. Kuzmin. “On anomalous electroweak baryon-
4726 number non-conservation in the early universe”. In: *Physics Letters B* 155 (1985), pp. 36–
4727 42.
- 4728 [144] M. Drewes & M. Shaposhnikov L. Canetti. “Matter and antimatter in the universe”. In: *New
4729 J. Phys.* 14.095012 (2012).
- 4730 [145] CMS Collaboration. “Search for black holes and sphalerons in high-multiplicity final states
4731 in proton-proton collisions at $\sqrt{s} = 13$ TeV”. In: *Journal of High Energy Physics* 11 (2018).
- 4732 [146] B. Shuve & Y. Cui. “Probing baryogenesis with displaced vertices at the LHC”. In: *Journal
4733 of High Energy Physics* 2 (2015).
- 4734 [147] The ACME Collaboration. “Order of Magnitude Smaller Limit on the Electric Dipole Mo-
4735 ment of the Electron”. In: *Science* 343 (2014), pp. 269–272.
- 4736 [148] N. Neri et al. “On the search for the electric dipole moment of strange and charm baryons
4737 at LHC”. In: *The European Physical Journal C* 77 (2017), p. 181.
- 4738 [149] J. Stevens & M. Sher. “Detecting a heavy neutrino electric dipole moment at the LHC”. In:
4739 *Physics Letters B* 777 (2018), pp. 246–249.
- 4740 [150] D.S. Harmer & K.C. Hoffman R. Davis Jr. “Search for Neutrinos from the Sun”. In: *Physical
4741 Review Letters* 20 (1968), pp. 1205–1209.
- 4742 [151] B. Pontecorvo. “Neutrino Experiments and the Problem of Conservation of Leptonic Charge”.
4743 In: *Sov. Phys. JETP* 26 (1968), pp. 984–988.
- 4744 [152] SNO Collaboration. “Direct Evidence for Neutrino Flavor Transformation from Neutral-
4745 Current Interactions in the Sudbury Neutrino Observatory”. In: *Physical Review Letters*
4746 89.011301 (2002).
- 4747 [153] M. Nakagawa & S. Sakata Z. Maki. “Remarks on the Unified Model of Elementary Parti-
4748 cles”. In: *Progress of Theoretical Physics* 28 (1962), pp. 870–880.
- 4749 [154] P. Minkowski. “ $\mu \rightarrow e\gamma$ at a rate of one out of 10^9 muon decays?” In: *Physics Letters B*
4750 67 (1977), pp. 421–428.
- 4751 [155] R.N. Mohapatra & G. Senjanović. “Neutrino Mass and Spontaneous Parity Nonconserva-
4752 tion”. In: *Phys. Rev. Lett.* 44 (1980), pp. 912–915.
- 4753 [156] CERN. Geneva. LHC Experiments Committee. *CMS Physics Technical Design Report Vol-
4754 ume II: Physics Performance*. Tech. rep. CERN-LHCC-2006-021 ; CMS-TDR-8-2. CMS
4755 Collaboration, 2006.
- 4756 [157] P.W.F. Valle. “Neutrino physics overview”. In: *J. Phys.: Conf. Ser.* 53 (2006), pp. 473–505.
- 4757 [158] T. Massam et al. “Experimental observation of antideuteron production”. In: *Il Nuovo Ci-
4758 mento A* 63 (1965), pp. 10–14.
- 4759 [159] ALEPH Collaboration. “Determination of the number of light neutrino species”. In: *Physics
4760 Letters B* 231 (1989), pp. 519–529.
- 4761 [160] CERN, ed. (1985).

BIBLIOGRAPHY

- 4762 [161] CERN, ed. (1986).
- 4763 [162] CERN, ed. (1994).
- 4764 [163] CERN, ed. (1998).
- 4765 [164] CERN, ed. (1999).
- 4766 [165] CERN. Geneva. LHC Experiments Committee. *Letter of Intent for A Large Ion Collider*
4767 *Experiment [ALICE]*. Tech. rep. CERN-LHCC-93-016. ALICE Collaboration, 1993.
- 4768 [166] CERN. Geneva. LHC Experiments Committee. *ATLAS : technical proposal for a general-*
4769 *purpose pp experiment at the Large Hadron Collider at CERN*. Tech. rep. CERN-LHCC-94-
4770 43. ATLAS Collaboration, 1994.
- 4771 [167] CERN. Geneva. LHC Experiments Committee. *CMS : letter of intent by the CMS Col-*
4772 *laboration for a general purpose detector at LHC*. Tech. rep. CERN-LHCC-92-003. CMS
4773 Collaboration, 1992.
- 4774 [168] CERN. Geneva. LHC Experiments Committee. *LHCb : letter of intent*. Tech. rep. CERN-
4775 LHCC-95-5. LHCb Collaboration, 1995.
- 4776 [169] L. Evans and P. Bryant. “LHC Machine”. In: *JINST* 3 (2008). S08001.
- 4777 [170] LHCb Collaboration. “Observation of $J/\psi p$ Resonances Consistent with Pentaquark States
4778 in $\Lambda_b^0 \rightarrow J/\psi K^- p$ Decays”. In: *Physical Review Letters* 115 (2015). 072001.
- 4779 [171] LHCb Collaboration. “Observation of $J/\psi \phi$ Structures Consistent with Exotic States from
4780 Amplitude Analysis of $B^+ \rightarrow J/\psi \phi K^+$ Decays”. In: *Physical Review Letters* 118 (2017).
4781 022003.
- 4782 [172] ALICE Collaboration. *First results from proton-lead collisions*. URL: <http://aliceinfo.cern.ch/Public/en/Chapter1/results-pPb.html>.
- 4783
- 4784 [173] ATLAS Collaboration. “Observation of a New χ_b State in Radiative Transitions to $\Upsilon(1S)$
4785 and $\Upsilon(2S)$ at ATLAS”. In: *Physical Review Letters* 108 (2012). 152001.
- 4786 [174] LHCb Collaboration. “First Evidence for the Decay $B_s^0 \rightarrow \mu^+ \mu^-$ ”. In: *Physical Review*
4787 *Letters* 110 (2013). 021801.
- 4788 [175] CERN. Geneva. *High-Luminosity Large Hadron Collider (HL-LHC) Technical Design Re-*
4789 *port V. 0.1*. Tech. rep. CERN-2017-007-M. 2017.
- 4790 [176] CERN. Geneva. LHC Experiments Committee. *CMS, the Compact Muon Solenoid : tech-*
4791 *nical proposal*. Tech. rep. CERN-2015-005. 2015.
- 4792 [177] CERN. Geneva. LHC Experiments Committee. *The Phase-2 Upgrade of the CMS Muon*
4793 *Detectors*. Tech. rep. CERN-LHCC-2017-012, CMS-TDR-016. CMS Collaboration, 2017.
- 4794 [178] CERN. Geneva. LHC Experiments Committee. *The CMS muon project : Technical Design*
4795 *Report*. Tech. rep. CERN-LHCC-97-032. CMS Collaboration, 1997.
- 4796 [179] X. Tata M. Drees. “Signals for heavy exotics at hadron colliders and supercolliders”. In:
4797 *Physics Letters B* 252 (1990), pp. 695–702.
- 4798 [180] D.A. Milstead et al. “Stable massive particles at colliders”. In: *Physics Reports* 438 (2007),
4799 pp. 1–63.
- 4800 [181] Z. Ligeti et al. “Supermodels for early LHC”. In: *Physics Letters B* 690 (2010), pp. 280–
4801 288.
- 4802 [182] V. Khachatryan et al. “Search for long-lived charged particles in proton-proton collisions at
4803 $\sqrt{s} = 13$ TeV”. In: *Phys. Rev. D* 94 (2017). 112004.

- 4804 [183] M. Shaposhnikov A. Kusenko. “Supersymmetric Q-balls as dark matter”. In: *Physics Letters B* 418 (1998), pp. 46–54.
- 4805
- 4806 [184] B. Koch et al. “Black holes at LHC?” In: *J. Phys. G: Nucl. Part. Phys.* 34 (2007). S535.
- 4807 [185] J. Schwinger. “Magnetic Charge and Quantum Field Theory”. In: *Phys. Rev.* 144 (1966). 1087.
- 4808
- 4809 [186] M Yu Khlopov et al. “Dark matter with invisible light from heavy double charged leptons of almost-commutative geometry?” In: *Class. Quantum Grav.* 23 (2006). 7305.
- 4810
- 4811 [187] PoS, ed. *Search for Heavy Stable Charged Particles in CMS*. Vol. EPS-HEP2009. 2009, p. 438.
- 4812
- 4813 [188] CERN. Geneva. LHC Experiments Committee. *High-Luminosity Large Hadron Collider (HL-LHC) Preliminary Design Report*. Tech. rep. CERN-LHCC-94-38. CMS Collaboration, 1994.
- 4814
- 4815
- 4816 [189] CERN. Geneva. LHC Experiments Committee. *The Phase-2 Upgrade of the CMS Level-1 Trigger - Interim Report to the LHCC*. Tech. rep. CERN-LHCC-2017-013, CMS-TDR-017. CMS Collaboration, 2017.
- 4817
- 4818
- 4819 [190] CERN. Geneva. LHC Experiments Committee. *Technical Proposal for the Phase-II Upgrade of the CMS Detector*. Tech. rep. CERN-LHCC-2015-010, CMS-TDR-15-02. CMS Collaboration, 2015.
- 4820
- 4821
- 4822 [191] F.Sauli. “GEM: A new concept for electron amplification in gas detectors”. In: *Nucl. Instr. Meth. Phys. Res.* 386 (1997), pp. 531–534.
- 4823
- 4824 [192] CERN. Geneva. LHC Experiments Committee. *CMS Technical Design Report for the Muon Endcap GEM Upgrade*. Tech. rep. CERN-LHCC-2015-012, CMS-TDR-013. CMS Collaboration, 2015.
- 4825
- 4826
- 4827 [193] A. Gelmi. *CMS iRPC at HL-LHC: background study*. 2018. URL: https://indico.cern.ch/event/732794/contributions/3021836/attachments/1657792/2654574/iRPC_bkg_study_Upgrade29_05_18.pdf.
- 4828
- 4829
- 4830 [194] P.Bortignon. “Design and performance of the upgrade of the CMS L1 muon trigger”. In: *Nucl. Instr. Meth. Phys. Res.* 824 (2016), pp. 256–257.
- 4831
- 4832 [195] The European Parliament and the Council of the European Union. “Regulation (EU) No 517/2014 of 16 April 2014 on fluorinated greenhouse gases and repealing Regulation (EC) No 842/2006”. In: *Official Journal of the European Union* 150 (2014), pp. 195–230.
- 4833
- 4834
- 4835 [196] R. Santonico and R. Cardarelli. “Development of resistive plate counters”. In: *Nucl. Instr. Meth. Phys. Res.* 187 (1981), pp. 377–380.
- 4836
- 4837 [197] Yu.N. Pestov and G.V. Fedotovich. *A picosecond time-of-flight spectrometer fot eh VEPP-2M based on local-discharge spark counter*. Tech. rep. SLAC-TRANS-0184. SLAC, 1978.
- 4838
- 4839 [198] W.W. Ash, ed. *Spark Counter With A Localized Discharge*. Vol. SLAC-R-250. 1982, pp. 127–131.
- 4840
- 4841 [199] I. Crotty et al. “The non-spark mode and high rate operation of resistive parallel plate chambers”. In: *NIMA* 337 (1993), pp. 370–381.
- 4842
- 4843 [200] I. Crotty et al. “Further studies of avalanche mode operation of resistive parallel plate chambers”. In: *NIMA* 346 (1994), pp. 107–113.
- 4844
- 4845 [201] R. Cardarelli et al. “Avalanche and streamer mode operation of resistive plate chambers”. In: *NIMA* 382 (1996), pp. 470–474.
- 4846

BIBLIOGRAPHY

- 4847 [202] R. Cardarelli et al. “Performance of a resistive plate chamber operating with pure CF_3Br ”.
4848 In: *NIMA* 333 (1993), pp. 399–403.
- 4849 [203] M. Abbrescia et al. “Performance of a Resistive Plate Chamber operated in avalanche mode
4850 under ^{137}Cs irradiation”. In: *NIMA* 392 (1997), pp. 155–160.
- 4851 [204] M. Abbrescia et al. “Properties of C2H2F4-based gas mixture for avalanche mode operation
4852 of resistive plate chambers”. In: *NIMA* 398 (1997), pp. 173–179.
- 4853 [205] P. Camarri et al. “Streamer suppression with SF6 in RPCs operated in avalanche mode”. In:
4854 *NIMA* 414 (1998), pp. 317–324.
- 4855 [206] E. Cerron Zeballos et al. “Effect of adding SF6 to the gas mixture in a multigap resistive
4856 plate chamber”. In: *NIMA* 419 (1998), pp. 475–478.
- 4857 [207] E. Cerron Zeballos et al. “A new type of resistive plate chamber: The multigap RPC”. In:
4858 *NIMA* 374 (1996), pp. 132–135.
- 4859 [208] M.C.S. Williams. “The development of the multigap resistive plate chamber”. In: *Nucl.
4860 Phys. B* 61 (1998), pp. 250–257.
- 4861 [209] H. Czyrkowski et al. “New developments on resistive plate chambers for high rate opera-
4862 tion”. In: *NIMA* 419 (1998), pp. 490–496.
- 4863 [210] CERN. Geneva. LHC Experiments Committee. *ATLAS muon spectrometer: Technical de-
4864 sign report*. Tech. rep. CERN-LHCC-97-22. ATLAS Collaboration, 1997.
- 4865 [211] CERN. Geneva. LHC Experiments Committee. *ALICE Time-Of-Flight system (TOF) : Tech-
4866 nical Design Report*. Tech. rep. CERN-LHCC-2000-012. ALICE Collaboration, 2000.
- 4867 [212] The CALICE collaboration. “First results of the CALICE SDHCAL technological proto-
4868 type”. In: *JINST* 11 (2016).
- 4869 [213] PoS, ed. *Density Imaging of Volcanoes with Atmospheric Muons using GRPCs*. International
4870 Europhysics Conference on High Energy Physics - HEP 2011. 2011.
- 4871 [214] C. Lippmann. “Detector Physics of Resistive Plate Chambers”. PhD thesis. Johann Wolf-
4872 gang Goethe-Universität, 2003.
- 4873 [215] W. Riegler. “Induced signals in resistive plate chambers”. In: *NIMA* 491 (2002), pp. 258–
4874 271.
- 4875 [216] M. Abbrescia et al. “Effect of the linseed oil surface treatment on the performance of resis-
4876 tive plate chambers”. In: *NIMA* 394 (1997), pp. 13–20.
- 4877 [217] G.Battistoni et al. “Sensitivity of streamer mode to single ionization electrons”. In: *NIMA*
4878 235 (1985), pp. 91–97.
- 4879 [218] M. Abbrescia et al. “Cosmic ray tests of double-gap resistive plate chambers for the CMS
4880 experiment”. In: *NIMA* 550 (2005), pp. 116–126.
- 4881 [219] JINST, ed. *Performance of the Resistive Plate Chambers in the CMS experiment*. The 9th
4882 International Conference on Positioin Sensitive Detectors. 2012.
- 4883 [220] PoS, ed. *The CMS RPC detector performance during Run-II data taking*. The European
4884 Physical Society Conference on High Energy Physics (EPS-HEP2017). 2018.
- 4885 [221] Honeywell International Inc. *Solstice(R) ze Refrigerant (HFO-1234ze): The Environmental
4886 Alternative to Traditional Refrigerants*. Tech. rep. FPR-003/2015-01. 2015.
- 4887 [222] E. Cerron Zeballos et al. “A comparison of the wide gap and narrow gap resistive plate
4888 chamber”. In: *NIMA* 373 (1996), pp. 35–42.

- 4889 [223] ALICE Collaboration. “A study of the multigap RPC at the gamma irradiation facility at
4890 CERN”. In: *NIMA* 490 (2002), pp. 58–70.
- 4891 [224] B. Bonner et al. “A multigap resistive plate chamber prototype for time-of-flight for the
4892 STAR experiment at RHIC”. In: *NIMA* 478 (2002), pp. 176–179.
- 4893 [225] S. Yang et al. “Test of high time resolution MRPC with different readout modes for the
4894 BESIII upgrade”. In: *NIMA* 763 (2014), pp. 190–196.
- 4895 [226] A. Akindinov et al. “RPC with low-resistive phosphate glass electrodes as a candidate for
4896 the CBM TOF”. In: *NIMA* 572 (2007), pp. 676–681.
- 4897 [227] JINST, ed. *Development of the MRPC for the TOF system of the MultiPurpose Detector*.
4898 RPC2016: XII Workshop on Resistive Plate Chambers and Related Detectors. 2016.
- 4899 [228] M.C.S. Williams. “Particle identification using time of flight”. In: *Journal of Physics G* 39
4900 (2012).
- 4901 [229] A. Alici et al. “Aging and rate effects of the Multigap RPC studied at the Gamma Irradiation
4902 Facility at CERN”. In: *NIMA* 579 (2007), pp. 979–988.
- 4903 [230] M. Abbrescia et al. “The simulation of resistive plate chambers in avalanche mode: charge
4904 spectra and efficiency”. In: *NIMA* 431 (1999), pp. 413–427.
- 4905 [231] JINST, ed. *Description and simulation of physics of Resistive Plate Chambers*. RPC2016:
4906 XII Workshop on Resistive Plate Chambers and Related Detectors. 2016.
- 4907 [232] V. Francais. “Description and simulation of the physics of Resistive Plate Chambers”. PhD
4908 thesis. LPC - Laboratoire de Physique Corpusculaire - Clermont-Ferrand, 2017.
- 4909 [233] H. Bethe. “Zur Theorie des Durchgangs schneller Korpuskularstrahlen durch Materie”. In:
4910 *Annalen der Physik* 397 (1930), pp. 325–400.
- 4911 [234] International Commission on Radiation Units and Measurements. *Stopping Powers for Elec-*
4912 *trons and Positions*. Tech. rep. Report 37. 1984.
- 4913 [235] International Commission on Radiation Units and Measurements. *Stopping Power and Ranges*
4914 *for Protons and Alpha Particles*. Tech. rep. Report 49. 1994.
- 4915 [236] H. Bichsel. “A method to improve tracking and particle identification in TPCs and silicon
4916 detectors”. In: *NIMA* 562 (2006), pp. 154–197.
- 4917 [237] W. W. M. Allison and J. H. Cobb. “Relativistic charged particle identification by energy
4918 loss”. In: *Annual Review of Nuclear and Particle Science* 30 (1980), 253–298.
- 4919 [238] International Commission on Radiation Units and Measurements. *Average energy to pro-*
4920 *duce an ion pair*. Tech. rep. Report 31. 1994.
- 4921 [239] I.B. Smirnov. “Modeling of ionization produced by fast charged particles in gases”. In:
4922 *NIMA* 554 (2005), pp. 474–493.
- 4923 [240] J. Phys.: Conf. Ser., ed. <https://doi.org/10.1088/1742-6596/587/1/012035> *Results of the CAL-*
4924 *ICE SDHCAL technological prototype*. 16th International Conference on Calorimetry in
4925 High Energy Physics (CALOR 2014). 2015.
- 4926 [241] W. Riegler et al. “Detector physics and simulation of resistive plate chambers”. In: *NIMA*
4927 500 (2003), pp. 144–162.
- 4928 [242] I.B. Smirnov. *HEED++ simulation program*. 2010. URL: <http://ismirnov.web.cern.ch/ismirnov/heed>.
- 4929 [243] S.F. Biagi. “Monte Carlo simulation of electron drift and diffusion in counting gases under
4930 the influence of electric and magnetic fields”. In: *NIMA* 421 (1999), pp. 234–240.

BIBLIOGRAPHY

- 4932 [244] W. H. Furry. “On Fluctuation Phenomena in the Passage of High Energy Electrons through
4933 Lead”. In: *Phys. Rev.* 52 (1937), pp. 569–581.
- 4934 [245] H. Genz. “Single electron detection in proportional gas counters”. In: *Nucl. Instr. and Meth.*
4935 112 (1973), pp. 83–90.
- 4936 [246] M. Abbrescia et al. “Resistive plate chambers performances at cosmic rays fluxes”. In:
4937 *NIMA* 359 (1995), pp. 603–609.
- 4938 [247] M. Abbrescia et al. “Resistive plate chambers performances at low pressure”. In: *NIMA* 394
4939 (1997), pp. 341–348.
- 4940 [248] M. Abbrescia. “Operation, performance and upgrade of the CMS Resistive Plate Chamber
4941 system at LHC”. In: *NIMA* 732 (2013), pp. 195–198.
- 4942 [249] F. Thyssen. “Commissioning, Operation and Performance of the CMS Resistive Plate Cham-
4943 ber System”. PhD thesis. Universiteit Gent, 2014.
- 4944 [250] M. Bianco. “ATLAS RPC certification and commissioning with cosmic rays”. PhD thesis.
4945 Università del Salento, 2007.
- 4946 [251] M. Bianco. “ATLAS RPC certification with cosmic rays”. In: *NIMA* 602 (2009), pp. 700–
4947 704.
- 4948 [252] M. Abbrescia et al. “Study of long-term performance of CMS RPC under irradiation at the
4949 CERN GIF”. In: *NIMA* 533 (2004), pp. 102–106.
- 4950 [253] H.C. Kim et al. “Quantitative aging study with intense irradiation tests for the CMS forward
4951 RPCs”. In: *NIMA* 602 (2009), pp. 771–774.
- 4952 [254] S. Agosteo et al. “A facility for the test of large-area muon chambers at high rates”. In:
4953 *NIMA* 452 (2000), pp. 94–104.
- 4954 [255] PoS, ed. *CERN GIF ++ : A new irradiation facility to test large-area particle detectors for*
4955 *the high-luminosity LHC program*. Vol. TIPP2014. 2014, pp. 102–109.
- 4956 [256] D. Pfeiffer et al. “The radiation field in the Gamma Irradiation Facility GIF++ at CERN”.
4957 In: *NIMA* 866 (2017), pp. 91–103.
- 4958 [257] CAEN. *Mod. V1190-VX1190 A/B, 128/64 Ch Multihit TDC*. 14th ed. 2016.
- 4959 [258] CAEN. *Mod. V1718 VME USB Bridge*. 9th ed. 2009.
- 4960 [259] A. Fagot. *GIF Cosmic Muon Monte Carlo Simulation*. 2017. URL: <https://github.com/a-fagot/Cosmics-Simulation>.
- 4962 [260] G. Pugliese et al. “Long-term performance of double gap resistive plate chambers under
4963 gamma irradiation”. In: *NIMA* 477 (2002), pp. 293–298.
- 4964 [261] G. Pugliese et al. “Aging study for resistive plate chambers of the CMS muon trigger detec-
4965 tor”. In: *NIMA* 515 (2003), pp. 342–347.
- 4966 [262] M. Capeans et al. on behalf of the GIF and GIF++ User Communities. “A GIF++ Gamma
4967 Irradiation Facility at the SPS H4 Beam Line”. CERN-SPSC-2009-029 / SPSC-P-339. 2009.
- 4968 [263] R. Guida et al. “Results about HF production and bakelite analysis for the CMS Resistive
4969 Plate Chambers”. In: *NIMA* 594 (2008), pp. 140–147.
- 4970 [264] F. Bellini et al. “Study of HF production in BaBar Resistive Plate Chambers”. In: *NIMA* 594
4971 (2008), pp. 33–38.
- 4972 [265] J. Eysermans. *WebDCS GIF++*. CERN. 2016. URL: <https://www.webdcs.cern.ch>.

BIBLIOGRAPHY

- 4974 [266] S. Carrillo A. Fagot. *GIF++ Offline Analysis v6*. 2017. URL: https://github.com/afagot/GIF_OfflineAnalysis.
- 4975
- 4976 [267] H. Reithler. *Filters for GIF++*. RWTH Aachen University, CMS-CERN. 2013. URL: <https://edms.cern.ch/document/1324028/1>.
- 4977
- 4978 [268] R. Cardarelli et al. “RPC performance vs. front-end electronics”. In: *NIMA* 661 (2012), S198–S200.
- 4979
- 4980 [269] IEEE, ed. *Petiroc, a new front-end ASIC for time of flight application*. Vol. 2013 IEEE Nuclear Science Symposium and Medical Imaging Conference (2013 NSS/MIC). 2014.
- 4981
- 4982 [270] JINST, ed. *Petiroc and Citiroc: front-end ASICs for SiPM read-out and ToF applications*. Vol. Topical Workshop on Electronics for Particle Physics 2013 (TWEPP-13). 2014.
- 4983
- 4984 [271] A. Fagot. *GIF++ Data Acquisition Software for CMS RPC*. 2016. URL: https://github.com/afagot/GIF_DAQ.
- 4985
- 4986 [272] W-Ie-Ne-R. *VME 6021-23 VXI*. 5th ed. 2016.
- 4987 [273] Wikipedia. *INI file*. 2017. URL: https://en.wikipedia.org/wiki/INI_file.